IBRACON

IBRACON Structures and Materials Journal
Revista IBRACON de Estruturas e Materiais

IBRACON Structures and Materials Journal
Revista IBRACON de Estruturas e Materiais

Contents

Cover: Parametric Tower

Courtesy: Marcela Noronha P. de O. e Sousa

Aims and Scope

Aims and Scope

The IBRACON Structures and Materials Journal (in Portuguese: Revista IBRACON de Estruturas e Materiais) is a technical and scientific divulgation vehicle of IBRACON (Brazilian Concrete Institute), published every two months. Each issue has 12 to 15 articles and, possibly, a technical note and/or a technical discussion regarding a previously published paper. All contributions are reviewed and approved by professionals with recognized scientific competence in the area. The IBRACON Structures and Materials Journal is an open access Journal, free of charges for authors and readers.

Objectives

The IBRACON Structures and Materials Journal´s main objectives are:

- Present current developments and advances in concrete structures and materials.
- Make possible the better understanding of structural concrete behavior, supplying subsidies for a continuous interaction among researchers, producers, and users.
- Stimulate the development of scientific and technological research in the areas of concrete structures and materials, through papers peer-reviewed by a qualified Editorial Board.
- Promote the interaction among researchers, constructors and users of concrete structures and materials and the development of Civil Construction.
- Provide a vehicle of communication of high technical level for researchers and designers in the areas of concrete structures and materials.

Submission Procedure

The procedure to submit and revise the contributions, as well as the formats, are detailed in the Journal Website (ismj.org).

The papers and the technical notes are revised by at least two reviewers indicated by the editors. Discussions and replies are accepted for publication after a review by the editors and at least one member of the Editorial Board. In case of disagreement between the reviewer and the authors, the contribution will be sent to a specialist in the area, not necessarily linked to the Editorial Board. Conflict of interests is carefully handled by the Editors.

Contribution Types

The Journal will publish original papers, short technical notes, and paper discussions. Original papers will be accepted if they are in accordance with the objectives of the Journal and present quality of information and presentation. A technical note is a brief manuscript. It may present a new feature of research, development, or technological application in the areas of Concrete Structures and Materials, and Civil Construction. This is an opportunity to be used by industries, companies, universities, institutions of research, researchers, and professionals willing to promote their works and products under development.

A discussion is received no later than 3 months after the publication of the paper or technical note. The discussion must be limited to the topic addressed in the published paper and must not be offensive. The right of reply is granted to the Authors. The discussions and the replies are published in the subsequent issues of the Journal.

The submission file should be in accordance with the paper template available at the Journal Website. It is recommended that the length of the papers does not exceed 25 pages. Where available, URLs for the references should be provided.

The IBRACON Structures and Materials Journal will conduct the review process for manuscripts submitted in English. Titles, abstracts, and keywords are presented in English, and in Portuguese or Spanish. Articles and technical notes are peer-reviewed and only published after approval of the reviewers and the Editorial Board.

Once accepted, an article is typeset according to the journal layout. The author will be required to review and approve the galleys before publishing. At this stage only typesetting errors will be considered.

Internet Access

The IBRACON Structures and Materials Journal Webpage is available at http://ismj.org.

Sponsors

The funds for the maintenance of the Journal are currently obtained from the IBRACON. The Journal is not supposed to be maintained with funds from private sponsorship, which could diminish the credit of the publications.

Photocopying

Photocopying in Brazil. Brazilian Copyright Law is applicable to users in Brazil. IBRACON holds the copyright of contributions in the journal unless stated otherwise at the bottom of the first page of any contribution. Where IBRACON holds the copyright, authorization to photocopy items for internal or personal use, or the internal or personal use of specific clients, is granted for libraries and other users registered at IBRACON.

IBRACON

Av. Queiroz Filho, 1700 – sala 407/408 – Torre D
Villa Lobos Office Park
05319-000 – Vila Hamburguesa
São Paulo – SP
Phone: +55 (11) 3735-0202
E-mail: riem@ibracon.org.br

Disclaimer

Papers and other contributions and the statements made, or opinions expressed therein are published on the understanding that the authors of the contribution are the only responsible for the opinions expressed in them and that their publication does not necessarily reflect the views of IBRACON or of the Journal Editorial Board.

Editorial Board

Editorial Board

Direction

IBRACON Structures and Materials Journal
Revista IBRACON de Estruturas e Materiais

ORIGINAL ARTICLE

Concrete modeling using micromechanical multiphase models and multiscale analysis

Modelagem do concreto usando modelos micromecânicos de múltiplas fases e análise multiescala

Rodrigo Mero Sarmento da Silva[a] (iD)
Aline da Silva Ramos Barboza[b] (iD)

[a]Instituto Federal de Alagoas - IFAL, Maceió, AL, Brasil
[b]Universidade Federal de Alagoas - UFAL, Centro de Tecnologia - CTEC, Programa de Pós-Graduação em Engenharia Civil - PPGEC, Maceió, AL, Brasil

Abstract: Concrete in its macrostructure is a multiphase cementitious composite material, however, by reducing its scale, it is possible to identify the phases that compose it, among the phases are those embedded in the microscale: the hydrated silicates, in the mesoscale: the cement paste, transition zones and aggregates and in the macro phase: the composite itself. Modeling this type of material with two-phase micromechanical models is common in the literature, but there are already proven limitations that two-phase models can provide high modeling errors and are not recommended for this type of study. Faced with this problem, an alternative would be to use multiple-phase models, combined with a multiscale perspective in an attempt to minimize the error in modeling this material. The present paper models the concrete in two different constructions: without an interfacial transition zone and with the inclusion of the interfacial transition zone, verifying the modeling error when neglecting this important phase. The entire homogenization process is performed using the decoupled multiscale technique, obtaining results that rule out the use of two-phase models and methodologies that do not evaluate the interfacial transition zone in conventional concrete. The results obtained with the use of multiple-phase models reduced the relative error to practically zero (compared to experimental tests), demonstrating that micromechanics can be a concrete modeling tool provided that the multiscale process considers as many as possible phases and robust models that take this nature into account.

Keywords: multiscale modeling, micromechanics, concrete.

Resumo: O concreto em sua macroestrutura é um material compósito cimentício multifásico, contudo ao se reduzir sua escala consegue-se identificar as fases quem compõe o mesmo, dentre as fases estão as embutidas na microescala: os silicatos hidratados, na mesoescala: a pasta de cimento, zonas de transições e agregados e na fase macro: o próprio compósito. Modelagens desse tipo de material com modelos micromecânicos bifásicos são comuns na literatura, porém existe limitações já comprovadas de que modelos de duas fases podem aferir erros altos a modelagem não sendo recomendado para esse tipo de estudo. Diante dessa problemática, uma alternativa seria empregar modelos de múltiplas fases, aliado a uma perspectiva multiescala na tentativa de minimizar o erro na modelagem desse material. O presente trabalho modela o concreto em duas construções distinta: sem zona de transição interfacial e com a inclusão da zona de transição interfacial, verificando o erro de modelagem à negligência essa importante fase. Todo processo de homogeneização é realizado utilizando a técnica multiescala desacoplada obtendo resultados que descartam a utilização de modelos bifásicos e metodologias que não avaliam a zona de transição interfacial em concretos convencionais. Os resultados obtidos com a utilização de modelos de múltiplas fases reduziram o erro relativo a praticamente zero (em comparação com ensaios experimentais), demonstrando que a micromecânica pode ser uma ferramenta de modelagem do concreto desde que o processo multiescala leve em consideração o maior número possíveis de fases e modelos robustos que levem em conta essa natureza.

Palavras-chave: modelagem multiescala, micromecânica, concreto.

1 INTRODUCTION

Multiscale modeling is a technique that has been developed over the last decades with several applications in the most varied fields of science. The idea is to simulate continuous behavior from information obtained at lower scales [1].

In his paper Fish et al. [1] he presents a review of the most interesting applications of multiscale modeling including the prediction of electrical, magnetic, and chemical properties of complex materials (for example composites).

For each application, it is possible to define the multiscale approach that will be used, explaining its advantages and disadvantages in addition to the degree of complexity inherent to its technique [2]. Multiscale modeling consists of evaluating each level and how they influence each other as the composite is built. Lloberas-Valls et al. [2] defines two types of multiscale modeling, namely: hierarchical multiscale technique and concurrent multiscale technique.

The hierarchical multiscale technique can be divided into decoupled or weak coupled, in the decoupled technique the boundary condition problem is already solved, and the effective properties are carried from one scale to another (common in micromechanical homogenization). When the problem is analyzed by weak coupling, properties can be taken from global to local scale and vice versa, and the boundary problem is not initially solved. In the concurrent multiscale technique, the different scales are solved simultaneously, maintaining the condition of equilibrium and displacements, explaining a strong coupling [2].

Given this premise of expansion of knowledge and since concrete can be considered a complex material (composite) due to its multiphase and cementitious nature, this work proposes to estimate the mechanical properties of concrete using multiscale, micromechanical modeling of mean fields, bringing as a contribution to the application of models involving multiple phases, including the interfacial transition zone, in addition to verification and comparison with classical biphasic models. To validate the multiscale modeling, a comparison is made with experimental tests.

On a macroscopic scale, concrete may be considered as a homogenous material, however, as the scale decreases (meso and microscale), it cannot be considered homogenous – it is heterogenous, explaining its respective phases relate in [3], [4], [5]. Knowing the phases that compose the concrete, its respective fractions, and how they interact with one another is fundamental to maximizing its use.

Rodrigues [6] explains that the region that comprehends the mesoscale is a target of interest for several researchers: Häfner et al. [7], Eckardt and Könke [8], Eckardt [9], Nguyen et al. [10] since this phase defines the concrete as a composite and multiphase material.

In their study, Pichler and Hellmich [11] characterize well the multiscale modeling of some phases of the concrete (decoupled technique), namely: cement paste and the process of hydration of the paste that contemplates portions of the hydrated silicates, water/capillary pores, and clinker.

Further on, multiscale modeling of concrete was proposed, contemplating an experimental campaign to validate the models previously proposed by Göbel et al. [12].

Siventhirarajah et al. [13] can go further, through a multiscale analysis reducing the cement paste in some levels, reaching the nanometric scale, evaluating the hydrated calcium silicates HCS that compose the clinker (C_3S, C_2S, C_3A, C_4AF), tricalcium silicate, dicalcium silicate, tricalcium aluminate, tetracalciumalumino ferrite, respectively. In 2004 Scrivener [14] published an important paper on the characterization and measurement of concrete phases, especially the phases that make up a cement past.

Figure 1 illustrates the multiscale diagram of concrete showing its phases and dimensions from the microscale, through the mesoscale to the macroscale [3], [4], [9], [10], [11].
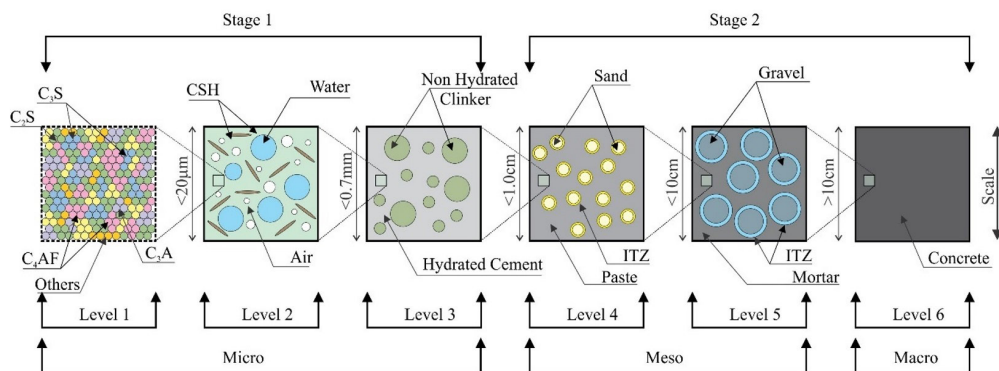
Figure 1: Multiscale micromechanical diagram, processes, levels, and stages of concrete.
Source: Author, adapted from Bernard et al. [3], Siventhirarajah et al. [13].

Rev. IBRACON Estrut. Mater., vol. 16, no. 5, e16501, 2023

2/14

Siventhirarajah et al. [13] subdivides the analysis of concrete into two stages – the first stage being responsible for integrating models of humidity, thermodynamics, and the hydration of the cement paste to evaluate the volumetric fractions of the comprehended phases between levels 1 to 3 (microscale). With the respective fractions and properties of the phases of stage 1, it is possible to estimate the property of the cement paste. The second stage is related to the mechanical evaluation of the composite (meso and macroscale), comprehending the phases of the sand and gravel, the respective interfacial transition zone (ITZ), and mortar.

In this stage (< level 6), the concrete can be understood as a composite, cementitious and multiphase material, which makes it complex, and simplified tests cannot evaluate its behavior.

Still, at level 5, the literature has long tried to understand the participation of each component of this mixture in the final characteristics of the composite, much has already been discovered, since the great influence of inclusions [15], [16], [17], [18], as well as a third, more fragile phase located at the matrix-inclusion interface (interfacial transition zone), which is difficult to measure but which has already been extensively tested by several techniques [19], [20], [21].

Silva [18] highlight the relationship between these phases and the possible behavior of each one when subject to request. When the inclusion phase is dominant in the stiffness of the composite, the matrix phases and the transition zone deform to a greater extent, which is probably the preferred path for cracking and fracturing of the composite.

However, even if the interfacial transition zone generated by the gravel is included, there are other phases, highlighting: sand pores, interfacial transition zone generated by sand, and even smaller phases such as non-hydrated clinker, hydrated silicates, among others, passing through all the levels shown in Figure 1.

Each of these phases has distinct properties and volumetric fractions and good modeling is directly associated with the characterization of each one of them. This dependence on concrete modeling as a function of the number of phases is remedied with a multiscale modeling using multi-phase micromechanical models, as proposed in this article.

2 INITIAL CONSIDERATIONS ON COMPOSITE HOMOGENIZATION

2.1. Representative Volume Element

A given body admitted homogenous and continuous in its macro-structure when reduced to a sufficiently small scale, does not behave as homogenous material, but as heterogeneous one, besides presenting discontinuities.

The literature brings several definitions about which volume will be representative of its macro-scale as seen in [11], [22], [23], [24], [25], [26].

Stroven et al. [25] discourses about the diverse definitions related to RVE (representative volume element), proposing a form of its measuring, taking into consideration a statistic dispersion associated with a specific property, when its scale is reduced. Still, in the paper [25] the following definitions are highlighted:

Hashin [22] admits that a volume is representative if it contains all of the phases that characterize the microstructure of the heterogeneous material studied and a sufficient number of these phases for the corresponding mean properties to the RVE to be independent of the applied conditions of contour, once these conditions are macroscopically uniform, or, in other words, the values oscillate around a mean value with a small standard deviation, becoming insignificant at a small distance of the surface.

Drugan and Willis [23] indicate that the representative volume element is associated with the smaller volume that can represent the mean properties of the composite.

Ostoja-Starzewski [24] defines RVE in two situations: when the system is periodic in its micro-structure and there is a cell that represents it, and in the second case when there is a volume (great enough) that can incorporate several phases in its micro-structure, presenting homogenous structures.

The reference quoted above about RVE differs a little, however, RVE is always considered inferior to the macroscale of the composite, which can represent its phases and must have little dispersion in the evaluation of its properties when its volume is disturbed [25].

Drago and Pindera [26] bring a definition of RVE as being a heterogenous system in its micro-structure, where when the specific contour conditions are applied for each representative volume, the answer does not differ from the material in its macroscale. Drago and Pindera [26] still explained the concept of the unitary cell of repetition, which is widely used when the problem has a condition of periodical contour.

In their review about RVE the authors described several studies that aimed at the characterization of the representative volume element, especially for concretes, once they were trying to know if the samples evaluated in fact could represent the composite. These studies established a parametric analysis of the volume and its phases submitted

Rev. IBRACON Estrut. Mater., vol. 16, no. 5, e16501, 2023

3/14

to several conditions of homogenous contour. These investigations tried to define the number of inclusions contained in the RVE that would be sufficient for the evaluation of the properties of the composite.

Pichler and Hellmich [11] define representative volume element due to the analysis scales. In a simplified manner, the definitions quoted above continue to be valid, however, there may be a representative element inside another representative element to be able to evaluate its properties on an even smaller scale.

Suppose that a representative volume element on scale A, composed of $n1, n2, \ldots, nm$

phases, in such a way that when the analysis scale is reduced to B, it is possible that some of its $n1, n2, \ldots, nm$, phase have to be represented by other $k1, k2, \ldots, km$, phases, expanding the range of phases for the multi-scale analysis, well defined in concrete. e.g.: Pichler and Hellmich [11] and approached in this study.

Micromechanical analyzes are normally conducted based on the concept of a representative volume element (RVE). The composite material can be understood as the sum of the matrix volume with the sum of the volume of all the inclusions, which can be voids, materials, cracks, etc [27]. Equation 1, below, represents this method.

$$V = V_m + \sum_{\alpha=1}^{n} V_i \tag{1}$$

Where V_m is the volume of the matrix, V_i is the volume of inclusions, and V is the total volume of the representative element. When taking the ratio between the matrix volume and the total volume, as well as the volume of inclusions and the total volume, the following volumetric fractions are obtained, considering Equations 2 and 3, respectively.

$$f_m = \frac{V_m}{V} \tag{2}$$

$$f_i = \frac{1}{V}\sum_{i=1}^{n} V_i \tag{3}$$

Volumetric fractions are extremely important in this type of analysis. The simplest proposes a weighted average as a function of fractions, of properties for global analysis, also known as the rule of mixtures. Over time, several methods were developed to solve the micromechanical problem, highlighting the Equivalent Inclusion Method, developed by Eshelby [28], one of the great contributions to the development of the micromechanics of effective media.

From the method proposed by Eshelby [28] other methods were developed, highlighting: Self Consistent [29], Mori-Tanaka [30], and Differential Scheme [31], among others.

The study of the micromechanics of effective media admits the hypothesis that the representative stresses and strains of a composite material (matrix + inclusions) can be represented by the average of stresses and strains in the representative volumes of each phase. Based on this principle, the total average stress, in the matrix and the inclusions, can be expressed by (Equations 4-6):

$$\bar{\sigma} = \frac{1}{V}\int_V \sigma(x)dv \tag{4}$$

$$\bar{\sigma}_m = \frac{1}{V_m}\int_{V_m} \sigma(x)dv \tag{5}$$

$$\bar{\sigma}_i = \frac{1}{V_i}\int_{V_i} \sigma(x)dv \tag{6}$$

Knowing that:

$$\int_V \sigma(x)dv = \int_{V_m} \sigma(x)dv + \sum_{i=1}^{n}\int_{V_i} \sigma(x)dv \tag{7}$$

replacing Equation 7, in Equation 4 there have been (Equation 8):

$$\bar{\sigma} = f_m\bar{\sigma}_m + \sum_{i=1}^{n} f_i\bar{\sigma}_i \tag{8}$$

Arrived at an expression that can determine the total average stress as a function of the stresses in the matrix and the inclusions and their respective volumetric fractions. Assuming that V is a representative volume, it can be stated that the average total stress $\bar{\sigma}$ is equal to the effective stress in the material $\langle\sigma\rangle$. Similarly, we have the total mean strain, in the matrix and the inclusions are given by the Equations 9-11:

$$\bar{\varepsilon} = \frac{1}{V}\int_V \varepsilon(x)dv \tag{9}$$

$$\bar{\varepsilon}_m = \frac{1}{V_m}\int_{V_m} \varepsilon(x)dv \tag{10}$$

$$\bar{\varepsilon}_i = \frac{1}{V_i}\int_{V_i} \varepsilon(x)dv \tag{11}$$

Knowing that:

$$\int_V \varepsilon(x)dv = \int_{V_m} \varepsilon(x)dv + \sum_{i=1}^{n}\int_{V_i} \varepsilon(x)dv \tag{12}$$

replacing Equation 12, in Equation 9 there have been (Equation 13):

$$\bar{\varepsilon} = f_m\bar{\varepsilon}_m + \sum_{i=1}^{n} f_i\varepsilon_i \tag{13}$$

Assuming that matrix and inclusions are elastic materials. So, it can be said that (Equations 14-16):

$$\langle\sigma\rangle = \bar{\mathbb{C}}:\langle\varepsilon\rangle \tag{14}$$

$$\langle\sigma_m\rangle = \mathbb{C}_m:\langle\varepsilon_m\rangle \tag{15}$$

$$\langle\sigma_i\rangle = \mathbb{C}_i:\langle\varepsilon_i\rangle \tag{16}$$

Where, $\bar{\mathbb{C}}$, $\mathbb{C}_m$, and $\mathbb{C}_i$ are respectively the global constitutive tensor, the matrix constitutive tensor, and the inclusion constitutive tensor, being the same fourth-order tensors. If the material is linear elastic, the global constitutive tensor is constant.

The concentration tensors of a composite are tensors that relate the average stresses and strains in the composite with the matrix and the inclusions. Substituting Equations 14-16 to Equation 8, we obtain (Equations 17-18):

$$f_m\mathbb{C}_m:\langle\varepsilon_m\rangle = \bar{\mathbb{C}}:\langle\varepsilon\rangle - \sum_{i=1}^{n} f_i\mathbb{C}_i:\langle\varepsilon_i\rangle \tag{17}$$

$$f_m\mathbb{C}_m:\frac{1}{V_m}\left[\int_V \varepsilon(x)dv - \sum_{i=1}^{n}\int_{V_i} \varepsilon(x)dv\right] = \bar{\mathbb{C}}:\langle\varepsilon\rangle - \sum_{i=1}^{n} f_i\mathbb{C}_i:\langle\varepsilon_i\rangle \tag{18}$$

With a little algebra one can arrive at (Equation 19):

$$(\bar{\mathbb{C}} - \mathbb{C}_m):\langle\varepsilon\rangle = \sum_{i=1}^{n} f_i(\mathbb{C}_i - \mathbb{C}_m):\langle\varepsilon_i\rangle \tag{19}$$

This equation relates the constitutive tensors of the matrix, the inclusion and the global tensor, the global deformations, and the inclusion.

Rev. IBRACON Estrut. Mater., vol. 16, no. 5, e16501, 2023

5/14

2.2. The Eshelby Problem

In 1957 Eshelby [28] proposed to determine the elastic field of an ellipsoidal inclusion in a solid (Figure 2).
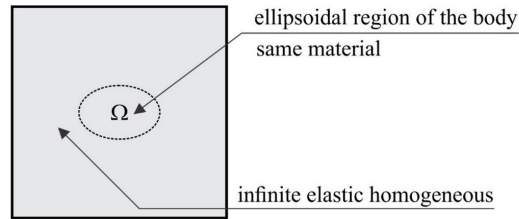
Figure 2: Esheby's inclusion problem

It is assumed that the Ω region undergoes a geometric transformation so that in the absence of the material that surrounds the ellipse region it would correspond to a homogeneous deformation. In this hypothesis, Eshelby was able to assess what the elastic fields would be like inside and outside the ellipsoidal region. To exemplify Eshelby's strategy, initially, the ellipsoidal region, where the strain is initially zero, is removed, and a homogeneous strain is applied as shown in Figure 3.
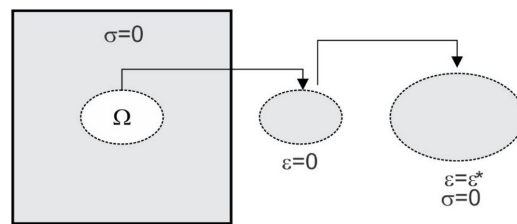
Figure 3: Eshelby's problem strategy.

The next step is to apply external forces to the region so that it returns to its initial volume. When these external forces are applied, the volume of the ellipsoidal region decreases, however, a tension field is associated with this force in the body (Figure 4).
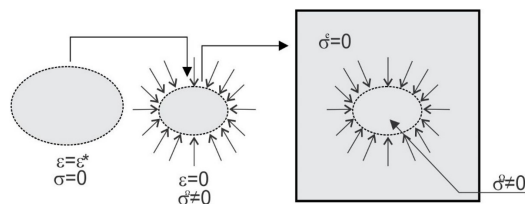
Figure 4: Eshelby's problem strategy.

The next step consists of returning to the ellipsoidal region, now with a tension field in the region of the representative element, removing the external actions that surrounded the ellipsoidal region, as can be seen in Figure 5.
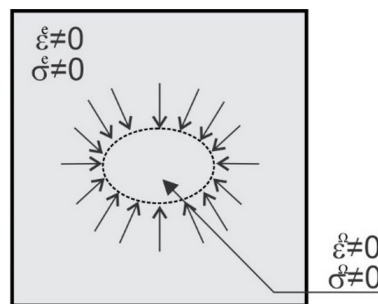
Figure 5: Eshelby's problem strategy.

Rev. IBRACON Estrut. Mater., vol. 16, no. 5, e16501, 2023

6/14

Eshelby [28] states that within the ellipsoidal inclusion Ω, the stresses and strains are constant but dependent on the geometry of the inclusion. With this, we define the [28] relation between the deformations in the ellipsoid and the deformation imposed on the system by a transformation tensor, called the Eshelby tensor ($\mathbb{S}$), in the form:

$$\varepsilon^{\Omega} = \mathbb{S}^{\Omega} \varepsilon^{*} \tag{20}$$

The assembly of the Eshelby tensor can be seen in the original paper [28]. With the same strategy mentioned above, it is enough to modify the property of the ellipsoid to arrive at the equivalent inclusion method that was the precursor of the mean-fields micromechanics.

2.3. Composite Homogenization Models

There are homogenization models that have the purpose of establishing limits, the best known being the rule of mixtures (Reuss and Voigt Model) [32] and the Hashin-Shtrikman models [33]. Models should not be used to estimate the homogenized properties of composites, as they have several simplifying hypotheses such as the constant stress or strain field, or the combination of the two states, another simplification occurs in the non-evaluation of the interaction between the particles, among others.

To circumvent the limitations of limit models, methods based on the Eshelby equivalent inclusion problem stand out, the best known being the Mori-Tanaka model [34], before the paper of Mori and Tanaka [34], Hill [35] proposed the "Self-Consistent" model, which was later expanded by Christensen and Lo [27]. Also, noteworthy are the paper of Benveniste [29], with the model of equivalent inclusion [30], and his model called "Differential Scheme" and the model "Double Inclusion" [21].

Kaw [32] divides composite homogenization models into the mechanic of materials, semi-empirical models, and elasticity theory models. The present paper adopts as a reference this subdivision proposed by Kaw [32] adding the models that are derived from the mean-fields micromechanical formulation.

Table 1: Characteristics of homogenization models.

Models	Particulars and recurrence equation	Source
Reuss	Its limitation is the imposition of a constant state of tension, in addition to not evaluating the interaction between inclusions $\mathbb{C}^{H} = \mathbb{C}_{m} : \mathbb{C}_{i} : [\mathbb{C}_{i}(1 - f_{i}) + \mathbb{C}_{m} f_{i}]^{-1}$	[36]
Voigt	Its limitation is a constant of strain state, in addition to not evaluating the integration between the inclusions $\mathbb{C}^{H} = \mathbb{C}_{m}(1 - f_{i}) + \mathbb{C}_{i} f_{i}$	[32]
Hashin	It does not estimate constant stress and strain fields, instead, it estimates auxiliary fields representing a variation of the reference solution. When the formulation of the energy obtained is maximized, the upper limit is found and when it is minimized, the lower limit is found. $K^{-} = K_{m} + \left[\dfrac{f_{i}}{\left[\dfrac{1}{K_{i} - K_{m}} + \dfrac{3(1 - f_{i})}{3K_{m} + 4G_{m}} \right]} \right]$ $K^{+} = K_{i} + \left[\dfrac{1 - f_{i}}{\left[\dfrac{1}{K_{m} - K_{i}} + \dfrac{3f_{i}}{3K_{i} + 4G_{i}} \right]} \right]$ $G^{-} = G_{m} + \left[\dfrac{f_{i}}{\left[\dfrac{1}{G_{i} - G_{m}} + \dfrac{6(1 - f_{i})(K_{m} + 2G_{m})}{5G_{m}(3K_{m} + 4G_{m})} \right]} \right]$ $G^{+} = G_{i} + \left[\dfrac{1 - f_{i}}{\left[\dfrac{1}{G_{m} - G_{i}} + \dfrac{6f_{i}(i + 2G_{i})}{5G_{i}(3K_{i} + 4G_{i})} \right]} \right]$	[33]
Mori-Tanaka	It is the most used model for homogenization of composites, it considers the interaction between the particles and can be used with larger volumetric fractions. $\mathbb{C}^{H} = \mathbb{C}_{m} : \dfrac{\{ \mathbb{I} + f_{i}(\mathbb{S} - \mathbb{I}) : [(\mathbb{C}_{m} - \mathbb{C}_{i})^{-1} : \mathbb{C}_{m} - \mathbb{S}]^{-1} \} : ^{-1}}{\{ \mathbb{I} + f_{i} \mathbb{S} : [(\mathbb{C}_{m} - \mathbb{C}_{i})^{-1} : \mathbb{C}_{m} - \mathbb{S}]^{-1} \}}$	[34]
Dilute Suspension	It is limited by the amount of volumetric fraction of inclusion in the homogenization process, and can only be applied to low inclusion rates $\mathbb{C}^{H} = \mathbb{C}_{m} + f_{i}(\mathbb{C}_{i} - \mathbb{C}_{m}) : \mathbb{A}_{i}$	[37]

Table 1: Continued...

Models	Particulars and recurrence equation	Source
Self-Consistent	$\mathbb{A}_i = [\mathbb{I} - \mathbb{S}:\mathbb{C}_m:(\mathbb{C}_m - \mathbb{C}_i)]$	[35]
	$\mathbb{C}^H{}_{n+1} = \mathbb{C}_m + f_i(\mathbb{C}_i - \mathbb{C}_m):[\mathbb{I} - \mathbb{S}^H{}_n:\mathbb{C}^{H^{-1}}{}_n:(\mathbb{C}^H{}_n - \mathbb{C}_i)]^{-1}$	
	Step 1:	
	$\mathbb{S}^H = \mathbb{S}, \mathbb{C}^H = \mathbb{C}_m$	
	$\dfrac{\|\mathbb{C}^H{}_n - \mathbb{C}^H{}_{n-1}\|}{\|\mathbb{C}^H{}_{n-1}\|} < \delta$	
Generalized Self-Consistent	Based on the theory of elasticity, it manages to evaluate the interaction between inclusions being developed as a three-phase model, essentially it only evaluates two phases. It considers the inclusion-matrix interaction and between inclusions	[27]
	$A\left[\dfrac{G^H}{G_m}\right]^2 + B\left[\dfrac{G^H}{G_m}\right] + C$	
	A, B, and C, are constants that can be obtained in Christensen and Lo [27]	
	$K^H = \left[K_m + \dfrac{f_i(K_i - K_m)(3K_m + 4G_m)}{3K_m + 4G_m + 3(1 - f_i)(K_i - K_m)}\right]$	
Differential Scheme	Unlike other methods that assume an inclusion immersed in an infinite matrix, the differential scheme works with incremental doses of inclusions.	[30]
	$\mathbb{C}^H{}_{n+1} = \mathbb{C}^H{}_n + \dfrac{\Delta f_i}{1 - f_i}(\mathbb{C}_i - \mathbb{C}^H{}_n):\mathbb{A}_i{}^D$	
	$\mathbb{A}_i{}^D = [\mathbb{I} - \mathbb{S}^H{}_n:\mathbb{C}^H{}_n{}^{-1}:(\mathbb{C}^H{}_n - \mathbb{C}_i)]^{-1}$	
	Step 1:	
	$\mathbb{S}^H = \mathbb{S}, \mathbb{C}^H{}_n = \mathbb{C}_m$	
Four-phases	which is based on the three-phase model (Generalized Self-Consistent), associated with an analytical model, namely: "Composite Sphere Assemblage (CSA)" [22] or "Composite Cylinder Assemblage (CCA)" [33].	[21]
	$K^H = \left[K_m + \dfrac{f_i(K_i - K_m)(3K_m + 4G_m)}{3K_m + 4G_m + 3(1 - f_i)(K_i - K_m)}\right]$	
	$E_L^H = f_i E_i + f_m E_m + \dfrac{4f_i f_m (v_i - v_m)^2 G_m}{1 + \dfrac{3f_i G_m}{3K_m + G_m} + \dfrac{3f_m G_m}{3K_i + G_i}}$	
	$K_T^H = K_m + \dfrac{G_m}{3} + \dfrac{f_i}{\left[\dfrac{3}{3K_i + G_i - 3K_m - G_m}\right] + \left[\dfrac{3f_i}{3K_m + 4G_m}\right]}$	
	$G_L^H = \dfrac{(f_i G_i + f_m G_m + G_i)G_m}{f_m G_i + f_i G_m + G_m}$	
	$v_{LT}^H = f_i E_i + f_m E_m + \dfrac{3f_i f_m (v_i - v_m)G_m\left[\dfrac{f_i G_m}{3K_m + G_m} + \dfrac{f_m G_m}{3K_i + G_i}\right]}{\left[\dfrac{3}{3K_i + G_i - 3K_m - G_m}\right] + \left[\dfrac{3f_i}{3K_m + 4G_m}\right]}$	
Multiphase	That bases its formulation on the famous study of double inclusion [38]. The model proposed [39], takes into consideration the assemblage of the Eshelby [28] tensor for all of the layers of existing materials in the modeling.	[39]
	$f_m + \sum_1^n (f_i + f_r) = 1$	
	$\mathbb{A}_i{}^D = I + \mathbb{S}_i:\Phi_i + \Delta\mathbb{S}:\Phi_r$	
	$\mathbb{A}_r{}^D = I + \mathbb{S}_r:\Phi_r + \dfrac{f_i}{f_r}\Delta\mathbb{S}:(\Phi_i - \Phi_r)$	
	$\Delta\mathbb{S} = \mathbb{S}_i - \mathbb{S}_r$	
	$\Phi_i = -\left[(\mathbb{S}_i + \mathbb{A}_i) + \Delta\mathbb{S}:\left(\mathbb{S}_i + \mathbb{A}_i - \dfrac{f_i}{f_r}\Delta\mathbb{S}\right):\left(\mathbb{S}_r + \mathbb{A}_r - \dfrac{f_i}{f_i}\Delta\mathbb{S}\right)^{-1}\right]^{-1}$	
	$\Phi_r = -\left[\Delta\mathbb{S} + (\mathbb{S}_i + \mathbb{A}_i):\left(\mathbb{S}_i + \mathbb{A}_i - \dfrac{f_i}{f_r}\Delta\mathbb{S}\right)^{-1}:\left(\mathbb{S}_r + \mathbb{A}_r - \dfrac{f_i}{f_i}\Delta\mathbb{S}\right)\right]^{-1}$	
	$\mathbb{A}_i = (\mathbb{C}_i - \mathbb{C}_m)^{-1}:\mathbb{C}_m$	
	$\mathbb{A}_r = (\mathbb{C}_r - \mathbb{C}_m)^{-1}:\mathbb{C}_m$	
	$\mathbb{C}^H = \mathbb{C}_m + \left[f_r(\mathbb{C}_r - \mathbb{C}_m):\mathbb{A}_r{}^D + f_i(\mathbb{C}_i - \mathbb{C}_m):\mathbb{A}_i{}^D\right]$	

Where $\mathbb{C}$ is the constitutive tensor for a linear elastic material, $\mathbb{S}$ is the Eshelby tensor, f is the volumetric fractions, $\mathbb{A}$ is the strain concentration tensor, $\mathbb{I}$ identity matrix, E is the modulus of elasticity, v is the Poisson ratio, G the shear modulus and K the volumetric module, with the indices i, m, r, H, L, T respectively referring to inclusion, matrix, interphase, homogenized, longitudinal and transversal, the superscript D indicates dilute.

The Dilute Suspension model, although mentioned in Table 1, was not used in the micromechanical modeling of concrete due to its limitation when the volumetric fraction is high [37].

3 MULTI-SCALE HOMOGENIZATION OF CONCRETE

The procedure of homogenization adopted in this studied case considers the phases of construction of the material. To define the homogenized properties of concrete, the phases of the constitution of the composite (Figure 6) are considered in its meso-macroscale.
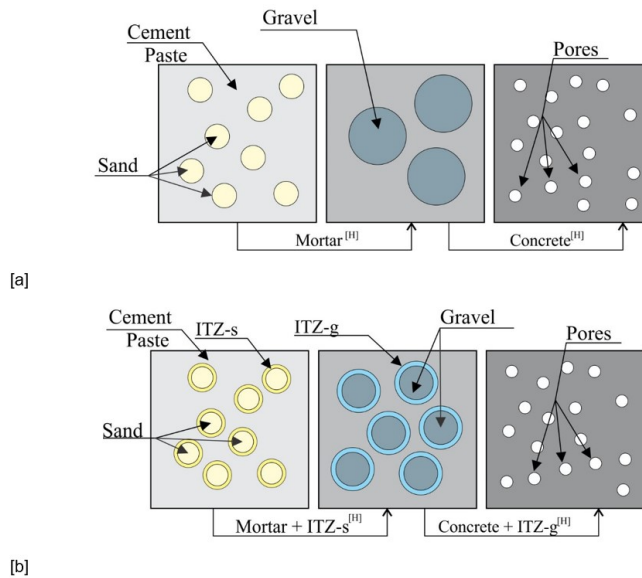
Figure 6: Three-level homogenization considering (without [a] /with [b]) interfacial transition zone and three- and multiple-phase models. Source: Author.

This way, each step receives as input a matrix and a random inclusion and provides as output the homogenized material. The elastic properties of the materials used for the composite construction are defined in Table 2. These parameters were quoted by Silva [18].

Table 2: Property of the composite phases (Experimental).

Material	Module of Elasticity (GPa)	Poisson ratio	Volumetric Fraction (%)
Cement Paste	21.34	0.25	15.40
Gravel	51.31	0.15	40.30
ITZ-1	10.17	0.30	2.30
Sand	77.60	0.15	26.90
ITZ-2	12.70	0.25	15.10
Concrete	34.50	-	-

Source: adapted from Li et al. [40].

In the first analysis, the composite is treated in a simplified way (Figure 6a), disregarding the presence of the transition zone, and the effective properties are calculated with two-phase models, in the second analysis, the four-phase and multiphase models including two more phases in the construction of the composite (Figure 6b). For both analyzes, in addition to the modulus of elasticity, the Poisson ratio and the estimated characteristic compressive strength of the concrete are evaluated.

Silva [41] explains that the longitudinal Young modulus (E_c) is a requirement for determining the characteristic strength of concrete (f_{ck}), being a parameter for several empirical models of strength prediction found in the literature. Some models can be seen in Table 3.

Table 3: Normative equations to estimate the modulus of elasticity of concrete.

Norm	Module of Elasticity estimate	Comments
NBR 6118 (2014)	$20 \leq f_{ck} \leq 50$ MPa $E_c = \alpha \cdot 5600\sqrt{f_{ck}}$ $55 \leq f_{ck} \leq 90$ MPa $E_c = 21.5 \cdot 10^3 \cdot \alpha \sqrt[3]{\frac{f_{ck}}{10}} \cdot 1.25$	$\alpha = 1.2$ (Basalt, dense limestone aggregates)
		$\alpha = 1.0$ (Quartzite aggregates)
		$\alpha = 0.9$ (Limestone aggregates)
ACI 3018 (2014)	$E_c = 5170\sqrt{f_{ck}}$	$\alpha = 0.7$ (Sandstone aggregates)
Fib Model Code (2010)	$12 \leq f_{ck} \leq 80$ MPa $E_c = 21.5 \cdot 10^3 \cdot \alpha \sqrt[3]{\frac{f_{ck}+8}{10}}$	$\alpha = 1.2$ (Basalt, dense limestone aggregates)
		$\alpha = 1.0$ (Quartzite aggregates)
		$\alpha = 0.9$ (Limestone aggregates)
		$\alpha = 0.7$ (Sandstone aggregates)
Eurocode 2 (2004)	$12 \leq f_{ck} \leq 90$ MPa $E_c = 23.1 \cdot 10^3 \cdot \alpha \left(\frac{f_{ck}+8}{10}\right)^{0.3}$	$\alpha = 1.2$ (Basalt, dense limestone aggregates)
		$\alpha = 1.0$ (Quartzite aggregates)
		$\alpha = 0.9$ (Limestone aggregates)
		$\alpha = 0.7$ (Sandstone aggregates)

In this way, the f_{ck} value can be found as a function of the longitudinal Young modulus, verifying the relative error between the homogenized concrete (with and without the ITZ) and the experimental value.

4 RESULTS AND DISCUSSIONS

To assess the calibration of micromechanical models with experimental results, the concept of relative error is used between the result obtained with the micromechanical analysis and the value obtained in the laboratory.

In the analysis of relative errors to obtain the effective elastic properties of the concrete, it was considered that the longitudinal Young modulus of 34.5 GPa, which was obtained experimentally by Li et al. [40], was considered.

One of the hypotheses raised would be the verification of limit models: models of Reuss, Voigt, and limits of Hashin. For this hypothesis, the construction of the composite without a transition zone was used (Figure 6a), with the corrections of the volumetric fractions for each of the three levels adopted in these two initials analyses shown in Table 4.

Table 4: Correction of volumetric fractions in the homogenization steps.

Level 4		Volumetric Fraction in Composite	Volumetric Fraction in Homogenization Level
Mortar homogenized	Cement paste	15.40%	36.41%
	Sand	26.90%	63.59%
	Total	42.30%	100.00%
Level 5		**Volumetric Fraction in Composite**	**Volumetric Fraction in Homogenization Level**
Concrete homogenized	Mortar homogenized	42.30%	48.79%
	Gravel	40.30%	51.21%
	Total	42.30%	100.00%
Level 6		**Volumetric Fraction in Composite**	**Volumetric Fraction in Homogenization Level**
Homogenized concrete adjusted	Concrete homogenized	100.00%	97.22%
	Pores	2.42%	2.78%
	Total	102.48%	100.00%

It should be noted that the errors for the analyzed analytical models are above 40% at the last level, which is not adequate. It is also observed that in the last homogenization step, the Reuss and Hashin [-] models are poorly conditioned since the pore modulus of elasticity is null and the relative error calculation would produce negative errors, which would not make physical sense (Table 5).

Continuing the modeling, two-phase models were used, disregarding the interfacial transition zone both in the sand and in the gravel, obtaining the following result in the homogenization steps (Table 6). When considering the two-phase numerical models in the homogenization process, a decrease in the concrete modeling error can be seen.

Rev. IBRACON Estrut. Mater., vol. 16, no. 5, e16501, 2023

10/14

Table 5: Homogenization results for the limit models.

Models	Modulus of elasticity (GPa)			Error %		
	Level 4	Level 5	Level 6	Level 4	Level 5	Level 6
Reuss	39.596	44.559	-	14.770	26.156	-
Voigt	57.324	54.400	52.887	66.157	57.680	53.295
Hashin +	51.179	51.262	48.496	48.345	48.584	40.569
Hashin -	45.614	48.341	-	32.210	40.118	-
Concrete [40]	34.50					

Table 6: Homogenization results for the biphasic models.

Models	Modulus of elasticity (GPa)			Error %		
	Level 4	Level 5	Level 6	Level 4	Level 5	Level 6
Mori-Tanaka	45.614	48.341	45.671	32.215	40.118	32.379
Self-Consistent	49.304	50.290	47.436	42.909	45.768	37.496
Generalized Self-Consistent	46.144	48.624	45.937	33.751	40.938	33.325
Differential Scheme	46.772	48.923	46.981	35.571	41.806	36.177
Concrete [40]	34.50					

It can be seen that the two-phase homogenization models are not primarily responsible for

the high value of the relative error, with peaks of up to 37.496%, while the limit models had errors of 53.295%. This error is directly associated with the disregard of the interfacial transition zone in the composite construction and analysis process, even though the two-phase micromechanical models have limitations for concrete modeling.

The following analysis consists of modeling the concrete considering the interfacial transition zone, with models capable of evaluating more than two phases. The correction of volumetric fractions for these models can be seen in Table 7.

Table 7. Correction of volumetric fractions in the homogenization steps.

Level 4		Volumetric Fraction in Composite	Volumetric Fraction in Homogenization Level
Mortar homogenized + Interfacial Transition Zone of Sand	Sand	26.90%	46.86%
	ITZ-s	15.10%	26.31%
	Cement Paste	15.40%	26.83%
	Total	57.40%	100.00%

Level 5		Volumetric Fraction in Composite	Volumetric Fraction in Homogenization Level
Concrete homogenized + Interfacial Transition Zone of Gravel	Gravel	40.30%	40.30%
	ITZ-g	2.30%	2.30%
	Mortar homogenized + Interfacial Transition Zone of Sand	57.40%	57.40%
	Total	100.00%	100.00%

Level 6		Volumetric Fraction in Composite	Volumetric Fraction in Homogenization Level
Homogenized concrete adjusted	Concrete homogenized + Interfacial Transition Zone of Gravel	100.00%	97.64%
	Pores	2.42%	2.36%
	Total	102.48%	100.00%

In the last level of homogenization, the Mori-Tanaka model was used to correct the composite with pores. The obtained results reduced the error found by Li et al. [40] from 8% to below 5%, with the multiphase model reaching an insignificant error for the four-phase model, indicating a substantial gain when using a more robust homogenization model. Table 8 illustrates the decrease in error for each homogenization step.

As expected, more robust homogenization models combined with more experimented phases brought very satisfactory results. The error below 1% indicates that micromechanical models can accurately predict the homogenized properties of cementitious composites.

When evaluating the Poisson ratio homogenized for both the multiphase modeling (with ITZ and without ITZ), there were no significant differences, being in both models within the expected pattern Tables 9-10.

Table 8. Numerical results by homogenization steps.

Model	Modulus of elasticity (GPa)			Error %		
	Level 4	Level 5	Level 6	Level 4	Level 5	Level 6
Four-Phases	30.638	36.167	34.501	11.193	4.830	0.0031
Multiphase	32.101	37.774	36.302	6.952	9.488	4.441
Concrete [40]			34.50			

Table 9: Numerical results by homogenization steps for Poisson's ratio (without ITZ).

Models	Poisson ratio		
	Level 4	Level 5	Level 6
Mori-Tanaka	0.1997	0.1751	0.1759
Self-Consistent	0.1829	0.1671	0.1683
Generalized Self-Consistent	0.1942	0.1732	0.1741
Differential Scheme	0.182	0.172	0.173
NBR 6118		$0.11 - 0.22$	

Table 10. Numerical results by homogenization steps for Poisson's ratio (with ITZ).

Model	Poisson ratio		
	Level 4	Level 5	Level 6
Four-Phases	0.183	0.173	0.174
Multiphase	0.201	0.182	0.182
NBR 6118		$0.11 - 0.22$	

An estimate for the characteristic strength of concrete considered the values of Young's modulus found at Level 6 of the multiscale procedure, associated with two-phase models (without ITZ) Table 6 and multiple-phase models (with ITZ) Table 8. In the analysis, it was adopted a = 1 (Quartzite aggregates).

The estimated results for the characteristic strength of concrete, disregarding the interfacial transition zone, can be seen in Table 11.

Table 11: f_{ck} estimated using empirical models and homogenization (Level 6).

Models	f_{ck} estimates (MPa)				Error %			
	NBR 6118	ACI 3018	Fib Model Code	Eurocode 2	NBR 6118	ACI 3018	Fib Model Code	Eurocode 2
Mori-Tanaka	66.512	78.036	87,850	88.997	75.244	75.244	99.736	195.878
Self-Consistent	71.753	84.185	99.401	102.066	89.053	89.052	198.340	239.326
Generalized Self-Consistent	67.289	78.948	89.537	90.893	77.291	77.292	168.735	202.181
Differential Scheme	70.383	82.577	96.340	98.586	85.443	85.441	189.153	227.757
Concrete [40]	37.954	44.530	33.318	30.079	-	-	-	-

It is observed that there is an upward growth curve of the relative error, further demonstrating that it is not interesting to use two-phase models to estimate the strength of concrete. When using models that consider the interfacial transition zone, it is noted that the relative error also grows, but they are much smaller about two-phase models, which can be a support tool (Table 12).

Table 12: f_{ck} estimated using empirical models and homogenization (Level 6).

Models	f_{ck} estimates (MPa)				Error %			
	NBR 6118	ACI 3018	Fib Model Code	Eurocode 2	NBR 6118	ACI 3018	Fib Model Code	Eurocode 2
Four-Phases	37.956	44.533	33.321	30.083	0.005	0.007	0.009	0.013
Multiphase	42.022	49.303	40.136	37.122	10.718	10.719	20.463	23.415
Concrete [40]	37.954	44.530	33.318	30.079	-	-	-	-

It should be noted that the neglect of the transition zone directly influences the modeling of this type of concrete, and therefore, it should be included in the analysis. For conventional concretes, the use of two-phase models is not recommended, as it is not possible to introduce the interfacial transition zone in the analysis even if one wants to.

Increasing the levels of micromechanical multiscale modeling would be a hypothesis for use of two-phase models, but it could lead to problems of the inclusions not being spherical, or the matrix not being infinite which would go against the micromechanical formulation.

5 CONCLUSIONS

With conventional concrete, it is proven that two-phase models need to be well adjusted to being able to evaluate the homogenized properties of concrete [40] using essentially two-phase models with adaptations to include the interfacial transition zones in the analysis since the literature already confirms that their absence interferes drastically in the final result of the modeling. The errors obtained by Li et al. [40] were 8.7% using his strategy.

By modifying the strategy used by Li et al. [40] proposing a multiscale analysis with robust models of multiple phases, satisfactory results are effectively achieved, reducing the error to 4% in the multiphase model and zero when using the four-phase model.

This panorama indicates that in conventional concrete it is essential to evaluate the interfacial transition zone with more complex models, however a robust experimental apparatus to model this cementitious composite is still needed. Any neglected phase can significantly interfere in the micromechanical modeling and the possibility of removing any of its phases must be investigated on a case-by-case basis.

Every micromechanical multiscale procedure was applied to the meso and macro scale of concrete, however, every analysis methodology can be used on the microscale and also on smaller scales such as the nanoscale, always considering the definition of a representative volume element [37].

ACKNOWLEDGEMENTS

1 REFERENCES

[1] J. Fish, G. J. Wagner, and S. Keten, "Mesoscopic and multiscale modelling in materials," *Nat. Mater.*, vol. 20, pp. 777–786, Jun. 2021.

[2] O. Lloberas-Valls, D. J. Rixen, A. Simone, and L. J. Sluys, "Multiscale domain decomposition analysis of quasi-brittle heterogeneous materials," *Int. J. Numer. Methods Eng.*, vol. 89, pp. 1337–1366, Nov. 2011.

[3] O. Bernard, F.-J. Ulm, and E. Lemarchand, "A multiscale micromechanics-hydration model for the early-age elastic properties of cement-based materials," *Cement Concr. Res.*, vol. 33, pp. 1293–1309, Sep. 2003.

[4] G. Constantinides and F.-J. Ulm, "The effect of two types of C-S-H on the elasticity of cement-based materials: results from nanoindentation and micromechanical modeling," *Cement Concr. Res.*, vol. 34, no. 1, pp. 67–80, Jan. 2004.

[5] J. F. Unger and S. Eckardt, "Multiscale modeling of concrete," *Arch. Comput. Methods Eng.*, vol. 18, p. 341, Jul. 2011.

[6] E. A. Rodrigues, "Um modelo multiescala concorrente para representar o processo de fissuração do concreto," Ph.D. dissertation, Poli USP, São Paulo, Brazil, 2015.

[7] S. Häfner, S. Eckardt, T. Luther, and C. Könke, "Mesoscale modeling of concrete: geometry and numerics," *Comput. Struct.*, vol. 84, no. 7, pp. 450–461, Feb. 2006.

[8] S. Eckardt and C. Könke, "Adaptive damage simulation of concrete using heterogeneous multiscale models," *J. Algorithm Comput. Technol.*, vol. 2, no. 2, pp. 275–298, Jun. 2007.

[9] S. Eckardt, "Adaptive heterogeneous multiscale models for the nonlinear simulation of concrete," Ph.D. dissertation, BUW, Weimar, Germany, 2009.

[10] V. P. Nguyen, M. Stroeven, and L. J. Sluys, "Multiscale failure modeling of concrete: Micromechanical modeling,discontinuous homogenization and parallel computations," *Comput. Methods Appl. Mech. Eng.*, vol. 201-204, pp. 139–156, Jan. 2012.

[11] B. Pichler and C. Hellmich, "Upscaling quasi-brittle strength of cement paste and mortar: a multi-scale engineering mechanics model," *Cement Concr. Res.*, vol. 41, no. 5, pp. 467–476, May. 2011.

[12] L. Göbel, M. Königsberger, A. Dimming-Osburg, and B. Picheler, "Viscoelastic behavior of polymer-modified cement pastes: insight from downscaling short-term macroscopic creep tests by means of multiscale modeling," *Appl. Sci.*, vol. 8, no. 4, p. 487, Mar. 2018.

[13] K. Siventhirarajah, Y. Yoda, and Y. Elakneswaran, "A two-stage model for the prediction of mechanical properties of cement paste," *Cement Concr. Compos.*, vol. 115, p. 103853, Jan. 2021.

[14] K. L. Scrivener, "Backscattered electron imaging of cementitious microstructures: understanding and quantification," *Cement Concr. Compos.*, vol. 26, no. 8, pp. 935–945, Nov. 2004.

[15] M. S. Meddah, S. Zitouni, and S. Belâabes, "Effect of content and particle size distribution of coarse aggregate on the compressive strength of concrete," *Constr. Build. Mater.*, vol. 24, no. 4, pp. 505–512, Apr. 2010.

[16] K.-R. Wu, B. Chen, W. Yao, and D. Zhang, "Effect of coarse aggregate type on mechanical properties of high-performance concrete," *Cement Concr. Res.*, vol. 31, no. 10, pp. 1421–1425, Oct. 2011.

[17] H. Beushausen and T. Dittmer, "The influence of aggregate type on the strength and elastic modulus of high strength concrete," *Constr. Build. Mater.*, vol. 74, pp. 132–139, Jan. 2015.

[18] N. V. Silva, "Método de determinação de resistência à tração e módulo de elasticidade de agragados graúdos naturais," M.S. thesis, USP, São Paulo, Brazil, 2018.

[19] G. Prokopskia and J. Halbiniakb, "Interfacial transition zone in cementitious materials," *Cement Concr. Res.*, vol. 30, no. 4, pp. 579–583, Apr. 2000.

[20] K. L. Scrivener, A. K. Crumbie, and P. Laugesen, "The Interfacial Transition Zone (ITZ) between cement paste and aggregate in concrete," *Interface Sci.*, vol. 12, pp. 411–421, Oct. 2004.

[21] G. Li, Y. Zhao, and S. Pang, "Four-phase sphere modeling of effective bulk modulus of concrete," *Cement Concr. Res.*, vol. 29, no. 6, pp. 839-845, Feb. 1999.

[22] Z. Hashin, "Analysis of composite materials–a survey," *ASME J. Appl. Mech.*, vol. 50, pp. 481–505, Sep. 1983.

[23] W. Drugan and J. Willis, "A micromechanics-based nonlocal constitutive equation and estimates of representative volume element size for elastic compositessize for elastic composites," *J. Mech. Phys. Solids*, vol. 44, pp. 497–524, Apr. 1996.

[24] M. Ostoja-Starzewski, "Microstructural randomness versus representative volume element in thermomechanics," *ASME J. Appl. Mech*, vol. 69, pp. 25–35, Jun. 2002.

[25] M. Stroven, H. Askes, and L. Sluys, "Numerical determination of representative volumes for granular materials," *Comput. Methods Appl. Mech. Eng.*, vol. 193, no. 30-32, pp. 3221–3238, Jul. 2004.

[26] A. Drago and M.-J. Pindera, "Micro-macromechanical analysis of heterogeneous materials: macroscopically homogeneous vs periodic microstructures," *Compos. Sci. Technol.*, vol. 67, no. 6, pp. 1243–1263, May. 2007.

[27] R. Christensen and K. Lo, "Solutions for effective shear properties in three phase sphere and cylinder models," *J. Mech. Phys. Solids*, vol. 27, no. 4, pp. 315–330, Aug. 1979.

[28] J. Eshelby "The determination of the elastic field of an ellipsoidal inclusion and related problems," *Proc. Royal Society London Ser. A*, vol. 241, pp. 376-396, Mar. 1957.

[29] Y. Benveniste, "A new approach to the application of Mori-Tanaka's theory in composite materials," *Mech. Mater.*, vol. 6, no. 2, pp. 147–157, Jun. 1987.

[30] Z. Hashin, "The differential scheme and its application to cracked materials," *J. Mech. Phys. Solids*, vol. 36, no. 6, pp. 719–734, 1988.

[31] L. Walpole, "On the overall elastic moduli of composite materials," *J. Mech. Phys. Solids*, vol. 17, no. 4, pp. 235–251, Sep, 1969.

[32] A. Kaw, *Mechanics of Composite Materials*, 2nd ed. New York, NY, USA: Taylor & Francis, 2006.

[33] Z. Hashin and S. Shtrikman, "On some variational principles in anisotropic and nonhomogeneous elasticity," *J. Mech. Phys. Solids*, vol. 10, no. 4, pp. 335–342, Oct./Dec., 1962.

[34] T. Mori and K. Tanaka "Average stree in matrix and average energy of materials with mis-fitting inclusions," *Act. Metall.*, vol. 21, no. 5, pp. 571-574, May. 1973.

[35] R. Hill, "A self-consistent mechanics of composite materials," *J. Mech. Phys. Solids*, vol. 13, pp. 213–222, Aug. 1965.

[36] A. Reuss, "Berechnung der fließgrenze von mischkristallen auf grund der plastizitätsbedingung für einkristalle," *J. Appl. Math. Mechanics*, vol. 9, pp. 49–58, 1929.

[37] H. Zhang, K. Anupam, A. Scarpas, and C. Kasbergen, "Comparison of different micromechanical models for predicting the effective properties of open graded mixes," *Transp. Res. Rec.*, vol. 2672, no. 28, pp. 404–415, Sep. 2018.

[38] M. Hori and S. Nemat-Nasser, "Double-inclusion model and overall moduli," *Mech. Mater.*, vol. 14, no. 3, pp. 189–206, Jan. 1993.

[39] C. Shi, H. Fan, and S. Li, "Interphase model for effective moduli of nanoparticle-reinforced composites," *J. Eng. Mechanic*, vol. 141, no. 12, pp. 141–153, Dec. 2020.

[40] Y. Li, Y. Li, and R. Wang, "Quantitative evaluation of elastic modulus of concrete with nanoidentation and homogenization method," *Constr. Build. Mater.*, vol. 212, pp. 295–303, Jul. 2019.

[41] N. V. Silva, "Propriedades mecânicas das fases e seus efeitos no comportamento mecânico do concreto," Ph.D. dissertation, Poli USP, São Paulo, Brazil, 2022.

ORIGINAL ARTICLE

Damage and plasticity evolution of reinforced concrete beams using laminated Euler-Bernoulli finite elements

Evolução do dano e da plasticidade em vigas de concreto armado utilizando elementos finitos de vigas de Euler-Bernoulli laminados

Ana Paula Imai[a]
Thiago de Oliveira Abeche[b]
Roberto Dalledone Machado[a,b]

[a]Universidade Federal do Paraná – UFPR, Programa de Pós-graduação em Engenharia Civil – PPGEC, Curitiba, PR, Brasil
[b]Universidade Federal do Paraná – UFPR, Programa de Pós-graduação em Métodos Numéricos em Engenharia – PPGMNE, Curitiba, PR, Brasil

Abstract: This paper analyses the behaviour of reinforced concrete beams subjected to progressive loads. Although this topic is addressed in recent works through tri-dimensional finite elements, the present study adopts a simpler alternative, using Euler-Bernoulli's beam finite element. The evolution of the generalized cracking is addressed by Damage Mechanics theory, and the nonlinear constitutive models of concrete and steel are considered, including plasticity and post-peak '. The laminated approach permits not only to ascertain the damage evolution but, in practical aspects, makes easy to define vertically symmetrical transversal sections and to distribute the reinforcement as desired, even if the steel rebars have different lengths. It is highlighted the changing of the neutral axis during the damage evolution process, which is updated automatically by the developed numeric-computational code. To validate the proposed methodology, two examples are detailed, both based on experimental tests found in the literature. The results obtained are close to the experimental ones and confirm the applicability of the proposed approach.

Keywords: reinforced concrete, nonlinear analysis, damage evolution, plasticity theory, laminated composite beams.

Resumo: Este trabalho analisa o comportamento de vigas de concreto armado submetidas a carregamentos progressivos. Embora este tema seja tratado em trabalhos mais recentes através de modelos de elementos finitos tridimensionais, o presente trabalho adota uma alternativa mais simples empregando elementos finitos de viga de Euler-Bernoulli. A evolução da fissuração generalizada é abordada pela teoria da Mecânica do Dano, e são considerados os modelos constitutivos não lineares do concreto e do aço, incluindo a plasticidade e o comportamento pós-pico. A abordagem laminada permite não só verificar a evolução do dano, mas, em aspectos práticos, facilita definir seções transversais verticalmente simétricas e distribuir a armadura conforme desejado, mesmo que as barras de aço tenham comprimentos diferentes. Destaca-se a mudança da linha neutra durante o processo de evolução do dano, que é atualizado automaticamente pelo código numérico-computacional desenvolvido. Para validar a metodologia proposta, são detalhados dois exemplos, ambos baseados em testes experimentais encontrados na literatura. Os resultados obtidos são muito próximos dos experimentais e confirmam a aplicabilidade da abordagem proposta.

Palavras-chave: concreto armado, análise não linear, evolução do dano, teoria da plasticidade, vigas laminadas.

1 INTRODUCTION

For civil engineering applications, the adoption of one-dimensional finite elements in structural analysis is frequent due to its low computational cost. Over the last years, however, the necessity of more complex analyses has been growing, to increase the structure reliability. The pursuance of conducting more advanced studies, however, usually demands more computational resources. Several research take advantage of one-dimensional finite elements, making necessary adjustments, according to the conditions. In reinforced concrete, subjected to cracking and plasticity, or dynamic loadings, many methodologies can be implemented to consider these effects in simulations.

Álvares [1] proposes a simplified methodology to consider the damage and plasticity, which are applied to the element's nodes. Biondi and Caddemi [2] presented a model which uses distributions such as unit step and Dirac's delta functions to simulate discontinuities in the curvature and in the slope functions of Euler–Bernoulli beams. Ghrib et al. [3] presented two computational procedures to recalculate the stiffness due to damage in Euler–Bernoulli beams, identified through static deflection measurements. One of the formulations is based on the principle of the equilibrium gap along with a finite-element discretization, obtaining a solution by minimizing a regularized functional using a Tikhonov total variation scheme. The second formulation refers to a minimization of a data-discrepancy functional between measured and model-based deflections. In order to account for multi-axial coupling of axial force, shear, flexure and torsion in a beam element, Corvec [4] proposes a model with warping degrees of freedom at arbitrary points of the cross-section, in order to accommodate higher order strain kinematics. Regarding dynamic effects, Xie et al. [5] compared results obtained from beam and plane state finite elements in rail-wheel interaction, obtaining similar outcomes on both models.

To consider the physical non-linearity, some research adopt the beam element's discretization into fibers or layers. Spacone et al. [6] present a fibre beam-column element in which the equilibrium state is obtained through an iterative algorithm that satisfies the element constitutive relation. The method is suitable for the simulating reinforced concrete columns under varying axial load, subjected to non-linear hysteretic behaviour of softening members. Mazars et al. [7] presented a multifiber beam element capable of reproducing shear from Timoshenko's theory or shear due to torsion. *Oliveira* et al. [8] studied the bond-slip effects on the steel–concrete interface of reinforced concrete beams. For such, is presented a beam-layered model, which accounts the materials interaction. Lezgy-Nazargah et al. [9] proposed a refined global-local laminate theory, based on the superposition hypothesis for bending and vibration analyses of the laminated/sandwich composite beams.

By dividing a transversal section into layers, the following advantages may be highlighted:

a) each concrete layer may have its own stress state and may be damaged differently;

b) any type of vertically symmetrical transversal section can be adopted;

c) the reinforcement bars can be distributed as desired in any position of cross-section; and

d) the verification of the neutral axis can be updated for each step.

The laminated beam theory for Euler-Bernoulli model is adopted in the present work. Details about this methodology, based on the work of Abeche et al. [10], are addressed. The concrete is taken as bi-modular material, with different behaviour for tension, compression and both combined with shear. The damage criterion in this work is the Mazars' damage model [11] and it is applied for each layer in all Gaussian points of the elements. If the damage occurs, the neutral axis is updated since the cross-section's stiffness is changing. An elastic perfectly plastic stress-strain constitutive model is adopted for the steel reinforcement, with same behaviour for tension and compression. The shear stress and the consideration of stirrups are also addressed in this work. The bonding between concrete and steel rebars is assumed perfect without slipping.

To validate this approach, two examples are presented. The first one is a single supported beam which was modeled and tested by Mazars and Grange [12]. The second problem is related to the famous work of Bresler and Scordelis [13], who tested many reinforced concrete beams with different cross-sections and for many kinds of reinforcements. Many models were developed [14], [15], [16] aiming to reproduce the experimental results of Bresler and Scordelis [13].

The present work developed a finite element code in C++ programming language wrapped with *MATLAB*. It can solve linear and nonlinear static models. For progressive loads, a multi-step scheme is adopted with the Newton-Raphson iterative technique for the nonlinear problems.

This work is divided into seven more items following this Introduction. A brief review of Euler-Bernoulli beam theory is presented in the subsequent section, which also brings the laminated beam theory. The following section addresses the constitutive models for concrete and steel. The damage model is discussed, highlighting the Mazars' model. Then, some aspects of the variation of neutral axis are pointed out, followed by an item that presents the scheme for nonlinear static equilibrium. The next section details the two examples analysed in this work, and the results are presented. The last item is reserved for discussion and conclusions.

2 THE EULER-BERNOULLI BEAM ELEMENT

2.1 The classical EB beam element

The classical Euler-Bernoulli beam finite element is presented for modelling reinforced concrete beams. The main hypotheses are presented, where x_1 and x_2 are, respectively, the horizontal and vertical axes:
1. the existence of a neutral axis;
2. plane sections stay plane after the bending;
3. the material is linear elastic and homogeneous;
4. normal and shear stresses, σ_{x_2} and $\tau_{x_1 x_2}$, are too small in relation of σ_{x_1} and may be ignored;
5. the $x_1 x_2$ is a principal plane.

The differential equation that represents the problem is (Equation 1)

$$EI \frac{d^4 u_2}{dx_1^4} - q(x_1) = 0, \tag{1}$$

Where E is the Young's modulus, I is the beam's moment of inertia, q is the external applied force and u_2 is the vertical displacement. It must be highlighted that these parameters depend on the position and load steps for physical nonlinearities, as presented in further sections.

In finite element approach, the approximated displacement in vertical direction, $\bar{u}_2$ may be obtained by interpolating the nodal responses, a_i, with the shape functions ϕ_l, that is,

$$\bar{u}_2 = \sum_{l=1}^4 \phi_l \bar{a}_i. \tag{2}$$

By using the approximated variable, Equation 2, there are residues, ε, in the domain, Ω, and in the contour, Γ, such that (Equation 3),

$$EI \frac{d^4 \bar{u}_2}{dx_1^4} - q(x_1) \neq 0 = \varepsilon_\Omega \cup \varepsilon_\Gamma. \tag{3}$$

The weighted residual sentence is used to minimize them,

$$\int_\Omega w_l \varepsilon_\Omega d\Omega + \int_\Gamma \bar{w}_l \varepsilon_\Gamma d\Gamma = 0, \tag{4}$$

Where w_l and $\bar{w}_l$ are, respectively, the weighting functions in Ω and Γ.

In finite element method the Dirichlet boundary conditions are automatically satisfied prior to solving the system of equations, making null the second integral of Equation 4. In this sense, only the domain portion of the equation should be considered. Furthermore, by using the Petrov-Galerkin method, weighting functions, w, are the shape functions, ϕ_l, themselves. Thus, one can obtain (Equation 5)

$$\int_\Omega \phi_l \varepsilon_\Omega d\Omega = \int_\Omega \phi_l \left(EI \frac{d^4 \bar{u}_2}{dx_1^4} - q(x_1) \right) d\Omega = 0. \tag{5}$$

Taking the element domain as $[-L/2, +L/2]$ and transferring the differential operator acting in the variable of interest, two times, to the shape function, through Green's divergence theorem, one obtains (Equation 6)

$$\phi_l EI \frac{d^3 \bar{u}_2}{dx_1^3} \Big|_{x_1=-\frac{L}{2}}^{x_1=+\frac{L}{2}} - \frac{d\phi_l}{dx_1} EI \frac{d^2 \bar{u}_2}{dx_1^2} \Big|_{x_1=-\frac{L}{2}}^{x_1=+\frac{L}{2}} + \int_{-\frac{L}{2}}^{+\frac{L}{2}} \left(EI \frac{d^2 \bar{u}_2}{dx_1^2} \frac{d^2 \phi_l}{dx_1^2} - \phi_l q(x_1) \right) dx_1 = 0, \tag{6}$$

or, in expanded way, in terms of nodal degrees of freedom, $\bar{a}_{i1}$, $\bar{\theta}_{i1}$, $\bar{a}_{i2}$, $\bar{\theta}_{i2}$, which means the approximated vertical displacements and rotations at initial and final nodes (Equation 7)

$$\frac{EI}{L^3}\begin{bmatrix} 12 & 6L & -12 & 6L \\ 6L & 4L^2 & -6L & 2L^2 \\ -12 & -6L & 12 & -6L \\ 6L & 2L^2 & -6L & 4L^2 \end{bmatrix}\begin{Bmatrix} \bar{a}_{i1} \\ \bar{\theta}_{i1} \\ \bar{a}_{i2} \\ \bar{\theta}_{i2} \end{Bmatrix} = \begin{Bmatrix} \frac{qL}{2} \\ \frac{qL^2}{12} \\ \frac{qL}{2} \\ -\frac{qL^2}{12} \end{Bmatrix} + \begin{Bmatrix} EI\frac{d^3\bar{u}_2}{dx_1^3}\Big|_{x_1=-\frac{L}{2}} \\ -EI\frac{d^2\bar{u}_2}{dx_1^2}\Big|_{x_1=-\frac{L}{2}} \\ -EI\frac{d^3\bar{u}_2}{dx_1^3}\Big|_{x_1=\frac{L}{2}} \\ EI\frac{d^2\bar{u}_2}{dx_1^2}\Big|_{x_1=\frac{L}{2}} \end{Bmatrix} \tag{7}$$

Rearranging the terms in Einstein notation, one has (Equation 8)

$$K_{ij}\bar{u}_{2_i} = F_i + F_{\partial\Omega_i}, \tag{8}$$

Where K_{ij} is the FEM stiffness matrix, F_i is the applied external forces vector and $F_{\partial\Omega_i}$ is the vector which contains the local components of bending moment and shear force that are canceled when assembling the global system.

The stiffness matrix can also be defined through FEM B tensor, as further detailed ahead, by (Equation 9)

$$K_{ij} = \int_\Omega B_j^T EI B_j \, d\Omega. \tag{9}$$

2.2 The laminated beam element

To consider the nonlinear behaviour of reinforced concrete by Damage Mechanics and Plasticity Theory in the Euler-Bernoulli FEM beam model, the cross-section is divided in layers, as indicated in Figure 1.
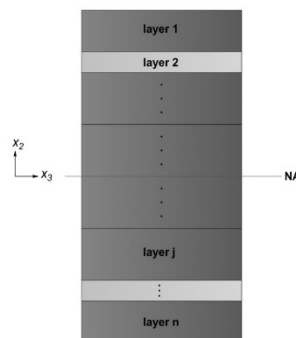
Figure 1. Cross-section of a laminated Euler-Bernoulli beam element.

During the progressive loading, the mechanical properties of each layer (elasticity modulus, damage parameter, etc.), and the effective area and moment of inertia of the whole section may be changed. Therefore, stresses and strains for each layer may be computed individually.

2.2.1 Mapping and equivalent stiffness concept

Despite the finite element of Euler-Bernoulli beam is a one-dimensional element with 2 degrees of freedom per node, it is possible to consider the other dimensions and physical parameters through mapping it to an auxiliary mesh, as represented by Figure 2.
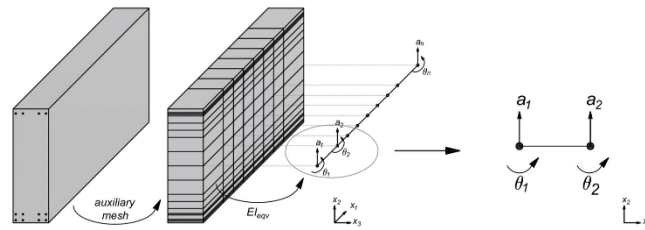
Figure 2. Consider of other dimensions, physical parameters, and local refinement in laminated Euler-Bernoulli beam element.

For this reason, it is necessary to determine an equivalent stiffness for each element. In the particular case of x_2 symmetry in laminated beams of composite materials with constant width b, the bending equivalent stiffness EI_{eqv} can be determined by [17] (Equation 10)

$$EI_{eqv} = \frac{1}{3}b \sum_{i=1}^{n} E_i[(x_2)_i^3 - (x_2)_{i-1}^3],$$ (10)

In which $(x_2)_i$ is the ith layer's bottom edge cartesian coordinate and $(x_2)_{i-1}$ is the $(i-1)^{th}$ layer's bottom edge cartesian coordinate.

2.2.2 Gaussian quadrature

The Gaussian quadrature is a procedure that numerically approximates the value of an integral exactly, enables practical use in domains whose integral functions are not standardized and minimizes computational processing time. Therefore, its use in association with FEM is very opportune.

Through this numerical integration method, it is only necessary to choose a quantity of points sufficiently to integrate a function exactly. As the Euler-Bernoulli beam element utilize Hermitian third order polynomial functions, 2 points are enough to approximate it with exact precision. These points have coordinates $\pm 1/\sqrt{3}$ and unitary weights. Those are the number of points and coordinates adopted in this study.

In addition to bringing a precision advantage to linear FEM analysis when calculating responses at Gaussian points instead of directly evaluating them at nodes, from the Damage Mechanics and Plasticity Theory perspectives it is also better to evaluate the nonlinearities effects at these points and then extrapolate the responses to the nodes, since numerical precision can affect the responses path due to the dependence of response history, especially in concrete damage.

2.2.3 The B FEM tensor evaluated in Gaussian points

In bending beams theory, the rotation θ is defined by (Equation 11)

$$\theta(x_1) = \frac{du_2}{dx_1}.$$ (11)

The strain in direction x_1 of Euler-Bernoulli's beam is calculated by

$$\varepsilon_{x_1} = -x_2 \frac{d\theta}{dx_1} = -x_2 \frac{d^2 u_2}{dx_1^2} = -x_2 \sum_{l=1}^{n} \frac{d^2 \phi_l}{dx_1^2} \bar{a}_l.$$ (12)

As can be seen, the strain defined by Equation 12 is defined in x_1 coordinate. To calculate the strains in the Gaussian points, it is necessary to substitute the variable x_1 to the variable s_1. Using the chain rule to transform the coordinate system, the B_l tensor is defined dependently of the Jacobian J, as shown below (Equation 13),

$$B_l = -\frac{d^2\phi_l}{dx_1^2} = -\frac{d^2\phi_l}{ds_1^2}\frac{1}{J^2}. \tag{13}$$

In this sense, the strain in each point of the cross-sections' layers is evaluated at Gaussian integration points of the elements, P_i, in the following way (Equation 14)

$$\varepsilon_{x_1} = -x_2 \sum_{l=1}^{n} \frac{d^2\phi_l}{ds_1^2}\frac{1}{J^2}\bar{a}_l = x_2 B_l \bar{a}_l, \tag{14}$$

Where $\bar{a}_l$ are the nodal degrees of freedom, or the approximated nodal responses of displacements and rotations.

Since a variable substitution was performed, the stiffness matrix in Einstein notation, Equation 9 can be now calculated by (Equation 15)

$$\begin{aligned} K_{ij} &= \int_{-\frac{L}{2}}^{+\frac{L}{2}} B_j^T EIB_j \, dx_1 = \int_{-1}^{+1} B_j^T EIB_j J \, ds_1 \\ &= \sum_{i=1}^{n_{x_1}} B_j^T(P_i)E(P_i)I(P_i)B_j(P_i)JW_i, \end{aligned} \tag{15}$$

Where the Jacobian is defined by $J = \frac{dx_1}{ds_1} = +\frac{L}{2}$, and L is the length of the local finite element.

3 CONSTITUTIVE MODELS AND THE CONSIDERATION OF NONLINEARITIES

It is possible to introduce the effects of physical nonlinearities in a sub local region, or better, in a representative volume element, RVE. Thus, the third hypothesis presented of the classical Euler-Bernoulli beam element can now be disregarded.

Unlike a linear elastic regime, the stiffness of the problem now depends on the nodal degrees of freedom, displacements, and rotations, which in turn depend on the position vector of each layer. In this sense, we have (Equation 16)

$$K_{ij} = K_{ij}[\bar{u}_2(\overrightarrow{x_1})]. \tag{16}$$

3.1 Fundamentals of solid thermodynamics

3.1.1 Clausius-Duhem inequality

By combining the first and second laws of thermodynamics, so that a mechanical process if thermodynamically admissible, through Clausius-Duhem inequality [18], one has (Equation 17)

$$\rho\Theta\dot{S} + \sigma_{ij}\dot{\varepsilon}_{kl} - \rho\dot{u} - \frac{1}{\Theta}\nabla\Theta q \geqslant 0, \tag{17}$$

Being (Equation 18)

$$\dot{u} = \dot{u}_{\text{stored}} + \dot{u}_{\text{dissipated}}, \tag{18}$$

And (Equation 19)

$$\rho\dot{u}_{\text{stored}} + \rho\dot{u}_{\text{dissipated}} = \dot{U}_{\text{stored}} + \dot{U}_{\text{dissipated}} = \sigma_{ij}\dot{\varepsilon}_{kl}, \tag{19}$$

Where ρ is the mass density and Θ is the absolute temperature defined as a scalar field of positive values at each point in the domain Ω under consideration. S is the specific entropy per mass unit, σ_{ij} is the stress tensor, $\dot{\varepsilon}_{kl}$ is the strain rate,

Rev. IBRACON Estrut. Mater., vol. 16, no. 5, e16502, 2023

6/19

q is the heat flow vector. $\dot{U}_{\text{stored}}$ is the rate of change of the stored energy, $\dot{U}_{\text{dissipated}}$ is the rate of change of the dissipated energy, $\dot{u}_{\text{stored}}$ and $\dot{u}_{\text{dissipated}}$ are the rate of change in the density of internal energy, stored and dissipated, respectively, per mass unit.

In a pure mechanical process, the Clausius-Duhem inequality is defined by

$$\dot{U}_{\text{stored}} \leqslant \sigma_{ij}\dot{\varepsilon}_{kl}. \tag{20}$$

3.1.2 Thermodynamic formalism of Damage Mechanics

Part of $\dot{U}_{\text{stored}}$ remains stored in the system while another portion, recoverable, is a function of a reversible state variable, such as elastic strain. In this sense, $\dot{U}_{\text{stored}}$ is a function that depends on elastic strain and associated internal variables, that in rate terms is defined as [18]

$$\dot{U}_{\text{stored}} = \frac{\partial U_{\text{stored}}}{\partial \varepsilon_{kl}^e}\dot{\varepsilon}_{kl}^e + \frac{\partial U_{\text{stored}}}{\partial V_k}\dot{V}_k, \tag{21}$$

Being $\dot{\varepsilon}_{kl}^e$ is the elastic strain rate for small strains consideration and $\dot{V}_k$ is the internal state variables rate of change.

Combining the Equation 20 and Equation 21, one can obtain [18]

$$\sigma_{ij}\dot{\varepsilon}_{kl} - \overbrace{\frac{\partial U_{\text{stored}}\,\dot{\varepsilon}_{kl}^e}{\partial \varepsilon_{kl}^e}}^{\text{recoverable}} - \overbrace{\frac{\partial U_{\text{stored}}}{\partial V_k}\dot{V}_k}^{\text{unrecoverable}} \geqslant 0. \tag{22}$$

The Equation 22 is extremely important for understanding of nonlinear physical processes, such as damage and plasticity. The second law of thermodynamics states that the rate of dissipated internal energy is always positive. In Equation 22, a portion of the recoverable stored energy rate and an unrecoverable one is observed. If the unrecoverable portion, third term, is null, remaining only the recoverable portion, there will be a fully reversible process. Therefore, the recoverable portion is always reversible. Purely elastic processes have no energy dissipation, being fully recoverable and reversible. In this sense, the energy dissipated can only arise from the unrecoverable portion of the energy rate stored in the system [18].

The unrecoverable portion is divided according to the material's state variables. In the most general case, the unrecoverable portion is divided into a reversible and an irreversible portion, which is the dissipated energy. The unrecoverable and not dissipated portion can be reversible, but only by an additional thermal process. In purely mechanical processes, this portion remains blocked in the volume. It can be unrecoverable, but it is not completely irreversible. Part of it is irreversible, dissipated, and another part, not dissipated, is reversible, but only by an additional thermal process [18].

In damaged elastic medium, as for the concrete, there are only recoverable energy and dissipated energy, that is, the entire portion of the unrecoverable energy is dissipated. In this sense, if the third term of Equation 22 is null there will be no dissipated energy, that is, being a fully reversible process. If it is greater than zero, on the other hand, there will be dissipated energy. In elastoplastic responses with hardening, as for the reinforcement, otherwise, there is a portion of recoverable energy, reversible, an unrecoverable portion dissipated, irreversible, and an unrecoverable portion not dissipated, blocked in volume and reversible only by additional thermal process [18].

3.2 Damage Mechanics

Here, some concepts of Damage Mechanics will be briefly presented.

3.2.1 Elastic media with damage

In the case of elastic damaged materials, when unloading process occurs all strains can be recovered. Nevertheless, the Young's modulus is directly affected by the damage. In this way, the internal energy is determined by two state variables, the strain tensor ε_{kl} and the damage parameter D, the latter being an internal variable. Thus, $U = U(\varepsilon_{kl}, D)$. Consequently [11], [19],

$$\dot{U} = \frac{\partial U}{\partial \varepsilon_{kl}}\bigg|_{D=\text{fixed}} \cdot \dot{\varepsilon}_{kl} + \frac{\partial U}{\partial D}\dot{D} = \dot{U}_{\text{stored}} + \dot{U}_{\text{dissipated}}. \tag{23}$$

In uniaxial models, strain energy can be defined as follows [19],

$$U = \frac{1}{2}(1-D)E\varepsilon^2. \tag{24}$$

By combining the Equation 23 in Equation 24, one obtains [19] (Equation 25)

$$\dot{U}_{\text{stored}} = (1-D)E\varepsilon.\dot{\varepsilon} \tag{25}$$

And (Equation 26)

$$\dot{U}_{\text{dissipated}} = -\frac{1}{2}\varepsilon^2\dot{D} = Y\dot{D} \geqslant 0, \tag{26}$$

Where (Equation 27)

$$Y = -\frac{1}{2}E\varepsilon^2 \tag{27}$$

is the damage energy release rate associated with the damage variable.

3.2.2 The damage of each layer

In each layer of each cross-section of its respective Gaussian point, are attained a strain and a stress tensorial states, ε and σ, dependents of the distance from the neutral axis, the stirrup distribution, and the moment of inertia variation. In these are calculated the concrete's damage and the steel's plasticity evolution processes.

The beam can suffer damage effect in a generalized way. The following hypotheses are considered:
a) in a local scale, the damage effect occurs due to stretching;
b) the damage is represented by a scalar variable in the sense that, when the variable reaches a certain value, a damage evolution happens;
c) the damage is considered here as an isotropic variable;
d) it is assumed that concrete is a nonlinear elastic medium with damage.

The damage evolution is based on the stretch that the material is subjected during the loading. For the equivalent strain of the Damage Mechanics, $\tilde{\varepsilon}$, it is used the definition proposed by Mazars and Pijaudier-Cabot [20], in order to adequate the density energy release rate for concrete's mechanical behaviour, defined as (Equation 28)

$$\tilde{\varepsilon} = \sqrt{\sum_{i=1}^{3}(\langle\varepsilon_i\rangle_+)^2}, \tag{28}$$

With (Equation 29)

$$\langle\varepsilon_i\rangle_+ = \begin{cases} \varepsilon_i, & \varepsilon_i > 0 \\ 0, & \varepsilon_i \leq 0 \end{cases}, \tag{29}$$

Where $\langle\cdot\rangle_+$ are the Macauley brackets and ε_i are the principal strains.

When $\tilde{\varepsilon}$ reaches certain value, the damage process begins. Taking D as the damage variable, ε_{d0} the maximum linear strain for the uniaxial tension test, and $S(D)$ a function that links the beginning damage strain with the damage variable, this process can be expressed by the damage loading function (Equation 30)

$$f(\tilde{\varepsilon}, D) = \tilde{\varepsilon} - S(D) \leqslant 0, \ S(0) = \varepsilon_{d0}. \tag{30}$$

So, the damage evolution can be measured by the rate of damage variable using the Karush-Kuhn-Tucker conditions, which is [21] (Equation 31),

$$\dot{D} = \begin{cases} 0, & \text{if } f \leq 0 \text{ and } \dot{f} < 0 \\ F(\tilde{\varepsilon})\langle\dot{\tilde{\varepsilon}}\rangle_+, & \text{if } f = 0 \text{ and } \dot{f} = 0 \end{cases}, \tag{31}$$

In which $\dot{D}$ is the damage rate, $\langle\dot{\tilde{\varepsilon}}\rangle_+$ is the positive portion of the equivalent strain rate, $F(\tilde{\varepsilon})$ is a continuous and positive function of the equivalent strain $\tilde{\varepsilon}$ such that $\dot{D} \geq 0$ for any $\tilde{\varepsilon}$. This ensures that the damage is increasing and irreversible. In this sense, the function $F(\tilde{\varepsilon})$ must be able to reproduce the experimental behaviour of one-dimensional, two-dimensional, and three-dimensional experiments.

According to Mazars [11], two rate damage variables can be deal with, $\dot{D}_T$ and $\dot{D}_C$, for the traction and compression, respectively (Equation 32),

$$\dot{D}_T = F_T(\tilde{\varepsilon})\langle\dot{\tilde{\varepsilon}}\rangle_+, \ \dot{D}_C = F_C(\tilde{\varepsilon})\langle\dot{\tilde{\varepsilon}}\rangle_+, \tag{32}$$

Where $F_T(\tilde{\varepsilon})$ and $F_C(\tilde{\varepsilon})$ are the $F(\tilde{\varepsilon})$ function for the tension and compression situations, respectively.

Since the damage is a dissipative and accumulative process, the damage variable can raise in traction or in compression. This is an important aspect to be highlighted since all points in a beam can suffer tension or compressions due to loading and unloading or, for dynamic cases, due to dynamic responses and induced vibrations, as proposed by Abeche et al. [10].

The damage variable is split into two parts (Equation 33)

$$D = \alpha_T D_T + \alpha_C D_C, \tag{33}$$

Where D_T and D_C are the damage variables in tension and compression, respectively. They are combined with the weighting coefficients α_T and α_C, defined as functions of the principal values of the strains, due to positive and negative stresses [20] (Equation 34),

$$\alpha_T = \sum_{i=1}^{3}\left(\frac{\langle\varepsilon_i^t\rangle\langle\varepsilon_i\rangle}{\tilde{\varepsilon}^2}\right)^{\beta} \tag{34}$$

And (Equation 35)

$$\alpha_C = \sum_{i=1}^{3}\left(\frac{\langle\varepsilon_i^c\rangle\langle\varepsilon_i\rangle_+}{\tilde{\varepsilon}^2}\right)^{\beta}, \tag{35}$$

In which $\langle\varepsilon^t\rangle$ is the tensile strain vector, in other words, the strain associated with tensile stresses. In the same way, $\langle\varepsilon^c\rangle$ is the compressive strain vector, associated with compressive stresses. β is an adjustment relative to the response to the material's shear behaviour and, usually, is defined as $\beta = 1$. For the case of the material is subjected to uniaxial tension, $\alpha_T = 1$ and $\alpha_C = 0$. Similarly, if the material is under uniaxial compression, $\alpha_T = 0$ and $\alpha_C = 1$ [22].

The damage variables D_T and D_C can be calculated through the Mazars' damage constituve model [11], as (Equation 36)

$$D_T(\tilde{\varepsilon}) = 1 - \frac{\varepsilon_{d0}(1 - A_T)}{\tilde{\varepsilon}} - \frac{A_T}{e^{B_T(\tilde{\varepsilon} - \varepsilon_{d0})}} \tag{36}$$

And (Equation 37)

$$D_C(\tilde{\varepsilon}) = 1 - \frac{\varepsilon_{d0}(1 - A_C)}{\tilde{\varepsilon}} - \frac{A_C}{e^{B_C(\tilde{\varepsilon} - \varepsilon_{d0})}},$$ (37)

Where A_T, B_T, A_C and B_C are characteristics parameters obtained from single tension and compression state tests. Mazars [11] initially suggested the following limits for these variables, to define the constitutive relation that associates the physical and mathematical formalisms of Damage Mechanics (Equation 38),

$$\begin{array}{ll} 0.7 \leqslant A_T \leqslant 1.0 & 10^4 \leqslant B_T \leqslant 10^5 \\ 1.0 \leqslant A_C \leqslant 1.5 & 10^3 \leqslant B_C \leqslant 2.10^3. \\ \quad 10^{-5} \leqslant \varepsilon_{d0} \leqslant 10^{-4} \end{array}$$ (38)

Mazars later proposed changes in the limits of the calibration parameters [12]. The stress-strain diagrams for the tension and compression cases considering the damage process are illustrated in Figure 3.
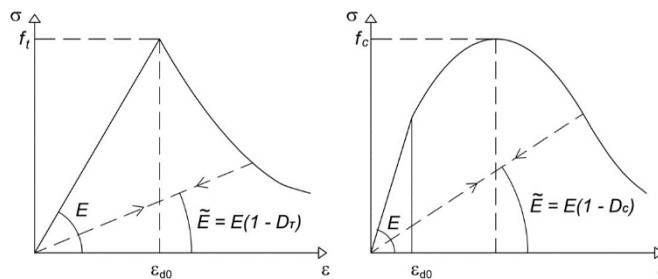
Figure 3. Concrete damage model for tension and compression stresses.

3.2.3 The plasticity in steel layers

The steel rebars of the reinforced concrete beam are reshaped into steel layers, maintaining its area and center of gravity properties. For the behaviour of the steel layers in Euler-Bernoulli beam finite element, a bilinear constitutive model with yielding and permanent strains is used, with symmetric behaviour in tension and compression, as illustrated in Figure 4.
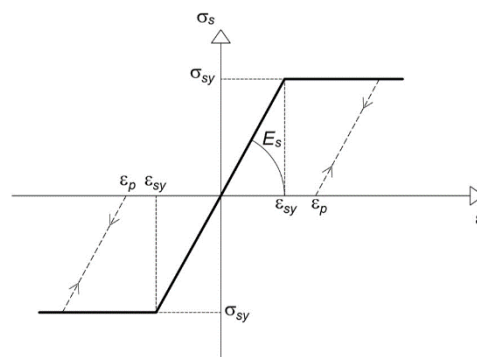
Figure 4. Steel constitutive model.

The constitutive relation is described by (Equation 39)

$$|\sigma| = \begin{cases} E_s|\varepsilon - \varepsilon_p|, & |\varepsilon| \leq |\varepsilon_{sy} + \varepsilon_p| \\ |\sigma_{sy}|, & |\varepsilon| > |\varepsilon_{sy} + \varepsilon_p| \end{cases}.$$ (39)

4 FURTHER CONSIDERATIONS ON THE LAMINATED EULER-BERNOULLI NONLINEAR BEAM ELEMENT

4.1 Analytical variation of the neutral axis position

If the variation of the neutral axis position, $(x_2)_{NA}$, is not contemplated, i.e, remaining unchanged in relation to the initial position, this prescribes that damages of the layers above the neutral axis, or above the center of gravity, would always occur by compression while the layers below the unchanged neutral axis would always suffer the phenomenon of traction. This can be valid if the neutral axis changes slightly.

On the other hand, if the position of the neutral axis varies significantly, the damage evolution itself can occur differently, and the consideration of a stagnant neutral axis can no longer be made. For example, a layer that would initially suffer compression phenomenon, in the case of ascension of the neutral axis, can now suffer the traction effect. The work of Abeche et al. [10] considers the variation of the neutral axis position iteratively. This paper considers the variation of the neutral axis' position analytically, inside each element, as follows (Equation 40)

$$(x_2)_{NA}^i = \frac{\sum_{j=1}^{\text{layers}} (x_2)_j^i E_j^i A_j^i}{\sum_{j=1}^{\text{layers}} E_j^i A_j^i}, \tag{40}$$

Where A is the area of the j-th layer of the i-th element.

This consideration allows a great reduction of the computational effort to find the equilibrium position, in comparison with iterative procedures.

After updating the position of the neutral axis $(x_2)_{NA}^i$, the new coordinates are updated analytically according to the absolute coordinates of the layers and the new position of the neutral axis as follows (Equation 41)

$$\{(x_2)_{\text{rel}}\}^i = \{(x_2)_{\text{abs}}\}^i - (x_2)_{\text{NA}}^i. \tag{41}$$

Where $\{(x_2)_{\text{rel}}\}^i$ is the vector that stores these updated x_2 coordinates of each element inside each iteration.

4.2 Variation of the moments of inertia of the layers

In addition to considering the variation of the position of the neutral axis in an analytical way, this work adds as innovation the variation of the moments of inertia of each layer when the damage process occurs.

No studies were found that considered the variation in the moments of inertia of the layers when the damage process occurs. This physical consideration is plausible, since by varying the Young's modulus in the damage process the position of the neutral axis varies and, consequently, the moments of inertia of the layers, indeed, also vary.

The absolute global coordinates of the center of gravity of each layer are stored in the $\{y_{cg}\}$ vector. After updating the position of the neutral axis, according to Equation 40, the vector containing the moments of inertia of each layer of each element's Gaussian points is recalculated using Steiner's theorem, as follows (Equation 42)

$$I^i = \sum_{j=1}^{\text{layers}} \left((I_g)_j^i + A_j^i \left| (x_2)_{NA}^i - (y_{cg})_j^i \right|^2 \right). \tag{42}$$

The Figure 5 illustrates the variation of the moment of inertia of the layers.
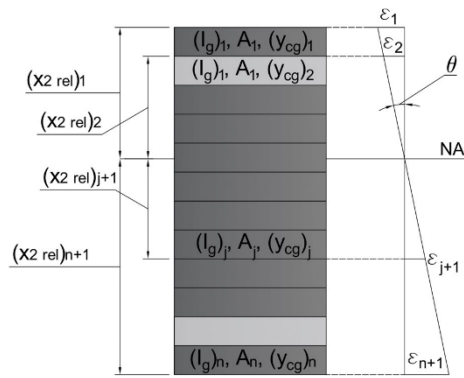
Figure 5. Layer properties and strain in each layer.

4.3 Shear stress and stirrups

Despite the classical Euler-Bernoulli beam theory neglects the shear deformation in its formulation, when the segmentation of finite elements in layers is applied, the shear strain and stresses can have a major influence on its Damage evolution.

To consider the shear stresses at the jth layer of a Euler-Bernoulli beam, one has [23] (Equation 43)

$$\left(\tau_{x_1 x_2}\right)_j = \frac{VS((x_2)_j)}{Ib}, \tag{43}$$

Where $S((x_2)_j)$ is the jth layer's first moment of inertia and V is the shear force acting on the element.

When a layer is subjected to axial stresses due to bending and to shear stresses due to shearing forces, one must consider the principal stresses and strains to calculate the Damage according to Equations 36-37.

If the beam has stirrups, these must be accounted when calculating the shear stresses. When the concrete is still intact, that is, $D = 0$, the concrete is responsible for the shear resistance. The stirrup's contribution occurs when the first microcracks appear ($D > 0$), acting on the tensioned axis of the principal plane generated by the shear stress portion. This contribution, in terms of shear forces, is given by [24] (Equation 44)

$$V_{sw} = \sigma_{sw}\rho_{sw}bd, \tag{44}$$

in which d is the effective depth of section, ρ_{sw} the transversal reinforcement ratio, given by $A_{sw}/(sb)$, where A_{sw} is the stirrup cross-section area and s is the spacing between stirrups. The stirrup axial stress, σ_{sw}, is obtained through (Equation 45)

$$\sigma_{sw} = |E_{sw}\varepsilon_{1P}\sin(\alpha)|, \tag{45}$$

where E_{sw} is the stirrup's Young Modulus, α the orientation of the principal plane $1P$, and ε_{1P} the principal strain associated with the axis $1P$, wherein $|\sigma_{1P}| \leq |\sigma_{2P}|$.

To calculate the Damage, one must regard only the fraction supported by the concrete. Therefore, the effective shear force to be considered on the concrete, V_c, is given by (Equation 46)

$$V_c = V - V_{sw}. \tag{46}$$

5 NONLINEAR STATIC EQUILIBRIUM

To capture the effect of the damage evolution, the total load is divided into load steps, ΔF, so that the model looks for the equilibrium damage state.

In each iteration, the displacements are obtained, the finite element matrix $(B_j = L_j \phi_j^T)$ is calculated at the Gauss integration points of the beam elements. The strains of each layer are calculated at the same direction of Gaussian integration points, and, in these points, the damage status is checked. It is important to point that the neutral axis position is updated in each iteration. When damage occurs in any layer, the model updates the stiffness matrix, rechecks the balance setting, as the loss of stiffness due to the Damage Mechanics in any layer may result in some damage in another part of the structure.

Then, the stress tensor is calculated considering the damage and, consequently, the global internal force vector is obtained with the contribution of degrees of freedom.

5.1 Deformed configuration, the second Piola-Kirchhoff stress tensor and its variation for varied materials

As shown, the nonlinear static equilibrium in this model is analysed in the undeformed configuration, β_0, that is, the total Lagrangian description is used. The stresses are calculated by the second Piola-Kirchhoff tensor, S_{ij}. Although the Green-Lagrange strain tensor should be used in this case, in the context of small strains field, it is possible to use the infinitesimal strain tensor, ε_{kl}. It can be noted that the Cauchy stress tensor, σ_{ij}, could also be used through the updated Lagrangian description, β_t, as both descriptions are simply two ways for expressing the same problem [25].

The Damage Mechanics approach takes into consideration the concept of the effective stress tensor [18]. The variation of the position of the neutral axis and the moments of inertia of the layers, due to damage, cause a change in the components of the stress tensor. Since the effective stress tensor depends on the damage variable, the stiffness loss increases the stress components.

5.2 Gain of moment of inertia of damaged layers due to the increase of distance from the neutral axis

When the damage process occurs in any layer there will be loss of resistance due to the reduction of Young's modulus. However, such degradation causes the position of the neutral axis to move away from the damaged layer, increasing their distance and resulting in a gain of the layer's moment of inertia.

One should note that this consideration could cause an equivocal gain of stiffness. Nonetheless, the gain of moment of inertia is never greater than the loss of Young's modulus, since the beam will never increase its original stiffness, as the damage is progressive.

5.3 Nonlinear static equation

The global equation considering physical nonlinearities and discretized through laminated Euler-Bernoulli beam finite element is (Equation 47)

$$K_{ij}^{\text{global}} (\bar{u}_2)_i^{\text{global}} = F_i^{\text{global}} . \tag{47}$$

Although the verification occurs in the undeformed configuration, the damage is recalculated at each iteration within each loading step through Newton-Raphson iterative technique.

The convergence criterion here includes both terms of forces and displacements in relation to the tolerated equilibrium values, comparing the internal energy increment during each iteration, which is the amount of work done by the unbalanced load vector in displacement increments, with the initial internal energy increment [26] (Equation 48),

$$\{\Delta u_2\}^{(i)T}(\{F_{\text{ext}}\} - \{F_{\text{int}}\}^{(i-1)}) \leqslant tol_E [\{\Delta u_2\}^{(1)T}(\{F_{\text{ext}}\} - \{F_{\text{int}}\})], \tag{48}$$

Where tol_E is the energy convergence tolerance that includes both the convergence tolerances in terms of force and displacement.

6 COMPUTATIONAL MODEL APPLICATIONS IN EXPERIMENTAL TESTS

A computational model was developed in *C++* programming language with *MATLAB* wrapper to consider physical nonlinearities models by Damage Mechanics and Plasticity Theory in laminated Euler-Bernoulli beam finite elements.

Rev. IBRACON Estrut. Mater., vol. 16, no. 5, e16502, 2023

13/19

This model allows the local mesh and layers refinement, analytical variation of the neutral axis position and consequent change of the layers' moment of inertia. The proposed model was developed for nonlinear static simulations.

Hereafter are presented the reinforced concrete beams that were simulated in the present work. In order to validate the proposed model, the specimen are associated with experimental [12], [13] and numerical results presented by other authors [12]. Therefore, two examples are analysed. The first one compares the numerical results with those presented by Mazars and Grange [12], which adopted multifiber beam elements. In the second one, the numerical results are compared with the classical experimental results of Bresler and Scordelis [13].

Firstly, in recent works, Mazars et al. proposed the μ damage model [27], presenting both experimental and numerical results of beams subjected to distinct loading conditions. In this paper, a numerical simulation was performed to compare with the beam presented in Mazars and Grange [12]. The experiment consists in a four-point bending, as shown in Figure 6a. Due to the model setup, the flexural behaviour is admitted as the main solicitation of the beam. The geometry and reinforcement details are sown in the Figure 7a. The steel properties are presented in the Table 1. The concrete properties and damage parameters are the same as the adopted by Mazars and Grange [12], and are presented in the Tables 2-3, respectively. In this paper, this beam is referred as Mazars' beam.

Table 1. Steel properties.

	Bottom steel		Top steel		Stirrups			
	E_s (GPa)	f_y (MPa)	E_s (GPa)	f_y (MPa)	E_s (GPa)	f_y (MPa)	Φ (mm)	S (mm)
Mazars	200	500	200	500	200	500	10	150
BS-OA2	218	555	-	-	-	-	-	-
BS-A2	218	555	201	345	190	325	6.4	210
BS-B2	218	555	201	345	190	325	6.4	190
BS-C2	218	555	201	345	190	325	6.4	210
BS-OA3	218	555	-	-	-	-	-	-
BS-A3	218	555	201	345	190	325	6.4	210
BS-B3	218	555	201	345	190	325	6.4	190
BS-C3	218	555	201	345	190	325	6.4	210

Table 2. Concrete properties.

	E_c (GPa)	f_c (MPa)	f_t (MPa)
Mazars	45	95	6
BS-OA2	15	23.7	4.34
BS-A2	15	24.3	3.73
BS-B2	15	23.2	3.76
BS-C2	15	23.8	3.93
BS-OA3	15	37.6	4.14
BS-A3	15	35.1	4.34
BS-B3	15	38.8	4.22
BS-C3	15	35.1	3.86

Table 3. Damage variables.

	ε_{d0}	A_C	B_C	A_T	B_T
Mazars	$1.33 \cdot 10^{-4}$	1.35	300	0.9	20000
BS-OA2	$2.12 \cdot 10^{-4}$	1.2	1170	0.8	1850
BS-A2	$1.99 \cdot 10^{-4}$	1.2	1105	0.8	2180
BS-B2	$2.01 \cdot 10^{-4}$	1.2	1165	0.8	2145
BS-C2	$2.10 \cdot 10^{-4}$	1.2	1145	0.8	2060
BS-OA3	$2.21 \cdot 10^{-4}$	1.2	680	0.8	1945
BS-A3	$2.31 \cdot 10^{-4}$	1.2	740	0.8	1850
BS-B3	$2.25 \cdot 10^{-4}$	1.2	660	0.8	1965
BS-C3	$2.06 \cdot 10^{-4}$	1.2	730	0.8	2140

Secondly, to analyse the shear effects in reinforced concrete beams, Bresler and Scordelis [13] elaborated a set of 12 experimental beams, with different cross-section geometry, span and reinforcement ratio. These 12 beams are divided into 3 series of 4 beams with similar aspect ratios L/h. Due to the use of the Euler-Bernoulli beam element, one of these series will not be investigated in this work on the account of its short span. The regarded beams presented in this work are referred as BS-OA2, BS-A2, BS-B2, BS-C2, BS-OA3, BS-A3, BS-B3 and BS-C3. The relevance of these experimental tests, presented in Bresler and Scordelis [13], for the engineering structures field granted it to be investigated in several works [15], [16], [28].
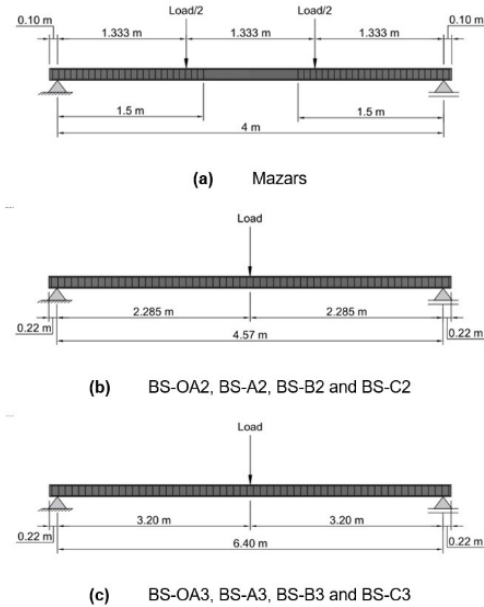
Figure 6. Elevation details.

The test setup consists in three-point bending, as presented in Figure 6b-6c. Each cross-section geometry and reinforcement details are shown in Figure 7b-7i. The steel properties are described in the Table 1 and the concrete properties, obtained experimentally, are presented in the Table 2. The Damage parameters, presented in the Table 3, were calibrated to accord with the concrete resistances obtained by Bresler and Scordelis [13].
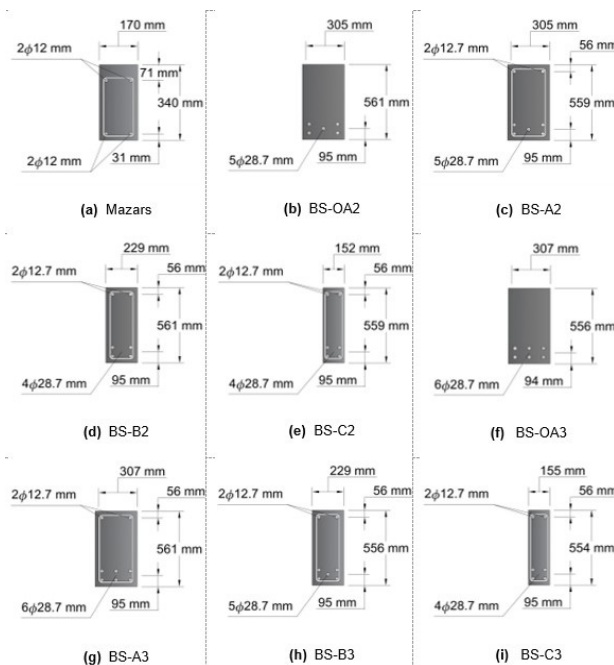
Figure 7. Cross-section details.

Rev. IBRACON Estrut. Mater., vol. 16, no. 5, e16502, 2023

15/19

7 RESULTS

The maximum vertical displacement of the Mazars' beam is presented in the Figure 8. With the proposed model, the beam presented a flexure-tensile failure mode. As the load increased, the bottom concrete layers were submitted to damage due to tension, and neutral axis started to ascend. The lower steel rebars then reached the elastic threshold and the yielding amplified the damage process, leading the beam to large displacements.

The damage evolution of the Mazars' beam is presented in the Figure 9. It is noticeable, through the analysis of the neutral axis position and the damage configuration, that the damage occurred from bottom to top.
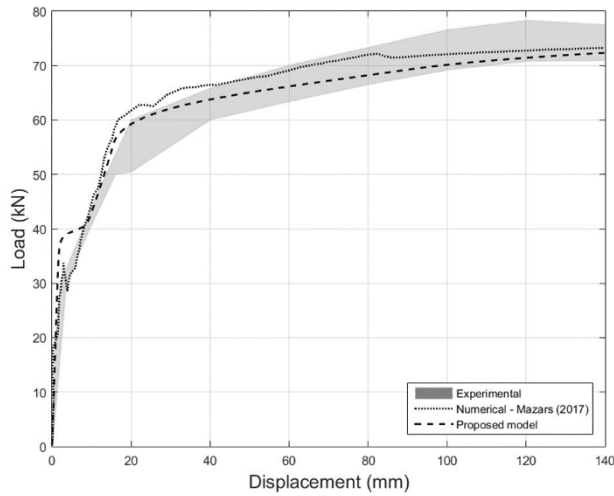
Figure 8. Maximum displacement in the Mazars' beam.
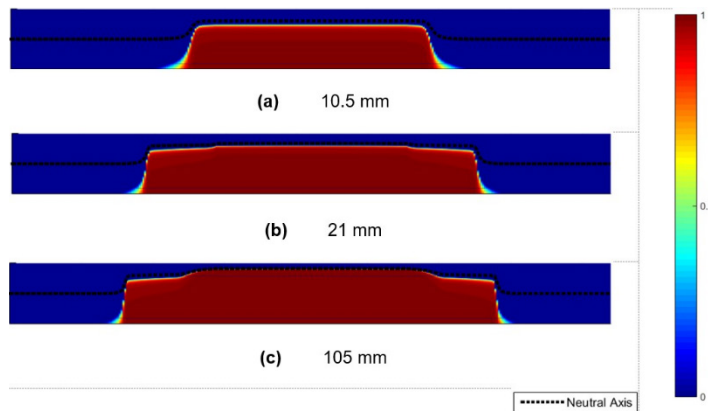
Figure 9. Damage configuration for different midspan displacements in Mazars' beam.

The Figure 10 shows the maximum vertical displacement for the Bresler-Scordelis' beams. At the experimental tests, the BS-OA2 and BS-OA3 failed due to diagonal tension (D-T). The failure was reported as sudden and brittle-like [16]. These beams are similar to the BS-A2 and BS-A3, respectively. The difference is the presence of stirrups in the latter, which granted a higher ultimate load strength. The failure mode of the BS-A2, BS-B2 and BS-C2 beams were reported as a combination between shear and compression stresses (V-C).

Lastly, the BS-A3, BS-B3 and BS-C3, due to the longer span, failed due to flexure-compression (F-C) [16]. The top concrete was crushed because of the great amount of bottom steel reinforcement. The proposed model was able to reproduce this effect numerically in the simulation. On the numerical analysis with the proposed model, was noticeable that in these beams, the damage started at the bottom concrete layers. However, differently from the Mazars' beam, the amount of bottom rebars maintained the beam's stiffness and the neutral axis near its original position. The position of the neutral axis presents significant importance to the beginning of damage on the top concrete layers, once the distance

between the neutral axis and a certain layer height is proportional to the strain of this layer. As the load increases, the damage also increases in both top and bottom layers, due to compression and tension, respectively. The final damage configurations of these beams are presented in the Figures 11-12.
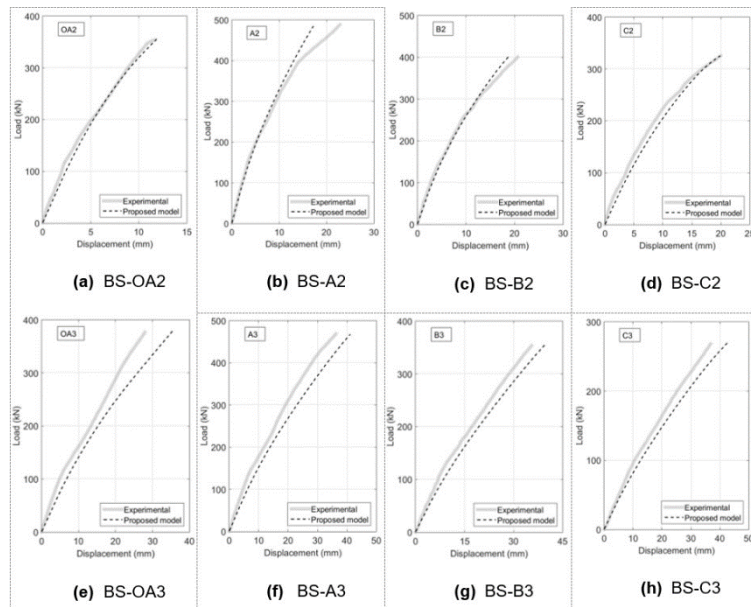
Figure 10. Maximum displacement in the BS beams.

8 CONCLUSIONS

The laminated Euler-Bernoulli beam theory was used here to analyse nonlinear reinforced concrete beams subjected to damage and plasticity due to progressive loading. The numerical results were compared with experimental values and numeric ones found in the literature. The nonlinear behaviour expressed in terms of load-displacement curves was accurately approximated by the proposed method, as can be seen in Figures 8 and 10. The damage process was well captured by the laminated beam model and the variation of neutral axis position can be highlighted in Figures 9, 11 and 12.
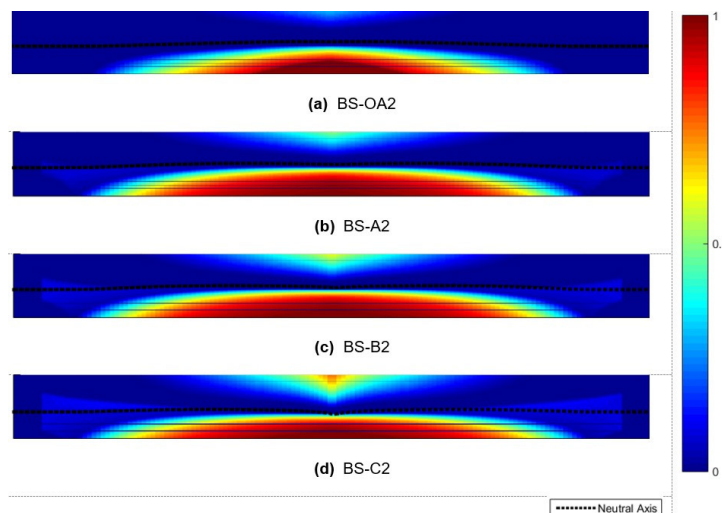
Figure 11. Final damage configuration for Bresler-Scordelis' series 2 beams.

The present methodology was applied in experimental cases which the collapse was due to bending since the model adopted is based on the Euler-Bernoulli beam theory.

The relevance of considering the variation of the neutral axis in the damage and yielding procedures was highlighted, especially in comparison with bending tests on beams with a low rate of tensile reinforcement.

Furthermore, the previous consideration combined with the moment of inertia variation, the Damage Mechanics of concrete and Plasticity Theory of the steel and the shear stresses acting on the beam was able to numerically reproduce, with satisfactory approach, the results of the experimental tests both from the recent [12] work and the classic [13] research, when comparing force-displacement responses and damage configurations during the progressive loading.
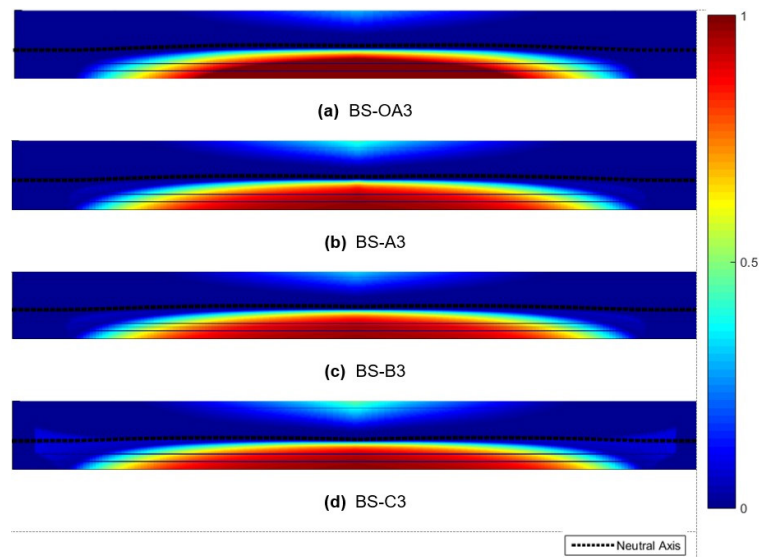
Figure 12. Final damage configuration for Bresler-Scordelis' series 3 beams.

ACKNOWLEDGEMENTS

REFERENCES

[1] M. S. Álvares, "Contribuição ao estudo e emprego de modelos simplificados de dano e plasticidade para a análise de estruturas de barras em concreto armado," Ph.D. dissertation, Univ. São Paulo, São Carlos, Brazil, 1999.

[2] B. Biondi and S. Caddemi, "Euler-Bernoulli beams with multiple singularities in the flexural stiffness," *Eur. J. Mech. A, Solids*, vol. 26, pp. 789–809, Sep./Oct. 2007.

[3] F. Ghrib, L. Li, and P. Wilbur, "Damage identification of euler-bernoulli beams using static responses," *J. Eng. Mech.*, vol. 138, pp. 405–415, Oct. 2012.

[4] V. Corvec, "Nonlinear 3d frame element with multi-axial coupling under consideration of local effects," Ph.D. dissertation, Univ. California, Berkeley, USA, 2012.

[5] Q. Xie, Y. X. Zhou, Y. Zhan, K. Y. Sze, and W. S. Han, "A comparative study on the beam and continuum finite element models for the rail-wheel vibration," *Int. J. Struct. Stab. Dyn.*, vol. 19, p. 1950076, Apr. 2019.

[6] E. Spacone, F. C. Filippou, and F. F. Taucer, "Fibre beam--column model for non-linear analysis of R/C frames: part I. Formulation," *Earthquake Eng. Struct. Dynam.*, vol. 25, pp. 711–725, Jul. 1996.

[7] J. Mazars, P. Kotronis, F. Ragueneau, and G. Casaux, "Using multifiber beams to account for shear and torsion: applications to concrete structural elements," *Comput. Methods Appl. Mech. Eng.*, vol. 195, pp. 7264–7281, Nov. 2006.

[8] R. S. Oliveira, M. A. Ramalho, and M. R. S. Corrêa, "A layered finite element for reinforced concrete beams with bond-slip effects," *Cement Concr. Compos.*, vol. 30, pp. 245–252, Mar. 2008.

[9] M. Lezgy-Nazargah, M. Shariyat, and S. Beheshti-Aval, "A refined high-order global-local theory for finite element bending and vibration analyses of laminated composite beams," *Acta Mech.*, vol. 217, pp. 219–242, Oct. 2011.

[10] T. O. Abeche, R. D. Machado, J. E. Abdalla Fo., F. L. M. Beghetto, and L. A. F. Souza, "Damage effects from dynamic interaction between vehicles, irregularities and railway bridges in the nonlinear dynamic response of structures," in *Proc. Third Int. Conf. Railway Tech.: Res., Develop. Maintenance*, J. Pombo, A. G. Correia, S. C. d' Aguiar, Y. Momoya, P. K. Woodward, S. Krajnovic et al., Eds. 2016, p. 278.

[11] J. Mazars, "Application de la mécanique de l'endommagement au comportement non linéaire et á la rupture du béton de structure," Ph.D. dissertation, Univ. Pierre Marie Curie, Paris, France, 1984.

[12] J. Mazars and S. Grange, "Simplified strategies based on damage mechanics for concrete under dynamic loading," *Philos. Trans. R. Soc. A*, vol. 375, p. 20160170, Jan. 2017.

[13] B. Bresler and A. C. Scordelis, "Shear strength of reinforced concrete beams," *J. Proc.*, vol. 60, no. 1, pp. 51–74, Jan. 1963.

[14] G. F. F. Bono, A. Campos Fo., and A. R. Pacheco, "A 3D finite element model for reinforced concrete structures analysis," *Rev. IBRACON Estrut. Mater.*, vol. 4, no. 4, pp. 548–560, Oct. 2011.

[15] R. S. B. Stramandinoli and H. L. Rovere, "FE model for nonlinear analysis of reinforced concrete beams considering shear deformation," *Eng. Struct.*, vol. 35, pp. 244–253, Feb. 2012.

[16] F. J. Vecchio and W. Shim, "Experimental and analytical reexamination of classic concrete beam tests," *J. Struct. Eng.*, vol. 130, pp. 460–469, Feb. 2004.

[17] Y. W. Kwon and H. Bang, *The Finite Element Method Using MATLAB*. Boca Raton, FL, USA: CRC Press, 2000.

[18] J. Lemaitre and R. Desmorat, *Engineering Damage Mechanics: Ductile, Creep, Fatigue and Brittle Failures*. New York; Berlin, Germany; Vienna, Austria: Springer-Verlag, 2005.

[19] J. Lemaitre, *A Course on Damage Mechanics*. New York; Berlin, Germany; Vienna, Austria: Springer-Verlag, 1992.

[20] J. Mazars and G. Pijaudier-Cabot, "Continuum damage theory-application to concrete," *J. Eng. Mech.*, vol. 115, pp. 345–365, Feb. 1989.

[21] J. Lemaitre and J. L. Chaboche, *Mécanique des Matériaux Solides*. Paris, France: Dunod, 1985.

[22] J. Shen, M. R. T. Arruda, and A. Pagani, "Concrete damage analysis based on higher-order beam theories using fracture energy regularization," *Mech. Adv. Mater. Structures*, pp. 1–15, Jul. 2022. Online.

[23] S. Eugster and C. Glocker, "Determination of the transverse shear stress in an Euler-Bernoulli beam using non-admissible virtual displacements," *Proc. Appl. Math. Mech.*, vol. 14, no. 1, pp. 187–188, May. 2014.

[24] E. A. Liberati, C. G. Nogueira, E. D. Leonel, and A. Chateauneuf, "Nonlinear formulation based on FEM, Mazars damage criterion and Fick's law applied to failure assessment of reinforced concrete structures subjected to chloride ingress and reinforcements corrosion," *Eng. Fail. Anal.*, vol. 46, pp. 247–268, 2014.

[25] T. Belytschko, W. K. Liu, B. Moran, and K. I. Elkhodary, *Finite Elements for Nonlinear Continua and Structures*. Hoboken, NJ, USA: Wiley, 2014.

[26] K.-J. Bathe, *Finite Element Procedures*. Englewood Cliffs, NJ, USA: Prentice-Hall, 1996.

[27] J. Mazars, F. Hamon, and S. Grange, "A new 3D damage model for concrete under monotonic, cyclic and dynamic loadings," *Mater. Struct.*, vol. 48, pp. 3779–3793, Oct. 2015.

[28] F. O. Navas, J. Navarro-Gregori, G. L. Herdocia, P. Serna, and E. Cuenca, "An experimental study on the shear behaviour of reinforced concrete beams with macro-synthetic fibres," *Constr. Build. Mater.*, vol. 169, pp. 888–899, Apr. 2018.

Rev. IBRACON Estrut. Mater., vol. 16, no. 5, e16502, 2023

19/19

IBRACON Structures and Materials Journal
Revista IBRACON de Estruturas e Materiais

ORIGINAL ARTICLE

Reliability analysis of reinforced concrete frames subjected to post-construction settlements

Análise de confiabilidade de pórticos em concreto armado sujeitos a recalques pós-construção

Wanderlei Malaquias Pereira Junior[a]
Matheus Henrique Morato de Moraes[b]
André Teófilo Beck[c]
Daniel Lima de Araújo[d]
Antover Panazzolo Sarmento[a]
Mauro Alexandre Paula de Sousa[b]

[a]Universidade Federal de Catalão – UFCAT, Engineering College, Department of Civil Engineering, Catalão, GO, Brasil
[b]Universidade Federal de São Carlos – UFSCar, Department of Civil Engineering, Civil Engineering Graduate Program, São Carlos, SP, Brasil
[c]Universidade de São Paulo – USP, Engineering School, Department of Engineering Structures, São Carlos, SP, Brasil
[d]Universidade Federal de Goiás – UFG, Department of Civil Engineering, Goiânia, GO, Brasil

Abstract: Most papers in the literature address reliability analysis of isolated elements, like beams and columns. However, symmetry and regularity are often exploited in the construction of regular RC frames, resulting in the same or similar designs for all columns of a floor or all beams of a building. This leads to significant differences in member reliability, due to different axial load to bending moment ratios, in different parts of the structure. Moreover, load effects increase, and symmetry is lost under individual support settlements. In this scenario, reliability analyses are performed, for an intact 4-floors and 3-spans RC frame; and considering different settlement conditions. Monte Carlo simulation is performed, considering uncertainties in dead and live loading, and steel and concrete strengths. The results show that a settlement of 10 mm, corresponding to an angular distortion of 1/500, reduced the average reliability of the frame by only 14%, just the same, it reduced the reliability index of several cross-sections of the beams to up to 2.40, value lower than that recommended in the Model Code 2010. It is concluded that the methodology used in this work presents an important tool for the analysis of events not foreseen in the design, supporting the decision making about the need for intervention in the structures.

Keywords: reinforced concrete, reliability analysis, Monte Carlo simulation, foundation settlements.

Resumo: A maior parte dos artigos encontrados na literatura endereça a confiabilidade de elementos isolados, como vigas e colunas. No entanto, simetria e regularidade são frequentemente exploradas na construção de pórticos regulares de concreto armado, o que resulta em projetos iguais ou semelhantes para todas as colunas de um andar ou todas as vigas de um prédio. Isto leva a diferenças na confiabilidade dos elementos, em função das diferentes razões entre carga axial e momento fletor, em diferentes partes da estrutura. Mais ainda, há um aumento dos esforços solicitantes e perda de simetria na presença de recalques de apoios. Neste cenário são realizadas análises de confiabilidade para um pórtico de 4 andares e 3 vãos, na situação intacta e considerando diferentes recalques de apoio. É realizada simulação de Monte Carlo, considerando incertezas nas ações permanentes e de utilização, e na resistência do aço e do concreto. Os resultados mostram que um recalque de 10 mm, correspondente a uma distorção angular de 1/500, reduziu a confiabilidade média do pórtico em apenas 14%, contudo reduziu o índice de confiabilidade de várias seções transversais das vigas para até 2.40, valor inferior ao recomendado no Model Code 2010. Conclui-se que a metodologia utilizada neste artigo se

apresenta como uma ferramenta importante para a análise de eventos não previstos em projeto, auxiliando na tomada de decisão sobre a necessidade de intervenção nas estruturas.

Palavras-chave: concreto armado, confiabilidade estrutural, simulação de Monte Carlo, recalque de fundações.

1 INTRODUCTION

In the structural engineering context, uncertainties are related to the inability to predict some characteristics of the structural system, such as loads, material properties, and assumptions of the structural model adopted [1], [2]. Despite these uncertainties, design codes employ design methodologies to obtain resistant, safe and robust structures.

Although the structural design considers these uncertainties in the design variables, it is still possible that a structure will be exposed to a condition not foreseen in the design [3]. Given these new conditions in the service situation, it is necessary to evaluate the new safety level of the structure, verifying the necessity of reinforcements or even the demolition of the system in more severe cases.

In terms of assessing the safety level of an existing structure, reliability theory can be employed for this purpose. Some authors have dedicated themselves to studying and evaluating the safety level of existing structures using such a theory. Works such as Facholli and Beck [4] and Beck et al. [5] have employed reliability theory to evaluate the safety level in structural element loss events. Küttenbaum et al. [6], Mankar et al. [7] and Souza et al. [8] evaluated the variations of the mechanical properties of materials and their impact on the system's reliability in situations of structure use. In Ávilla et al. [9] reliability analysis was applied to verify the safety level of historic buildings in regions susceptible to earthquakes.

In terms of structural design, many engineers still design structures without considering the effects of settlement [10]. Amancio [11] states that such a condition often occurs since predicting settlements in structures is still a complex factor due to the difficulty of obtaining parameters such as soil strength and deformability. Thus, this paper aims to contribute to the soil-structure interaction theme by developing a conceptual study to verify the influence of settlements on the safety of reticulated reinforced concrete structures. Therefore, this work intends to develop an analysis methodology that can contribute to decision-making regarding the maintenance of reinforced concrete structures of multiple floors submitted to actions arising from foundation settlement.

This paper is divided into six sections. The first three sections introduce the initial concepts of beam design and structural reliability. Section 4 discusses the conceptual problem of a frame structure submitted to settlement conditions. Sections 5 and 6 present the results and conclusions about this research.

2 DESIGN OF BEAMS UNDER PURE BENDING

This section presents the concepts related to structural analysis and the format of the limit state equation. The normative used were Brazilian standards ABNT NBR 8681 [12] and ABNT NBR 6118 [13].

The frame analysis was carried out for vertical loads. Equation 1 characterizes the ultimate limit state (g) of the beam's cross-section resistance capacity at stage III due to normal loads, as defined by ABNT NBR 6118 [13].

$$g(f_y, f_c, D, L) = E_R \cdot M_R(f_y, f_c) - M_S(D, L, f_c) \tag{1}$$

$$M_R = A_s \cdot f_y \cdot \left(d - \frac{\lambda}{2} \cdot x\right) \tag{2}$$

$$x = \frac{A_s \cdot f_y}{f_c \cdot b_w \cdot \alpha_c \cdot \lambda} \tag{3}$$

The loading moment M_S indicates the maximum demand of bending moment on the cross-section, determined herein using linear analysis. The resistant moment M_R indicates capacity of the RC cross-section. A_s is the steel area of the cross-section, λ and α_c are factors that depend on the characteristic compressive strength of concrete (f_c). These factors can be consulted in section 17.2.2 of ABNT NBR 6118 [13]. f_y represents the yield strength of the passive reinforcement steel used. d and b_w represent the effective height and width of the RC section. E_R represents model error variable for beam bending.

Rev. IBRACON Estrut. Mater., vol. 16, no. 5, e16503, 2023

2/12

2.1 Determination of internal loads

The effects of the loads on the frames studied are evaluated by employing a linear-elastic static analysis. The mechanical model is based on the matrix analysis of structures, with frame-type elements (see Figure 1) and three degrees of freedom per node. Static linear analysis is sufficient for an approximate study of the load distribution in frame structures, allowing the redistribution of loads once the equilibrium and ductility conditions of ABNT NBR 6118 [13] are satisfied. However, in this paper, the analyses were performed without considering the redistribution of internal forces.

The nodal displacement vector d is obtained by a system containing the global stiffness matrix K and the external forces vector (f). Thus, the system of equations that represents the discretized structural system will be given by Equation 4.

$$K \cdot d = f \tag{4}$$
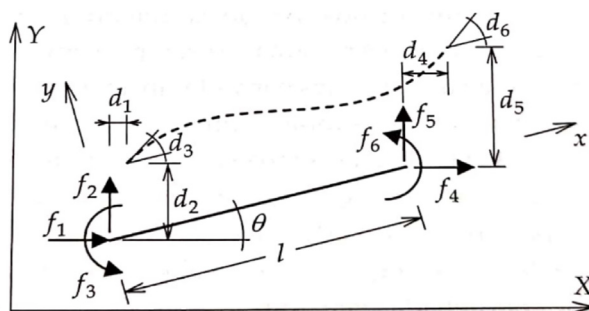
Figure 1. Frame element.

3 STRUCTURAL RELIABILITY AND MONTE CARLO METHOD

In this section, the basic concepts of the reliability evaluation of a structure are presented. The Monte Carlo method, employed herein for reliability analyses, is also presented.

The basic reliability problem is represented by the multiple integral of Equation 5, where p_f represents the failure probability of the structure, X is the n-dimensional vector representing the random variables of the system, $f_x(x)$ represents the joint probability density function over the failure domain, and $G(X)$ is the limit state equation. $G(X) \leq 0$ represents a failure condition.

$$p_f = P(G(X) \leq 0) = \int \ldots \int_{G(X) \leq 0} f_x(x)\, dx \tag{5}$$

The probability of failure is a complementary concept to structural reliability. Failure probability measures the propensity of a structure or structural system to fail to satisfy the technical design requirements (function, strength, equilibrium) within a specified design life, respecting the operational and design conditions [2].

Several methods can be applied to solve Equation 5. In this work, the stochastic Monte Carlo method was applied. This algorithm was developed in the 1940s during the end of World War II and the beginning of the Cold War. It was initially employed by the mathematicians Stanislav Ulam and John von Neumann, who were working on developing the hydrogen bomb [14].

Among several variations of the Monte Carlo method, the Crude Monte Carlo was used in this work, which consists of random tests with a certain number of samples. The failure probability calculation is given by an approximation of Equation 5. The estimation of the failure probability using the Monte Carlo method is given by Equation 6.

$$\overline{p_f} = \frac{1}{n_s} \cdot \sum_{i=1}^{n_s} I[G(X)] = \frac{n_f}{n_s} \tag{6}$$

$$I[G(X)] = 1 \; if \; G(X) \leq 0 \tag{7}$$

$$I[G(X)] = 0 \; if \; G(X) > 0 \tag{8}$$

In Equation 6, n_s is the number of samples and n_f is the number of system failure events observed in n_s samples ($I[G(X)] = 1$).

The reliability index (β_{MC}) of the structure is obtained by Equation 9, which involves the inverse Standard Gaussian cumulative probability distribution. The numerical solution of this inverse function can be found in Beck [2].

$$\beta_{MC} = -\Phi^{-1}(\overline{p_f}) \tag{9}$$

3.1 Target Reliability Index

The reliability index will define a level of safety for the structure, but the design standards must be calibrated to a minimum level of safety required for any given structure. For existing structures, the minimum required value is given in Table 1.

Table 1. Suggested target reliability indices for existing structures, Model Code 2010 [15].

Limit State	β_{target}	Reference period
SLS	1.50	Service life
ULS	Between 3.10 and 3.80	50 years
	Between 3.40 and 4.10	15 years
	Between 4.10 and 4.70	1 year

These target index values are often used to estimate the partial safety coefficients in structural design standards such as ABNT NBR 8681 [12]. Applications of this calibration process can be seen in Santiago et al. [16].

4 STUDY OBJECT

This section presents the characteristics of the structural model used in the reliability analysis of a frame structure subjected to differential settlement and the numerical method employed in the reliability analysis.

The example used to evaluate structural safety is a four floors plane frame, as described in Facholli and Beck [4]. Figure 2 presents the geometry of the structural frame, which has three spans of 5 meters and a floor height of 3 meters. Table 2 shows the cross-section values for each element represented in Figure 2.
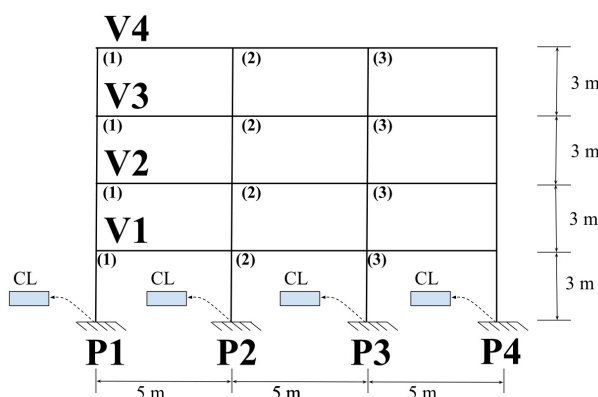
Figure 2. Plane frame in reinforced concrete analyzed and nomenclature of the columns, beams, and column layout (CL).

The structural design of the plane frame elements of Figure 2 was performed according to ABNT NBR 6118 [13]. All elements were considered to be constituted by a concrete with characteristic compressive strength of 30 MPa, and tangent and secant modulus of elasticity according to item 8.2.8 of ABNT NBR 6118 [13] (granite type aggregate). The beams are subjected to a live load to dead load ratio of 0.61 ($D_k = 26.38\ kN/m$, $L_k = 16\ kN/m$) as described in Facholli and Beck [4]. The live loads are established considering a residential building, with the rooms classified as "Pantry and laundry area", with 2.0 kN/m². For permanent loads, a total of 3.30 kN/m² is considered. The building slabs have a thickness of 0.10 meters [4]. It is worth noting that usual cases of the L/D ratio for reinforced concrete beams of buildings can vary between 0.1 and 0.60 [17].

The geometry of the element sections and the steel area are described in Figure 3. It is worth noting that the analyzed sections refer to beam-column connections (negative bending moment), which are the most loaded sections in a plane frame. For this work, the redistribution of internal loads in the reliability analysis was not considered.

It is also worth mentioning that beam V1 was used as a reference for the design of the typical floor and beam V4 has its own detailing because it is a roof element. Therefore, V1, V2 and V3 have the same structural detailing.

Table 2. Geometric properties of the elements.

Type element	Element ID	b_w (cm)	h (cm)
Beam	V1 = V2 = V3	20	45
	V4	20	45
Column	P1 = P4	40	20
	P3 = P3	50	20

Table 3. Settling conditions and angular distortion imposed on the foundation.

Load case	ρ-P1 (mm)	ρ-P2 (mm)	ρ-P3 (mm)	ρ-P4 (mm)	p (Arbitrary)	γ
ρ_{P1-5}	(i) 5.00	(j) 0	-	-	70%	1/1000
ρ_{P1-10}	(i) 10.00	(j) 0	-	-	25%	1/500
ρ_{P1-50}	(i) 50.00	(j) 0	-	-	5%	1/100
ρ_{P2-5}	-	(i) 5.00	(j) 0	-	70%	1/1000
ρ_{P2-10}	-	(i) 10.00	(j) 0	-	25%	1/500
ρ_{P2-50}	-	(i) 50.00	(j) 0	-	5%	1/100

The imposed frame settlements are shown in Table 3. The created patterns aim to produce an angular distortion (γ) between columns of the building. The angular distortion is given by Equation 11:

$$\Delta_{ij} = |\rho_i - \rho_j| \tag{10}$$

$$\gamma = \frac{\Delta_{ij}}{L} \tag{11}$$

where Δ_{ij} indicates the differential settlement between columns, ρ_i and ρ_j are the individual settlements of each foundation and L is the span between foundations i and j.

The probabilities (p) of occurrence of each settlement magnitude in Table 3 were arbitrated but following a pattern which is typical of random phenomena affecting structural performance: the higher the magnitude, the lower the probability of occurrence. This same pattern is observed for extreme wind and live loads, earthquakes, floods, etc. This pattern has led to what is today known as Performance Based Engineering (see [2], [18]–[21]). To obtain more realistic failure probability estimates, actual foundation settlements for particular types of soils should be considered. Traditional bibliographies on the subject can be consulted, such as Skempton and MacDonald [22], Das [23], Burland et al. [24], and Nour [25]. In addition, the angular distortions established in Table 3 range from a less aggressive scale to rotation-to-rotation values which induce severe damage to the structure studied.

Reliability analysis by Crude Monte Carlo simulation (Equation 6) involves a heavy computational burden, due to the repetitive solutions of the numerical models. Due to this complexity, soil-structure interaction effects during settlement were not considered. This is left as a suggestion for future studies.
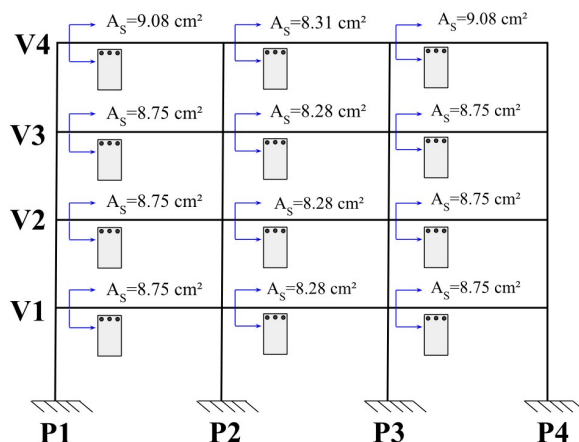
Figure 3. Steel area of the plane frame beams.

Table 4 presents the random variables considered in the reliability study. The other variables of the beam design problem (b_w, d, α_c, λ, and A_s) were considered deterministic.

Table 4. Random variable statistics.

Description	Variable	Distribution	Mean (μ)	Unit	C.o.V	Ref.
Dead load	D	Normal	$1.06 . D_k = 27.96$	kN/m	0.12	
Live load	L	Gumbel	$0.92 . L_k = 14.72$	kN/m	0.24	Santiago et al. [16]
Concrete	f_c	Normal	$1.22 . f_c = 36.60$	MPa	0.15	
Steel	f_y	Normal	$1.22 . f_y = 610.00$	MPa	0.04	
Model Error	E_r	Normal	1.02	---	0.06	Novak et al. [26]

Python language coding was used to perform the simulations. For the structural analyzer, the FINITO framework [27] was employed and for reliability analysis, an specific algorithm was developed.

The reliability analysis used the Crude Monte Carlo method described in section 3. The equation that defines only the ultimate limit state of the beams is given according to section 2, characterizing a bending failure without considering the effects of the beam-to-column connection. For the Monte Carlo analyses performed in this paper, a total of 2.10^5 samples of the five random variables (D, L, f_c, f_y, and E_r) were considered.

5 RESULTS AND DISCUSSION

The first part of this section presents the results concerning the reliability evaluation of the intact system, i.e., without foundation settlements. In the sequence are presented the results of the structure reliability for situations in which the differential settlements shown in Table 3 are inserted.

5.1 Reliability evaluation of the Intact Structure

The first part of the reliability results consists of evaluating the plane frame without the foundation settlements. Figure 4 shows the initial study of the number of samples required in the Monte Carlo method to have a convergence pattern. It can be seen, that after 150,000 samples the value of β does not change appreciably. Therefore, the sequence of reliability analyses was performed using $n_s = 200,000$ samples.

For the intact structure, reliability index (β_{MC}) for each beam element is presented in Figure 5.
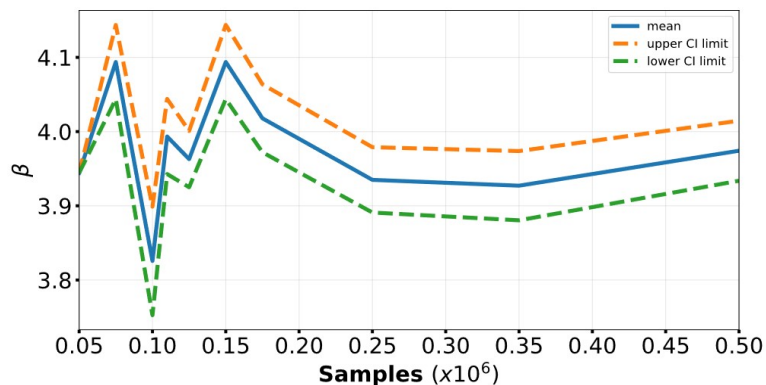
Figure 4. Convergence and Confidence Interval (95% confidence level) of the failure probability (β) for beams of the structural system.
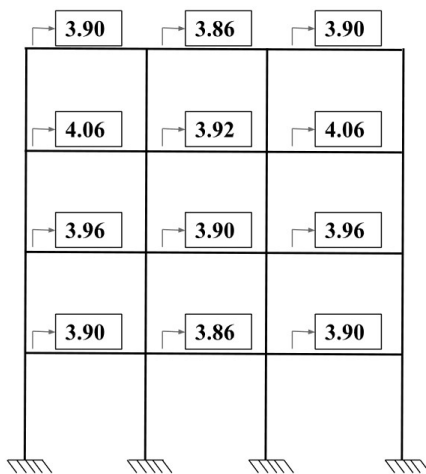
Figure 5. Reliability index β_{MC} for the beam elements.

It can be concluded from Figure 5 that the β_{MC} indexes are in agreement with the values in Table 1 that indicate a minimum required target index for the structure between 3.80 and 4.10 for a service life of 50 years. The higher reliability index value in beams V2 and V3 is expected since the control element for the typical floor design was beam V1.

It was also evaluated which of the five random variables in Table 4 have greater influence on Equation 1 which characterizes the ultimate limit state for bending. For this, a global sensitivity analysis is performed for each of the independent variables (Table 5) by a method based on variance decomposition, Sobol index [28] and by two regression-based methods, Standardized Regression Coefficients (SCR) and Partial Rank Correlation Coefficients (PRCC) [29].

In the Sobol technique, the first-order sensitivity S_i reports the influence of a variable x_i on the output and the total sensitivity index S_i^T refers to the influence of a variable x_i and the interactions of x_i with the other variables to the model output. The SRC technique quantifies the linear effect of each input variable on the response variable [30]. And the PRCC technique is the same as the Partial Correlation Coefficients (PCC), however the input and output values of the model are ranked. This technique allows qualitatively to verify only the order of importance of the variables, not how much the variable is more or less important than the others, the sensitivity of the response variable is determined as a function of the independent variable under study, disregarding the effect of the other variables [31], [32]. Table 5 shows the sensitivity values obtained from each independent variable for the methods used. In Table 5, negative values indicate strength variables, whereas positive values indicate load variables.

Table 5. Sensitivity analysis for the beams of the structural system.

Variable	S_i^T	SCR	PRCC
D	0.1514	0.4011	0.8033
L	0.2678	0.5414	0.8646
f_c	0.0403	-0.2167	-0.5815
f_y	0.1213	-0.3513	-0.7627
E_r	0.3492	-0.6093	-0.9005

S_i^T - Sobol Index; SCR - Standardized Regression Coefficients; and PRCC - Partial Rank Correlation Coefficients; D – Dead load L –Live Load; f_c – concrete strength; f_y – steel strength; and E_r – model error.

Through the global sensitivity analysis, it is possible to observe that despite different values for each of the different methods, the order of importance of the independent variables was the same. The independent variable of greater importance in the model (limit state) is the model error, E_r, represented by a total Sobol index of 0.35. The live load (L) was ranked second in the influence of the response variable, followed by the dead load (D), the steel strength (f_y), and lastly the concrete strength (f_c). This situation reveals the importance of the variability of the resistance model on the safety of the structure defined in the project. However, it is worth noting that the sensitivity analysis can be modified when the L_k/D_k ratio is altered. In the case of this work this ratio is 0.61.

5.2 Frame Reliability Evaluation after Settlements

Figures 6-8 present the reliability indexes of the differential settlement situations idealized in Table 3. It can be concluded that imposed settlements result in a reduction in the reliability index of the beams, reaching critical situations as in cases 3 and 6 with an imposed settlement of 50 mm and distortion 1/100. Clearly, the most affected beams are the reference beams (V1 and V4) that, theoretically, would be close to an optimal design ($R_d = S_d$).

To quantify the influence of settlement in the reduction of the reliability index of the beams, a reliability reduction index (D_μ) was associated for each of the cases of settlement analyzed. This index has already been used to determine the impact that explosive loads cause in existing structures, as can be verified in Momeni et al. [33]. Such an index is calculated by Equation 12 where β_{MC-INT} represents the reliability index of the intact structure and β_{MC-STL} the reliability index after the insertion of the settlement described in Table 3.

$$D_\mu = 1 - \frac{\beta_{MC-STL}}{\beta_{MC-INT}} \tag{12}$$

To quantify a single value for the D_μ index, an average value was established for the entire structure. This value represents an average of the D_μ values for each of the beams.
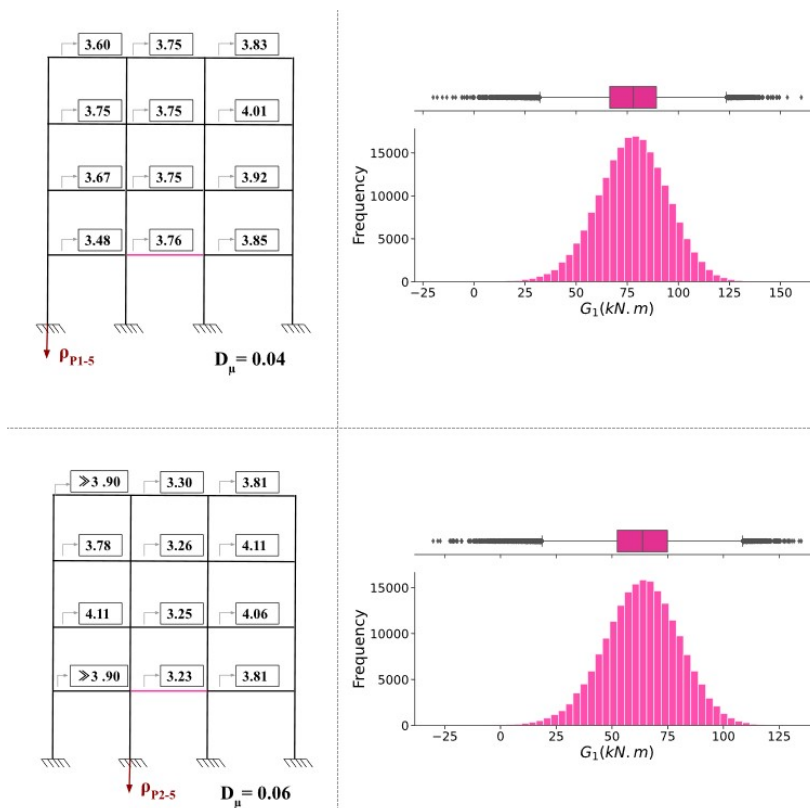
Figure 6. Reliability index β_{MC} for the beam elements considering the foundation settlement type ρ_{P1-5} and ρ_{P2-5}.

Figure 6 presents the reliability indices of the beams for the cases of settlement type ρ_{P1-5} and ρ_{P2-5}. Firstly, an index $D_\mu = 0.04$ and $D_\mu = 0.06$ is noted, which indicates an average reduction of about 5% in the reliability index of the original structure.

In terms of reducing the safety margin of the beams, defined by the reduction of the β_{MC} indices, the span most affected by the settlement at the internal column (ρ_{P2-5}) was span (2). Span (1) was more affected by the settlement at the external column (ρ_{P1-5}). In quantitative terms, the settlement at the internal column P2 promoted a more significant reduction in the reliability index of the beams. It is worth noting that this behavior also occurs for the 10 mm settlements (Figure 7).
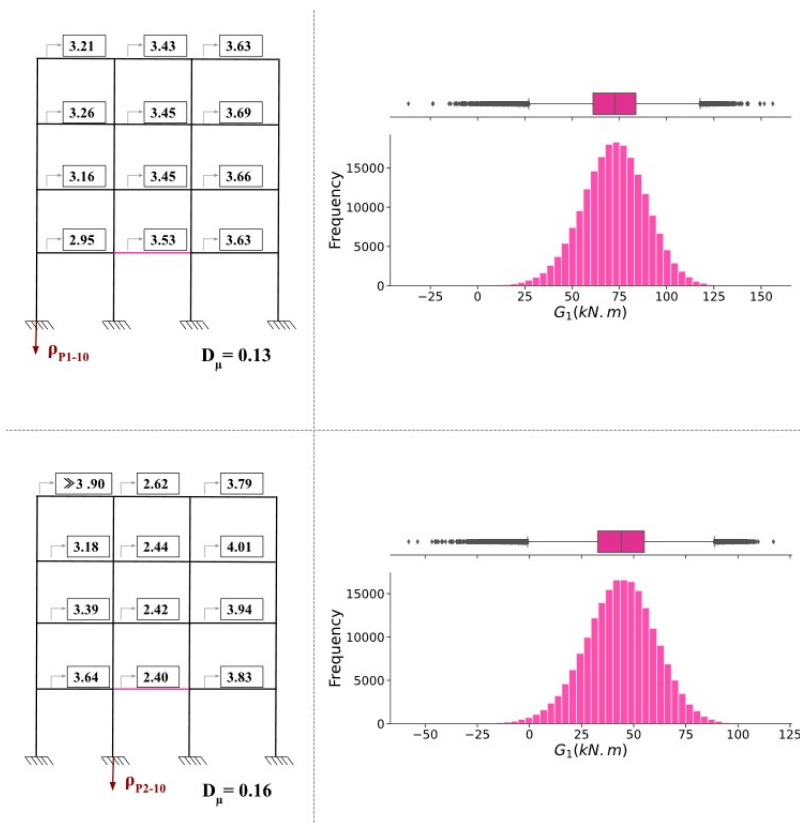
Figure 7. Reliability index β_{MC} for the beam elements considering the foundation settlement type ρ_{P1-10} and ρ_{P2-10}.
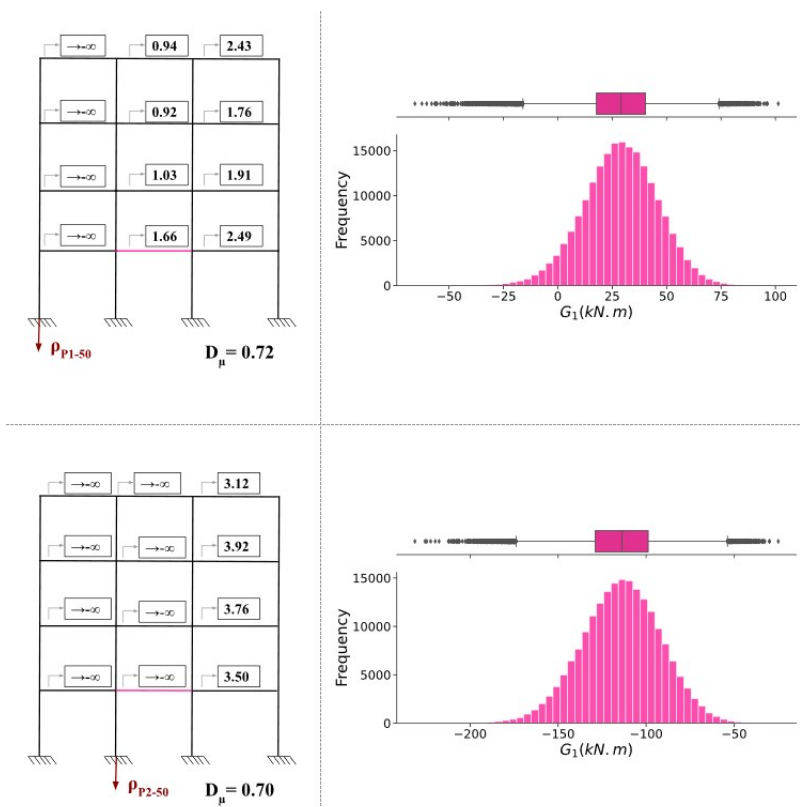
Figure 8. Reliability index β_{MC} for the beam elements considering the foundation settlement type ρ_{P1-50} and ρ_{P2-50}.

Figure 8 present the results of the reliability analysis for the last cases of settlement reported in Table 3. It can be perceived from these figures an appreciable reduction of the reliability indices of the beams for distortions of 1/500 and 1/100, especially the latter, which suggests that an ultimate limit state may have been reached, either by section failure or plastic hinge formation ($\beta_{MC} \to -\infty$ and $p_f \to 1$). This phenomenon occurs in spans (1) and (2) of the frame beams when the settlement occurs at column P2 and only in span (1) when the settlement occurs at the outer column P1, for settlement of 50 mm.

The Total Probability Theorem (Equation 13) was applied for each case to determine the total probability of failure of the structure for each of the effects of settlement on the reliability index of the structure, where event B represents a settlement event and A_i the mutually exclusive settlement events described in Table 3.

$$P[B] = P[B|A_1] \cdot P[A_1] + P[B|A_2] \cdot P[A_2] + \ldots + P[B|A_N] \cdot P[A_N] \tag{13}$$

For:

$$A_i \cap A_j = 0, i \neq j \tag{14}$$

$$A_1 + A_2 + \ldots + A_N = \Omega \tag{15}$$

The probability of occurrence of each of the effects were arbitrated in Table 3. The analysis of the reliability index after applying the theorem is shown in Figure 9.
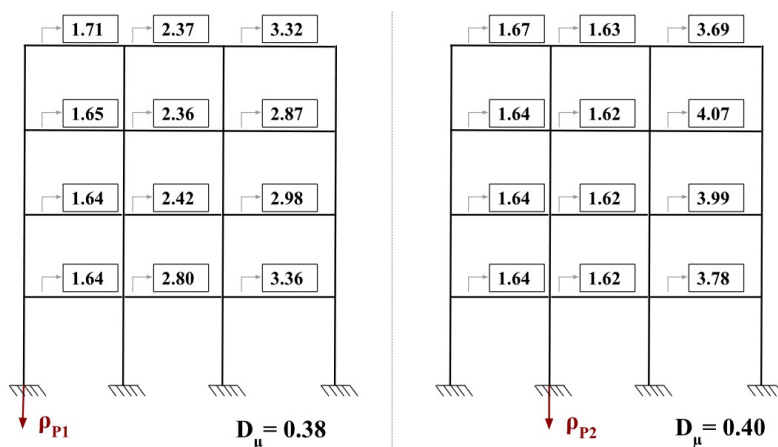
Figure 9. Reliability index β_{MC} for the internal (ρ_{P2}) and external (ρ_{P1}) settlements.

In terms of reduction of the index β_{MC} it is possible to confirm the information obtained in Figure 8 where the settlement condition in an external column (ρ_{P1}) led to a more attenuated failure condition compared to the settlement in the internal column (ρ_{P2}), with reductions of 38% and 40% respectively. Importantly, these values need to be confirmed by other studies addressing more realistic (measured) settlement statistics.

In order to reestablish reliability of the structure, some recovery measures are possible, as follows. If settlements have ceased, strengthening of the affected elements (beams, columns) or level off floor with hydraulic floor jacks is possible. When settlements are still ongoing, the foundation should be strengthened, by way of introducing new deep piles, use of belts to stabilize the foundation, and so on.

6 CONCLUSIONS

In this paper, the reliability of a reinforced concrete frame subjected to settlement was evaluated. The study revealed the importance of evaluating existing structures against events not foreseen in the project since many of these events can reduce the structure's safety. Moreover, the methodology presented here can assist engineers in determining the safety indexes of structures when exposed to unexpected settlements and thus help in the decision about the need for eventual reinforcements to restore the structure's original safety.

Rev. IBRACON Estrut. Mater., vol. 16, no. 5, e16503, 2023

10/12

In the frame analyzed in this paper, it was found that, on average, the settlement in a column located at the end of the building reduced the reliability of the beams to a greater extent when compared to the effects produced by the settlement in an internal column.

In quantitative terms, the settlement of 10 mm (corresponding distortion of 1/500) reduced reliability of the structure's beam elements by about 14%. Although this reduction may look small, it lead to reliability index values β_{MC} as low as 2.40, which is lower than minimum recommended by the Model Code 2010 [15]. Thus, if the frame does not present significant load redistribution, the analysis indicates that the structure will present a safety level lower than that predicted in the design.

In this study, arbitrary values were considered for the probabilities of different magnitudes of foundation settlement, following the concept of performance-based design: larger settlement magnitudes are associated to smaller probabilities of occurrence. Results in Figure 9 should be reviewed considering more realistic (measured) foundation settlements for specific soil types.

In terms of the sensitivity of the variables, it can be concluded that the Error model (E_r) was the most important factor in the analyzed frame. The second most influential variable in this analysis was the live load (L).

In this work only one type of condition not foreseen in the project was addressed, which was the support settlements. However, other situations can be addressed in the future with this methodology, such as, for example, the assessment of the reliability of structures submitted to reinforcement corrosion. With this, the methodology can assist in decision-making about the need for corrective actions in structures deteriorated by the corrosion process.

REFERENCES

[1]   R. E. Melchers and A. T. Beck, *Structural Reliability Analysis and Prediction*, 3rd ed. Hoboken, NJ: Wiley, 2018.

[2]   A. Beck, *Confiabilidade e Segurança das Estruturas*, 1. ed. São Paulo: GEN LTC, 2021.

[3]   M. Holický, J. V. Retief, and C. Viljoen, "Reliability basis for assessment of existing building structures with reference to sans 10160," *J. S. Afr. Inst. Civ. Eng.*, vol. 63, no. 1, 2021, http://dx.doi.org/10.17159/2309-8775/2021/v63n1a1.

[4]   P. H. P. Facholli and A. T. Beck, "Distribution of load effects and reliability of reinforced concrete frames: intact and with columns removed," *Rev. IBRACON Estrut. Mater.*, vol. 15, no. 2, pp. e15207, 2022, http://dx.doi.org/10.1590/s1983-41952022000200007.

[5]   A. T. Beck, L. da Rosa Ribeiro, M. Valdebenito, and H. Jensen, "Risk-based design of regular plane frames subject to damage by abnormal events: a conceptual study," *J. Struct. Eng.*, vol. 148, no. 1, pp. 04021229, Jan 2022, http://dx.doi.org/10.1061/(ASCE)ST.1943-541X.0003196.

[6]   S. Küttenbaum, T. Braml, A. Taffe, S. Keßler, and S. Maack, "Reliability assessment of existing structures using results of NONDESTRUCTIVE testing," *Struct. Concr.*, vol. 22, no. 5, pp. 2895–2915, Oct 2021, http://dx.doi.org/10.1002/suco.202100226.

[7]   A. Mankar, I. Bayane, J. D. Sørensen, and E. Brühwiler, "Probabilistic reliability framework for assessment of concrete fatigue of existing RC bridge deck slabs using data from monitoring," *Eng. Struct.*, vol. 201, pp. 109788, Dec 2019, http://dx.doi.org/10.1016/j.engstruct.2019.109788.

[8]   R. R. Souza, L. F. F. Miguel, G. McClure, F. Alminhana, and J. Kaminski Jr., "Reliability assessment of existing transmission line towers considering mechanical model uncertainties," *Eng. Struct.*, vol. 237, pp. 112016, Jun 2021, http://dx.doi.org/10.1016/j.engstruct.2021.112016.

[9]   F. Ávila, E. Puertas, and R. Gallego, "Probabilistic reliability assessment of existing masonry buildings: The church of San Justo y Pastor," *Eng. Struct.*, vol. 223, pp. 111160, Nov 2020, http://dx.doi.org/10.1016/j.engstruct.2020.111160.

[10] G. Savaris, P. H. Hallak, and P. C. A. Maia, "Influence of foundation settlements in load redistribution on columns in a monitoring construction - Case Study," *Rev. IBRACON Estrut. Mater.*, vol. 3, pp. 346–356, Sep 2010.

[11] L. B. Amancio, "Previsão de recalques em fundações profundas utilizando redes neurais artificiais do tipo Perceptron," M.S. thesis, Univ. Fed. Ceará, Fortaleza, CE, 2013.

[12] Associação Brasileira de Normas Técnicas, *Actions and Safety of Structures – Procedure*, ABNT NBR 8681, 2003.

[13] Associação Brasileira de Normas Técnicas, *Projeto de Estruturas de Concreto – Procedimento*, ABNT NBR 6118, 2014.

[14] P. Furness, "Applications of Monte Carlo Simulation in marketing analytics," *J. Direct Data Digit. Mark. Pract.*, vol. 13, no. 2, pp. 132–147, Oct 2011, http://dx.doi.org/10.1057/dddmp.2011.25.

[15] Fédération Internationale du Béton, *Model Code 2010, vol. 1*. Germany: fib. The International Federation for Structural Concrete, 2010. http://dx.doi.org/10.35789/fib.BULL.0090.

[16] W. C. Santiago, H. M. Kroetz, S. H. C. Santos, F. R. Stucchi and A. T. Beck, "Reliability-based calibration of main Brazilian structural design codes," *Lat. Am. J. Solids Struct.*, vol. 17, no. 1, pp. e245, 2020, http://dx.doi.org/10.1590/1679-78255754.

[17] D. M. Santos, F. R. Stucchi, and A. T. Beck, "Confiabilidade de vigas projetadas de acordo com as normas brasileiras," *Rev. IBRACON Estrut. Mater.*, vol. 7, pp. 723–746, Oct 2014, http://dx.doi.org/10.1590/S1983-41952014000500002.

[18] A. Ghobarah, "Performance-based design in earthquake engineering: state of development," *Eng. Struct.*, vol. 23, no. 8, pp. 878–884, Aug 2001, http://dx.doi.org/10.1016/S0141-0296(01)00036-0.

[19] G. Augusti and M. Ciampoli, "Performance-Based Design in risk assessment and reduction," *Probab. Eng. Mech.*, vol. 23, no. 4, pp. 496–508, Oct 2008, http://dx.doi.org/10.1016/j.probengmech.2008.01.007.

[20] M. Ciampoli, F. Petrini, and G. Augusti, "Performance-based wind engineering: towards a general procedure," *Struct. Saf.*, vol. 33, no. 6, pp. 367–378, Sep 2011, http://dx.doi.org/10.1016/j.strusafe.2011.07.001.

[21] M. A. Fathali and S. R. H. Vaez, "Optimum performance-based design of eccentrically braced frames," *Eng. Struct.*, vol. 202, pp. 109857, Jan 2020, http://dx.doi.org/10.1016/j.engstruct.2019.109857.

[22] A. W. Skempton and D. H. Macdonald, "The allowable settlements of buildings," *Proc. Inst. Civ. Eng.*, vol. 5, no. 6, pp. 727–768, Nov 1956, http://dx.doi.org/10.1680/ipeds.1956.12202.

[23] B. M. Das, *Shallow Foundations: Bearing Capacity and Settlement*, 3rd ed. Boca Raton: CRC Press, 2017.

[24] J. B. Burland, B. B. Broms, and V. F. De Mello, "Behaviour of foundations and structures," in *Proc. 9th Int. Conf. on Soil Mech. Foundations Eng.*, vol. 2, pp. 495–549, 1978. SOA report.

[25] A. Nour, A. Slimani, and N. Laouami, "Foundation settlement statistics via finite element analysis," *Comput. Geotech.*, vol. 29, no. 8, pp. 641–672, Dec 2002, http://dx.doi.org/10.1016/S0266-352X(02)00014-9.

[26] A. S. Nowak, A. M. Rakoczy, and E. K. Szeliga "Revised Statistical Resistance Models for R/C Structural Components," in *ACI Symposium Publication*, Jan. 2012, vol. 218, pp. 1–16.

[27] FINITO, "Finito FEM Toolbox User's Manual." 2022. [Online]. Available: https://wmpjrufg.github.io/FINITO_TOOLBOX/

[28] A. Saltelli, P. Annoni, I. Azzini, F. Campolongo, M. Ratto, and S. Tarantola, "Variance based sensitivity analysis of model output. Design and estimator for the total sensitivity index," *Comput. Phys. Commun.*, vol. 181, no. 2, pp. 259–270, Feb 2010, http://dx.doi.org/10.1016/j.cpc.2009.09.018.

[29] R. Gagnon, L. Gosselin, and S. Decker, "Sensitivity analysis of energy performance and thermal comfort throughout building design process," *Energy Build.*, vol. 164, pp. 278–294, Apr 2018, http://dx.doi.org/10.1016/j.enbuild.2017.12.066.

[30] A. Saltelli, editor *Global sensitivity analysis: the primer.* Chichester, England; Hoboken, NJ: John Wiley, 2008.

[31] A. M. L. Lindahl et al., "Stochastic modeling of diffuse pesticide losses from a small agricultural catchment," *J. Environ. Qual.*, vol. 34, no. 4, pp. 1174–1185, Jul 2005, http://dx.doi.org/10.2134/jeq2004.0044.

[32] S. Marino, I. B. Hogue, C. J. Ray, and D. E. Kirschner, "A methodology for performing global uncertainty and sensitivity analysis in systems biology," *J. Theor. Biol.*, vol. 254, no. 1, pp. 178–196, Sep 2008, http://dx.doi.org/10.1016/j.jtbi.2008.04.011.

[33] M. Momeni, C. Bedon, M. A. Hadianfard, and A. Baghlani, "An efficient reliability-based approach for evaluating safe scaled distance of steel columns under dynamic blast loads," *Buildings*, vol. 11, no. 12, pp. 606, Dec 2021, http://dx.doi.org/10.3390/buildings11120606.

Editors: Sergio Hampshire C. Santos, Guilherme Aris Parsekian.

IBRACON Structures and Materials Journal
Revista IBRACON de Estruturas e Materiais

ORIGINAL ARTICLE

Influence of shear walls on the structural behavior of a multi-storey concrete building according to Brazilian Technical Code ABNT NBR 15421:2006

Influência de pilares-parede no comportamento estrutural de um edifício de múltiplos pavimentos de concreto de acordo com a norma técnica brasileira ABNT NBR 15421:2006

Carlos Alexandre Seruti[a] (ID)
Eduardo Fernandes Lima[a] (ID)
Silvio de Souza Lima[a] (ID)
Sergio Hampshire de Carvalho Santos[a] (ID)

[a]Universidade Federal do Rio de Janeiro – UFRJ, Programa de Projeto de Estruturas da Escola Politécnica, Rio de Janeiro, RJ, Brasil

Abstract: This paper presents a comparative study of the influence of shear walls on the behavior of a multi-storey concrete building when subjected to seismic actions. Two structures with different earthquake-resistant systems were evaluated. One is composed of concrete frames with usual detailing in both directions (x and y), and the other one is formed by a dual system, composed of frames and shear walls with usual detailing. The Equivalent Lateral Force procedure and the Modal Response Spectrum analysis presented by the Brazilian Technical Code ABNT NBR 15421:2006 were considered. The dual system building presented a greater stiffness with the shear walls arranged parallel to direction y. In the x direction, the responses are equivalent in both buildings. The horizontal forces obtained by the Equivalent Lateral Force method at the base of the buildings were greater than the Modal Response Spectrum method.

Keywords: seismic analysis, equivalent lateral force procedure, modal response spectrum analysis.

Resumo: Este trabalho apresenta um estudo comparativo da influência de pilares-parede no comportamento de um edifício de concreto de vários andares quando submetido a ações sísmicas. Foram avaliadas duas estruturas com diferentes sistemas sísmicos. Uma é composta por pórticos de concreto com detalhamento usual em ambas as direções (x e y), e a outra é formada por um sistema dual, composto por pórticos e pilares-parede com detalhamento usual. Os Métodos das Forças Horizontais Equivalentes e Espectral apresentados pela norma técnica brasileira ABNT NBR 15421:2006 foram considerados. Verificou-se que a edificação de sistema dual apresentou maior rigidez com os pilares-parede dispostos paralelamente à direção y. Na direção x, as respostas são equivalentes em ambos os edifícios. Os esforços horizontais obtidos pelo método das forças equivalentes na base dos edifícios foram maiores que os espectrais.

Palavras-chave: análise sísmica, método das forças horizontais equivalentes, método espectral.

1 INTRODUCTION

Brazil seismic occurrence is low compared to other South American countries, such as Argentina, Chile, Colombia, Ecuador, and Peru. These countries are located on the edge of the seismic plate which gives rise to the Andes, where earthquakes are frequent. Brazil, despite most of its territory is in a region of low seismicity, located internally in a tectonic plate, there are areas that show a potential for the occurrence of earthquakes. The greatest registered accelerations in the country occurred in the Northeast region (Ceará and Rio Grande do Norte) and in west of the North region, in Amazonas and Acre, as shown by Santos et al. [1] and Paiva et al. [2]. Therefore, such activity is not totally null, and even being of low intensity, it should not be disregarded in Brazilian civil engineering projects.

The Brazilian Association of Technical Codes (ABNT) published in 2006 the first version of a technical code in this subject, ABNT NBR 15421 [3]. This code was based on the Seismic Hazard presented by Giardini et al. [4] on the Global Seismic Hazard Assessment Program (GSHAP). However, seismic zones, such as northern Mato Grosso do Sul State, were not properly considered in the GSHAP and ended up not being represented in the technical code map. Thus, there is a need to update the Brazilian seismic map, as mentioned by Miranda et al. [5].

In the international technical literature, it is possible to find numerous references involving seismic studies, see for instance [6]-[15]. In Brazil, however, there are few studies on this subject. This is due to the low occurrence of earthquakes of large magnitudes in the Brazilian territory. Among the Brazilian general studies on earthquakes, some can be cited: Pereira et al. [16] evaluates the seismic reliability assessment of a reinforced concrete (RC) frame designed in accordance with ABNT NBR 6118 [17] without considering the seismic design prescribed by ABNT NBR 15421 [3]; Aguero et al. [18] proposed a structural retrofit method for evaluation of a RC casing in columns with increase in bending moments under seismic loads; Matos [19] and Alva et al. [20] studied the influence of masonry on the strength of buildings subjected to seismic excitations; Gidrão et al. [21] simulated seismic effects in a 12-story reinforced concrete building; Peña and Carvalho [22] studied the influence of the structural configuration on the seismic response of a reinforced concrete structure.

This paper aims to compare the influence of shear walls on the stiffness of the reinforced concrete structure of a building in terms of resulting forces in its base and displacements in the top of the structure. For the calculations, two methods for seismic analysis described in ABNT NBR 15421 [3], were considered: (*i*) Equivalent Lateral Forces and (*ii*) Modal Response Spectrum.

2 CASE STUDY

Two hypothetical building models with distinct earthquakes-resistant basic systems are evaluated. One is composed only by concrete frames with the usual detailing in both directions (*x* and *y*), and the other one presents a dual system, composed of frames and concrete shear walls, both with usual detailing. Thus, the difference lies in the presence of shear walls in one of them since the dimensions of the structural elements are the same in both models. The main characteristics of the building can be seen in Table 1.

Table 1. Building characteristics.

Elements and properties	Values
Columns section	(60×60) cm^2
Beams section	(30×60) cm^2
Slabs thickness	20 cm
Walls thickness	30 cm
Floor height	3.0 m
Concrete compression strength (f_{ck})	30 MPa
Concrete specific weight	25 kN/m^3
Concrete modulus of elasticity	30000 MPa
Poisson coefficient	0.20

It is important to note that in this research it is not being considered whether the structure, from de design point of view, is acceptable. Loads were verified only at the base of the structure.

The studied buildings have 12 storeys and height of 36 m, with dimensions in plan of 12 m x 16 m, as shown in Figure 1. The modeling was performed in the Robot Structural Analysis Professional 2021 computer program [23] and it is depicted in Figure 2. In the dual system, each shear wall was discretized into 12 shell finite elements of dimensions 1 m x 1 m. The properties of these shear walls are the same as the structure and are defined in Table 1.
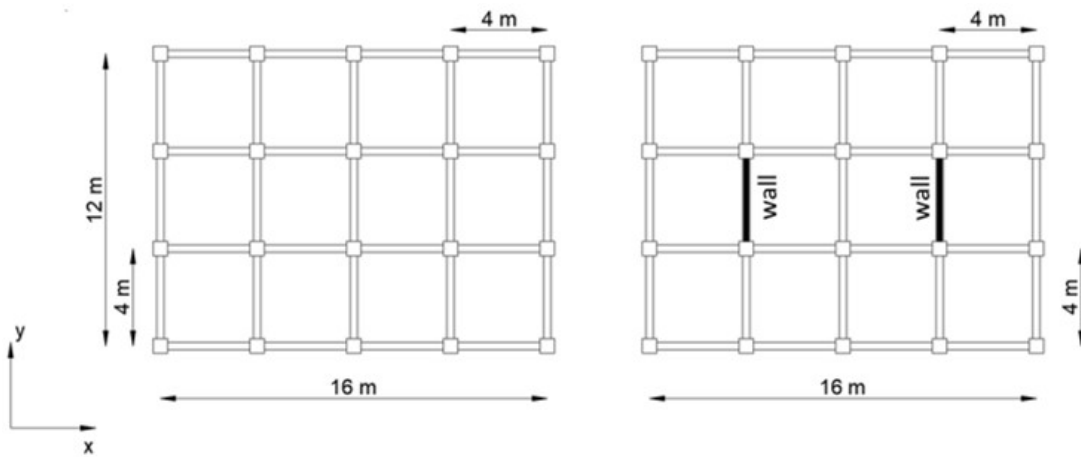
Figure 1. Plan dimensions of the earthquake-resistant basic systems.
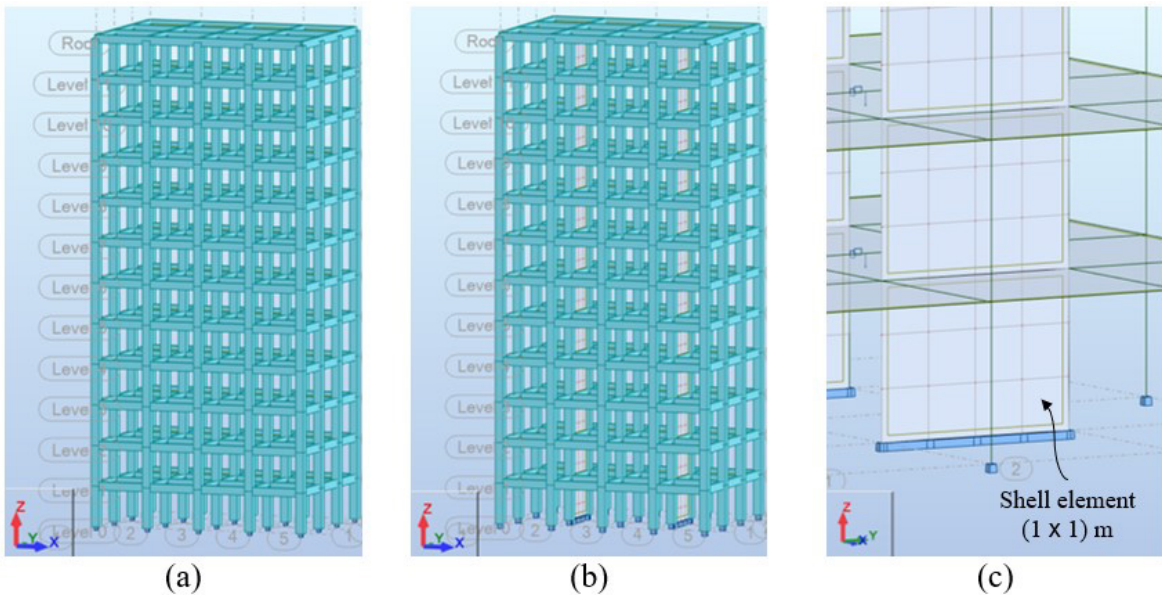
Figure 2. Structural systems: (a) framed with usual detailing in both directions; (b) dual system, composed of frames and shear walls with usual detailing; (c) shear walls in shell finite elements.

It was considered that the location of the model buildings is in the Acre State, in Brazilian Seismic Zone 4, in a site where the basic horizontal seismic acceleration (a_g) is 0.15g, being g the gravity acceleration, as defined by ABNT NBR 15421 [3] and shown in Figure 3. The considered site class is D, corresponding to "stiff soil" and the seismic category is C. The average properties for the 30 m below the ground top, i.e., the average velocity of propagation of shear waves, $\overline{V_S}$, and the average blows SPT test number, $\overline{N}$, are in the ranges, respectively, 370 m/s $\geq \overline{V_S} \geq$ 180 m/s and $50 \geq \overline{N} \geq 15$. The values defined as nominal for seismic actions are those that have a 10% probability of being exceeded during a period of 50 years, which corresponds to a recurrence period of 475 years.

Elastic response spectrum of accelerations can be obtained considering the soil characteristics and the standard code definitions (see Figure 4). The figure expresses the relationship between the structural periods T(s) and horizontal accelerations S_a(m/s²), corresponding to the elastic response of a one-degree-of-freedom system with a critical damping ratio equal to 0.05.
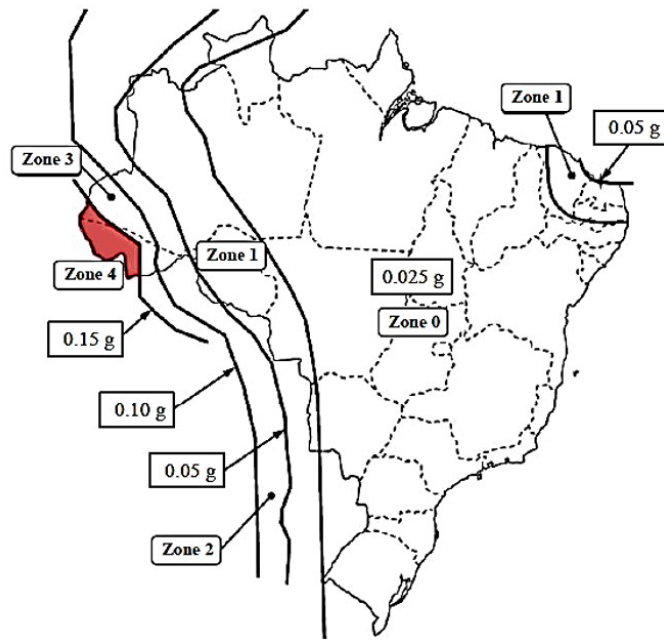
Figure 3. Horizontal nominal seismic accelerations in Brazil and region of location of building [3].
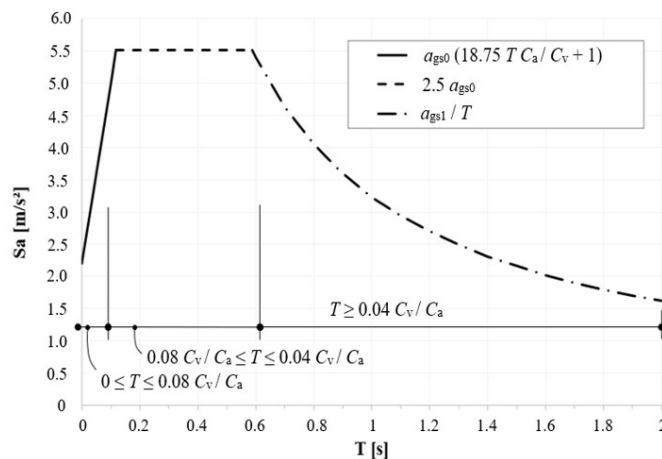
Figure 4. Elastic response spectrum of accelerations.

The spectrum does not depend on the basic earthquake-resistant systems defined in the two resistant models studied, but on the site class (D) and the characteristic horizontal seismic acceleration (a_g). The seismic amplification factors, C_a and C_v, are in this case, respectively, 1.5 and 2.2 (Table 3 of ABNT NBR 15421 [3]). The spectral acceleration for the periods of 0 s (a_{gs0}) and 1 s (a_{gs1}) were obtained by multiplying C_a e o C_v by a_g.

3 METHODOLOGY

In this study, analyses considering two NBR 15421 calculation methods are performed. The methods are:

(i)   Equivalent Lateral Force;

(ii) Modal Response Spectrum.

Two earthquake-resistant systems were evaluated: (a) Only concrete frames with usual detailing and (b) dual system, composed of frames and concrete shear walls, both with usual detailing. The results are forces and displacements obtained in the two analyses. The absolute displacements δ and relative displacements Δ were compared, verifying the influence of the shear walls on the response of the buildings.

3.1 Equivalent lateral force (ELF) procedure

3.1.1 Total horizontal force

The ELF procedure leads to a static linear analysis. The total horizontal force at the base of the structure H, in each direction, can be determined by Equation 1.

$$H = C_s\, W \tag{1}$$

where C_s = is the seismic response coefficient; W = total weight of the structure, considering only permanent loads.

The seismic response coefficient, C_s, is defined according to Equation 2:

$$C_s = \frac{2.5\, I\, a_{gs0}}{g\, R} \tag{2}$$

where I = use importance factor, adopted in this case equal to 1.0 (see Table 4 of the ABNT NBR 15421 [3]); a_{gs0} = spectral acceleration for the period of 0.0 s; g = gravity acceleration, considered equal to 9.81 m/s²; R = response modification coefficient.

According to ABNT NBR 15421 [3], the minimum value of the C_s is 0.01, and it need not exceed that given by Equation 3:

$$C_s = \frac{I\, a_{gs1}}{g\, R\, T} \tag{3}$$

where a_{gs1} = spectral acceleration for the period of 1.0 s; T = natural period of the structure.

3.1.2 Period determination

The natural period of the structure, T, can be obtained by a modal extraction process, provided that it does not exceed the product of the modal limiting coefficient C_{up} times the approximate natural period of the structure T_a. The value of the C_{up}, which is defined considering the seismic zone 4, is given as 1.5 (Table 10 of ABNT NBR 15421 [3]). The approximate natural period of the structure, T_a, can be obtained by the Equation 4:

$$T_a = C_T\, h_n^{\,x} \tag{4}$$

where C_T = coefficient function of the earthquake-resistant system; x = parameter that varies also according to the earthquake-resistant system; h_n = height of the structure above the base.

The building does not have double symmetry since the dimensions in directions x and y are different and therefore the fundamental periods are also different. As a model has shear walls, in order to make a comparison with the composed only of concrete frames, it is necessary to obtain the period in the direction in which it provides the greatest influence on stiffness, which is in the direction y, and thus obtain the values of displacements and loads at the base of the building proposed in the research.

3.1.3 Vertical distribution of seismic forces

The total static horizontal force on the base H (Equation 1) is distributed vertically between the several elevations of the structure, so that at each elevation x, a force F_x is applied as defined by Equation 5:

$$F_x = C_{vx}\, H \tag{5}$$

The vertical distribution coefficient, C_{vx}, is defined according to Equation 6:

$$C_{vx} = \frac{w_x\, h_x^k}{\sum_{i=1}^{n} w_i\, h_i^k} \tag{6}$$

where w_i and w_x = total effective weight parts corresponding to elevations i or x, respectively; h_i and h_x = heights between the base and the elevations i or x, respectively; k = distribution exponent, related to the natural period of structure T, with the following values:

-   for structures with period less than 0.5 s: $k = 1$;
-   for structures with periods between 0.5 s and 2.5 s, $k = (T + 1.5) / 2$;
-   for structures with period greater than 2.5 s: $k = 2$.

3.1.4 Torsional moment consideration

In addition to the distribution of horizontal seismic loads, the design must include an inherent torsional moment (M_t) in the floors, caused by the eccentricity of the centers of mass relative to the centers of rigidity, plus an accidental torsional moment, M_{ta}. This moment is determined considering a displacement of the center of mass in each direction equal to 5% of the dimension of the structure, in a direction parallel to the axis perpendicular to the direction of application of the horizontal forces. As the building has double symmetry, the centers of gravity (CG) of the slabs are located at the intersections of the main axes. Such slabs behave like rigid diaphragms. In seismic category C structures, where the models of this paper are included, if there are structural irregularities of type 1 (torsional), M_{ta} must be multiplied by an amplification factor of the torsional moment A_x, obtained by Equation 7.

$$A_x = \left(\frac{\delta_{máx}}{1.2\, \delta_{avg}}\right)^2 \tag{7}$$

where $\delta_{máx}$ = maximum horizontal displacement in one direction, in the dimension x; δ_{avg} = average of displacements in the same direction, at the extreme points of the structure on an axis transverse to this direction.

3.1.5 Absolute and relative displacements

The displacements resulting from the static analysis, δ_e, are obtained directly from the computer program after the application of the referred horizontal forces F_x and moments M_{ta}. The absolute displacements, δ, evaluated at the centers of mass, are determined by multiplying δ_e by the ratio between the amplification coefficient of the displacements C_d (variable according to the earthquake-resistant system) and by the importance factor I. The relative displacements, Δ, are determined as the difference between the absolute displacements in the centers of mass in the elevations above and below the storey in consideration. The latter are limited to 2% of the floor height ($0.020\, h_s$).

3.1.6 Second-order effects

As for second-order effects, ABNT NBR 15421 [3] disregards their consideration on a given storey if the stability coefficient θ (Equation 8) is less than 0.10.

$$\theta = \frac{P_i\, \Delta_i}{H_i\, h_{si}\, C_d} \tag{8}$$

where P_i = vertical force acting on the floor i, obtained with multiplying factors of load taken equal to 1.0; Δ_i = relative displacement of the floor; H_i = seismic shear force acting on floor i; h_{si} = distance between the two elevations corresponding to the storey in analysis; C_d = amplification coefficient of the displacements.

The value of the stability coefficient θ cannot exceed the maximum value $\theta_{máx}$, defined according to the Equation 9:

$$\theta_{máx} = \frac{0.5}{C_d} \tag{9}$$

The ABNT NBR 15421 [3] limits $\theta_{máx} \leq 0.25$. If the value of θ is between 0.1 and $\theta_{máx}$, the forces on the elements and the displacements shall be multiplied by the factor $1.0 / (1 - \theta)$.

3.2 Modal Response Spectrum analysis

The Complete Quadratic Combination (CQC) modal responses are used to obtain the maximum value of any elastic effect, d_{ij}. In this case, it was used to obtain the forces and displacements in the building. The CQC formulation, proposed by Wilson et al. [24], which is based on the theory of random vibrations, is given in Equation 10:

$$d_{ij} = \sqrt{\sum_{i=1}^{N} \sum_{j=1}^{N} d_i\, \rho_{ij}\, d_j} \tag{10}$$

The correlation coefficient, ρ_{ij}, can be approximated by Equation 11:

$$\rho_{ij} = \frac{8\, (\xi_i \xi_j)^{1/2}\, (\xi_i + r_{ij} \xi_j)\, r_{ij}^{3/2}}{\left(1 - r_{ij}^2\right)^2 + 4\, \xi_i \xi_j\, r_{ij}\, (1 + r_{ij}^2) + 4\, (\xi_i^2 + \xi_j^2)\, r_{ij}^2} \tag{11}$$

where ξ_i and ξ_i = damping ratios for modes i and j, respectively; r_{ij} = ratio of the natural frequencies, given by Equation 12:

$$r_{ij} = \frac{\omega_i}{\omega_j} \tag{12}$$

Rev. IBRACON Estrut. Mater., vol. 16, no. 5, e16504, 2023

6/17

The modal responses obtained in terms of forces are multiplied by a I/R factor, and the displacements are multiplied by a C_d/R factor.

3.3 Model building with concrete frame structural system

The first analyses are the ones conducted in the building with an earthquake-resistant system composed only of frames and concrete slabs, in both directions. The analyses by the two methods are presented next.

3.3.1 Seismic analysis by Equivalent Lateral Forces procedure

The total permanent load of the building is composed of the dead load (G) and the live load (Q). In the system composed of concrete frames with usual detailing, the dead load is formed by the weight of the columns, walls, and concrete slabs. In the dual system, the weight of the shear walls is included. It was established, according to ABNT NBR 6120 [25], for office buildings, a live load of 2.5 kN/m², considered on all floors; on the roof, the live load is 1.5 kN/m².

Linear analyses were performed considering the Exceptional Combination of the Ultimate Limit State (ULS) of ABNT NBR 6118 [17]. These analyses involve the total permanent loads and the seismic forces obtained by the Equivalent Lateral Forces method. Equation 13 presents the combination used:

$$F_d = 1.2\ G + 1.0\ Q + 1.0\ Q_{exc} \tag{13}$$

where F_d = design load for the combination of the Ultimate Limit State; G = dead load; Q = live load; Q_{exc} = seismic horizontal force.

The total permanent load of building with concrete frame structural system is 24697 kN. The response modification coefficient R is equal to 3.0 (Table 6 of ABNT NBR 15421 [3]) and the utilization importance factor is $I = 1.0$ (Table 4 of ABNT NBR 15421 [3]). As in this system, horizontal seismic forces are 100% resisted by frames of concrete in both directions, not being these connected to more rigid systems that prevent their free deformation when subjected to seismic action, C_T and x coefficients for determining the approximate natural period of the structure T_a are 0.0466 and 0.9, respectively, with $h_n = 36$ m.

For the analyses referring to the ELF method, for the T periods in the x and y directions, those obtained in the first frequency mode with the modal analysis of the structure are considered. The values in each direction are show in Table 2:

Table 2. Building with concrete frame structural system in both directions: Parameters.

Parameters	Direction x	Direction y
1st period of structure (T) – obtained computationally:	0.88 s	0.92 s
Period limitation coefficient (C_{up}) - Table 10*:	1.5	1.5
Period coefficients: C_T:	0.0466	0.0466
x:	0.9	0.9
Height of the structure above the base (h_n):	36 m	36 m
Approximate natural period of the structure (T_a): $C_T \cdot h_n^x$	1.17 s	1.17 s
$C_T \cdot h_n^x \cdot C_{up} > T$	1.78 s	1.78 s
Use importance factor (I) - Table 4*:	1.0	1.0
Response modification coefficient (R) – Table 6*:	3.0	3.0
I/R ratio:	0.3333	0.3333
Design characteristic acceleration (a_g): 0.15 g (Zone 4) – Table 1*:	1.47 m/s²	1.47 m/s²
Seismic amplification factor for the period of 0.0 s (C_a) – Table 3*:	1.5	1.5
Spectral acceleration for the period of 0.0 s (a_{gs0}): $C_a \cdot a_g$	2.21 m/s²	2.21 m/s²
Seismic amplification factor for the period of 1.0 s (C_v) – Table 3*:	2.2	2.2
Spectral acceleration for the period of 1.0 s (a_{gs1}): $C_v \cdot a_g$	3.23 m/s²	3.23 m/s²
Seismic response coefficient (C_s): 2.5 $I\ a_{gs0}/(g\ R)$	0.19	0.19
Maximum seismic response coefficient (C_s): $I\ a_{gs1}/(g\ R\ T)$	0.13	0.12
Distribution exponent (k) for 0.5 s < T < 2.5 s: $(T + 1.5)/2$	1.19	1.21
Amplification coefficient of the displacements (C_d) – Table 6*:	2.5	2.5
C_d/R ratio:	0.8333	0.8333

*See ABNT NBR 15421 [3].

The values of the equivalent lateral forces F_x, F_y, $M_{ta,x}$ and $M_{ta,y}$ are presented in Table 3. The displacements at the nodes of the centers of mass obtained by the static analysis, δ_e, the absolute displacements δ, the relative displacements Δ and the stability coefficients θ are shown in Table 4.

According to Table 4, the values of the stability coefficients θ_x and θ_y did not exceed the value 0.1 (see Equation 8), so the second-order effects on the floors may be disregarded. Then, it was not necessary to increase forces and displacements. The relative displacements were also not greater than the limit of 0.020 h_s = 0.020 × 300 = 6 cm.

Rev. IBRACON Estrut. Mater., vol. 16, no. 5, e16504, 2023

7/17

It is worth mentioning that the structure did not present any irregularity in the plane, Therefore, the torsional moments were not amplified by A_x.

Table 3. Building with concrete frame structural system: horizontal forces F per floor with the ELF method.

Storey	w_x [kN]	Direction x			Direction y		
		C_{vx}	F_x [kN]	$M_{ta,x}$ [kN·m]	C_{vy}	F_y [kN]	$M_{ta,y}$ [kN·m]
1st	2058.09	0.0086	26.08	15.65	0.0083	24.10	19.28
2nd	2058.09	0.0198	59.58	35.75	0.0193	55.76	44.61
3rd	2058.09	0.0320	96.61	57.96	0.0315	91.09	72.87
4th	2058.09	0.0451	136.12	81.67	0.0446	129.03	103.22
5th	2058.09	0.0589	177.60	106.56	0.0584	169.03	135.23
6th	2058.09	0.0732	220.71	132.42	0.0728	210.77	168.62
7th	2058.09	0.0880	265.22	159.13	0.0878	254.01	203.20
8th	2058.09	0.1031	310.98	186.59	0.1031	298.56	238.85
9th	2058.09	0.1187	357.85	214.71	0.1190	344.31	275.45
10th	2058.09	0.1346	405.74	243.44	0.1351	391.14	312.91
11th	2058.09	0.1507	454.55	272.73	0.1517	438.97	351.17
Roof	2058.09	0.1672	504.22	302.53	0.1685	487.72	390.18
Σ (Base)	24697.07	1.0	3015.28		1.0	2894.48	

Table 4. Building with concrete frame structural system: relative displacements and stability coefficients from the ELF procedure.

Storey	Direction x				Direction y			
	δ_{xe} [cm]	δ_x [cm]	Δ_x [cm]	θ_x [× 10^{-4}]	δ_{ye} [cm]	δ_y [cm]	Δ_y[cm]	θ_y [× 10^{-4}]
1st	0.25	0.64	0.64	85.19	0.25	0.64	0.64	88.80
2nd	0.69	1.72	1.08	66.91	0.70	1.74	1.10	71.00
3rd	1.15	2.88	1.16	44.38	1.17	2.94	1.20	47.60
4th	1.62	4.04	1.16	30.87	1.66	4.14	1.20	33.37
5th	2.07	5.16	1.12	22.37	2.13	5.32	1.18	24.34
6th	2.49	6.23	1.07	16.58	2.58	6.45	1.13	18.16
7th	2.89	7.23	1.00	12.40	3.00	7.50	1.06	13.66
8th	3.25	8.13	0.90	9.22	3.39	8.47	0.96	10.24
9th	3.57	8.91	0.79	6.73	3.73	9.32	0.85	7.55
10th	3.83	9.57	0.65	4.73	4.01	10.03	0.72	5.38
11th	4.03	10.07	0.50	3.09	4.24	10.60	0.56	3.61
Roof	4.17	10.41	0.35	1.79	4.40	11.01	0.41	2.19

3.3.2 Seismic analysis by the Modal Response Spectral analysis

An important factor in dynamic analysis is the mass mobilization of the structure analyzed by the vibration mode. According to ABNT NBR 15421 [3], the number of modes to be considered in the spectral analysis must be sufficient to capture at least 90% of the total mass in each of the orthogonal directions considered in the analysis. For the 12-story building with framed system, 90% of the building mass is mobilized upon reaching the 3rd vibration mode, that is, 90.3% (direction x) and 90.2% (direction y). Figure 5 shows the mass participation of each mode in relation to the total. Figure 6 and Figure 7 present the three fundamental modes and vibration period of building, in x and y directions.
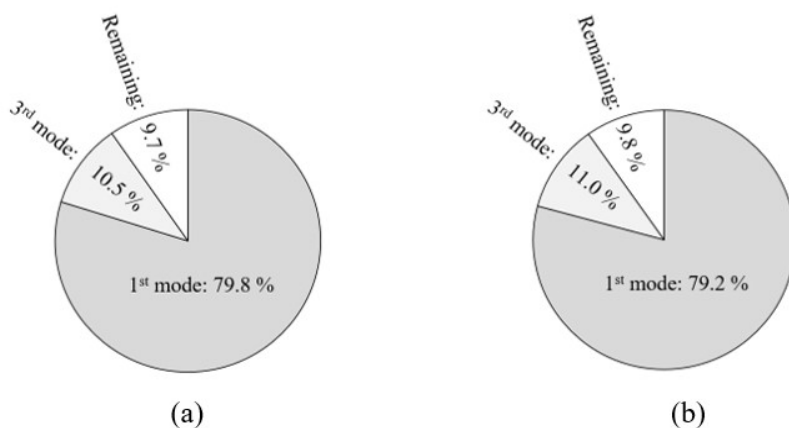
Figure 5. Mass mobilized by vibration mode: (a) x direction; (b) y direction.

Rev. IBRACON Estrut. Mater., vol. 16, no. 5, e16504, 2023

8/17

(a)

(b)

(c)
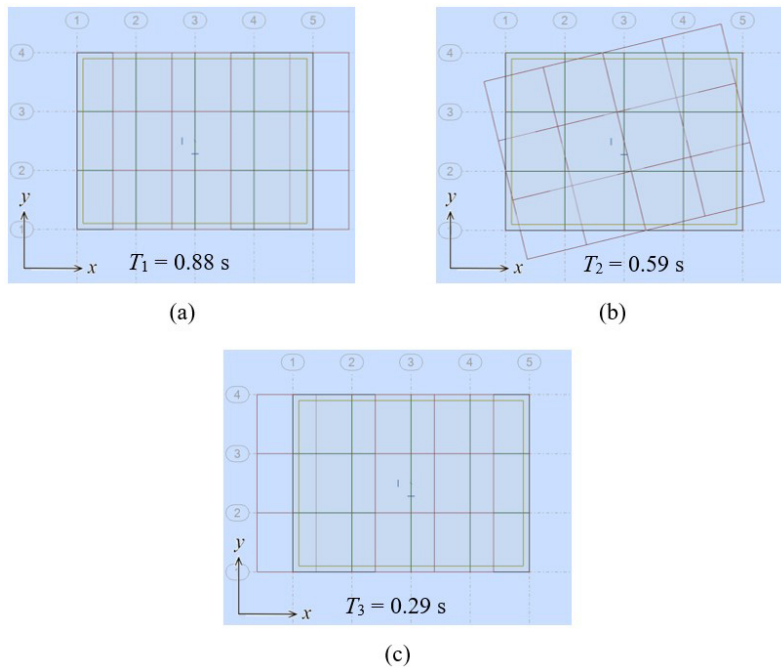
Figure 6. Structural system formed only by concrete frames - three fundamental modes of vibration in x direction: (a) 1st mode: predominantly translation; (b) 2nd mode: predominantly torsional; (c) 3rd mode: translation.

(a)

(b)

(c)
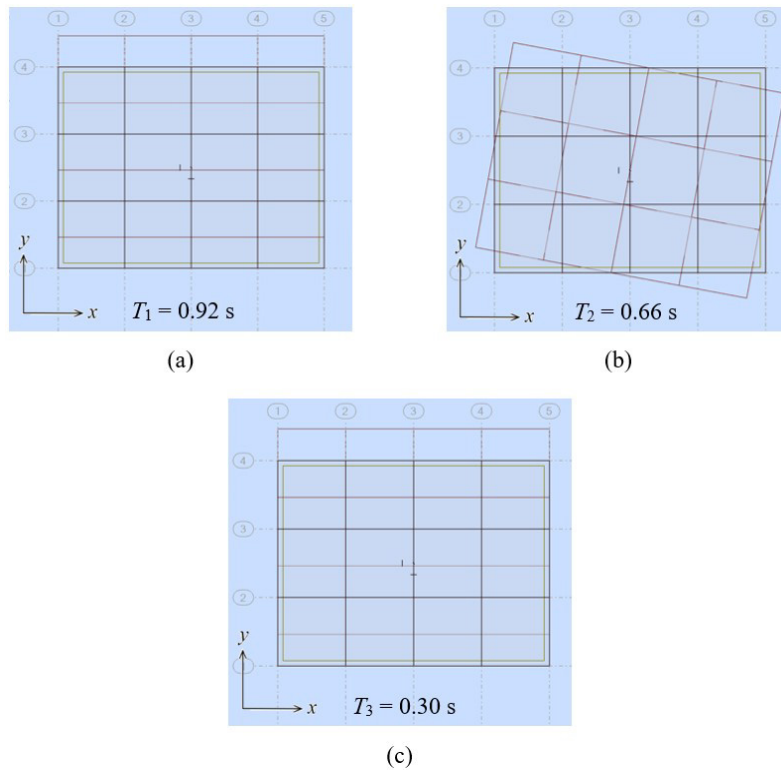
Figure 7. Structural system formed only by concrete frames - three fundamental modes of vibration in y direction: (a) 1st mode: predominantly translation; (b) 2nd mode: predominantly torsional; (c) 3rd mode: translation.

Considering the periods of vibration in the building, their highest values occur in the 1st mode in the x and y directions and are, respectively, 0.88 s and 0.92 s.

Rev. IBRACON Estrut. Mater., vol. 16, no. 5, e16504, 2023

9/17

By the Modal Response Spectral analysis, the displacements δ_e were obtained directly by the computer program. The absolute displacements are obtained by the multiplication of δ_e by C_d / R equal to 0.8333. This value is valid for the x and y directions of the structure. Table 5 shows the values of these displacements.

Table 5. Building with concrete frame structural system: nodal displacements with the Modal Response Spectral analysis.

Storey	Direction x			Direction y		
	δ_{xe} [cm]	δ_x [cm]	Δ_x [cm]	δ_{ye} [cm]	δ_y [cm]	Δ_y[cm]
1st	0.63	0.52	0.52	0.63	0.52	0.52
2nd	1.68	1.40	0.88	1.70	1.42	0.89
3rd	2.80	2.34	0.93	2.85	2.37	0.96
4th	3.90	3.25	0.91	3.98	3.32	0.94
5th	4.94	4.12	0.87	5.07	4.22	0.91
6th	5.92	4.93	0.81	6.09	5.07	0.85
7th	6.80	5.67	0.74	7.02	5.85	0.78
8th	7.59	6.33	0.66	7.87	6.55	0.70
9th	8.26	6.89	0.56	8.59	7.16	0.61
10th	8.81	7.34	0.46	9.20	7.66	0.50
11th	9.22	7.68	0.34	9.66	8.05	0.39
Roof	9.50	7.92	0.23	10.00	8.33	0.28

3.4 Model building with dual system, composed by frame and frame/shear walls

For the building with dual system the weight of the shear walls equal to 2.5 kN/m² was included. The total permanent load is 26856 kN. In this case, the earthquake-resistant system is different in both directions: (*i*) on the x axis, it is composed of frames; (*ii*) on the y axis, it is formed by a dual system (frames and shear walls).

3.4.1 Seismic analysis by the Equivalent Lateral Forces procedure

As well as the building previously analyzed, in this one, in the direction x, the seismic horizontal forces are resisted only by concrete frames. Therefore, $C_T = 0.0466$ and $x = 0.9$ (see item 9.2 of ABNT NBR 15421 [3]). In the direction y, the seismic resistant system is dual, composed of concrete frames and shear walls, both with usual detailing. In this direction, $C_T = 0.0488$ and $x = 0.75$. The values in each direction are show in Table 6 and the values of F_x, F_y, $M_{ta,x}$ and $M_{ta,y}$ are shown in Table 7.

Table 6. Building with dual frame system: Parameters.

Parameters	Direction x	Direction y
1st period of structure (T) – obtained computationally:	0.92 s	0.65 s
Period limitation coefficient (C_{up}) - Table 10*:	1.5	1.5
Period coefficients: C_T:	0.0466	0.0488
x:	0.9	0.75
Height of the structure above the base (h_n):	36 m	36 m
Approximate natural period of the structure (T_a): $C_T \cdot h_n{}^x$	1.17 s	0.72 s
$C_T \cdot h_n{}^x \cdot C_{up} > T$	1.78 s	1.08 s
Use importance factor (I) - Table 4*:	1.0	1.0
Response modification coefficient (R) – Table 6*:	3.0	4.5
I / R ratio:	0.3333	0.2222
Design characteristic acceleration (a_g): 0.15 g (Zone 4) – Table 1*:	1.47 m/s²	1.47 m/s²
Seismic amplification factor for the period of 0.0 s (C_a) – Table 3*:	1.5	1.5
Spectral acceleration for the period of 0.0 s (a_{gs0}): $C_a \cdot a_g$	2.21 m/s²	2.21 m/s²
Seismic amplification factor for the period of 1.0 s (C_v) – Table 3*:	2.2	2.2
Spectral acceleration for the period of 1.0 s (a_{gs1}): $C_v \cdot a_g$	3.23 m/s²	3.23 m/s²
Seismic response coefficient (C_s): 2.5 $I\, a_{gs0} / (g\, R)$	0.19	0.13
Maximum seismic response coefficient (C_s): $I\, a_{gs1} / (g\, R\, T)$	0.12	0.11
Distribution exponent (k) for 0.5 s < T < 2.5 s: ($T + 1.5$) / 2	1.21	1.08
Amplification coefficient of the displacements (C_d) – Table 6*:	2.5	4.0
C_d / R ratio:	0.8333	0.8889

*See ABNT NBR 15421 [3].

Table 7. Building with dual frame system: Horizontal forces F per floor with the ELF procedure.

Storey	w_x [kN]	Direction x			Direction y		
		C_{vx}	F_x [kN]	$M_{ta,x}$ [kN·m]	C_{vy}	F_y [kN]	$M_{ta,y}$ [kN·m]
1st	2238.00	0.0083	26.81	16.09	0.0110	33.34	26.67
2nd	2238.00	0.0193	62.00	37.20	0.0232	70.24	56.19
3rd	2238.00	0.0315	101.24	60.75	0.0358	108.61	86.89
4th	2238.00	0.0446	143.38	86.03	0.0488	147.97	118.38
5th	2238.00	0.0584	187.80	112.68	0.0621	188.08	150.47
6th	2238.00	0.0728	234.14	140.48	0.0755	228.81	183.05
7th	2238.00	0.0878	282.12	169.27	0.0891	270.05	216.04
8th	2238.00	0.1031	331.57	198.94	0.1029	311.73	249.39
9th	2238.00	0.1189	382.34	229.40	0.1168	353.81	283.05
10th	2238.00	0.1351	434.30	260.58	0.1308	396.24	316.99
11th	2238.00	0.1516	487.37	292.42	0.1449	438.99	351.19
Roof	2238.00	0.1684	541.46	324.84	0.1591	482.04	385.63
Σ (Base)	26856.00	1.0	3214.54		1.0	3029.91	

The obtained displacements δ_e, δ, Δ and θ are shown in Table 8. Structural irregularities are not observed; therefore, it was not necessary to increase the displacements or amplify the accidental torsion moment.

Table 8. Building with concrete frame structural system: relative displacements and stability coefficients with the ELF procedure.

Storey	Direction x				Direction y			
	δ_{xe} [cm]	δ_x [cm]	Δ_x [cm]	θ_x [× 10⁻⁴]	δ_{ye} [cm]	δ_y [cm]	Δ_y[cm]	θ_y [× 10⁻⁴]
1st	0.26	0.66	0.66	88.11	0.06	0.26	0.26	23.13
2nd	0.72	1.79	1.13	70.39	0.20	0.79	0.53	21.88
3rd	1.21	3.01	1.23	46.99	0.38	1.50	0.71	18.28
4th	1.70	4.24	1.22	32.75	0.59	2.34	0.84	15.03
5th	2.17	5.43	1.19	23.74	0.81	3.25	0.91	12.27
6th	2.62	6.56	1.13	17.60	1.05	4.20	0.95	9.98
7th	3.05	7.61	1.05	13.15	1.29	5.15	0.95	8.09
8th	3.43	8.57	0.95	9.78	1.52	6.08	0.93	6.53
9th	3.76	9.40	0.83	7.14	1.74	6.96	0.89	5.25
10th	4.04	10.09	0.69	5.01	1.95	7.80	0.84	4.21
11th	4.25	10.62	0.53	3.29	2.15	8.58	0.78	3.37
Roof	4.40	10.99	0.37	1.92	2.33	9.31	0.73	2.64

3.4.2 Seismic analysis by the Modal Response Spectral analysis

By the Spectral analysis, the absolute displacements δ were obtained by multiplying δ_e by a C_d / R factor, and for each direction different values resulted (see item 3.4.1 – Table 6). Thus, in the x direction, $\delta_x = 0.8333\ \delta_{xe}$, and in the y direction, $\delta_y = 0.8889\ \delta_{ye}$. The displacements values can be seen in Table 9.

Table 9. Building with dual frame system: nodal displacements with the Modal Response Spectrum analysis.

Storey	Direction x			Direction y		
	δ_{xe} [cm]	δ_x [cm]	Δ_x [cm]	δ_{ye} [cm]	δ_y [cm]	Δ_y[cm]
1st	0.64	0.53	0.53	0.21	0.19	0.19
2nd	1.73	1.44	0.91	0.65	0.58	0.39
3rd	2.89	2.41	0.97	1.23	1.10	0.52
4th	4.03	3.36	0.95	1.92	1.71	0.61
5th	5.11	4.26	0.90	2.67	2.37	0.66
6th	6.12	5.10	0.84	3.44	3.06	0.69
7th	7.05	5.87	0.77	4.22	3.75	0.69
8th	7.86	6.55	0.68	4.98	4.43	0.68
9th	8.56	7.13	0.58	5.71	5.07	0.64
10th	9.12	7.60	0.47	6.39	5.68	0.61
11th	9.55	7.96	0.35	7.03	6.25	0.57
Roof	9.84	8.20	0.24	7.62	6.77	0.52

For the 12-storey building with framed and dual system, 93.6% of the building mass is mobilized in the 4th vibration mode in direction x. In the direction y, 92.6% is mobilized in the 6th mode. Figure 8 shows the mass participation of each mode in relation to the total. Figures 9-10 present the three fundamental modes and vibration period of building, in x and y directions.

The highest values of periods of vibration in the building with dual system occur also in the 1st mode in the x and y directions and are, respectively, 0.92 s and 0.65 s.

By the Spectral Analysis, the displacements δ_e were obtained directly in the computer program. The absolute displacements δ are obtained by the multiplication of δ_e by C_d / R, with C_d and R having different values in the x and y axis. Tables 4 and 6 shows the values of these displacements.

(a)

(b)
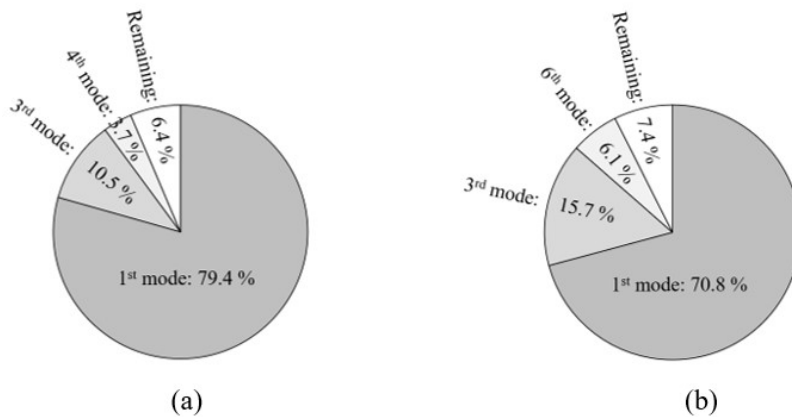
Figure 8. Mass mobilized by vibration mode in building with dual frame system: (a) x direction; (b) y direction.

(a)

(b)

(c)
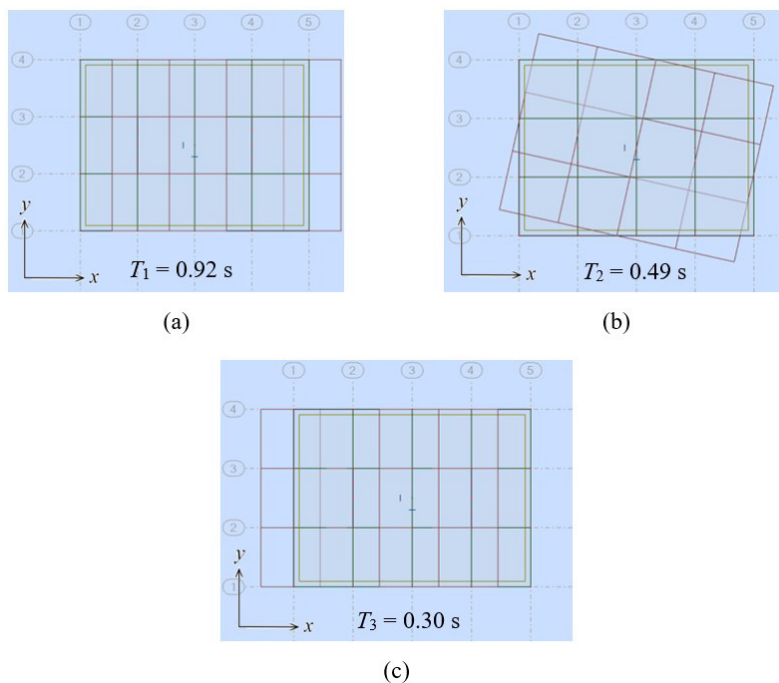
Figure 9. Building with dual frame system - three fundamental modes of vibration in x direction: (a) 1st mode: predominantly translation; (b) 2nd mode: predominantly torsional; (c) 3rd mode: translation.

Rev. IBRACON Estrut. Mater., vol. 16, no. 5, e16504, 2023

12/17
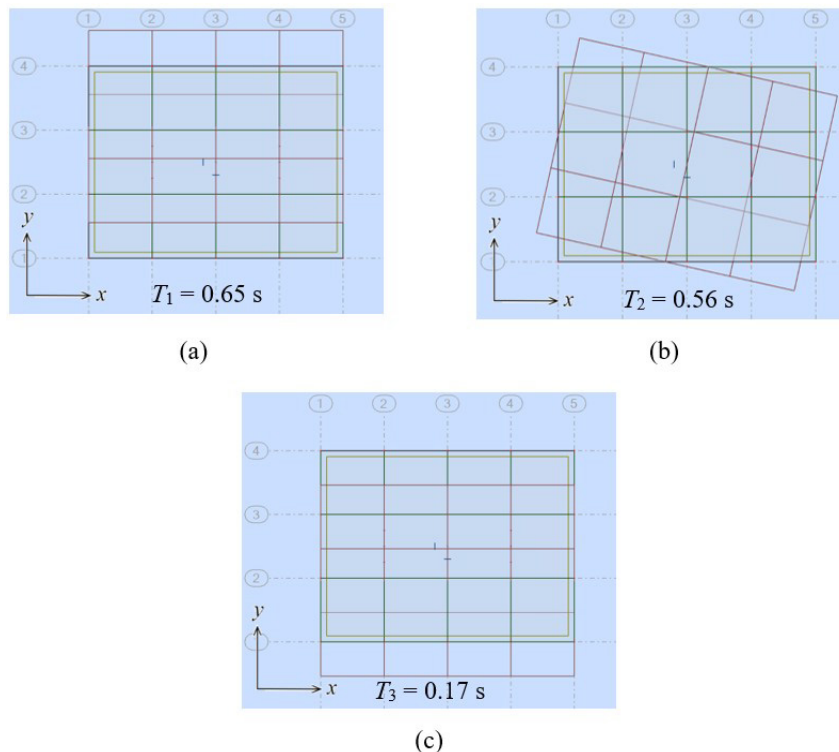
Figure 10. Structural system formed only by concrete frames - three fundamental modes of vibration in y direction: (a) 1st mode: predominantly translation; (b) 2nd mode: predominantly torsional; (c) 3rd mode: translation.

4 RESULTS AND DISCUSSIONS

This section discusses the results obtained in terms of displacements and forces at the base of buildings from the analyzes by the Equivalent Lateral Forces procedure and Modal Response Spectrum analysis described in the previous items.

4.1 Model building with concrete frame structural system

The ABNT NBR 15421 [3] stipulates that the project modal responses at the base of the building (H_{tx} and H_{ty}) are obtained by multiplying the elastic responses (H_{txe} and H_{tye}), arising from the computational analysis, by the I / R factor.

In the case of a building with an earthquake-resistant system formed only by frames, $I / R = 0.3333$, in both directions. As $H_{txe} = 7459$ kN and $H_{tye} = 7152$ kN, then $H_{tx} = 2486$ kN and $H_{ty} = 2384$ kN. By the Equivalent Lateral Forces procedure, the forces at the base are $H_x = 3015$ kN and $H_y = 2895$ kN.

However, if the total horizontal force at the base determined by the spectral process, H_t, in one direction, is less than $0.85\ H$ (less than 85% of the horizontal force determined by the static process), all elastic forces obtained in this direction must be multiplied by $0.85\ H/H_t$. This correction does not apply to absolute and relative displacements. Therefore, in direction x, $0.85\ H_x = 0.85 \times 3015 = 2563$ kN.

As 2486 kN is less than 2563 kN, so $H_x = 3015 \times 0.85\ (3015 / 2486) = 3198$ kN. In direction y, $0.85\ H_y = 0.85 \times 2895 = 2461$ kN. As 2384 kN is less than 2461 kN, so $H_y = 2895 \times 0.85\ (2895 / 2384) = 2988$ kN.

In summary, the modal responses are $H_{tx} = 2486$ kN and $H_{ty} = 2384$ kN; the elastic responses are $H_x = 3198$ kN and $H_y = 2988$ kN. Differences are of approximately 22% and 20% between the values obtained by the two methods in each direction.

Figure 11 presents the responses in terms of absolute displacements on each floor in the x and y directions obtained by the two analyses methods and the horizontal resulting forces in the base of the building. The percentages in parentheses represent the differences in terms of absolute displacements between the two methods. The black arrows are the horizontal forces at the base by the Equivalent Lateral Forces (ELF) procedure and the gray arrows are the forces at the base obtained by the Modal Response Spectrum analysis.

Rev. IBRACON Estrut. Mater., vol. 16, no. 5, e16504, 2023

13/17
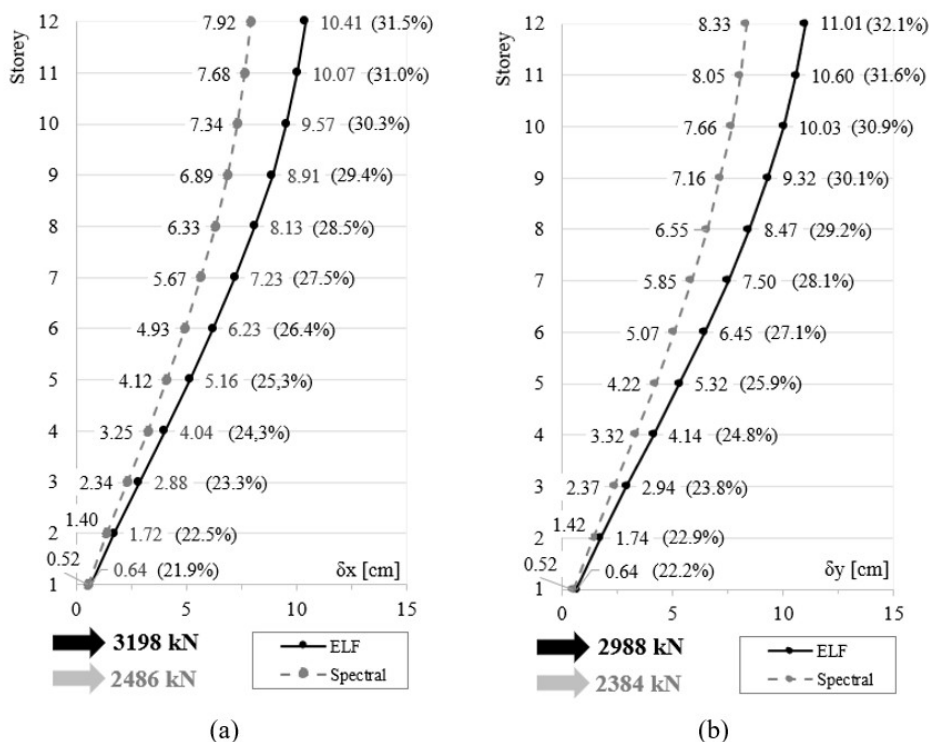
Figure 11. Frame system: Absolute displacements and total horizontal forces at the base: (a) Direction *x*; (b) Direction *y*.

According to Figure 11, the static method is more conservative, since the absolute displacements obtained were greater than those obtained by the spectral method in both directions. These are greater in *y*, since in this direction the stiffness of the structure is lower. As expected, the largest displacements were on the 12th floor with the greatest difference also between the two methods. The relative displacements, however, were higher on the lower floors (see Tables 4-5).

4.2 Model building with dual system with concrete frame and shear walls

In the case of the building with dual earthquake-resistant system, the I / R ratio has different values in the *x* and *y* directions (see item 3.4.1). The modal responses in terms of forces at the base of the building obtained by the computational analysis, H_{txe} and H_{tye}, are, respectively, 7845 kN and 10008 kN, and that multiplied by the I / R factors equal to 0.3333 and 0.2222 generated $H_{tx} = 2615$ kN and $H_{ty} = 2224$ kN. By the Equivalent Lateral Forces procedure, the forces at the base are $H_x = 3215$ kN and $H_y = 3030$ kN.

In direction *x*, 0.85 $H_x = 0.85 \times 3215 = 2733$ kN. As 2615 kN is less than 2733 kN, so $H_x = 3215 \times 0.85$ (3215 / 2615) = 3360 kN. In direction *y*, 0.85 $H_y = 0.85 \times 3030 = 2576$ kN. As 2224 kN is also less than 2576 kN, so $H_y = 3030 \times 0.85$ (3030 / 2224) = 3509 kN.

In summary, the modal responses are $H_{tx} = 2615$ kN and $H_{ty} = 2224$ kN; the elastic responses are $H_x = 3360$ kN and $H_y = 3509$ kN. Differences are of approximately 22% and 37% between the values obtained by the two methods in each direction.

Figure 12 shows the responses in terms of absolute displacements on each floor in the *x* and *y* directions obtained by the two analyses methods and the horizontal resulting forces in the base of the building. The percentages in parentheses represent the differences in terms of absolute displacements between the two methods. The black arrows are the horizontal forces at the base by the Equivalent Lateral Forces (ELF) procedure and the gray arrows are the forces at the base obtained by the Modal Response Spectrum analysis.
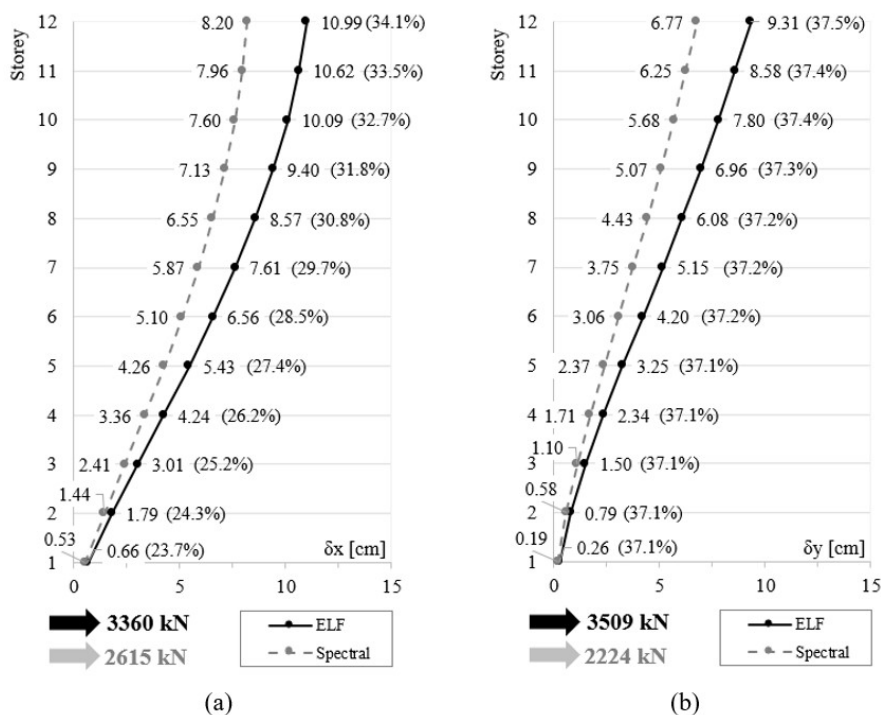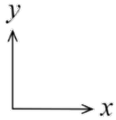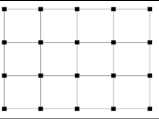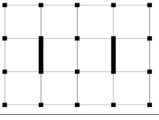
Figure 12. Frame / shear walls system: Absolute displacements and total horizontal forces at the base:
(a) Direction *x*; (b) Direction *y*.

According to Figure 12, the static method is also more conservative for this building, with the absolute displacements in *y* greater than those in *x*. As in the building with only frames, the relative displacements were higher on the lower floors (see Tables 8-9).

Finally, Table 10 presents a summary of the results obtained by the two analyses in terms of loads applied to the base of the buildings and absolute displacements in the roof. The positive sign in the differences in results between the two analysis methods indicates an increase in the evaluated term; negative sign indicates reduction.

Table 10. Results in terms of loads applied at the base of building and absolute displacements in the roof.

	Direction *x*				Direction *y*			
	ELF		Spectral		ELF		Spectral	
	H_x [kN]	δ_x [cm]	H_{tx} [kN]	δ_{tx} [cm]	H_y [kN]	δ_y [cm]	H_{ty} [kN]	δ_{ty} [cm]
	3198	10.41	2486	7.92	2988	11.01	2384	8.33
	3360	10.99	2615	8.20	3509	9.31	2224	6.77
Difference [%]	+ 5.1	+ 5.6	+ 5.2	+ 3.5	+ 17.4	- 15.4	- 6.7	- 18.7

According to the results presented in Table 10, it is possible comment:

(i)   In the direction *x*, by the two analysis methods, building formed with the dual structural system presented a higher load on the base in relation to the one formed only by frames. A similar increase of about 5.1% in

responses. The absolute displacements in the roof were also higher in this direction in the building with shear walls (about 5.6% in those obtained by the static method and 3.5% in those obtained by the dynamic method).

(ii)   In the direction y, the increase in the dual building occurred only in the load obtained by the horizontal forces method and it was more significant than that in the direction x, that is, an increase of 17.4%. As for that provided by the spectral method, there was a reduction of about 6.7%. The displacements also suffered a reduction of about 15.4% and 18.7%, respectively provided by the static and dynamic analysis, despite the increase in the applied load in the direction y. It can be concluded that the shear walls provide greater stiffness in the structure when arranged parallel to evaluated axis.

5 CONCLUSIONS

This research aimed to verify the influence of shear walls on the stiffness of the reinforced concrete structure in a multi-storey hypothetical building subjected to seismic action. Two models were developed in a computer program. One with an earthquake-resistant system composed only by frames in both directions and the other one with a dual system, composed of concrete shear walls, both with the usual detailing. Two analysis methods were considered according to the Brazilian Code ABNT NBR 15421 [3]: Equivalent Lateral Forces procedure and Modal Response Spectrum analysis.

Analyzing the results, it was found that, by the static method, the absolute displacements obtained were greater than those achieved by the spectral method in both directions and in both buildings. In the building with a seismic resistant system formed only by frames, the displacements were higher in the y direction, even with the lower applied load in this direction. This can be explained by the lower stiffness of the structure in this direction. The building with shear walls, on the other hand, the opposite occurs. That is, greater displacements in the x direction, since the walls provide greater stiffness to the structure in the y direction.

Comparing the displacements in the roof in the x direction between the two buildings (Table 10), in both methods, the building with shear walls presented higher values than the one with the structure formed only by frames, because its dead load is greater, and the seismic forces are directly related to these loads. However, such values were shown to be equivalent in both models, since the relationship between applied loads and displacements is similar, that is, with a difference of about 5%.

Thus, it can be concluded that shear walls arranged perpendicularly to the x-axis do not provide a significant increase in building stiffness in this direction. In the y-axis, there is a reduction in absolute displacements of approximately 15.4% from the structural system composed only of concrete frames to the one with shear walls by the static method and 18.7% by the spectral method. It can be finally concluded, for this case, that the shear walls located parallel to axis y provided a significant increase in the building stiffness.

However, it is worth mentioning that, to draw more general conclusions, that analyses should be expanded. It would be more appropriate to analyze other structures (symmetrical or not) in different seismic regions with different shear walls (simple and composite).

REFERENCES

[1] W. L. Santos, C. A. Crisóstomo, A. R. F. Barbosa, P. M. Silva, and F. I. C. Nascimento, "Atividades sísmicas na Amazônia: levantamento e caracterização de terremotos na Amazônia Sul-ocidental – Acre – Brasil," *GeoUECE.*, vol. 8, no. 15, pp. 66–77, Jul. 2019. Accessed: Oct. 10, 2021. [Online]. Available: https://revistas.uece.br/index.php/GeoUECE/article/view/2164

[2] J. B. Paiva No., P. G. B. Nóbrega, and S. H. S. Nóbrega, "Avaliação da resposta sísmica de edifícios de concreto na região Nordeste segundo métodos da NBR 15421," in *Proc. 58º Congr. Bras. Concreto.*, Oct. 2016, pp. 1–16.

[3] Associação Brasileira de Normas Técnicas, *Projeto de Estruturas Resistentes a Sismos – Procedimento, NBR 15421*, 2006.

[4] D. Giardini, G. Grünthal, K. M. Shedlock, and P. Zhang. "The GSHAP global seismic hazard map," *Ann. Geophys.*, vol. 42, no. 6, pp. 1225–1230, Dec. 1999. https://doi.org/10.4401/ag-3784.

[5] P. S. T. Miranda, H. S. A. Varum, and N. S. Vila Pouca, "Sismicidade brasileira: registros sísmicos indicam a configuração de um novo mapa," in *XIV Int. Conf. Building Pathology Constructions Repair.*, Jun. 2018, pp. 1–14.

[6] M. H. Beedalah and S. K. Mohaisen, "Performance of reinforced concrete building with shear wall under the effect of seismic loads," *Int. J. Modern Res. Eng. Technol.*, vol. 6, no. 21, pp. 367–375, Sep. 2021.

[7] M. A. Elwi and W. G. A. Hussein, "Study of effect of shear wall in the seismic response of existing buildings," *Periodicals Eng. Natural Sciences*, vol. 9, no. 3, pp. 494–508, Aug. 2021.

[8] S. A. Hossain and A. Bagchi, "Seismic performance of existing buildings concrete shear wall," in *5th World Cong. Civil, Structural, Environmental Eng.*, Oct. 2020, pp. 1–10.

[9] D. Ugalde and D. Lopez-Garcia, "Analysis of the seismic capacity of Chilean residential RC shear wall buildings," *J. Building Eng.*, vol. 31, 101369, Sep. 2020.

[10] S. A. Ahamad and K. V. Pratap, "Dynamic analysis of G + 20 multi storied building by using shear walls in various locations for different seismic zones by using Etabs," *Materials Today: Proc.*, vol. 43, Pt 2, pp. 1043–1048, Apr. 2021. https://doi.org/10.1016/j.matpr.2020.08.014.

[11] H. Alimohammadi, M. D. Esfahani, and M. L. Yaghin, "Effects of openings on the seismic behavior and performance level of concrete shear walls," *Int. J. Eng. Appl. Sciences*, vol. 6, no. 10, pp. 33–39, Oct. 2019. Accessed: Dec. 6, 2022. [Online]. Available: https://www.researchgate.net/publication/337596926

[12] T. A. Ozkul, A. Kurtbeyoglu, M. Borekci, and B. Zengin, "Effect of shear wall on seismic performance of RC frame buildings," *Eng. Failure Anal.*, vol. 100, pp. 60–75, Feb. 2019. https://doi.org/10.1016/j.engfailanal.2019.02.032.

[13] H. H. Jammani, J. V. Amiri, and H. Rajabnejad, "Energy distribution in RC shear wall-frame structures subject to repeated earthquakes," *Soil Dy. Earthq. Eng.*, vol. 107, pp. 116–128, Apr. 2018. https://doi.org/10.1016/j.soildyn.2018.01.010.

[14] J. Tarigan, J. Manggala, and T. Sitorus, "The effect of shear wall location in resisting earthquake," *IOP Conf. Series Mater. Sci. Eng.*, vol. 309, pp. 1–6, Mar. 2018. http://dx.doi.org/10.1088/1757-899X/309/1/012077.

[15] D. Ugalde and D. Lopez-Garcia, "Behavior of reinforced concrete shear wall buildings subjected to large earthquakes," *Procedia Eng.*, vol. 199, pp. 3582–3587, Sep. 2017.

[16] E. M. V. Pereira, G. H. F. Cavalcante, I. D. Rodrigues, L. C. M. Vieira Jr., and G. H. Siqueira "Seismic reliability assessment of a non-seismic reinforced concrete framed structure designed according to ABNT NBR 6118:2014," *Rev. IBRACON Estrut. Mater.*, vol. 15, no. 1, e15110, Aug. 2022. https://doi.org/10.1590/S1983-41952022000100010.

[17] Associação Brasileira de Normas Técnicas, *Projeto de Estruturas de Concreto – Procedimento*, NBR 6118, 2014.

[18] R. R. Aguero, J. R. Y. Aguirre, M. Schmitz, and C. H. H. Viegas. "Structural retrofitting method for evaluation RC jacketing in columns with amplification of moments under seismic loads," *Rev. IBRACON Estrut. Mater.*, vol. 15, no. 5, e15510, Apr. 2022. https://doi.org/10.1590/S1983-41952022000500010.

[19] D. B. M. Matos, "Otimização do posicionamento da alvenaria estrutural de vedação para minimização de deslocamentos laterais em edifícios submetidos a excitações sísmicas," M.S. thesis, Univ. Federal Rio Grande do Sul, Porto Alegre, Brazil, 2021.

[20] G. M. S. Alva, A. O. Rigão, J. Kaminski Jr., and M. A. S. Pinheiro "Seismic analysis of reinforced concrete building with participating masonry infills," *Rev. IBRACON Estrut. Mater.*, vol. 14, no. 3, e14315, Mar. 2021. https://doi.org/10.1590/S1983-41952021000300015.

[21] G. M. S. Gidrão, P. O. B. Costa, M. Della-libera, and R. M. Bosse, "Simulação dos efeitos sísmicos em um edifício de 12 pavimentos em concreto armado," *Rev. Eng. Tecnol.*, vol. 12, no. 4, pp. 13–25, Dec. 2020.

[22] L. A. P. Peña and G. N. D. Carvalho, "Estudo da influência da configuração estrutural na resposta sísmica de uma estrutura de concreto armado," *Rev. IBRACON Estrut. Mater.*, vol. 8, no. 6, pp. 800–826, Sep. 2017. https://doi.org/10.1590/S1983-41952015000600005.

[23] Autodesk. "Robot Structural Analysis professional version 2021." Autodesk. https://www.autodesk.com/products/robot-structural-analysis/overview (accessed May 8, 2021).

[24] E. L. Wilson, A. D. Kiureghian, and E. P. Bayo, "A replacement for the SRSS method in seismic analysis," *Earthq. Eng. Structural Dyn.*, vol. 9, no. 2, pp. 187–192, Jan. 1981.

[25] Associação Brasileira de Normas Técnicas, *Cargas para o Cálculo de Estruturas de Edificações, NBR 6120*, 2019.

Rev. IBRACON Estrut. Mater., vol. 16, no. 5, e16504, 2023

17/17

IBRACON Structures and Materials Journal
Revista IBRACON de Estruturas e Materiais

ORIGINAL ARTICLE

Deflection estimate of reinforced concrete beams by the lumped damage mechanics

Estimativa de flecha em vigas de concreto armado pela mecânica do dano concentrado

Adysson André Fortuna de Souza[a] ID
Wayne Santos de Assis[b] ID
David Leonardo Nascimento de Figueiredo Amorim[a,b] ID

[a]Universidade Federal de Sergipe, Programa de Pós-graduação em Engenharia Civil, Laboratório de Modelagem Matemática em Engenharia Civil, São Cristóvão, SE, Brasil
[b]Universidade Federal de Alagoas, Programa de Pós-graduação em Engenharia Civil, Maceió, AL, Brasil

Abstract: The evaluation of the deflection in beams is an indispensable step of the structural design. Currently, many standard codes adopt the Branson's model. However, the Branson's model underestimates the deflection of beams with a reinforcement rate of less than 1%. Therefore, this study proposes a new alternative to quantify the deflections in reinforced concrete beams, based on the Lumped Damage Mechanics (LDM). LDM is a nonlinear theory, which uses concepts from Fracture and Damage Mechanics combined with plastic hinges. The viability of the proposed model was verified through comparisons with results from experimental works developed by other authors and the application of the Branson's model. The obtained results showed that the proposed calculation model had a good approximation of the experimental data with satisfactory accuracy and equivalent values to the Branson's model in the investigated scenarios.

Keywords: reinforced concrete beams, deflection, lumped damage mechanics, plastic hinge, structural design.

Resumo: A avaliação de flechas em vigas é uma etapa indispensável no projeto estrutural. Atualmente, muitas normas adotam o modelo de Branson. Entretanto, o modelo de Branson subestima a flecha de vigas com taxa de armadura menor do que 1%. Desta forma, este estudo propõe uma alternativa para quantificar flechas em vigas de concreto armado com base na Mecânica do Dano Concentrado (MDC). A MDC é uma teoria não linear que utiliza conceitos das Mecânicas da Fratura e do Dano combinados com rótulas plásticas. A viabilidade do modelo proposto foi verificada por meio da comparação com resultados experimentais obtidos por outros autores bem como a aplicação do modelo de Branson. Os resultados obtidos mostram que o modelo proposto tem boa aproximação aos dados experimentais com acurácia satisfatória e valores equivalentes ao modelo de Branson nos cenários investigados.

Palavras-chave: vigas de concreto armado, flecha, mecânica do dano concentrado, rótula plástica, projeto estrutural.

1 INTRODUCTION

Structural response in service is an important issue in civil engineering. Design codes around the world estimate the immediate deflection of reinforced concrete (RC) beams based on the equation proposed by Branson [1], [2] for estimating the equivalent inertia moments of cracked RC members (e.g., [3]–[6]). Such design codes present small variations for the formulation proposed by Branson [1], [2].

Recently, other researchers have initiated improvements to Branson's model, especially for concrete reinforced with other materials, such as fibre-reinforced polymers [7]–[20]. Gribniak et al. [21] presented a statistical study of the immediate deflections of RC beams evaluated by different design codes [3], [22], [23] and smeared crack numerical analysis with several finite elements. Despite the accuracy of the finite element analysis (FEA) presented in [21], its application to design engineering practice is unfeasible.

Lumped damage mechanics (LDM) appears as an interesting alternative to FEA because of its use of few finite elements resulting from its combination of key concepts from classic fracture [24] and damage mechanics [25] with plastic hinges. For a review on LDM, see [26].

Hence, this study mainly aims to propose a simplified formulation for estimating the immediate deflections of RC beams based on the LDM framework. Different from the work in [1], [2], which is solely based on experimental observations, the model proposed in the current study is supported by the popular and widely accepted concepts of fracture and damage mechanics, such as effective stress, strain equivalence hypothesis and the Griffith energy criterion.

2 DEFLECTION OF REINFORCED CONCRETE BEAMS

To describe this nonlinear behaviour of RC beams, Branson [1] performed an experimental study on rectangular and 'T' beams applied with uniformly distributed short-term loads.

A formulation was subsequently proposed to calculate the immediate deflection based on an effective moment of inertia. This formula establishes a proportional relationship between the moment of inertia of the gross concrete section about the centroidal axis I_g; and the moment of inertia of the cracked section transformed into concrete I_{cr}. Based on a multiplier factor, the ratio between the first cracking moment M_{cr} and the maximum moment in the beam due to service loads at the deflection stage M_a is calculated. Branson's model [1] is expressed by Equation 1.

$$I_{eff} = (M_{cr}/M_a)^m I_g + [1 - (M_{cr}/M_a)^m]I_{cr} \tag{1}$$

Exponent m equal to 3 is adopted for the calculation of a reference section for the entire span. The calculation considers the sum of the effects of the loss of stiffness and the contribution of the concrete in the traction area between cracks, in the cracked region of the span, and also the region without visible cracks. For the calculation of an individual section, exponent m is assigned with a value of 4 [27].

According to Bischoff [15], Branson's Model [1] works well for RC beams with a reinforcement rate between 1% and 2%, which was the standard reinforcement rate in the past. However, the equation underestimates the deflection of RC beams with a reinforcement rate below 1%; corroborating the results obtained in this study.

3 LUMPED DAMAGE MECHANICS

Consider the beam element depicted in Figure 1, where L denotes the span. The deformed shape of such beam can be described by two relative rotations at edges i and j i.e. ϕ_i and ϕ_j, respectively (Figure 1a). These relative rotations, now called generalised deformations [28], are conjugated to two bending moments (m_i and m_j) named generalised stresses [28] (Figure 1a).

The transverse displacement along the beam element is represented by a cubic polynomial function w(x) (Figure 1b). Then, the boundary conditions are:

$$w(0) = w(L) = 0 \qquad -w_{,x}|_{x=0} = \phi_i \qquad -w_{,x}|_{x=L} = \phi_j \tag{2}$$

Therefore, the transverse displacement field is described as follows:

$$w(x) = (-x^3/L^2 + 2x^2/\text{L} - x)\phi_i + (-x^3/L^2 + x^2/\text{L})\phi_j \tag{3}$$

Rev. IBRACON Estrut. Mater., vol. 16, no. 5, e16505, 2023

2/15
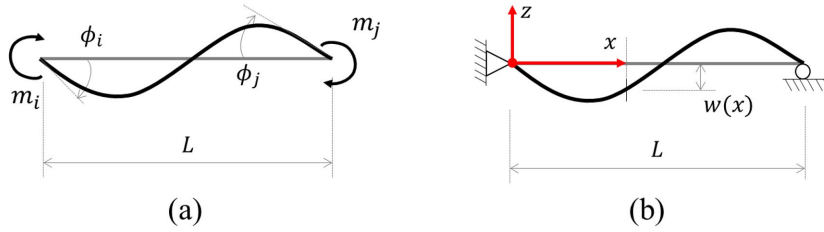
Figure 1. Deformed shape of a beam element: (a) generalised deformations and stresses; (b) transverse displacement field.

Now, considering that the generalised deformations are elastic, i.e. ϕ_i^e and ϕ_j^e, the bending moment distribution along the beam element can be written as:

$$M(x) = EI_g w_{xx} = EI_g\left[(-6x/L^2 + 4/L)\phi_i^e + (-6x/L^2 + 2/L)\phi_j^e\right] \tag{4}$$

As the bending moments at the edges of the beam element are m_i and m_j (Figure 1a), then:

$$M(0) = \left(4EI_g/L\right)\phi_i^e + \left(2EI_g/L\right)\phi_j^e = m_i \tag{5}$$

$$M(L) = -\left(2EI_g/L\right)\phi_i^e - \left(4EI_g/L\right)\phi_j^e = -m_j \tag{6}$$

Equations 5, 6 can be rewritten in terms of generalised deformations, i.e.

$$\phi_i^e = \left(L/3EI_g\right)m_i - \left(L/6EI_g\right)m_j \tag{7}$$

$$\phi_j^e = -\left(L/6EI_g\right)m_i + \left(L/3EI_g\right)m_j \tag{8}$$

Equations 7, 8 can be expressed in matrix form, as:

$$\{\boldsymbol{\phi}^e\} = [\mathbf{F_0}]\{\mathbf{M}\} \tag{9}$$

where $\{\boldsymbol{\Phi}^e\} = \{\phi_i^e\ \phi_j^e\}^T$ is the matrix of elastic generalised deformations, $\{\mathbf{M}\} = \{m_i\ m_j\}^T$ is the matrix of generalised stresses, $[\mathbf{F_0}]$ is the elastic flexibility matrix, described by:

$$[\mathbf{F_0}] = \begin{bmatrix} L/3EI_g & -L/6EI_g \\ -L/6EI_g & L/3EI_g \end{bmatrix} \tag{10}$$

and the superscript T means 'transpose of'.

LDM states that a beam element is understood as a composition of an elastic beam with two inelastic hinges at its edges (Figure 2a). Therefore, such hinges are responsible for inelastic effects.

Under the deformation equivalence hypothesis [26], the matrix of generalised deformations $\{\boldsymbol{\Phi}\}$ can be expressed as a sum of three parts:

$$\{\boldsymbol{\phi}\} = \{\boldsymbol{\phi}^e\} + \{\boldsymbol{\phi}^d\} + \{\boldsymbol{\phi}^p\} \tag{11}$$

Rev. IBRACON Estrut. Mater., vol. 16, no. 5, e16505, 2023

3/15

being $\{\boldsymbol{\Phi}^{\mathbf{e}}\}$ the elastic part, $\{\boldsymbol{\Phi}^{\mathbf{p}}\} = \{\phi_i^p \ \phi_j^p\}^T$ the plastic part, accounting for reinforcement yielding at the hinges (Figure 3b), and $\{\boldsymbol{\Phi}^{\mathbf{d}}\}$ the damaged one, expressed by [29]:

$$\{\boldsymbol{\phi}^d\} = [\mathbf{C(D)}]\{\mathbf{M}\} = \begin{bmatrix} \dfrac{Ld_i}{3EI(1-d_i)} & 0 \\ 0 & \dfrac{Ld_j}{3EI(1-d_j)} \end{bmatrix} \{\mathbf{M}\} \tag{12}$$

where, $[\mathbf{C(D)}]$ is the matrix of additional flexibility due to damage variables at the hinges (d_i and d_j); it represents concrete cracking (Figure 2c).

Finally, the following expression is obtained by substituting Equations 9 and 12 in (11):

$$\{\boldsymbol{\phi} - \boldsymbol{\phi}^p\} = [\mathbf{F(D)}]\{\mathbf{M}\} \tag{13}$$

where $[\mathbf{F(D)}]$ is the flexibility matrix of a damaged beam element; it is described as:

$$[\mathbf{F(D)}] = [\mathbf{F_0}] + [\mathbf{C(D)}] = \begin{bmatrix} \dfrac{L}{3EI(1-d_i)} & -\dfrac{L}{6EI} \\ -\dfrac{L}{6EI} & \dfrac{L}{3EI(1-d_j)} \end{bmatrix} \tag{14}$$
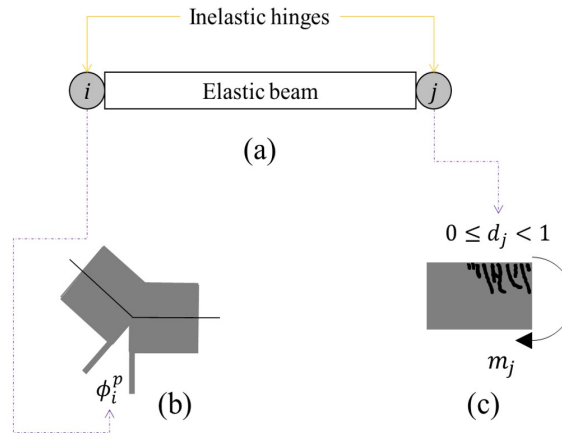
Figure 2. Lumped damage mechanics for RC beams: (a) elastic beam with inelastic hinges, (b) reinforcement yielding and (c) concrete cracking.

Note that both terms of the main diagonal of $[\mathbf{F(D)}]$ present the inertia moment penalised by a damage variable i.e. $I_g(1-d_i)$ and $I_g(1-d_j)$. Henceforth, this study focuses on only one of the hinges. The damage variable of such hinge is described herein without an index (d).

The concept of effective inertia moment (I_{eff}) is then introduced as a function of d [30]:

$$I_{eff} = I_g(1-d) \tag{15}$$

Cippolina et al. [29] experimentally presented a simple way to quantify the damage variable. Such experiment consisted of a simply supported beam, such as that depicted in Figure 3a.

During the test, unloading-reloading cycles were performed to quantify the beam stiffness (Figure 3b). For the first unloading-reloading cycle, the applied load was lower than the threshold for concrete cracking as an alternative to

measure elastic stiffness (S_0). Thereafter, the stiffness values for concrete cracking were obtained (Figure 3b), i.e. $S(d)$. The damage variable d for any cycle is then calculated [29]:

$$d = 1 - S(d)/S_0 \qquad (16)$$
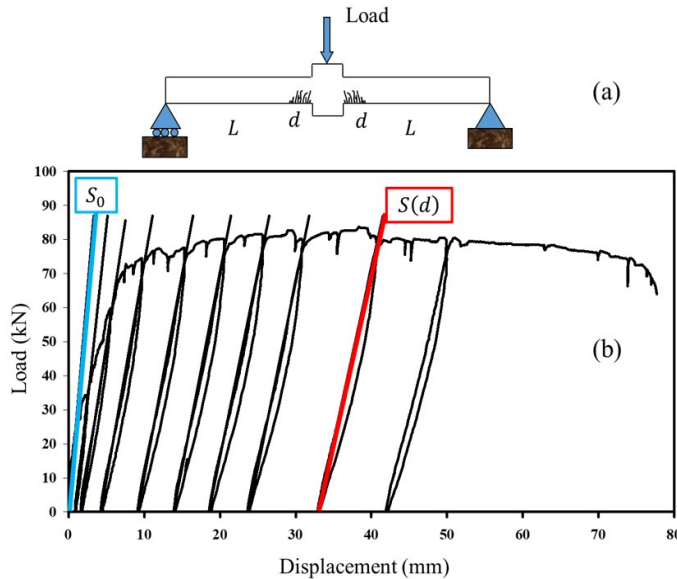
Figure 3. Graphical representation of damage measurement (adapted from [29]).

Experimental observations (e.g. [26], [29], [30]) show that the damage variable can be easily associated with the plastic bending moment (M_p) and ultimate bending moment (M_u), both of which are known quantities of classic RC theory.

Despite its accuracy at the load bearing condition of structural elements, the necessity of a lumped damage approach to analyse deflection in beams was observed by the application of the classic LDM for reinforced concrete structures [26] to a deflection test. In order to illustrate this issue, note that the classic LDM cracking evolution criterion is based on the generalised Griffith criterion, where the energy release rate (G) is equal to a crack resistance function (R), both defined as follows [26]:

$$G = R \Rightarrow m^2 L/\left[6EI_g(1-d)^2\right] = R_0 + q\ln(1-d)/(1-d) \qquad (17)$$

being R_0 the initial crack resistance and q a parameter associated to the longitudinal reinforcement.

Then, three conditions are known by the bending moment vs. damage obtained by Equation 17 i.e. by the classic LDM (see Figure 4):

$$m|_{d=0} = M_r \Rightarrow M_{cr}^2 L/\left(6EI_g\right) = R_0 \quad (18)$$

$$m|_{d=d_u} = M_u \Rightarrow M_{cr}^2 L/\left[6EI_g(1-d_u)^2\right] = M_{cr}^2 L/\left(6EI_g\right) + q\ln(1-d_u)/(1-d_u) \qquad (19)$$

$$\left.\frac{\partial m}{\partial d}\right|_{d=d_u} = 0 \Rightarrow (1-d_u)M_{cr}^2 L/\left(3EI_g\right) + q[1 + \ln(1-d_u)] = 0 \qquad (20)$$

where d_u is the ultimate damage i.e. the damage value at the ultimate condition.

For an experimental analysis carried out by Álvares [31] (Figure 4), the conditions in (18-20) result in: $R_0 = 0.32$kNmm, $q = -106.37$kNmm and $d_u = 0.63$. The experimental damage, depicted in Figure 4, is obtained by the following relation:

Rev. IBRACON Estrut. Mater., vol. 16, no. 5, e16505, 2023

5/15

$$d_{experiment} = 1 - w_{elastic}/w_{experiment} \tag{21}$$

being w the deflection.
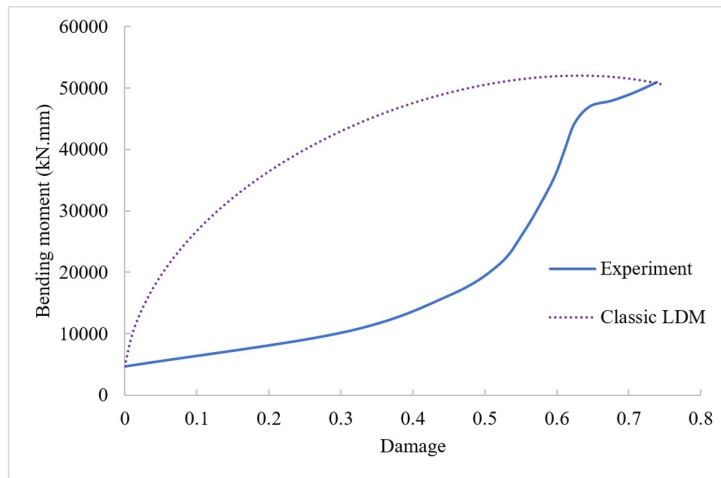
Figure 4. Experimental bending moment vs. damage results from Álvares [31] compared with the classic LDM [26].

4 PROPOSED MODEL

The proposed formulation for calculating deflection is derived by inserting an effective moment of inertia I_{eff}, calculated according to Equation 2.

$$I_{eff} = I_g(1 - d) \tag{22}$$

However, differently from classic LDM, the proposed approach must present a bending moment vs. damage relation closer to experimental analysis in order to evaluate deflected beams in service.

Therefore, an exponential expression for the acting moment (M_a) is proposed i.e.

$$M_a = M_{cr} + (M_u - M_{cr}) \exp\left[-\left(I_g^2/I_{cr}^2\right)(1 - d/d_u)\right] \tag{23}$$

In classic LDM, d_u is numerically obtained by solving the system composed by Equations 19, 20. However, for practical applications, the following equation is a satisfactory approximation for d_u:

$$d_u = 0.5\left[d_p + 0.5(d_p + 1)\right] \tag{24}$$

where d_p is the plastic damage i.e. the damage when the reinforcement is about to yield.

Again, for practical applications, a reasonable approximation for d_p is:

$$d_p = 1 - I_{cr}/I_g \tag{25}$$

Therefore, by substituting Equations 24, 25 in Equation 23, d is the acting damage on the structural element is calculated according to Equation 26:

$$d = \left\{\ln[(M_a - M_{cr})/(M_u - M_{cr})] + I_g^2/I_{cr}^2\right\}\left(1 - 3I_{cr}/4I_g\right) I_{cr}^2/I_g^2 \tag{26}$$

where M_a is the acting moment, M_{cr} is the first cracking moment, M_u is the ultimate moment.

Rev. IBRACON Estrut. Mater., vol. 16, no. 5, e16505, 2023

6/15
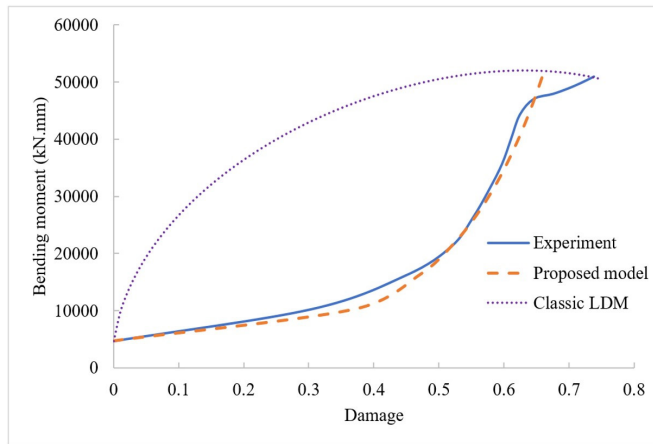
Figure 5. Experimental bending moment vs. damage results from Álvares [31] compared with the classic LDM [26] and the proposed model.

5 RESULTS

To analyse the proposed model, literature data including beams with different dimensions, strengths, elasticity modules and reinforcement rates were used. The selected works provided the results of the increase in displacements with the applied loads, in addition to the necessary information for the application in both Proposed and Branson's models.

As an illustration, the experimental results of Álvares [31] and Fernandes [32] are shown in Figures 4 and 5, respectively. The application of the Proposed Model to such experiments provided a satisfactory behaviour (Figures 4 and 5).
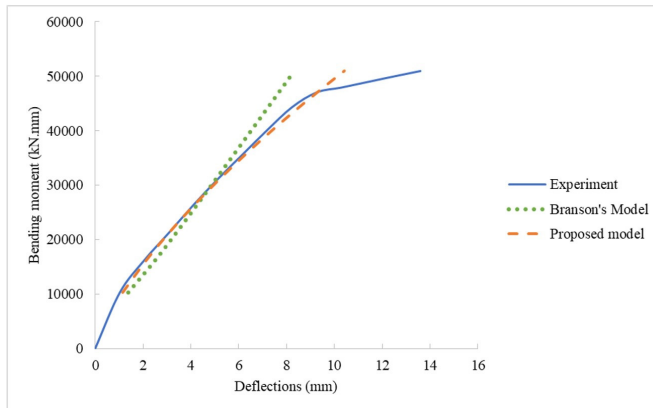
Figure 6. Experimental results from Álvares [31] compared with Branson's model and the proposed model.
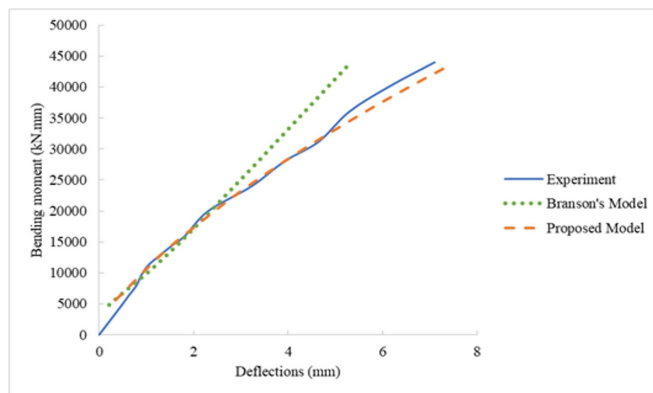
Figure 7. Experimental results from Fernandes [32] compared with Branson's model and the proposed model.

Subsequently, the Proposed Model was compared with 72 experiments by several authors [33]–[41] that were brought together in the work of Melo [42]. These works provided the necessary properties for the calculation of the deflection by the methods studied in this work, in addition to the values of force versus displacement for service situation. The properties of beams are depicted in Appendix A (Tables A1 to A6).

In order to analyse these results, it was necessary to group them according to the compressive strength (f_c) and the reinforcement rate. Figures 6 and 7 show the results of the deflections of reinforced concrete beams with f_c between 20 and 50 MPa. Figures 8, 9, 10, 11, 12 and 13, show the results of the deflections of the reinforced concrete beams with f_c between 50 and 90 MPa.

To statistically compare the Proposed Model results with the responses provided by the experiments considered and by Branson's Model, the most appropriate multiple comparison tests were used for each situation, according to the normality and homoscedasticity of the data considered. The normality test employed was the Shapiro-Wilk one, considering normality when the p-value was greater than the 5% significance level. In relation to the homoscedasticity test, both Bartlett and Levene were used. The Bartlett test was applied when the sample had a normal distribution; otherwise, Levene test was adopted. The studied samples met the conditions of homoscedasticity when the p-value was above the 5% significance level.
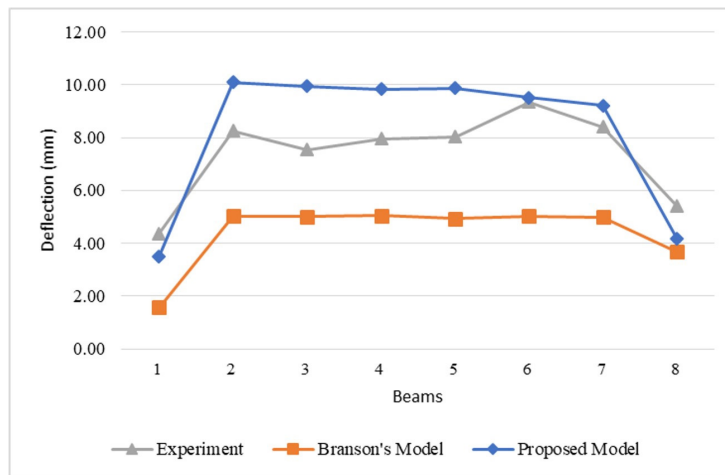
Figure 8. Beams with reinforcement rate from 0 to 1%.
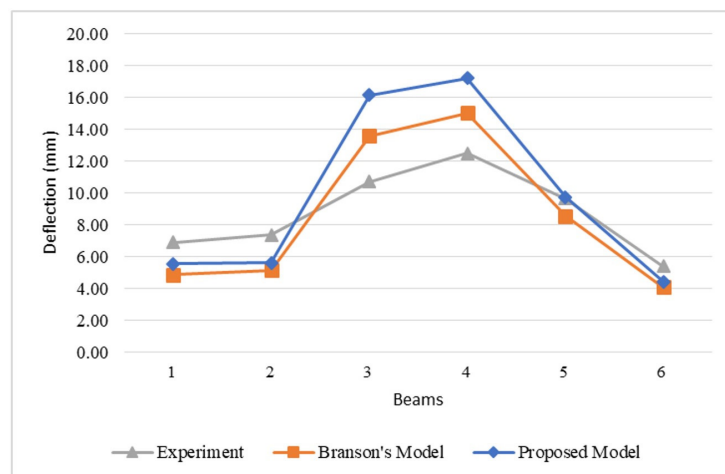
Figure 9. Beams with reinforcement rate from 1 to 2%.
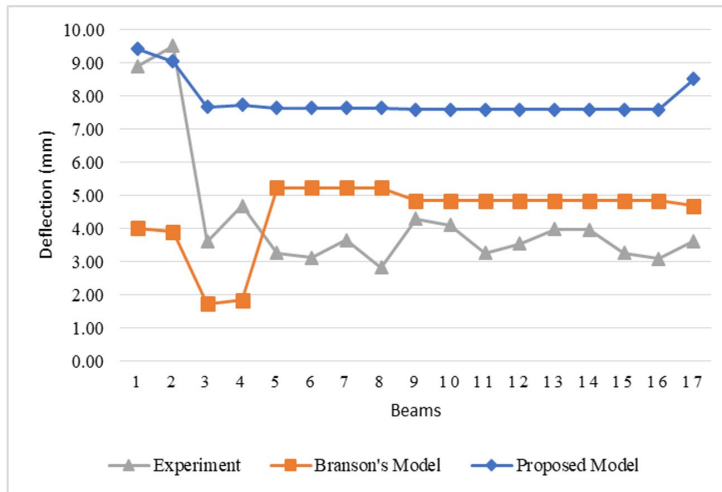
Figure 10. Beams with reinforcement rate from 0 to 1%.
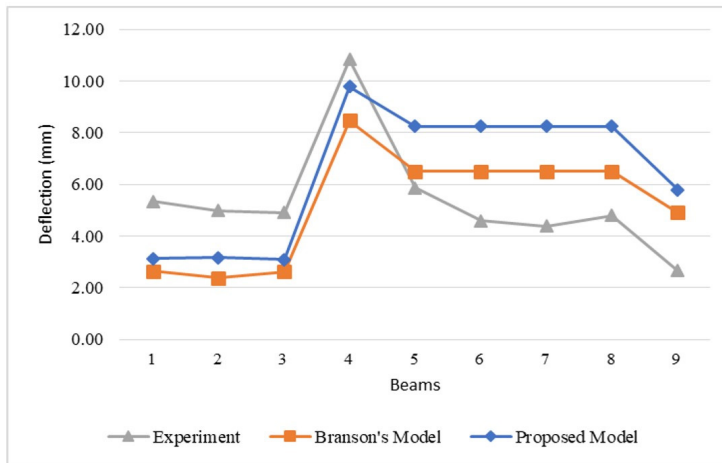
Figure 11. Beams with reinforcement rate from 1 to 2%.
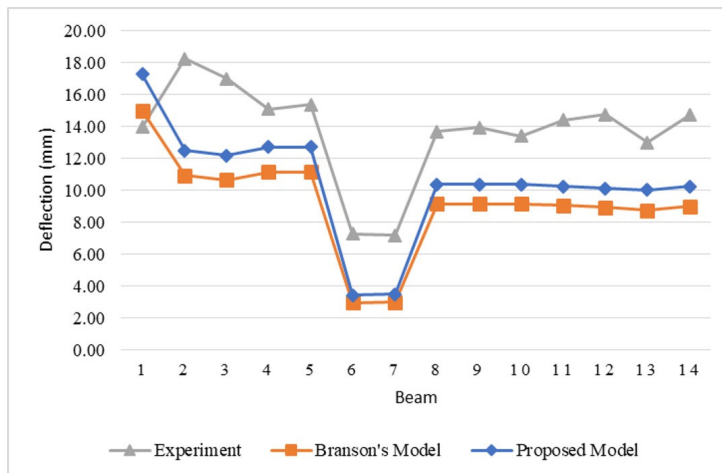
Figure 12. Beams with reinforcement rate from 2 to 3%.

Rev. IBRACON Estrut. Mater., vol. 16, no. 5, e16505, 2023

9/15
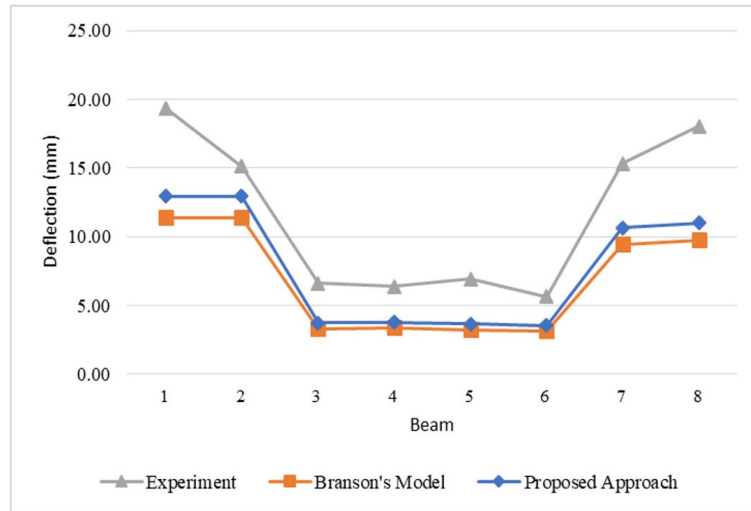
Figure 13. Beams with reinforcement rate greater than 3%.

Regarding the equivalence test between groups, ANOVA test was applied when the conditions of normality and homoscedasticity were satisfied, with the identification of difference between groups by the Fisher-Bonferroni test, considering that for p-value greater than 0.05 no difference was found. When the hypotheses related to the ANOVA test were not verified, the non-parametrical Kruskal-Wallis test was used, adopting a significance level of 5%.

To easier the analysis, the results were divided according to the concrete resistance f_c and the reinforcement rate, as specified in Tables 1 to 3.

Table 1. Beams analysis with f_c from 20 to 50 MPa with reinforcement rate from 0 to 1% and reinforcement rate from 1% to 2%.

f_c (MPa)	Reinforcement ratio (%)	Group	N° of beams by group	Normality (p-value)	Homoscedasticity (p-value)	Comparison of means/ medians	Difference	Difference (p-value)
20 – 50	0 – 1	Experiment	8	0.1267	0.5244	Experiment - Branson	No	0.0161
		Proposed		< 0.001		Branson - Proposed	Yes	
		Branson		< 0.001		Experiment - Proposed	No	
	1 – 2	Experiment	6	0.8571	0.2934	Experiment - Branson	No	0.8796
		Proposed		0.1235		Branson - Proposed	No	
		Branson		0.1631		Experiment - Proposed	No	

Table 2. Beams analysis with f_c from 50 to 90 MPa with reinforcement rate from 0 to 1% and reinforcement rate from 1% to 2%.

f_c (MPa)	Reinforcement ratio (%)	Group	N° of beams by group	Normality (p-value)	Homoscedasticity (p-value)	Comparison of means/ medians	Difference	Difference (p-value)
50 – 90	0 – 1	Experiment	17	< 0.001	0.2051	Experiment - Branson	No	< 0.001
		Proposed		< 0.001		Branson - Proposed	Yes	
		Branson		< 0.001		Experiment - Proposed	Yes	
	1 – 2	Experiment	21	0.0601	0.4582	Experiment - Branson	No	0.3215
		Proposed		0.0656		Branson - Proposed	No	
		Branson		0.0761		Experiment - Proposed	No	

A. A. F. Souza, W. S. Assis, and D. L. N. F. Amorim

Table 3. Beams analysis with f_c from 50 to 90 MPa with reinforcement rate from 2% to 3% and reinforcement rate greater than 3%.

f_c (MPa)	Reinforce-ment ratio (%)	Group	N° of beams by group	Normality (p-value)	Homoscedasticity (p-value)	Comparison of means/ medians	Difference	Difference (p-value)
50 – 90	2 – 3	Experiment	12	0.1067	0.9018	Experiment - Branson	Yes	< 0.001
		Proposed		0.0014		Branson - Proposed	No	
		Branson		0.0020		Experiment - Proposed	Yes	
	Greater than 3	Experiment	8	0.0499	0.0298	Experiment - Branson	No	0.1023
		Proposed		0.0104		Branson - Proposed	No	
		Branson		< 0,001		Experiment - Proposed	No	

According to the results obtained by the statistical analysis presented in Tables 1 to 3, it is possible to verify that:

• For f_c from 20 to 50 MPa and rates from the studied reinforcement, the statistical tests applied to the samples

• showed not only equivalent variance but also equal mean values between deflection obtained by either the experiments or the proposed model, derived from TDC. For reinforcement rates from 1% to 2%, it was also found that the normal distribution is associated with the results of the experimental deflections and the proposed formulation forecast.

• For f_c from 20 to 50 MPa and rates from the studied reinforcement, the statistical tests applied to the samples showed that the average deflection provided by the proposed model and Branson's model are equivalent, with adherence to the respective experimental results averages.

• For f_c from 50 to 90 MPa and reinforcement rates from 1% to 2% and greater than 3%, statistical tests applied to the samples showed not only equivalent variance values but also equal mean values between deflection obtained by either the experiments or the proposed model. At these reinforcement rates, it was also found that the average deflection values provided by both proposed and Branson models are equivalent, with adherence to the respective experimental results means.

• For the f_c in the range of 50 to 90 MPa, for reinforcement rates from 0 to 1%, the statistical tests applied to the samples showed the equality of the medians of the deflection values obtained by the experiments and the Branson's Model, both being different medians that obtained through the proposed formulation. However, it should be noted that, for these rates, the non-normality of the data for all groups was observed and the difference in the variance of the experimental results in relation to the variance of the values from the Branson's Model and the proposed formulation.

6 CONCLUSIONS

The main objective of this work was to propose an effective moment of inertia for the calculation of deflection in reinforced concrete beams, using the formulations of the Lumped Damage Mechanics as a basis, and to evaluate the proposed calculation model, comparing it with experimental results and with the Branson's Model.

The Proposed Model presented a satisfactory behaviour when the evolution of the deflection was verified and compared with the experimental works of Álvares [31] and Fernandes [32].

The statistical tests used showed that the reinforced concrete beams with the f_c in the range of 20 to 50 MPa, there is an equivalence of variance and equality of means between the Proposed Model and the experimental response, both in the reinforcement rates between 0 and 1% as well as the reinforcement rate of 1% to 2%. In this range of f_c, the Proposed Model also proved to be equivalent to the Branson's Model.

In the f_c range between 50 and 90 MPa and reinforcement rate from 0 to 1%, the statistical tests showed the equality of the medians between the deflection values of the experiment and the Branson's Model, but both are different from the median of the Proposed Model. In this group of beams the non-normality of the data and difference in variance between the experiment and the calculation methods studied were also verified.

Through the study, it was possible to verify that the application of the results of the Proposed Model provides a good approximation of the experimental response, equivalent to that provided by the Branson's Model in most of the investigated scenarios.

ACKNOWLEDGEMENTS

REFERENCES FORMATS

[1] D. E. Branson, *Instantaneous and Time-dependent Deflections of Simple and Continuous Reinforced Concrete Beams*, (HPR Report 7, pp. 1-78). College Park, MD, USA: Alabama Highway Department, Bureau of Public Roads, 1963.

[2] D. E. Branson, *Deformation of Concrete Structures*, New York, NY, USA: McGraw-Hill, 1977.

[3] ACI Committee 318, *Building code requirements for structural concrete*, ACI 318-19, 2019.

[4] Canadian Standards Association, *Design of Concrete Structures*, CSA A23.3, 2019.

[5] Associação Brasileira de Normas Técnicas, *Design of Concrete Structures – Procedure*, NBR 6118, 2014.

[6] Standards Australia, *Australian Standard for Concrete Structures*, AS3600, 2018.

[7] E. G. Nawy and G. E. Neuworth, "Fiberglass reinforced concrete slabs and beams," *J. Struct. Div.*, vol. 103, no. 2, pp. 421–440, 1977, http://dx.doi.org/10.1061/JSDEAG.0004559.

[8] C. W. Dolan, "Prestressed concrete using Kevlar reinforced tendons," Ph.D. thesis, Cornell Univ., New York, NY, 1989.

[9] A. Ghali, "Deflection of reinforced concrete members: a critical review," *ACI Struct. J.*, vol. 90, no. 4, pp. 364–373, 1993.

[10] H. A. Toutanji and M. Saafi, "Flexural behaviour of concrete beams," *J. Compos. Struct.*, vol. 2, no. 1, pp. 7–16, 2000., http://dx.doi.org/10.1051/e3sconf/202234701003.

[11] A. Ghali, T. Hall, and W. Bobey, "Minimum thickness of concrete members reinforced with fibre reinforced polymer bars," *Can. J. Civ. Eng.*, vol. 28, no. 4, pp. 583–592, 2001, http://dx.doi.org/10.1139/l01-021.

[12] H. Toutanji and Y. Deng, "Deflection and crack-width prediction of concrete beams reinforced with glass FRP rods," *Constr. Build. Mater.*, vol. 17, pp. 69–74, 2003, http://dx.doi.org/10.1016/S0950-0618(02)00094-6.

[13] H. A. Rasheed, R. Nayal, and H. Melhem, "Response prediction of concrete beams reinforced with FRP bars," *J. Compos. Struct.*, vol. 65, no. 2, pp. 193–204, 2004, http://dx.doi.org/10.1016/j.compstruct.2003.10.016.

[14] P. H. Bischoff, "Reevaluation of deflection prediction for concrete beams reinforced with steel and fiber reinforced polymer bars," *J. Struct. Eng.*, vol. 131, no. 5, pp. 752–767, 2005, http://dx.doi.org/10.1061/(ASCE)0733-9445(2005)131:5(752).

[15] P. H. Bischoff, "Deflection calculation of FRP reinforced concrete beams based on modifications to the existing Branson equation," *J. Compos. Constr.*, vol. 11, no. 1, pp. 4–14, 2007, http://dx.doi.org/10.1061/(ASCE)1090-0268(2007)11:1(4).

[16] H. Said, "Deflection prediction for FRP-strengthened concrete beams," *J. Compos. Constr.*, vol. 14, no. 2, pp. 244–248, 2010, http://dx.doi.org/10.1061/(ASCE)CC.1943-5614.0000069.

[17] P. H. Bischoff and S. P. Gross, "Equivalent moment of inertia based on integration of curvature," *J. Compos. Constr.*, vol. 15, no. 3, pp. 263–273, 2011, http://dx.doi.org/10.1061/(ASCE)CC.1943-5614.0000164.

[18] H. M. Mohammed and R. Masmoudi, "Deflection prediction of steel and FRP-reinforced concrete filled FRP tube beams," *J. Compos. Constr.*, vol. 15, no. 3, pp. 462–472, 2011, http://dx.doi.org/10.1061/(ASCE)CC.1943-5614.0000172.

[19] C. Dundar, A. K. Tanrikulu, and R. J. Frosch, "Prediction of load-deflection behavior of multi-span FRP and steel reinforced concrete beams," *Comp. Struct.*, vol. 132, pp. 680–693, 2015, http://dx.doi.org/10.1016/j.compstruct.2015.06.018.

[20] T. Lou and T. L. Karavasilis, "Time-dependent assessment and deflection prediction of prestressed concrete beams with unbonded CFRP tendons," *Compos. Struct.*, vol. 194, pp. 263–276, 2018, http://dx.doi.org/10.1016/j.compstruct.2018.04.013.

[21] V. Gribniak, V. Cervenka, and G. Kaklauskas, "Deflection prediction of reinforced concrete beams by design codes and computer simulation," *Eng. Struct.*, vol. 56, pp. 2175–2186, 2013, http://dx.doi.org/10.1016/j.engstruct.2013.08.045.

[22] Comité Européen de Normalisation, *Design of Concrete Structures – Part 1: General Rules and Rules for Buildings*, Eurocode 2, 2004.

[23] Concrete and Reinforced Concrete Research and Technology Institute, *Concrete and Reinforced Concrete Structures Without Pre-stressing*, SP 52-101-2003, 2006.

[24] D. Broek, *Elementary Engineering Fracture Mechanics*, Dordrecht, Netherlands: Martinus Nijhoff Publishers, 1984.

[25] J. Lemaitre and J. L. Chaboche *Mécaniques des matériaux solides*, Paris, France: Dunod, 1985.

[26] J. Flórez-López, M. E. Marante, and R. Picón *Fracture and damage mechanics for structural engineering frames: state of the art and industrial applications*, Hershey, Pennsylvania, USA: IGI Global, 2015, https://doi.org/10.4018/978-1-4666-6379-4

[27] Committee 435 Chairman, et al., "Deflections of continuous concrete beams", *J. Aci.*, vol. 70, no. 12, pp. 781–787, Dec. 1973.

[28] H. G. Powell, "Theory for nonlinear elastic structures," *J. Struct. Div.*, vol. 95, no. 12, pp. 2687–2701, 1969.

[29] A. Cipollina, A. López-Inojosa, and J. Flórez-López, "A simplified damage mechanics approach to nonlinear analysis of frames," *Comput. Struc.*, vol. 54, pp. 1113–1126, 1995, http://dx.doi.org/10.1016/0045-7949(94)00394-I.

[30] D. L. N. F. Amorim, S. P. B. Proença, and J. Flórez-López, "Simplified modeling of cracking in concrete: application in tunnel linings," *Eng. Struct.*, vol. 70, pp. 23–35, 2014, http://dx.doi.org/10.1016/j.engstruct.2014.03.031.

[31] M. S. Álvares, "Study of a damage model for concrete: formulation, parametric identification and application using the finite element method," M.S. thesis, Dept. Struct. Eng, Univ. São Paulo, São Carlos, SP, 1993.

[32] S. A. Fernandes, "Concrete deformations and behavior of beams analysis subjected to simple bending," M.S. thesis, Dept. Struct. Eng, Univ. São Paulo, São Carlos, SP, 1996.

[33] S. A. Ashour, F. F. Wafa, and M. I. Kamal, "Effect of the concrete compressive strength and tensile reinforcement ratio on the flexural behavior of fibrous concrete beams," *Eng. Struct.*, vol. 22, no. 9, pp. 1145–1158, 2000., http://dx.doi.org/10.1016/S0141-0296(99)00052-8.

[34] L. F. A. Bernardo and S. M. R. Lopes, "Neutral axis depth versus flexural ductility in high-strength concrete beams," *J. Struct. Eng.*, vol. 130, no. 3, pp. 452–459, 2004, http://dx.doi.org/10.1061/(ASCE)0733-9445(2004)130:3(452).

[35] M. A. Rashid and M. A. Mansur, "Reinforced high-strength concrete beams in flexure," *Struct. J.*, vol. 102, no. 3, pp. 462–471, 2005, http://dx.doi.org/10.14359/14418.

[36] A. A. Maghsoudi and H. A. Bengar, "Flexural ductility of HSC members," *Struct. Eng. Mech.*, vol. 24, no. 2, pp. 195–212, 2006, http://dx.doi.org/10.12989/SEM.2006.24.2.195.

[37] V. Gribniak, "Shrinkage influence on tension-stiffening of concrete structures," Ph.D. thesis, Vilnius Gediminas Technical Univ., Vilnius, 2009, https://doi.org/10.13140/RG.2.1.4869.5122.

[38] T. Elrakib, "Performance evaluation of HSC beams with low flexural reinforcement," *HBRC J.*, vol. 9, no. 1, pp. 49–59, 2013, http://dx.doi.org/10.1016/j.hbrcj.2012.12.006.

[39] Y. Sharifi, "Structural performance of self-consolidating concrete used in reinforced concrete beams," *KSCE J. Civ. Eng.*, vol. 16, no. 4, pp. 618–626, 2012, http://dx.doi.org/10.1007/s12205-012-1517-5.

[40] R. C. B. Silva, "Behavior of concrete beams armed with CFRP and GFRP bars for transport infrastructure," M.S. dissertation, Military Inst. Engineering, Rio de Janeiro, RJ, 2014.

[41] M. I. Mousa, "Flexural behaviour and ductility of high strength concrete (HSC) beams with tension lap splice," *Alex. Eng. J.*, vol. 54, no. 3, pp. 551–563, 2015, http://dx.doi.org/10.1016/j.aej.2015.03.032.

[42] L. M. A. Melo, "Evaluation of displacements in concrete beams with steel reinforcement and fiber reinforced polymers," M.S. dissertation, Fed. Univ. Alagoas, Maceió, AL, 2019.

Author contributions: AAFS: conceptualization, data curation, formal analysis, writing; WSA: conceptualization, supervision, methodology, formal analysis, writing; DLNFA: conceptualization, supervision, methodology, formal analysis, writing.

Rev. IBRACON Estrut. Mater., vol. 16, no. 5, e16505, 2023

13/15

APPENDIX A

Table A1. Beams data with f_c from 20MPa to 50MPa and reinforcement rate from 0 a 1%.

Authors	Beam	b (mm)	h (mm)	Service load (kN)	f_c (MPa)	ρ (%)	Experimental deflection (mm)	Proposed Model (mm)	Branson's Model (mm)
Sharifi [39]	SCCB1	200	300	13.27	31.60	0.51	4.38	3.52	1.59
Gribniak [37]	S-1	280	300	65.68	47.30	0.37	8.25	10.10	5.03
	S-1R	281	299	65.68	47.30	0.37	7.53	9.95	5.02
	S-2	280	300	67.20	48.70	0.37	7.96	9.83	5.05
	S-2R	282	300	66.46	48.20	0.37	8.02	9.86	4.93
	S-3	277	300	61.74	41.10	0.36	9.35	9.52	5.03
	S-3R	281	299	62.69	41.20	0.36	8.41	9.21	4.98
Silva [40]	V25A Sub	150	150	26.30	27.40	0.70	5.40	4.17	3.68

Table A2. Beams data with f_c from 20MPa to 50MPa and reinforcement rate from 1% to 2%.

Author	Beam	b (mm)	h (mm)	Service load (kN)	f_c (MPa)	ρ (%)	Experimental deflection (mm)	Proposed Model (mm)	Branson's Model (mm)
Sharifi [39]	SCCB2	200	300	33.19	32.84	1.05	6.90	5.54	4.86
	SCCB3	200	300	43.72	28.84	1.44	7.35	5.62	5.15
Ashour et al. [33]	B-N2	200	250	53.18	48.61	1.02	10.70	16.15	13.56
	B-N3	200	250	76.19	48.61	1.53	12.47	17.21	15.00
Rashid and Mansur [35]	A211	250	400	324.39	42.80	1.96	9.64	9.73	8.55
Silva [40]	V25A Super	150	150	37.00	35.77	1.40	5.40	4.41	4.08

Table A3. Beams data with f_c from 50MPa to 90MPa and reinforcement rate from 0 to 1%.

Authors	Beam	b (mm)	h (mm)	Service load (kN)	f_c (MPa)	ρ (%)	Experimental deflection (mm)	Proposed Model (mm)	Branson's Model (mm)
Gribniak [37]	S-4	277	300	62.21	54.20	0.36	8.90	9.41	4.01
	S-4R	283	301	63.62	54.20	0.36	9.50	9.04	3.89
Elrakib [38]	B503	250	400	61.50	52.00	0.30	3.59	7.66	1.72
	B753	250	400	77.51	73.00	0.38	4.67	7.73	1.83
Mousa [41]	A1	150	200	37.84	55.00	0.75	3.26	7.64	5.22
	A2	150	200	37.84	55.00	0.75	3.11	7.64	5.22
	A3	150	200	37.84	55.00	0.75	3.64	7.64	5.22
	A4	150	200	37.84	55.00	0.75	2.82	7.64	5.22
	B1	150	200	38.13	65.00	0.75	4.29	7.59	4.83
	B2	150	200	38.13	65.00	0.75	4.09	7.59	4.83
	B3	150	200	38.13	65.00	0.75	3.25	7.59	4.83
	B4	150	200	38.13	65.00	0.75	3.53	7.59	4.83
	B5	150	200	38.13	65.00	0.75	3.97	7.59	4.83
	B6	150	200	38.13	65.00	0.75	3.96	7.59	4.83
	B7	150	200	38.13	65.00	0.75	3.26	7.59	4.83
	B8	150	200	38.13	65.00	0.75	3.09	7.59	4.83
	B14	150	200	34.59	65.00	0.75	3.61	8.50	4.68

Rev. IBRACON Estrut. Mater., vol. 16, no. 5, e16505, 2023

14/15

Table A4. Beams data with f_c from 50MPa to 90MPa and reinforcement rate from 1% to 2%.

Authors	Beam	b (mm)	h (mm)	Service load (kN)	f_c (MPa)	ρ (%)	Experimental deflection (mm)	Proposed Model (mm)	Branson's Model (mm)
Ashour et al. [33]	B-M2	200	250	55.00	78.50	1.02	10.73	15.42	11.89
	B-M3	200	250	80.29	78.50	1.53	13.14	16.46	13.92
Bernardo and Lopes [34]	B1	120	270	75.10	79.20	1.40	12.67	11.04	9.24
	B2	120	270	111.05	78.90	1.94	14.13	12.25	10.34
	B3	120	270	110.99	78.50	1.94	14.55	12.25	10.34
	C1	120	270	111.60	82.90	1.94	16.34	12.25	10.32
	C2	120	270	111.73	83.90	1.94	17.35	12.25	10.32
	D1	120	270	75.79	88.00	1.24	12.79	11.08	9.19
	A1	120	270	74.13	62.90	1.40	10.16	11.02	9.35
	A2	120	270	106.07	64.90	1.94	12.15	12.54	10.62
	A3	120	270	105.90	64.10	1.94	10.95	12.54	10.62
Maghsoudi and Bengar [36]	B2	200	300	187.73	70.50	1.05	5.75	3.15	2.29
	B3	200	300	277.85	70.80	1.70	5.33	3.13	2.63
	BC2	200	300	186.81	63.48	1.05	4.98	3.16	2.37
	BC3	200	300	275.61	63.21	1.70	4.90	3.09	2.61
Rashid and Mansur [35]	B211a	250	400	346.29	73.60	1.96	10.83	9.78	8.48
Mousa [41]	B9	150	200	64.73	65.00	1.34	5.86	8.24	6.50
	B10	150	200	64.73	65.00	1.34	4.59	8.24	6.50
	B11	150	200	64.73	65.00	1.34	4.37	8.24	6.50
	B12	150	200	64.73	65.00	1.34	4.80	8.24	6.50
Silva [40]	V50A Super	150	150	48.99	53.90	1.40	2.65	5.78	4.90

Table A5. Beams data with f_c from 50MPa to 90MPa and reinforcement rate from 2% to 3%.

Authors	Beam	b (mm)	h (mm)	Service load (kN)	f_c (MPa)	ρ (%)	Experimental deflection (mm)	Proposed Model (mm)	Branson's Model (mm)
Ashour et al. [33]	B-M4	200	250	104.09	78.50	2.04	13.94	17.28	14.98
Bernardo and Lopes [34]	C3	120	270	137.18	83.60	2.48	18.25	12.49	10.91
	C4	120	270	140.37	83.40	2.48	16.99	12.17	10.65
	A4	120	270	128.27	63.20	2.48	15.07	12.69	11.14
	A5	120	270	128.95	65.10	2.48	15.35	12.72	11.15
Maghsoudi and Bengar [36]	BC4	200	300	359.41	71.45	2.09	7.26	3.42	2.94
	B4	200	300	360.01	72.80	2.09	7.18	3.48	2.99
Rashid and Mansur [35]	B311	250	400	495.86	72.80	2.95	13.67	10.35	9.13
	B312	250	400	495.86	72.80	2.95	13.92	10.35	9.13
	B313	250	400	495.86	72.80	2.95	13.40	10.35	9.13
	B321	250	400	499.63	77.00	2.95	14.39	10.25	9.03
	B331	250	400	495.86	72.80	2.95	14.73	10.12	8.93
	C211	250	400	415.89	85.60	2.37	12.98	10.01	8.73
	C311	250	400	480.51	88.10	2.77	14.70	10.24	8.99

Table A6. Beams data with f_c from 50MPa to 90MPa and reinforcement rate greater than 3%.

Authors	Beam	b (mm)	h (mm)	Service load (kN)	f_c (MPa)	ρ (%)	Experimental deflection (mm)	Proposed Model (mm)	Branson's Model (mm)
Bernardo and Lopes [34]	D2	120	270	169.34	85.80	3.18	19.35	12.95	11.39
	D3	120	270	169.41	86.00	3.18	15.11	12.95	11.39
Maghsoudi and Bengar [36]	BC5	200	300	668.36	72.98	4.11	6.62	3.72	3.30
	B5	200	300	664.90	71.00	4.11	6.38	3.79	3.37
	BC6	200	300	669.11	73.42	4.11	6.90	3.65	3.24
	BC7	200	300	668.36	72.98	4.11	5.63	3.54	3.14
Rashid and Mansur [35]	C411	250	400	598.96	85.60	3.57	15.30	10.67	9.44
	C511	250	400	707.01	88.10	4.33	18.04	11.01	9.77

IBRACON Structures and Materials Journal
Revista IBRACON de Estruturas e Materiais

ORIGINAL ARTICLE

Development of alkali-activated mortar from iron ore tailings

Desenvolvimento de argamassas álcali ativadas a partir de rejeito de barragem de minério de ferro

Keoma Defáveri do Carmo e Silva[a]
Fernanda Pereira da Fonseca Elói[b]
José Maria Franco de Carvalho[c]
Ricardo André Fiorotti Peixoto[b]
Guilherme Jorge Brigolini Silva[b]

[a]Universidade Federal de Lavras – UFLA, Laboratório de Pavimentação, Lavras, MG, Brasil
[b]Universidade Federal de Ouro Preto – UFOP, Laboratório de Materiais de Construção Civil, Ouro Preto, MG, Brasil
[c]Universidade Federal de Viçosa – UFV, Laboratório de Materiais Compósitos, Viçosa, MG, Brasil

Abstract: In this work, the authors explore the use of iron ore tailings (IOT) from a tailings dam as a recycled precursor material in producing a composite through alkali-activation technology. Two different composite types were evaluated: paste specimens made using only IOT and an alkaline activator, and mortar specimens using the same binder and quartz sand as fine aggregate. Three different grinding times were applied to activate the IOT; a NaOH solution was used as the alkaline activator with three molar concentrations (8, 10, and 12 mol/l); and, thermal curing of 100°C for 7 days was applied. These parameters were obtained by a hard-mini-test (HMT) experimental procedure. The physico-mechanical properties of the composites were obtained, and the results showed a compressive strength up to 110.0 MPa, which is like high-performance Portland cement concretes and alkali-activated cements derived from well-established precursors reported in the literature using thermal cure.

Keywords: alkali-activated, iron ore tailings, compressive strength, composite.

Resumo: Neste trabalho, os autores exploram o uso do rejeito de barragem de minério de ferro (RBMF), de uma barragem de rejeitos, como material precursor reciclado na produção de um compósito através da tecnologia de ativação alcalina. Dois compósitos diferentes foram avaliados: espécimes de pastas feitas usando somente RBMF e ativador alcalino, e espécimes de argamassa usando o mesmo aglomerante e areia como agregado miúdo. Três tempos de moagem diferentes foram aplicados para ativar o RBMF; uma solução de NaOH foi empregada como ativador alcalino com três concentrações molares (8, 10 e 12 mol/l); e cura térmica de 100ºC por 7 dias. Esses parâmetros iniciais foram obtidos através do procedimento experimental Endurecimento-Mini-Teste (EMC). As propriedades físico-mecânicas dos compósitos foram determinadas e os resultados mostraram uma resistência a compressão de até 110,0 MPa, que é compatível com concreto de cimento Portland de alto desempenho e cimentos álcali-ativados feitos a partir de precursores bem estabelecidos reportados na literatura usando cura térmica.

Palavras-chave: álcali-ativado, rejeito de barragem de minério de ferro, resistência à compressão, compósito.

1 INTRODUCTION

Alkali-activated cements can be defined as mineral polymer materials produced by the alkali activation of aluminosilicate materials. These materials belong to the same family of aluminosilicates as zeolites, although they are

essentially amorphous polymers or nanocrystals, unlike zeolites. The alkali activation occurs in a highly concentrated alkaline environment – yielded by a strong alkaline solution (e.g., potassium hydroxide or sodium hydroxide) and solid alkali activator (e.g., sodium metasilicate or sodium aluminate) – where the aluminosilicate starting material works as a precursor to the formation of a polymeric structure formed by interconnected Si-O-Al bonds. The starting materials dissolve in a high pH alkaline solution and the alkali-activated compounds are precipitated. An empirical formula for these mineral polymers was formulated as $M_n[-(SiO_2)_z-AlO_2]_n\cdot wH_2O$, where z is 1, 2, or 3; M is an alkali cation as sodium or potassium, and n is the degree of polymerization. Three polymeric structures could be recognized from the resultant type of chemical bonding: poly(sialate) (–Si–O–Al–O), poly(sialate-siloxo) (Si–O–Al–O–Si–O), and poly(sialate-disiloxo) (Si–O–Al–O–Si–O–Si–O–) [1]–[4].

A wide range of solid materials can be applied as precursor materials in alkali-activated production, for example, the bottom ash, rice husk, palm oil fuel ash, ground granulated blast furnace, metakaolin, fly ash, among others [5]–[8]. However, several studies have focused on reactive fly-ashes and metakaolin – well-established precursors [9]–[11]. The metakaolin-based alkali-activated have the disadvantage of extensive shrinkage and cracking, while some kinds of fly ash require heat treatment to achieve high early strength and faster setting time of the resultant alkali-activated pastes, as well as the dark appearance of pulverized fly ash can be an issue when used for building restoration [12], [13]. Furthermore, due to their limited availability, researchers have started to study the application of other residues such as mine tailings [14], [15].

The alkali activation of mine tailings is considered a feasible and alternative method for sustainable management and an interesting alternative to the well-established precursors. The recycling and valorization of mine tailings have been pointed out as one of the most effective strategies to minimize their tremendous volume and negative environmental impacts. Indeed, the alkali activation technology – among the recent sustainable management strategies – offers many advantages, such as (i) valorization of the volume of tailings in the construction industry, (ii) stabilization of polluted/inert mine tailings in the alkali-activated matrix, and (iii) reduction of greenhouse gas emissions generated using ordinary Portland cement (OPC) [16], [17].

In this context, there is a scarce number of studies using iron ore tailings (IOT) in the alkali-activated technology; and further, these tailings are generally applied as a blend or even as fine aggregate replacement in alkali-activated cement synthesized using the well-established precursors [18], [19]. On the other hand, using IOT in the construction industry is one way to produce green and sustainable products, as well as save landfill space and minimize the extraction of non-renewable materials [20]. Moreover, recent studies have shown that the IOT has interesting potential to produce several types of construction and building materials based on OPC – from sustainable paint to raw material to clinkerization [21]–[24].

The present paper focuses on the IOT use as a precursor material in formulating an alkali-activated based composite. Therefore, this paper aims to study the potential of IOT as a precursor material as well as the impact of a dispersed phase (fine aggregate). The first phase of the study focused on specifying the set of parameters for alkali activation, such as grinding time, concentration of the alkaline solution, and temperature of curing. In the second phase, the obtained parameters were used to produce paste and mortars specimens, and the resulting composites were submitted to physical and mechanical strength tests.

3 MATERIALS AND EXPERIMENTAL PROGRAM

3.1 Materials

The IOT used in this paper was collected from a tailings dam located in Minas Gerais State, Brazil. The quartz sand was used as fine aggregate for mortars production, and NaOH pellets with purity >98% were used for the alkaline activator production.

The chemical composition of the IOT and quartz sand, obtained by X-ray fluorescence (XRF), on a Panalytical Epson[3x] X-ray spectrometer, is shown in Table 1. The main elements of the IOT are iron oxide (48%), silica (40%), and alumina (8%). The quartz sand presented mostly silica (78%), alumina (10%), and iron oxide (6%). A long setting time is expected based on IOT's chemical composition and criteria of SiO_2/Al_2O_3 ratio [25]. It should be noted that IOT has a considerable amount of iron oxide, which could act in alkali-activated structure – the similarity of Fe^{3+} with Al^{3+} explains why Fe^{3+} ions act as network former occupying the tetrahedral sites [26]–[28].

Regarding the mineralogical compositions, the X-ray diffraction (XRD) of the IOT detected the presence of chamosite, chantalite, quartz, goethite, and hematite, while the quartz sand presented quartz, microcline, periclase, and biotite. The diffractogram of IOT and quartz sand showed no presence of a characteristic halo related to the amorphous phases, indicating a high crystallinity of these materials (Figure 1). The mineralogy of IOT is like those reported in the literature [29], [30] and its well-crystalline mineralogy could be associated with a non-reactivity or a low degree of reactivity [17].

K. D. C. Silva, F. P. F. Elói, J. M. F. Carvalho, R. A. F. Peixoto, and G. J. B. Silva

Table 1. Chemical composition of iron ore tailings and quartz sand.

Major elements as oxide	Raw materials	
	IOT (wt%)	Quartz sand (wt%)
MgO	0.17	-
Al_2O_3	8.78	10.80
SiO_2	40.09	78.50
P_2O_5	0.55	-
K_2O	0.29	1.70
CaO	0.14	0.70
TiO_2	0.13	1.00
Fe_2O_3	48.97	6.00
MnO	0.42	0.10
Al_2O_3/SiO_2 (wt%/wt%)	0.21	-
Si/Al (atomic ratio)	4.03	-
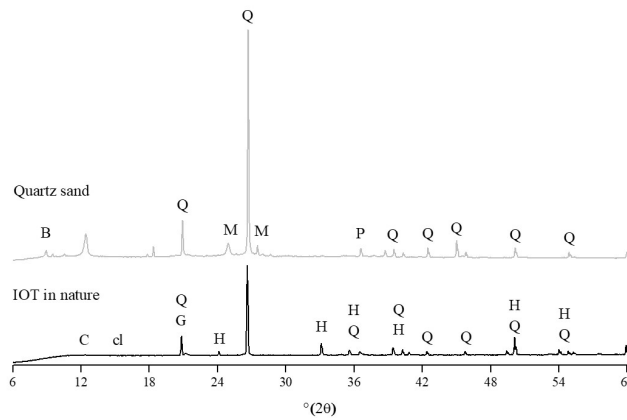
Figure 1. XRD pattern of the iron ore tailing in nature and quartz sand (B-biotite; C-chamosite; cl-chantalite; Q-quartz; G-goethite; H-hematite; M-microcline; P-periclase).

A sodium hydroxide solution was used as the alkaline activator and prepared in five molar concentrations: 6, 8, 10, 12, and 15 M (mol/L). It was prepared by dissolving NaOH pellets in deionized water.

Mortar composites were produced using the IOT and quartz sand as fine aggregate. The fine aggregate was particle separated by sieving in four equal fractions (2.4 – 1.2 mm; 1.2 – 0.6 mm; 0.6 – 0.3 mm; 0.3 – 0.15 mm) in accordance with ABNT NBR 7214 [31]. The fine aggregate was oven-dried at 105°C for 24 h to ensure a saturated surface dry (SSD) condition.

3.2. Experimental Program

As the IOT is not a common precursor or blend material to alkali-activated production, the experimental program was conducted in two phases – to understand the effects of IOT activation and to set the base parameters for the alkali-activated production. The experimental program and the tested parameters are schematized in Figure 2 and were based on the previous investigations [15], [32], [33].
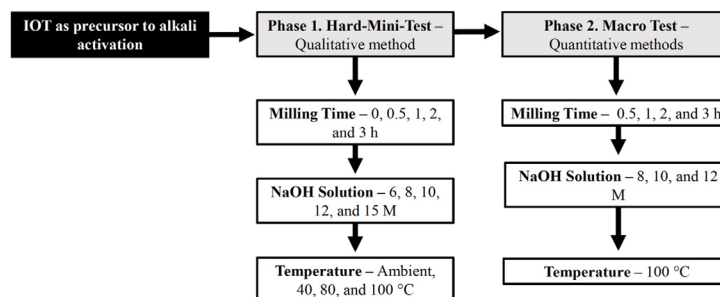
Figure 2. Schematic of the experimental program.

Two different types of mixture were tested: paste and mortar (see Table 2). The study of the pastes allowed the qualitative observation of reactivity and hardening properties of the IOT as a precursor material (Subtopic 3.2.1) and allowed to set base parameters. On the other hand, the study of the mortars allowed the quantitative experiment of the mechanical and microstructural properties of the composites produced using the IOT as the precursor material, as well as the effects of fine aggregate (Subtopic 3.2.2). An activator/precursor (A/P) ratio of 0.27 in mass was used for pastes and mortars to maintain suitable workability for all the investigated mixtures. A precursor/aggregate (P/Agg) ratio of 1:3, 1:2, and 1:0.5 was tested and, since the proportions of 1:3 and 1:2 did not show any cohesion in the flow table, was adopted the mix proportion of 1:0.5 was adopted for mortar specimens. Note that a paste with equal parameters (control) was prepared using only IOT and the alkaline activator to understand the role of fine aggregate on the composite properties.

Table 2. Mixture design of alkali-activated composites.

| Phase | Type | Mixture ID | Material | | A/P[c] (-) | P/Agg[d] (-) |
			IOT (g)	Quartz sand (g)		
1	Paste	P-6-0 to P-15-3[a,b]	20.00	-	0.27	-
2	Paste	P-8-1 to P-12-3[a,b]	1500.00	-	0.27	-
	Mortar	M-8-1 to M-12-3[*,b]	1100.00	550.00		1:0.5

[a] X-Y-W, where X denotes the type, Y denotes the concentration of the alkaline activator, and W denotes grinding time. [b] Including all specimens inside this range. [c] Activator/precursor. [d] Precursor/aggregate ratio.

3.2.1 Hard-Mini-Test (HMT)

In Phase 1, the hardening aspect of the IOT-based alkali-activated was qualitatively observed using a combination of three parameters: i) temperature of curing, ii) grinding time, and iii) concentration of alkaline activator. The thermal curing conditions were ambient temperature ($23 \pm 2°C$), 40, 80, and 100 °C. The IOT was ground in a horizontal ball mill (MARCONI instrument) for 30 min, 1, 2, and 3 h, and the particle size distribution of the milled IOT was determined using a laser diffraction analyzer (BETTERSIZE 2000 instrument). The effect of the concentration of the alkaline activator was observed using concentrations of 6, 8, 10, 12, and 15 M (mol/L). The combination of these three parameters produced 100 miniature specimens, which were used to evaluate the hardening properties of the IOT applying the alkaline activation method.

The preparation of the pastes began with the manually mixing of the IOT and alkaline activator for 5 min until complete homogenization. The resulting paste was then placed in a cylindrical polyvinyl chloride mold of diameter 20 mm and height 40 mm. Then the specimens were covered with plastic film to prevent evaporation during the curing process.

3.2.2 Macro test

In Phase 2, specific parameters were selected and used for quantitative tests in regular sizes (i.e., regular sizes according to specific standards). Based on the qualitative results observed in Phase 1 were chosen the set range of parameters: i) thermal curing of 100°C, ii) 1, 2, and 3 h of grinding, and iii) solution concentration of 8, 10, and 12 M. The applied criterion to choose the set of parameters will be discussed in detail in the following Subtopic 4.1.

In Phase 2, paste and mortar specimens were used. The preparation of these specimens was carried out in a laboratory mixer (JJ-5 Type), where first was homogenized the IOT and fine aggregate in a plastic container for 5 min. Then added the alkaline activator to the mixer bowl and solid materials (IOT and fine aggregate). Then, they were mixed for 3 min at low speed, paused for 30 s to scrap the mixer shovel, and mixed for 3 min at high speed. The fresh mortars were placed in stainless prismatic molds, with dimensions $40 \times 40 \times 160$ mm and covered with a glass plate to prevent evaporation during the curing process. The same preparation process was applied to the paste specimens, except homogenization of IOT and fine aggregate. Thermal curing was carried out in a laboratory oven, and the temperature of the alkaline activator at the mixing time was 23±2 °C.

Both pastes and mortars were cured for 7 days inside the molds at 100°C. After curing, their properties were determined, and each specimen was weighed and measured shortly before being tested. Results showed in this study represent the average of a specific number of tested specimens as better described hereafter. The physical and mechanical properties of the alkali-activated composites were obtained using the following methods:

i. The dimensional stability was determined by measuring the length of each specimen. The final dimensions of the specimens were measured using a caliper after the curing period. The average of the results of three specimens was taken for each mixture. The length change percentage was calculated using Equation 1.

$$Length\ Change\ (\%) = \left[\frac{(L1-L2)}{L1}\right].100\ (1)$$

where L1 is the reference length of the prismatic mold, and L2 is the length of the specimen, measured after the curing period.

ii. The nominal sample density was measured prior to the flexural strength test. The average value was calculated from three samples. The calculations were performed according to Equation 2.

$$Nominal\ sample\ density\ (g \cdot cm^{-3}) = \frac{W}{V}\ (2)$$

where W and V are the weight and volume of the sample after the curing period, respectively.

iii. The 7-days flexural and compressive strength tests were performed in accordance with NBR 13279 [34]. Three specimens of each mixture were used for the flexural strength test and six specimens of each mixture were used for the compressive strength test. The tests were carried out using a hydraulic press (EMIC DL 2000 instrument) with a load cell of 200 kN and a load increment of 0.25 MPa·s⁻¹.

iv. The water absorption tests were carried out in fragments collected from the specimens used in the mechanical tests and based on ASTM C67-07 [35]. The water absorption percentages were calculated using Equation 3.

$$Water\ absorption\ (\%) = \left[\frac{(W_{SSD}-W_d)}{W_d}\right].100\ (3)$$

where W_d is the dry weight of the sample and W_{SSD} is the weight of the sample after 48 h soaking in water (SSD condition).

4 RESULTS AND DISCUSSIONS

4.1 HMT characterization

The effect of grinding time on IOT particle fineness is shown in Figure 3. The grinding process yields a 56% reduction from 229.8 to 101.0 mm, considering the maximum size of the IOT. It can be observed that the IOT in nature shows a D90 of 172.9 mm, while the IOT ground for 30 min, 1, 2, and 3 h shows a D90 of 96.3, 76.6, 71.1, and 51.0 mm, respectively. As reported before, the mechanical properties of rice husk ash-based alkali activated depend on an array of factors, such as the particle size distribution of the precursor material. Moreover, the effect of particle size observed in fly ash-based alkali-activated is more pronounced at low temperatures and the reaction mechanism of early activation (i.e., nucleation and growth) does not alter with the change of particle fineness [36]. However, it is well stated that the fineness of the precursor materials leads to compact microstructure development and improved properties [37]–[39], which is confirmed in Subtopic 4.2 when analyzing the mechanical strength results.
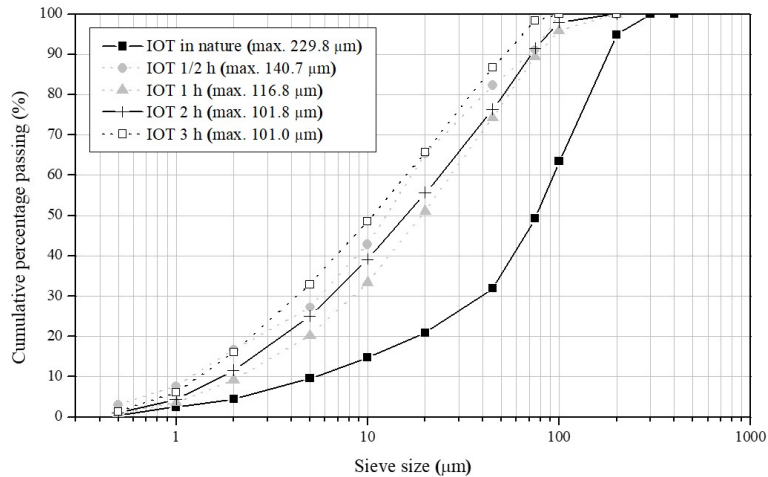
Rev. IBRACON Estrut. Mater., vol. 16, no. 5, e16506, 2023

5/12

Figure 3. Grading of iron ore tailings.

The qualitative results of the HMT tests are summarized in Table 3. It can be observed that the ambient temperature and temperature of 40 and 80°C were not sufficient for the alkaline activation of IOT – as the specimens not hardened at 7 days of curing. The concentration of alkaline activator of 6M was the unique parameter that showed at least one specimen that did not harden at 7 days at 100°C of thermal curing. These not-hardened specimens showed plastic deformation to the finger touch. Furthermore, it should be noted that the temperature degree was more effective than grinding time on the IOT reactivity and hardening property. It is notorious the effect of the thermal curing parameter, as previously observed by Ahmari and Zhang [15], Somna et al. [40] and Mehta and Siddique [41], since at high temperatures, there is an increase in dissolution of Si and Al oxides from the precursor material.

The alkaline activator concentration also had an interesting effect on the hardening properties. It was observed that the lowest alkaline concentration (i.e., 6 M) was not enough to harden, while a hardening effect was observed at all other alkaline concentrations – even at a lower temperature such as 80°C. It was found that the setting time increases as the alkaline concentration increases until an optimum limit, which could be related to the observed results [42], [43].

Based on these results, the temperature parameter of 100°C was chosen since all the specimens hardened for this condition. The molar concentration of 6M was excluded since some specimens did not harden. The concentration of 15M was also excluded since the results did not justify the high consumption. Furthermore, since not all specimens ground for 0 and 30 min have hardened, they were also excluded from Phase 2, thus resulting in the set of parameters presented in Subtopic 3.2.2.

Table 3. Hard-mini-test (HMT) results at 7 days of curing.

Mixture ID[a]	Temperature °C				Mixture ID	Temperature °C				Mixture ID	Temperature °C			
	22	40	80	100		22	40	80	100		22	40	80	100
P-6-0	X	X	X	X	P-10-0	X	X	X	✓	P-15-0	X	X	X	✓
P-6-1/2	X	X	X	X	P-10-1/2	X	X	X	✓	P-15-1/2	X	X	X	✓
P-6-1	X	X	X	✓	P-10-1	X	X	X	✓	P-15-1	X	X	X	✓
P-6-2	X	X	X	✓	P-10-2	X	X	X	✓	P-15-2	X	X	X	✓
P-6-3	X	X	X	✓	P-10-3	X	X	✓	✓	P-15-3	X	X	✓	✓
P-8-0	X	X	X	✓	P-12-0	X	X	X	✓					
P-8-1/2	X	X	X	✓	P-12-1/2	X	X	X	✓					
P-8-1	X	X	X	✓	P-12-1	X	X	X	✓					
P-8-2	X	X	✓	✓	P-12-2	X	X	X	✓					
P-8-3	X	X	✓	✓	P-12-3	X	X	✓	✓					

The abbreviation X means specimens that have not hardened. The abbreviation ✓ means specimens that have hardened. [a] P-Y-W, where P denotes paste, Y denotes the concentration of the alkaline activator, and W denotes grinding time

4.2. Macro Properties

4.2.1 Physical properties

Dimensional stability is usually considered a significant durability parameter for construction and building materials as it suggests the potential for cracking in the hardened state. The dimensional stability of the alkali-activated specimens, reported in terms of length change, is shown in Figure 4. It was observed that the paste specimens showed length change values between 3.1 and 7.2%, while the mortar specimens showed values between 1.0 and 2.7%. The addition of fine aggregate reduced the length change by over 35% when compared against the paste specimens. This reduction could be due to the fine aggregate particles that limit shrinkage by forming a supportive network with a fixed void volume. Overall, the results are significantly higher than those observed from alkali-activated materials derived from industrial wastes and metakaolin [40], [41].

The results also reveal that the grinding time is a key parameter in length change behavior. It should be noted that the length change is directly proportional to the grinding time in paste specimens. For example, it was noted that from 1 to 3h of grinding, the specimens showed an increase of 71% from 3.5 to 6.0%. On the other hand, for the mortar specimens, the increase in grinding time did not significantly alter the length change, suggesting that, in this case, the dimensional stability is governed by the fine aggregate supportive network.
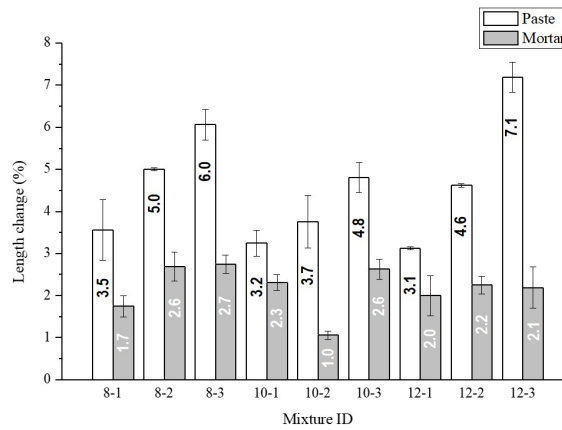
Figure 4. Length change of alkali-activated specimens.

Results of nominal sample density are shown in Figure 5. The paste specimens showed density values between 1.9 and 2.4 g·cm^{-3}, while the mortar specimen values were between 2.1 and 2.2 g·cm^{-3}. That is a non-surprising behavior given the shrinkage effect and the obtained values are in good agreement with values of clay bricks (between 1.8 to 2.0 g·cm^{-3}) [44] and strain hardening geopolymer composite (between 1.8 to 1.9 g·cm^{-3}) [45]. Meanwhile, paste and mortars density values were higher than fly ash-based alkali-activated, whose range was between 1.5 and 1.6 g·cm^{-3} [46].
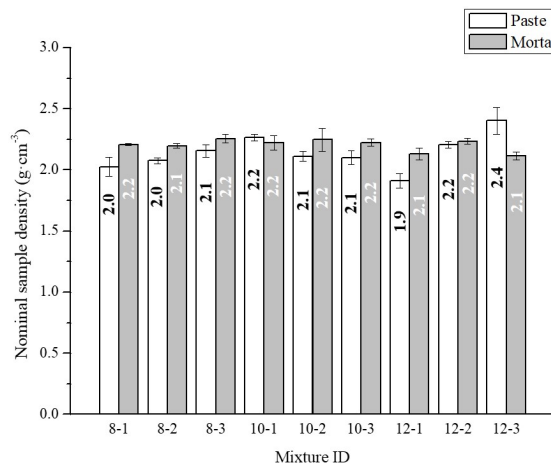
Figure 5. Nominal sample density of alkali-activated specimens.

4.2.2 Mechanical properties

The average 7-days flexural and compressive strengths for each mix are shown in Figure 6. The results showed that 7-days flexural strength for the paste specimens varied between 2.4 and 25.1 MPa, while mortars varied between 4.0 and 11.1 MPa. The addition of fine aggregate decreased the flexural strength, except for the specimens 12-1, 12-2, and 12-3 (12 M and 1, 2, and 3 h of grinding time, respectively). This result could be related to the increase in volume and porosity, as expected in composites with binder and dispersed phase (mortars), which are more sensitive to tensile stress. Moreover, the obtained results were slightly higher when compared to a few alkali-activated mortars based on metakaolin and fly-ash [47], [48].

Compressive strength is a key feature for construction and building materials and an interesting parameter to associate with alkaline activation – quality and amount of alkali-activated products. The 7-days compressive strength of the paste specimen values was between 19.0 and 110.0 MPa, while the mortars were between 26.0 and 67.0 MPa. In general, adding fine aggregates reduced the compressive strength by over 15%, except for the 75% increase observed in specimens 8-1. These results are like those reported by Tchakouté and Rüscher [49] and Hu et al. [50] for metakaolin- and fly ash-based alkali-activated, demonstrating the potential of IOT as a promising precursor material. Moreover, the higher mechanical performance of paste than mortars was also observed by Cristelo et al. [51], which probably was associated with differences in porosity and compaction.
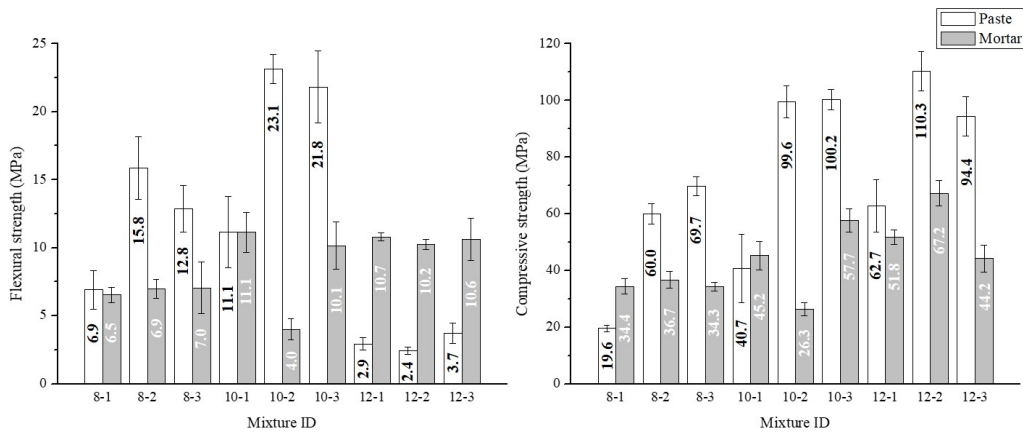

Figure 6. Mechanical properties of alkali-activated specimens at 7 days of curing.

The effect of the concentration of the alkaline activator on the compressive strength was important for paste and mortar specimens. Hence, as the molar concentration increased to the optimal content, the compressive strength of specimens also increased, reaching a maximum value. This effect may be related to the rate and degree of alkaline activation, which is facilitated by an increase in the alkaline activator concentration. It also can be observed for both alkali-activated type specimens that the optimal concentration was 12 M.

The increase in compressive strength was noteworthily influenced by the particle size distribution of the IOT, as evidenced by the results of the laser particle analyzer. The compressive strength increased by over 90% from 1 to 2 h of grinding time for paste specimens. However, the grinding time appears to be more effective in low concentration of alkaline activator (8M), suggesting that the high alkalinity overpass the effect of the IOT's particle fineness in the alkali-activated reaction. For example, the increase from 2 to 3 h of grinding time yield a 16% increase (from 60.0 to 69.7 MPa) in specimens activated with the 8M solution, while for specimens activated with the 12M solution, the same increase led to a 14% reduction. These results showed that the grinding method probably leads to finer and more homogeneous particles causing faster dissolution of reactive Si and Al pieces [17], [52].

It should be noted that the mortar specimen showed compressive strength slightly influenced by the IOT particle size distribution and was ruled by the pack arrangement due to the particle size distribution of the fine aggregate. These results agree with the effect of particle size distribution on mechanical behavior and specimen density.

After the compressive strength test, the specimens were collected for the water absorption test (Figure 7). The paste specimens showed a water absorption between 3.1 and 13.5%, while mortar specimens showed values between 2.3 and 10.6%. In general, the use of fine aggregate decreased water absorption values compared to the paste specimens. This decrease in water absorption could be the first sign that the use of fine aggregate did not generate greater porosity in

Rev. IBRACON Estrut. Mater., vol. 16, no. 5, e16506, 2023

8/12

the mortar specimens or, even if it did, the interconnectivity of the pores was low. The results of water absorption are consistent with previous research [53].

The water absorption of an alkali-activated composite depends on its chemical nature, structural morphology, and volume of pores. A higher degree of alkaline activation can lead to a denser and less permeable composite. It could be observed that the mortar specimens 8-1, 10-1, and 12-1 disintegrated after soaking in water. This fact might indicate that the specimens were in the lag phase (induction period) and showed a lack of sufficient structural integrity [54]. On the other hand, since this fact undergoes only in mortar specimens, this also might be related to differences in the alkali-activated reaction due to the presence of a dispersed phase in the composite.
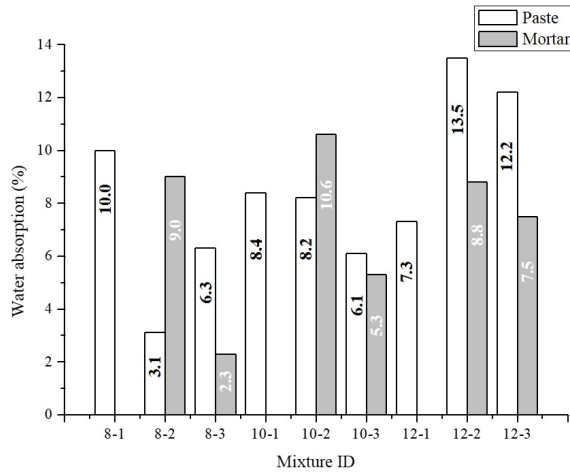

Figure 7. Water absorption of alkali-activated specimens.

4.2.3 Alkali-activated technology applied in iron ore tailings

The results obtained in both pastes and mortars show that IOT can be an interesting precursor to the manufacture of alkali-activated materials, resulting in the development of composites with high mechanical performance. The results show promising opportunities for IOT as the main precursor in alkali-activated technology.

There is a wide range of opportunities regarding using these composites as a construction and building material. According to the American Standards (ASTM), the composite based on IOT easily achieves the minimum strength of building bricks (20.7 MPa) [55], pedestrian and light traffic (55.2 MPa) [56], and the maximum water absorption (17% and 8%, respectively). Furthermore, the mechanical properties of pastes and mortars were superior to the Portland cement high-performance concrete (55.0 MPa), consuming a hard-to-manage tailing and yielding an eco-friendly composite.

5 CONCLUSIONS

The study investigated the effect of four major factors on the physical and mechanical properties of the IOT-based composites: i. the concentration of alkaline activator, ii. the particle size distribution of precursor material, iii. the temperature of curing, and iv. the use of fine aggregate. Through the experimental results, the main conclusions obtained in this paper are:

I. Using IOT as the precursor material to the alkali-activated process yielded composites with 7-days compressive and flexural strengths of 110.0 and 25.0 MPa, respectively. These results were greatly influenced by the concentration of the alkaline activator and the grinding time.

II. The temperature and alkaline concentration were controlling factors in the alkaline activation of IOT. The alkaline solution of 6 M was not sufficient to harden even at 100°C, while the temperature time played a key role in the alkaline activation. Furthermore, the grinding procedure seems to be an interesting alternative route rather than high molarity solutions.

III. Alkali-activated mortars also showed high strength values – 7-days compressive and flexural strength values reached 67.0 and 11.0 MPa, respectively. In general, the mortars showed strength reductions ranging from 15 to 40% compared to the corresponding alkali-activated pastes.

Rev. IBRACON Estrut. Mater., vol. 16, no. 5, e16506, 2023

9/12

IV. The alkali-activated pastes showed high length change, while the fine aggregate in the mortar specimens significantly reduced this effect. In general, the mortars also showed a decrease in water absorption when compared to the paste specimens. Both IOT paste and mortar specimens met the ASTM requirements for diverse construction and building materials.

V. The results showed promising applications of IOT as a construction and building material with appropriate mix proportions and activation process. The availability available and safety concerns related to the storage of IOT encourage its application as the precursor or even as a blend material to alkali-activated composites.

Few barriers such as water resistance, variability in composition, application of alkaline solutions, uncertainty in the exact degree of alkaline activation, and thermal curing may cause difficulties in widespread practical applications of this alkali-activated type. In this sense, the present work contributes to a more in-depth discussion and understanding of IOT reactivity, as well as the properties of IOT-based composites. However, additional research is needed for a more in-depth investigation of the effect of compaction, alkaline activation degree, and durability.

ACKNOWLEDGEMENTS

REFERENCES

[1] J. Davidovits, "Geopolymers: inorganic polymeric new materials," *J. Therm. Anal.*, vol. 37, no. 8, pp. 1633–1656, 1991.

[2] B. Majidi, "Geopolymer technology, from fundamentals to advanced applications: a review," *Mater. Technol.*, vol. 24, no. 2, pp. 79–87, 2009.

[3] N. Elmesalami, and K. Celik, "A critical review of engineered geopolymer composite: a low-carbon ultra-high-performance concrete," *Constr. Build. Mater.*, vol. 346, pp. 128491, 2022.

[4] O. Wan-En et al., "Towards greener one-part geopolymers through solid sodium activators modification," *J. Clean. Prod.*, vol. 378, pp. 134370, 2022.

[5] F. Okoye, J. Durgaprasad, and N. Singh, "Mechanical properties of alkali activated fly ash/Kaolin based geopolymer concrete," *Constr. Build. Mater.*, vol. 98, no. 15, pp. 685–691, 2015.

[6] P. Choeycharoen, W. Sornlar, and A. Wannagon, "A sustainable bottom ash-based alkali-activated materials and geopolymers synthesized by using activator solutions from industrial wastes," *J. Build. Eng.*, vol. 54, pp. 104659, 2022.

[7] Sk. Hossain, P. Roy, and C. Bae, "Utilization of waste rice husk ash for sustainable geopolymer: a review," *Constr. Build. Mater.*, vol. 310, pp. 125218, 2021.

[8] S. Kabir, U. J. Alengaram, M. Z. Jumaat, S. Yusoff, A. Sharmin, and I. I. Bashar, "Performance evaluation and some durability characteristics of environmentally friendly palm oil clinker based geopolymer concrete," *J. Clean. Prod.*, vol. 161, no. 10, pp. 477–492, 2017.

[9] V. Trincal et al., "Shrinkage mitigation of metakaolin-based geopolymer activated by sodium silicate solution," *Cement Concr. Res.*, vol. 162, pp. 106993, 2022.

[10] J. van Jaarsveld, J. van Deventer, and G. Lukey, "The effect of composition and temperature on the properties of fly ash- and kaolinite-based geopolymers," *Chem. Eng. J.*, vol. 28, no. 1-3, pp. 63–73, 2002.

[11] J. Cai, X. Li, J. Tan, and B. Vandevyvere, "Thermal and compressive behaviors of fly ash and metakaolin-based geopolymer," *J. Build. Eng.*, vol. 30, pp. 101307, 2020.

[12] P. Chindaprasirt, C. Jaturapitakkul, W. Chalee, and U. Rattanasak, "Comparative study on the characteristics of fly ash and bottom ash geopoylmers," *Waste Manag.*, vol. 2, no. x, pp. 539–543, 2009.

[13] C. Künzel, C. Cheeseman, L. Vandeperre, and A. Boccaccini, "An assessment of drying shrinkage in metakaolin-based geopolymer," *J. Am. Ceram. Soc.*, vol. 95, pp. 3270–3277, 2012.

[14] P. Ken, M. Ramli M and C. Ban, "An overview on the influence of various factors on the properties of geopolymer concrete derived from industrial by-products," *Constr. Build. Mater.*, vol. 77, pp. 370–395, 2015.

[15] S. Ahmari and L. Zhang, "Production of eco-friendly bricks from copper mine tailings through geopolymerization," *Constr. Build. Mater.*, vol. 29, pp. 323–331, 2012.

[16] X. He, Z. Yuhua, S. Qaidi, H. F. Isleem, O. Zaid, F. Althoey, and J. Ahmad, "Mine tailings-based geopolymers: a comprehensive review," *Ceram. Int.*, vol. 48, no. 17, pp. 24192–24212, 2022.

[17] S. Mabroum, S. Moukannaa, A. El Machi, Y. Taha, M. Benzaazoua, and R. Hakkou, "Mine wastes based geopolymers: a critical review," *Clean Eng Tech.*, vol. 1, pp. 100014, 2020.

[18] Z. Lu and M. Cai, "Disposal methods on solid wastes from mines in transition from open-pit to underground mining," *Procedia Environ. Sci.*, vol. 16, pp. 715–721, 2012.

[19] P. Duan, C. Yan, W. Zhou and D. Ren, "Development of fly ash and iron ore tailings based porous geopolymer for removal of Cu(II) from wastewater," *Ceram. Int.*, vol. 42, no. 12, pp. 13507–13518, 2016.

[20] P. Duan, C. Yan, W. Zhou and D. Ren, "Fresh properties, compressive strength and microstructure of fly ash geopolymer paste blended with iron ore tailing under thermal cycle," *Constr. Build. Mater.*, vol. 118, pp. 76–88, 2016.

[21] Z. Ismail and E. Al-Hashimi, "Reuse of waste iron as a partial replacement of sand in concrete," *Waste Manag.*, vol. 28, no. 11, pp. 2048–2053, 2008.

[22] S. Zhao, J. Fan, and W. Sun, "Utilization of iron ore tailings as fine aggregate in ultra-high performance concrete," *Constr. Build. Mater.*, vol. 32, pp. 540–548, 2013.

[23] J. Franco de Carvalho, P. A. M. Campos, K. Defáveri, G. J. Brigolini, L. G. Pedroti, and R. A. F. Peixoto, "Low environmental impact cement produced entirely from industrial and mining waste," *J. Mater. Civ. Eng.*, vol. 31, no. 2, pp. 040018391, 2019.

[24] J. Galvao, H. D. Andrade, G. J. Brigolini, R. A. F. Peixoto, and J. C. Mendes, "Reuse of iron ore tailings from tailings dams as pigment for sustainable paints," *J. Clean. Prod.*, vol. 200, pp. 412–422, 2018.

[25] P. De Silva, K. Sagoe-Crenstil, and V. Sirivivatnanon, "Kinetics of geopolymerzation: role of Al2O3 and SiO2," *Cement Concr. Res.*, vol. 37, no. 4, pp. 512–518, 2007.

[26] Y. Hu et al., "Role of Fe species in geopolymer synthesized from alkali-thermal pretreated Fe-rich Bayer red mud," *Constr. Build. Mater.*, vol. 200, pp. 398–407, 2019.

[27] N. Ye et al., "Transformations of Na, Al, Si and Fe species in red mud during synthesis of one-part geopolymers," *Cement Concr. Res.*, vol. 101, pp. 123–130, 2017.

[28] P. Lemougna, K. J. D. MacKenzie, G. N. L. Jameson, H. Rahier & U. F. Chinje Melo, "The role of iron in the formation of inorganic polymers (geopolymers) from volcanic ash: a 57Fe Mössbauer spectroscopy study," *J. Mater. Sci.*, vol. 48, no. 15, pp. 5280–5286, 2013.

[29] V. Piffer, K. Soares, and A. Galdino, "Evaluation of mechanical and thermal properties of PP/iron ore tailing composites," *Compos. Part B*, vol. 221, pp. 109001, 2021.

[30] P. Dauce, G. B., Castro, M. M. F. Lima, and R. M. F. Lima, "Characterisation and magnetic concentration of an iron ore tailings," *J. Mater. Res. Technol.*, vol. 8, no. 1, pp. 1052–1059, 2019.

[31] Associação Brasileira de Normas Técnicas, *Standard Sand for Cement Tests – Specification*, ABNT NBR 7214, 2015.

[32] F. Pacheco-Torgal, D. Moura, Y. Ding, & S. Jalali, "Composition, strength and workability of alkali-activated metakaolin based mortars," *Constr. Build. Mater.*, vol. 25, no. 9, pp. 3732–3745, 2011.

[33] S. Jeeva Chithambaram, S. Kumar, and M. Prasad, "Thermo-mechanical characteristics of geopolymer mortar," *Constr. Build. Mater.*, vol. 213, pp. 100–108, 2019.

[34] Associação Brasileira de Normas Técnicas, *Mortars applied on wall and ceilings – Determination of the flexural and the compressive strength in the hardened stage*, ABNT NBR 13279, 2015.

[35] American Society for Testing and Materials, *Standard Test Methods for Sampling and Testing Brick and Structural Clay Tile*, ASTM C67-07, 2007.

[36] S. Nath and S. Kumar, "Reactions kinetics of fly ash geopolymerization: Role of particle size controlled by using ball mill," *Adv. Powder Technol.*, vol. 30, no. 5, pp. 1079–1088, 2019.

[37] S. Kumar, F. Kristály, and G. Mucsi, "Geopolymerisation behaviour of size fractioned fly ash," *Adv. Powder Technol.*, vol. 26, no. 1, pp. 24–30, 2015.

[38] L. Assi, E. Deaver, and P. Ziehl, "Effect of source and particle size distribution on the mechanical and microstructural properties of fly Ash-Based geopolymer concrete," *Constr. Build. Mater.*, vol. 167, pp. 372–380, 2018.

[39] Z. Li, Y. Gao, J. Zhang, C. Zhang, J. Chen, and C. Liu, "Effect of particle size and thermal activation on the coal gangue based geopolymer," *Mater. Chem. Phys.*, vol. 267, pp. 124657, 2021.

[40] K. Somna, C. Jaturapitakkul, P. Kajitvichyanukul, and P. Chindaprasirt, "NaOH-activated ground fly ash geopolymer cured at ambient temperature," *Fuel*, vol. 22, no. 6, pp. 2118–2124, 2011.

[41] A. Mehta and R. Siddique, "An overview of geopolymers derived from industrial by-products," *Constr. Build. Mater.*, vol. 127, pp. 183–198, 2016.

[42] J. Cai., J. Pan, J. Han, Y. Lin, and Z. Sheng, "Impact behaviours of engineered geopolymer composite exposed to elevated temperatures," *Constr. Build. Mater.*, vol. 312, pp. 125421, 2021.

[43] J. Cai, J. Pan, J. Han, Y. Lin, and Z. Sheng, "Low-energy impact behavior of ambient cured engineered geopolymer composites," *Ceram. Int.*, vol. 48, no. 7, pp. 9378–9389, 2022.

[44] K. Lin, "Feasibility study of using brick made from municipal solid waste incinerator fly ash slag," *J. Hazard. Mater.*, vol. 137, no. 3, pp. 1810–1816, 2006.

[45] B. Nematollahi, J. Sanjayan, J. Qiu, and E.-H. Yang, "Micromechanics-based investigation of a sustainable ambient temperature cured one-part strain hardening geopolymer composite," *Constr. Build. Mater.*, vol. 131, pp. 552–563, 2017.

[46] G. Gorhan and G. Kurklu, "The influence of the NaOH solution on the properties of the fly ash-based geopolymer mortar cured at different temperatures," *Compos. Part B.*, vol. 58, pp. 371–377, 2013.

[47] M. Al-Majidi, A. Lampropoulos, A. Cundy, and S. Meikle, "Development of geopolymer mortar under ambient temperature for in situ applications," *Constr. Build. Mater.*, vol. 120, pp. 192–211, 2016.

[48] K. Onoue, Y. Sagawa, D. Atarashi, and Y. Takayama, "Optimization of mix proportions and manufacturing conditions of fly-ash-based geopolymer mortar by parameters design with dynamic characteristics," *Cement Concr. Compos.*, vol. 133, pp. 104645, 2022.

[49] H. Tchakouté and C. Rüscher, "Mechanical and microstructural properties of metakaolin-based geopolymer cements from sodium waterglass and phosphoric acid solution as hardeners: a comparative study," *Appl. Clay Sci.*, vol. 149, pp. 81–87, 2017.

[50] W. Hu, Q. Nie, B. Huang, X. Shu, and Q. He, "Mechanical and microstructural characterization of geopolymers derived from red mud and fly ashes," *J. Clean. Prod.*, vol. 186, pp. 799–806, 2018.

[51] N. Cristelo, J. Coelho, T. Miranda, Á. Palomo, and A. Fernández-Jiménez, "Alkali activated composites – Na innovative concept using iron and steel slag as both precursor and aggregate," *Cement Concr. Compos.*, vol. 103, pp. 43–47, 2019.

[52] X. Jiao, Y. Zhang, and T. Chen, "Thermal stability of a silica-rich vanadium tailings based geopolymer," *Constr. Build. Mater.*, vol. 38, pp. 43–47, 2013.

[53] A. Wongsa, V. Sata, B. Nematollahi, J. Sanjayan, and P. Chindaprasirt, "Mechanical and thermal properties of lightweight geopolymer mortar incorporating crumb rubber," *J. Clean. Prod.*, vol. 195, pp. 1069–1080, 2018.

[54] J. Provis and J. van Deventer, *Geopolymers: Structure, Processing, Properties and Industrial Applications*, Boston, MA, USA: Woodhead Publishing Limited, 2009.

[55] American Society for Testing and Materials, *Standard Specification for Building Brick (Solid Masonry Units Made from Clay or Shale)*, ASTM C65-10, 2010.

[56] American Society for Testing and Materials, *Standard Specification for Pedestrian and Light Traffic Paving Brick*, ASTM C902-07, 2007.

Editors: Fernando Pelisser, Guilherme Aris Parsekian.

IBRACON Structures and Materials Journal
Revista IBRACON de Estruturas e Materiais

ORIGINAL ARTICLE

Measuring packing density and water demand of Portland cement and SCMs by the mixing energy method

Medindo densidade de empacotamento e demanda de água do cimento Portland e MCSs pelo método da energia de mistura

Nicolle Talyta Arriagada Soto[a] (ID)
Gustavo Macioski[a] (ID)
Emanoel Cunha Araújo[a] (ID)
Juarez Hoppe Filho[b] (ID)
Nayara Soares Klein[a] (ID)

[a]Universidade Federal do Paraná – UFPR, Programa de Pós-Graduação em Engenharia Civil (PPGEC), Curitiba, PR, Brasil
[b]Universidade Federal do Oeste da Bahia – UFOB, Barreiras, BA, Brasil

Abstract: Wet packing methods evaluate the packing density of fine materials through the determination of the apparent density and voids content of pastes with different water to solids (w/s) ratios. Its goal is to estimate the minimum water demand to achieve the maximum solids concentration in the mixture, a parameter applied to the mix design of cementitious composites based on particle packing theories. Since most methods based on apparent density are time-consuming and require a high volume of materials, this paper aims to evaluate the mixing energy method as an alternative for the wet packing method and to adapt it to be used for SCMs (supplementary cementitious materials). With a reduced time and material to perform the test, results demonstrate a better precision of the mixing energy due to its discrete measurement. The ideal water flow and initial volume of materials to perform the test on cement and SCMs are discussed.

Keywords: particle packing, fine powder, compressive packing model, Arduino.

Resumo: Os métodos de empacotamento via úmida avaliam a densidade de empacotamento de materiais finos através da determinação da densidade aparente e teor de vazios de pastas com diferentes relações água/sólidos (a/s). Seu objetivo é estimar a demanda mínima de água para atingir a concentração máxima de sólidos na mistura, um parâmetro aplicado à dosagem de compósitos cimentícios utilizando teorias de empacotamento de partículas. Como a maioria dos métodos baseados na densidade aparente são demorados e requerem um grande volume de materiais, este trabalho visa avaliar o método de energia de mistura como uma alternativa ao método de empacotamento via úmida e adaptá-lo para ser usado para MCSs (materiais cimentícios suplementares). Com um tempo reduzido e menor quantidade de material realizar o teste, os resultados demonstram uma melhor precisão do método da energia de mistura, devido à sua medição discreta. O fluxo de água ideal e o volume inicial de materiais para realizar o teste em cimento e MCSs são discutidos.

Palavras-chave: empacotamento de partículas, pó fino, modelo de empacotamento compressível, Arduino.

1 INTRODUCTION

Concrete is a building material made from a mixture of aggregates of varied sizes embedded in a binding matrix (cement paste) that is responsible for filling the voids between the aggregates [1]. According to this concept, the

concrete mix design can be optimized based on particle packing theories to achieve more sustainable mixtures by reducing Portland cement consumption or replacing it with supplementary cementitious materials - SCMs [2]. In particle packing theory, particle fractions of different sizes are used to fill the voids between the larger particles generating a system with a reduced voids volume [3]. The water added to the cement will fill the voids between the particles and the excess water will lubricate the surface of the particles, giving the desired flowability to the mixes [4].

To design concrete based on particle packing theories, the packing density of Portland cement and other granular materials is one of the main parameters required for the application of several particle packing models such as the Furnas [5], Stovall et al. [6], and De Larrard [7] models. Over the years, several methods have been proposed to determine the packing density and/or water demand of fine particles, as shown in Table 1.

Table 1. Packing density methods available for Portland cement and fine materials.

Method	Evaluation criteria	Reference
Water demand France	Visual assessment of paste consistency	[7]
Water demand Germany	Visual assessment of paste saturation point	[8] apud [9]
Proctor test	Oven-dry humidity in compacted mixture	[10], [11]
Centrifugal consolidation	Excess water after centrifugation	[12], [13]
Water demand – Japan	Slump flow test results	[14]
Rheology – Krieger and Dougherty	Viscosity of the mix	[15]
Vicat test	Needle penetration	[16]
(Gas) pressure filtration	Pressure variation	[17]
Wet packing method	Apparent density of the paste	[11]
Water demand / mixing energy	Energy consumption during the mixture	[18] apud [9] [19] apud [20]

It can be observed in Table 1 that all the methods presented consider the presence of water for the measurements. Measuring the packing density of fine particles such as Portland cement in dry systems is a difficult task due to the agglomeration of particles smaller than 100μm [21]. In very small particles, due to their low mass and high surface area, Van der Walls forces, electrostatic charges and chemical bonds are higher than the forces that can separate the particles (shear gravity), and this effect causes the particles to agglomerate [22]. This determination on fine powders needs to be performed in the presence of water and superplasticizers to ensure powder dispersion [23]. Hence, dry packing methods such as [24]–[26] are not advised, because they tend to overestimate the voids content and underestimate the packing density of fine particles [11]. Furthermore, when these fine particles are used to produce concrete, water and chemical admixtures will be present in the mix, which makes measuring the packing density under these same conditions a more reliable parameter to be used for concrete mix design.

Most of the methods given in Table 1 have been evaluated by Fennis [9], who states that all tests give reasonably accurate results (the standard deviation obtained in each test is low), although they do not all comply with each other since the different techniques will lead to different values for the packing density. Therefore, studies comparing different methodologies are fundamental to prove the effectiveness and reliability of those techniques and their adaptations. Fennis also suggested that the water demand test from France [7], [27] and mixing energy test [18] are the ones that produce better results of packing density for powders. However, the water demand test from France is based on visual analysis, which makes the results highly dependent on the operator. The centrifugal consolidation test [28], [13] is also an accurate method, according to the author [9], as long as enough measurements are performed (at least three). Nevertheless, the centrifugal consolidation test demands special equipment for test performance, which is not commonly found in construction materials laboratories. Furthermore, the compaction energy is limited to the centrifugal energy used. The wet packing method [11] has been successfully used for measuring the packing density of cement pastes with a wide range of w/s ratios [29], [30] and it has also been successfully applied to the design of eco-friendly concretes [31]–[33] using particle packing theories, resulting in mixtures with low cement consumption.

The advantage of the wet packing method [11] relies on the use of regular laboratory equipment, and the application of similar conditions to which the concrete will be exposed during mixing and compaction, such as the use of chemical admixtures and the casting method (compacted, vibrated or gravity). On the other hand, it requires several pastes to be produced to obtain the results, which can be a downside regarding both time and the amount of material required for testing. This can become a concern when a combination of several binders and supplementary cementitious materials needs to be evaluated repeatedly. It is also not viable to produce the mixtures for the wet packing method in small batches, since the authors recommend using a minimal paste volume of 181ml or similar for the test. Since changing the mixing procedure could influence the results, its adaptation requires further investigation.

The mixing energy method also has the advantage of not relying on human judgment for the results to be obtained. Plus, it requires less material to run the test. Although the method allows a discrete measurement and high precision, its application depends on extra equipment to perform the energy monitoring of the mixer. Some low-cost approaches such as the use of a PC-connected multimeter and programmable microcontrollers are possible options, which will be used in the present work. Additionally, for the application of the mixing energy method for SCMs, adjustments in the procedure may be required.

The purpose of the present work is to compare the mixing energy method as an alternative to the wet packing method to measure the packing density and water demand of Portland cement. Additionally, the mixing energy method was adapted to be used for SCMs (supplementary cementitious materials). The monitoring of power consumption was successfully performed with a low-cost system attached to the standard mixer. Both wet packing and mixing energy methods will be further explained and detailed in the following sections, as well as the proposed adaptations.

From the proposed methods, a faster evaluation of the packing density of Portland cement and other fine materials is possible. Therefore, the development of eco-friendly mortars and concretes can be achieved based on particle packing theories, allowing a reduction in cement consumption, optimizing the use of SCMs, reducing carbon footprint, and increasing the durability of composites.

2 EXPERIMENTAL PROGRAM

2.1 Materials

In the present work, pastes were mixed using a single binder (Portland cement or SCMs (fly ash, limestone filler, metakaolin and densified silica)), with chemical admixture and water. The specific gravity of the powder materials was evaluated according to ASTM C188 [34].

A Brazilian high early strength Portland cement (CP V – ARI) [35] was used. The cement is equivalent to ASTM type III Portland cement [36]. All the SCMs used were commercialized in Brazil for concrete production. The particle size distribution of the materials was obtained by laser diffraction in a particle size analyzer (CILAS 920) using an 850 nm diode laser. The dispersion of the materials was performed by dissolution in water without any dispersing agent and ultrasound for 60 seconds during testing [3], [37]. For the densified silica, due to its smaller size, the particle size distribution was obtained by the Dynamic Light Scattering (DLS) technique (Microtrac Nanotrac), using a 785nm laser in reflected measurements. The dispersion was performed by dissolution in distilled water with 5% dispersant to the solvent volume (polycarboxylate base). The sample was diluted at a ratio of 2mg/ml in 50ml of the solution and dispersed in an ultrasonic washer (Schuster L-100, 160W, 42000 Hz) for 15 minutes.

A third-generation superplasticizer chemical admixture composed of polycarboxylate polymers was also used. The chemical admixture meets the requirements of ASTM C1017 [38] and presented a 1.12 g/cm^3 specific gravity.

2.2 Particle size distribution and specific gravity

The particle size distribution (PSD) of Portland cement and SCMs can be found in Figure 1. The specific gravity and characteristic average diameters (D_{50}) of the materials are presented in Table 2.
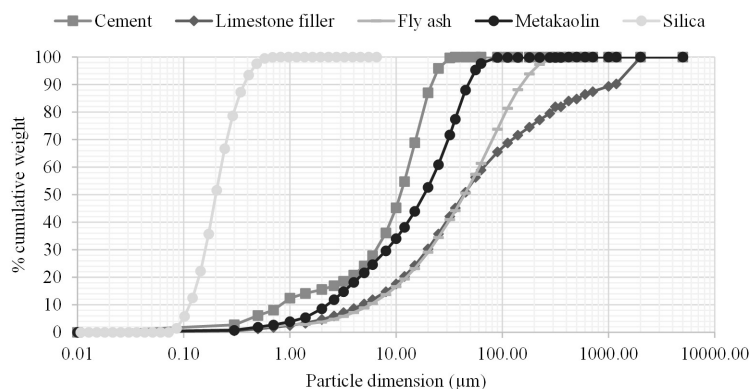

Figure 1. PSD of cement and SCMs

Rev. IBRACON Estrut. Mater., vol. 16, no. 5, e16507, 2023

3/14

Table 2. Specific gravity and average diameter of fine powders

Material	Specific gravity (g/cm^3)	D$_{50}$ (µm)
Portland cement	3.13	10.99
Fly ash	3.00	44.14
Limestone filler	2.78	43.55
Metakaolin	2.49	18.45
Silica	1.97	0.201

From the results presented in Figure 1, it can be noticed that all materials have a continuous distribution. Based on their PSDs, fly ash and the limestone have particles sizes with similar average diameter, while the silica presented the smaller average diameter. Additionally, the limestone filler presented about 20% of retained material in the 355 µm mesh sieve, hence with some coarse particles. Along with the particle morphology, those physical properties will directly influence the obtained results of water demand and packing density.

2.3 Mini-slump test

The saturation dosage test for the superplasticizer was performed using Kantro's cone test [39] for the Portland cement, by measuring the paste spreading diameter in the fresh state. During the test, the w/s ratio was kept constant at 0.3 for all mixes, and chemical admixture contents tested were 0.25%, 0.5%, 0.75%, 1.0%, 1.5%, 2.0%, 2.5% and 3.0% (by cement weight). The saturation point found was used in all mixes, including the SCMs. Due to the small particle size, the SCMs may demand higher dosages of chemical admixtures, but large dosages may result in a mechanical behavior different from when realistic dosages are used in the field [40].

The results of the chemical admixture saturation point test with Portland cement obtained in the Kantro test are shown in Figure 2. The pastes produced without chemical admixture did not provide the required consistency for the test, therefore, its results were considered zero.
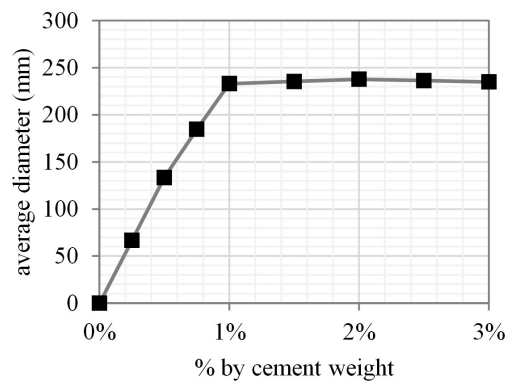
Figure 2. Superplasticizer saturation dosage test results

It can be observed in Figure 2 that the opening diameter obtained in the Kantro test increased significantly when the admixture content was increased up to 1.0%. For higher contents of the admixture, no significant increase in the fluidity was observed, although the manufacturer suggests ratios up to 5.0%. Therefore, 1.0% of the chemical admixture by cement weight is the saturation dosage for the superplasticizer tested and it was used to perform all the packing density tests in the present study. The saturation point of 1% by mass found was used in all mixes henceforth, including the SCMs mixtures.

2.4 Wet packing method

The first test performed to determine the packing density of Portland cement followed the procedures proposed by Wong and Kwan [11]. The method consists of producing cement pastes with different w/s ratios and determining their apparent density. The water-to-solids (w/s) ratio of the first cement paste produced was 0.35. After that, several other mixes were produced with smaller w/s ratios, which varied from 0.35 to 0.13, by weight. It corresponds to 1.08 to 0.40, by volume.

Rev. IBRACON Estrut. Mater., vol. 16, no. 5, e16507, 2023

4/14

The mixing method consisted of initially adding 50% of the cement to the mixer, followed by 80% of the water and the chemical admixture, mixing at low speed (140 rpm) for 3 minutes. Then, the remaining materials were added in 4 equal parts, mixing at low speed for 3 minutes after each addition. After the mixing process, the paste was placed in a cylindrical container in three layers, each layer being rod-compacted 30 times. Finally, the paste weight to fill the container was registered (the apparent density measurement) and the solids concentration and the voids ratio were calculated according to Equations 1 to 3.

$$V_s = \frac{M}{p_w.u_w + \sum_{i=1}^{n} p_i.R_i} \tag{1}$$

$$u = \frac{(V - V_s)}{V_s} \tag{2}$$

$$\phi = \frac{V_s}{V} \tag{3}$$

Where: V_s is the volume of solids in the mix (cm³); M the mixture mass (g); p_w the water density (g/cm³); u_w the w/s ratio, by volume (-); p_i the material i specific gravity (g/cm³); R_i the material i volume in relation to the total solids volume (-); u the voids ratio (-); V the container volume (cm³) and; ϕ is the solids concentration (-).

The test was repeated following the same procedures previously described, but the volume of the containers used for the apparent density measurements was changed to 200ml. The original test procedure used a container with 181ml, and it is indicated that the paste volume produced should be 50% higher than the container's volume. A regular mortar mixer (140 rpm) was used, and the test was performed twice for each w/s ratio. A summary of the mixing procedure is presented in Table 3.

Table 3. Test conditions evaluated for the wet packing method.

Mixing speed	140 rpm
Container	200ml
w/s ratio (by mass)	0.13 – 0.15 – 0.17 – 0.20 – 0.25 – 0.35
Mixing procedure	50% cement + 80% water + 100% superplasticizer Mix for 3min Add 4x (12.5% cement + 5% water) and mix for 3 min

Using several w/s ratios for testing through the wet packing method is necessary to reproduce the different conditions of grain-water interaction in mixtures, as presented in Figure 3. From Figure 3c it can be observed that when the w/s ratio is high, there is water between the particles, resulting in a high voids ratio. This situation is associated with a saturated mixture, where the particles are spaced apart from each other by excess water, hence the mixture presents a high fluidity. By reducing the w/s ratio, the voids ratio decreases, and the funicular state is reached as shown in Figure 3b. In this state, the granular particles remain surrounded by the water, but the water is not enough to fill all the voids between the particles, which will approximate the grains because of the capillary forces and generate the minimum voids ratio. When the voids ratio is minimum, the solids concentration is maximum, which corresponds to the packing density of the material in the wet condition. It is important to notice that under this circumstance the voids ratio cannot be further reduced, since the particles are already in contact with each other. If the w/s ratio is decreased beyond this point, the system enters the pendular state as presented in Figure 3a, when the amount of water is not sufficient to wet all the grains, forming ''water bridges'' in the points of contact between particles. The voids ratio will be increased in this situation and the particles will be pushed away from each other due to the water surface tension [17], [41], [42].
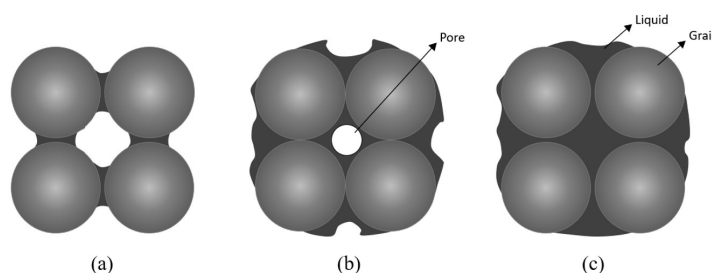

Figure 3. Different conditions of grain-water interaction in mixtures: (a)Pendular state, (b) Funicular state and (c) Saturated mixture.

Rev. IBRACON Estrut. Mater., vol. 16, no. 5, e16507, 2023

5/14

2.5 Mixing energy method

The packing density and water demand can also be evaluated by monitoring the energy spent to mix the paste, as proposed by the mixing energy method ([18] apud [9]; [43] apud [20]). When a mix is being produced and water is added slowly to the mixer bowl, the paste goes from the pendular to the funicular state, and if water keeps being added, the saturated state is reached, as described in Figure 3.

Thus, when performing the test, initially a small amount of water is added to mix the dry paste and low power consumption is registered since the mix is not yet homogeneous. By adding water to the system, it becomes more difficult for the mixer blade to rotate and homogenize the paste because even though more water was added, the mix is still dry. When the funicular state is reached the energy consumption is expected to be the maximum obtained since the mixture will reach higher shear stress due to the particle's proximity [20]. After this point, it is expected a decrease in power consumption due to the increase of the water layer surrounding the particles. Therefore, the packing density and the minimum water demand occur when the highest power consumption is registered, at the funicular state. With the increase in the amount of water, the thickness of the water layer surrounding the grains increases, pushing the particles away from each other, resulting in a reduction of the shear stress. A typical graphical result obtained in the test is given in Figure 4.
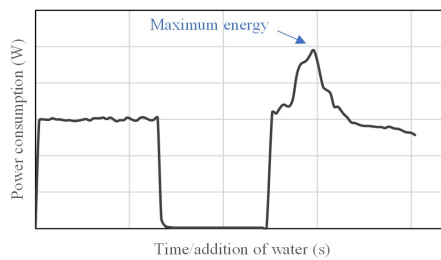
Figure 4. Representation of the mixing energy test result, with increasing energy consumption as a function of water addition over time

The test was performed twice, and the packing density was calculated by Equation 4 [44]. Where: ϕ is the solids concentration (-); V_s is the volume of solids (cm³); V_a is the admixture volume (cm³) and u_w is the w/s ratio, by volume (-), at the maximum power consumption.

$$\phi = \frac{V_s}{V_s + V_a + u_w} \tag{4}$$

The determination of the water demand by the mixing energy method ([43] apud [20]) was performed considering some adaptations. Fennis [9] suggests the use of a 1500g of cement along with 264g of water and superplasticizer chemical admixture, resulting in an initial w/s ratio of 0.176. After mixing for 60 seconds and an extra 60 seconds interval without mixing (resting and scraping), a constant water addition of 1.5 ml/s occurs using an intravenous (IV) drip while mixing until liquefaction of the mix. For the continuous additions of water, the IV drip was attached to the mixer as shown in Figure 5a and 5b, and placed as close as possible to the paddle center. The water drops should not touch the bowl, to ensure a proper incorporation of the water. The flow regulator was previously adjusted for the required water flux.
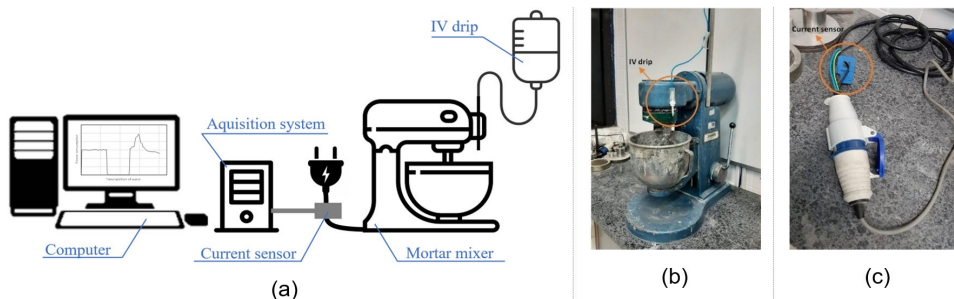
Figure 5. Mixing energy test: (a) set up schematic illustration (b) IV drip flow regulator and (c) current sensor

During the experiment, the mixing energy test was also performed reducing the cement to 1kg due to the high torque of the mixer that was causing paddle locking and energy peaks. Two water additions, 1.5 and 0.5 ml/s were also evaluated by the authors since a reduction in water flow will facilitate the energy peak identification. Hungers and Browers [20] suggest using 10 ml additions every 20 seconds, since there is a delay in the water effect when continuously added, hence, this water addition was also tested. Table 4 shows a summary of the mixing energy adaptations performed in the present study. The test was performed twice for each water addition.

Table 4. Adapted mixing energy test procedure

Initial w/s ratio	0.176 (0.55 in volume)			
Cement consumption	1.5 kg		1.0 kg	
Water addition rate	1.5ml/s	1.5 ml/s	0.5 ml/s	10ml/20s

During the mixing process, the current was monitored every 0.1s using a low-cost system with the aid of an open-source electronic prototyping board. For this, an Arduino Nano with SCT013 current sensor (±1% accuracy within 0-100A range) was used on the mixer power supply connections (single phase wiring), as shown in Figure 3a and 3c. Ohm's law was used to calculate the equivalent power consumption during the test. The use of sensors attached to Arduino systems has been successfully used in recent published cementitious composite studies [45]–[51].

For the proper application of the test procedure, it is essential to use a standard planetary mixer according to ASTM C305 with controlled rotation speed. In order to keep a constant rotation speed, a build-in frequency inverter in the equipment will adjust the applied current over time. Therefore, a variation in the measured current is expected when water is added. After establishing the reliability of the mixing energy method when compared to the wet packing method developed by Wong and Kwan [11], and the water addition of 0.5ml/s in 1.0kg of cement as the best setup for the test procedure, the method was applied to SCMs with some adaptions on the initial volume and water ratio were established experimentally during testing.

The initially proposed mass of fine material, 1 kg, proved to be inadequate to perform the method in silica fume. This mass presented a very large volume, inadequate to the capacity of the mixer bowl, and for this reason, the initial mass of silica fume was reduced by 25%. For the other materials, the initial mass of 1 kg allowed the normal performance of the test.

The initial water/solids (w/s) ratio was also adjusted to meet the particularity of each material analyzed. The adjustment on the initial volume of dry material and water/solids (w/s) for SCMs was required to prevent the mixer paddle from jamming and avoid potential dead zone problems during mixing, which may affect mixing curves. For metakaolin and silica fume, the ratio initially proposed was low, which resulted in a very long testing time. Thus, the water/solids ratio was increased for these mixtures to allow an adequate test time. For the limestone filler, the ratio originally proposed produced a very fluid mixture (with excess water) and was reduced by 50%. Table 5 summarizes the parameters used for the tested SCMs.

Table 5. Parameters used for each material when performing the mixing energy test

Material	Initial dry mass (kg)	Initial w/s ratio (weight)
Portland cement	1.00	0.176
Limestone filler	1.00	0.088
Fly ash	1.00	0.176
Metakaolin	1.00	0.264
Silica	0.75	0.606

To assess whether the parameters are adequate, the test results (water demand) between two consecutive measurements, and the increase in power consumption over time should present similar behavior among the tests, indicating a good dispersion of the water in the mixture.

3 RESULTS AND DISCUSSIONS

3.1 Wet packing method

The packing density of the cement was first determined by the wet packing method [11]. The voids ratio (u) and the solid concentration (ϕ) of the cement pastes are shown in Figure 6.
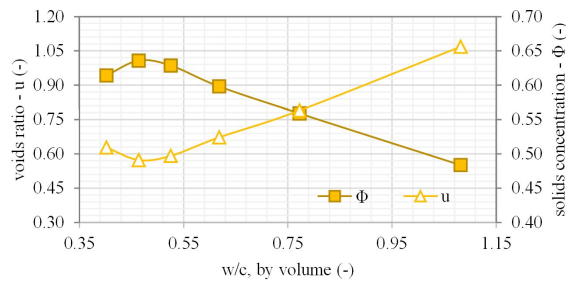
Figure 6. Void ratio and solids concentration of Portland cement

The maximum solid concentration is considered equal to the packing density of the cement particles in the wet condition. The value of packing density found was 0.636 and the minimum w/s ratio needed to produce a homogeneous paste (needed to reach the highest solids concentration) was 0.464 (by volume) or 0.150 (by weight).

3.2 Mixing energy method

3.2.1 Portland Cement

The results of the mixing energy test with different setups are given in Figure 7. It can be seen in the graphics an initial energy increases relative to the starting of the equipment torque at time zero. After this initial moment, energy consumption remains constant for the first 60 seconds of the mixture, while the amount of water is constant (w/s ratio equal to 0.176, as previously stated in Table 3). After that, the mixer is turned off for 60 seconds, during which there is no record of power consumption, and the amount of water remains unchanged. After this period the bowl is scraped, the mixer is turned on again and water is added according to Table 3. With the addition of water in the mix, there is an increase in the shear stress as the mix goes from the pendular to the funicular state and, consequently, an increase in the power consumption is observed. At the funicular state, the maximum energy consumption is reached when all particles are in contact with each other, and their surfaces are wet and connected by water films [20]. By adding more water, the particles start to move away from each other due to the increase of the water layer around them (saturated state), hence, the shear stress and the power consumption decrease. The test stopped after the power consumption dropped and reached a stable condition.
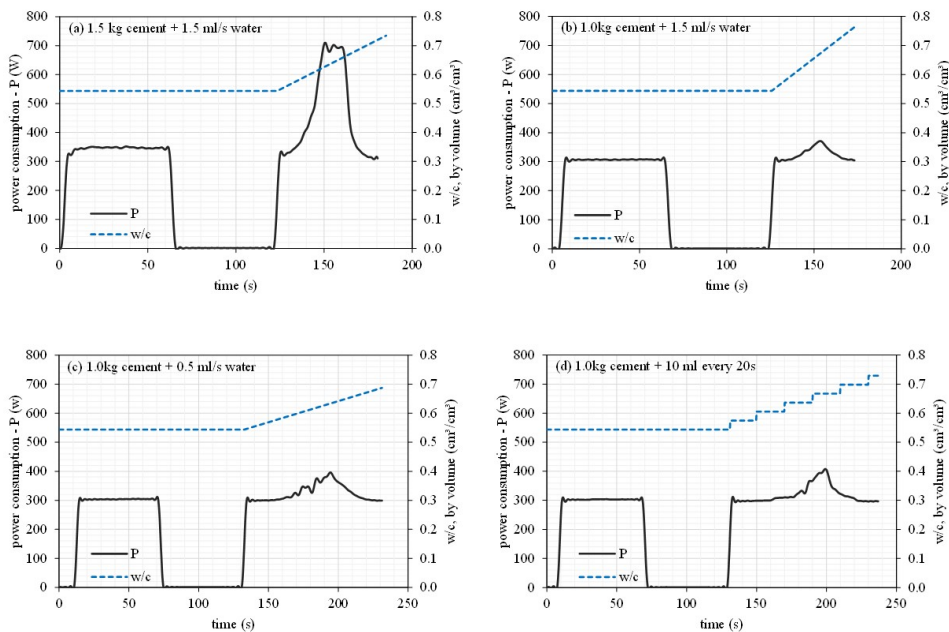

Figure 7. Mixing energy test results with a water addition rate of: (a) 1.5 ml/s with 1.5 kg of cement, (b) 1.5 ml/s with 1.0 kg of cement, (c) 0.5 ml/s and (d) 10 ml every 20 s

Based on the results shown in Figure 7, it is possible to observe that the Arduino Nano with SCT013 current sensor was able to perform a discrete measurement of the power consumption with good precision. From the obtained data, the use of 1.0 kg of cement reduced the power consumption during the initial mixing by 13% and also reduced the energy peak at the funicular state, as can be seen when comparing Figure 7a and Figure 7b. This reduction allowed a better measurement, since the use of 1.5 kg of cement generated power oscillations at the peak due to the high shear stress of the paste, while 1.0 kg of cement prevented the paddle jamming and promoted better data acquisition. While the wet packing method evaluated the water demand for every 0.05 w/s interval, the mixing energy test allowed the estimation of the water discretely every few milliliters of water, hence, with better precision.

Using 10 ml additions every 20 seconds generated an asymmetrical energy peak, as seen in Figure 7d, and the water effect became harder to identify. Besides, errors in the water additions could have happened due to the difficulty of adding small amounts of water precisely every 20s. Table 6 shows the packing density and water demand calculated using the mixing energy method.

Table 6. Packing density and water demand results obtained from the mixing energy method

Method for adding water to the mix	Packing density (-)	Minimum w/s, by volume (-)	Minimum w/s, by weight (-)
1.5 ml/s with 1.5 kg of cement	0.604	0.628	0.203
1.5 ml/s with 1.0 kg of cement	0.574	0.700	0.227
0.5 ml/s with 1.0 kg of cement	0.597	0.634	0.205
10 ml/20 s with 1.0 kg of cement	0.591	0.652	0.211

The packing density results shown in Table 6 varied from 0.574 to 0.604. The original mixing energy method performed with 1.5kg of cement and 1.5ml/s water additions presented a higher packing density (Φ=0.604). When the amount of cement was reduced from 1.5kg to 1.0kg, the packing density was reduced by 5%, while the w/s ratio increased to 0.700 (by volume), possibly because of the high-water flow used in a smaller amount of cement. Reducing the cement to 1.0kg and water additions to 0.5ml/s did not affect the results (variations below 1% from the original method). While the test performed with 1.5kg and 1.5ml/s took 26s to reach its peak, the test with 1.0kg and 0.5ml/s increased that time to 65s. This increase in time to reach the energy peak allowed a better estimation of the energy peak position and gave more time for the added water to interact with the cement, reducing any delay in its effect - mentioned as a downside of the method by Hunger and Browers [20]. Regarding the addition of 10ml every 20s, this setup presented similar packing density results to the original method, but increased the water demand by 4%, possibly due to the asymmetrical behavior of the energy consumption and delay in the water effect. A comparison of the results obtained from the wet packing and the mixing energy methods is illustrated in Figure 8.
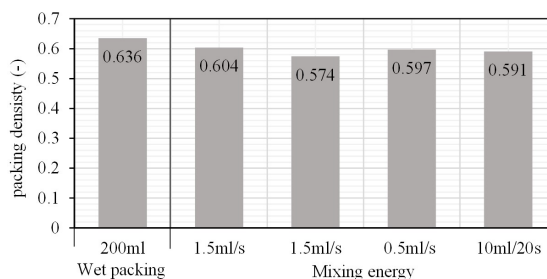
Figure 8: Packing density with the wet packing and the mixing energy methods

When observing the results presented in Figure 8, it can be noticed that both methods were able to measure the packing density of the cement pastes with a small deviation between the test results. The slightly higher packing density results obtained from the wet packing method are a consequence of the compaction step applied when measuring the apparent density. It induces higher energy to the pastes and, therefore, particles get closer to each other due to compaction. It also reduces the water demand, since the volume of water between the grains is smaller. When producing mortars and concretes this compaction energy is different from those used during casting, hence, the mixing energy method probably allows a better estimation of both the packing density and the water demand, since a discrete

measurement is performed, and every water addition can be evaluated during the mixing process. The mixing energy method also demands a smaller volume of material to perform the test. A reduced time to perform the mixing energy test is also positive since one mix is needed for the measurements, while the wet packing method requires at least five.

3.2.2 Supplementary cementitious materials

Figure 9 shows the results of the mixing energy test performed on the SCMs, and Table 7 presents the summary results of the packing density and water demand for those materials.
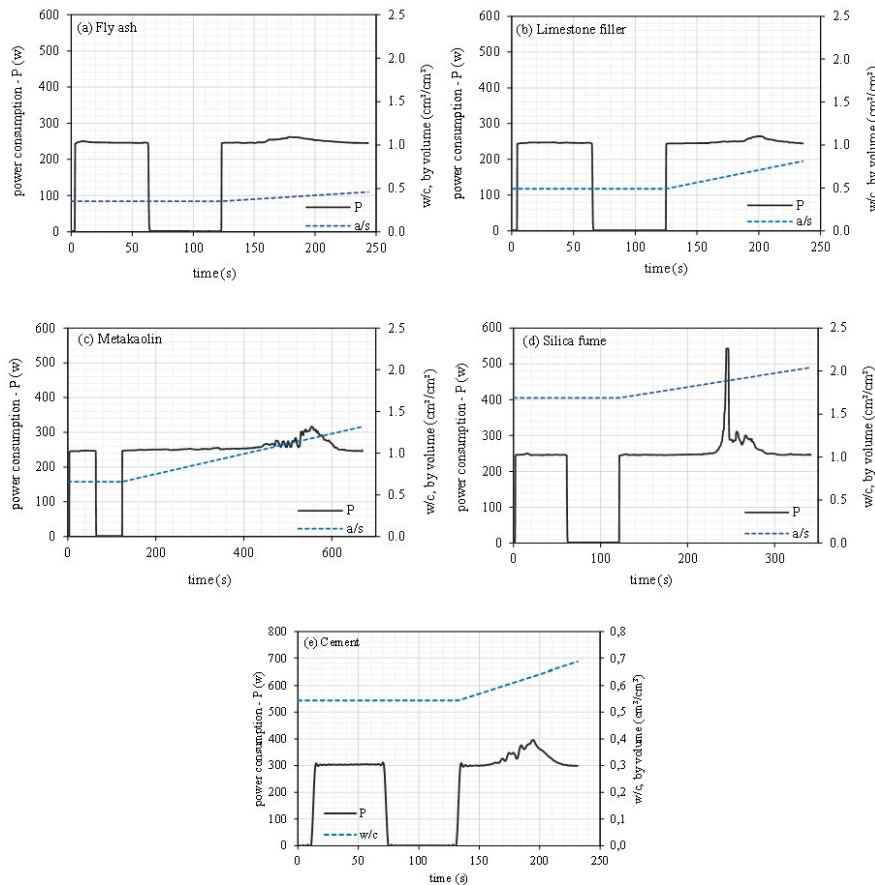
Figure 9. Mixing energy test results, with 0.5ml/s water additions for (a) Fly ash, (b) Limestone filler, (c) Metakaolin, (d) Silica and (e) Cement

Table 7. Packing density and water demand of Portland cement and mineral additions

Material	Packing density (-)	Minimum w/s, by volume (-)	Minimum w/s, by weight (-)
Portland cement	0.597	0.619	0.194
Fly ash	0.704	0.402	0.200
Limestone filler	0.578	0.704	0.126
Metakaolin	0.455	1.177	0.472
Silica	0.344	1.885	0.677

In the mixing energy test for the SCMs, the same behavior observed for the Portland cement was found. With the continuous addition of water, there was a gradual increase in power consumption, relative to the approximation of the particles, until the funicular state (maximum power consumption) was reached, where the particles are in contact, the packing density and the minimum water demand were set.

Regarding the energy consumption for mixing the pastes, it can be seen in Figure 9 that cement and metakaolin showed similar behaviors, with intermediate energy peaks. It is noteworthy that these materials had an average diameter of 11 and 18μm, respectively. The fly ash and the limestone filler (with diameters around 40 μm) required a low energy consumption at their peak. The silica fume (with an average diameter of 0,2 μm) presented an intense and well-defined peak of energy consumption during mixing. The peak energy consumption is more intense the smaller the diameter of the particles since smaller diameter particles will exert higher forces of attraction when compared to the test performed on coarser grains.

Comparing the materials presented in Table 7, it is observed that the highest value of packing density was obtained for fly ash, the lowest was found for silica fume, while the cement, limestone filler and metakaolin presented intermediate values. These differences are expected due to the differences in particle size distributions of each of the materials.

Values of the packing density of Portland cement are similar to those found in the literature: Wong and Kwan [11], using the originally proposed method, obtained a packing density of 0.622 in the presence of a chemical admixture [29]. Similar values for packing density were founded by Campos et al. [52] for Portland cement (0.610) and silica fume (0.354) using the wet method in the presence of chemical admixtures.

The packing density of silica fume is lower than the other SCMs. On the other hand, the water demand for this material was the highest among those studied. This fact demonstrates the need for a higher amount of water (w/s) to obtain the maximum solid concentration. Figure 10 shows a relationship between the water demand and packing density from the mixing energy test.
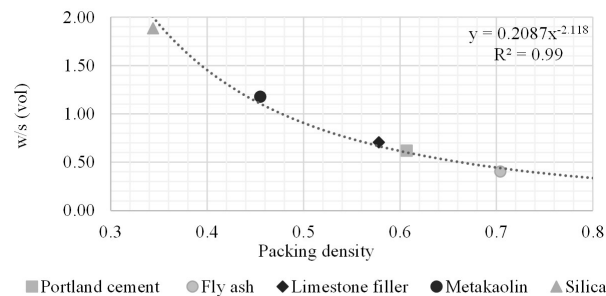

Figure 10. Packing density and water demand correlation from the mixing energy method

Since the packing density is based on a direct measurement of the solid concentration and water content in the mixture, the relationship presented in Figure 10 is expected and demonstrates that only with a low water demand is possible to achieve a high packing density. It was not possible to establish a direct relationship between the mixing energy test results and the average diameter of the particles since the PSD, specific surface, contact angle, water absorption and grain morphology will also influence the test results.

Although this paper evaluated single binders (cement or SCMs) aiming the determination of the packing density of each separate material, future applications of the mixing energy test method could also be performed on binary or ternary mixtures of binders.

4 CONCLUSIONS

The present work addresses the comparison of packing density results measured by the wet packing method and the mixing energy method. From the experimental program developed and the results obtained, the following conclusions can be taken:

- The packing density results achieved with the mixing energy method were like those achieved by the wet packing method in a 200ml container. Considering the best setup for each test (packing density of 0.597 in the mixing energy method with 0.5ml/s in 1.0kg of cement and packing density of 0.636 in the wet packing method with 200ml), the relative difference between the techniques is 6.1%. This variation is relative to the compaction applied to the wet packing test. The mixing energy method also consumed almost seven times less cement and was carried out in less than 15% of the time required for the wet packing method (since it requires only one mix for the measurements to be performed).

- In the mixing energy method, reducing the amount of cement to 1.0 kg avoided the paddle locking during mixing, and the continuous addition of water of 0.5ml/s proved to estimate the funicular state with better precision, giving the system more time to identify the energy peak and eliminating any delay on the paste rheology due to the water addition. While adding 10ml every 20s caused asymmetrical energy consumption that could be related to a delay in the water effect and influence the determination of the packing density and water demand.
- The mixing energy method allows a better estimation of the water demand and packing density since a discrete measurement can be performed with a small amount of cement without the influence of evaporation and compacting processes.
- The mixing energy test was effective in measuring the packing density and water demand of SCMs with a wide range of particle sizes. Some adaptations to the initial weight and water were required to properly measure the power consumption. A relationship between solid concentration and water content was found in the samples.

ACKNOWLEDGEMENTS

REFERENCES FORMATS

[1]   T. C. Powers, *Properties of Fresh Concrete.* New York, NY, USA: John Wiley & Sons, 1968.

[2]   I. R. Oliveira, A. R. Studart, R. G. Pileggi, and V. C. Pandolfelli, *Dispersão e empacotamento de partículas: Princípios e aplicações em processamento cerâmico.* São Paulo, SP, Brasil: Fazendo Arte, 2000.

[3]   B. L. Damineli, R. G. Pileggi, and V. M. John, "Influence of packing and dispersion of particles on the cement content of concretes," *Rev. IBRACON Estrut. Mater.*, vol. 10, no. 5, pp. 998–1024, Sep 2017, http://dx.doi.org/10.1590/s1983-41952017000500004.

[4]   J. J. Chen and A. K. H. Kwan, "Superfine cement for improving packing density, rheology and strength of cement paste," *Cement Concr. Compos.*, vol. 34, no. 1, pp. 1–10, Jan 2012, http://dx.doi.org/10.1016/j.cemconcomp.2011.09.006.

[5]   C. C. Furnas, Flow of gasses through beds of broken solids, *Bureau of Mines Bulletin*, vol. 307, pp. 1-144, 1929.

[6]   T. Stovall, F. de Larrard, and M. Buil, "Lineair packing density model of grain mixtures," *Powder Technol.*, vol. 48, pp. 1–12, 1986.

[7]   F. De Larrard, *Concrete Mixture Proportioning.* Boca Raton, FL, USA: CRC Press, 1999. http://dx.doi.org/10.1201/9781482272055.

[8]   W. Puntke, "Wasseranspruch von feinen Kornhaufwerken". Beton-Dusseldorf, vol. 52, no. 5, pp. 242–249, 2002.

[9]   S. A. A. M. Fennis, "Measuring water demand or packing density of micro powders: Comparison of methods," in *TUDelft Conference*, 2008, pp. 21.

[10] European Committee for Standardization, *Unbound and hydraulically bound mixtures - Part 2: Test methods for laboratory reference density and moisture content - Proctor compaction*, EN 13286-2, 2010.

[11] H. H. C. Wong and A. K. H. Kwan, "Packing density of cementitious materials: part 1—measurement using a wet packing method," *Mater. Struct.*, vol. 41, no. 4, pp. 689–701, May 2008, http://dx.doi.org/10.1617/s11527-007-9274-5.

[12] K. T. Miller, R. M. Melant, and C. F. Zukoski, "Comparison of the compressive yield response of aggregated suspensions: pressure filtration, centrifugation, and osmotic consolidation," *J. Am. Ceram. Soc.*, vol. 79, no. 10, pp. 2545–2556, Aug 2005, http://dx.doi.org/10.1111/j.1151-2916.1996.tb09014.x.

[13] A. M. Kjeldsen, *Consolidation Behavior of Cement-based systems. Influence of Inter-particle Forces*, Lyngby: Technical University of Denmark, 2007.

[14] H. Okamura and M. Ouchi, "Mix design for self-compacting concrete," *Concr. Libr. JSCE*, vol. 25, pp. 107–120, 1995.

[15] S. Mansoutre, P. Colombet, and H. Van Damme, "Water retention and granular rheological behavior of fresh C3S paste as a function of concentration," *Cement Concr. Res.*, vol. 29, no. 9, pp. 1441–1453, Sep 1999, http://dx.doi.org/10.1016/S0008-8846(99)00129-5.

[16] ASTM International, *Standard Test Methods for Time of Setting of Hydraulic Cement by Vicat Needle*, C191, 2019.

[17] S. Mansoutre, P. Colombet, and H. Van Damme, "Water retention and granular rheological behavior of fresh C3S paste as a function of concentration," *Cement Concr. Res.*, vol. 29, no. 9, pp. 1441–1453, Sep 1999, http://dx.doi.org/10.1016/S0008-8846(99)00129-5.

[18] I. Marquardt, *Ein Misschungskonzept für selbstverdichtenden Beton auf der Basis der Volumenkenngrössen und Wasseransprüche der Ausgangsstoffe*. Rostock (Germany): Rostocker Berichte, 2002. Beton 4/2002 ab Seite 197.

[19] L. Marquardt, "Determination of the composition of self-compacting concretes on the basis of the water requirements of the constituent materials – presentation of a new mix concept," *Bentonwerk + Fertigteiltechnik – BFT*, vol. 11, pp. 22–30, 2002.

[20] M. Hunger and H. J. H. Brouwers, "Flow analysis of water–powder mixtures: application to specific surface area and shape factor," *Cement Concr. Compos.*, vol. 31, no. 1, pp. 39–59, Jan 2009, http://dx.doi.org/10.1016/j.cemconcomp.2008.09.010.

[21] W. Pietsch, "Size enlargement by agglomeration," in *Handbook of Powder Science and Technology*, 2nd ed., E. E. Fayed and L. Otten, Eds., New York, NY, USA: John Wiley & Sons, Inc., 1997.

[22] B. Felekoğlu, "Effects of PSD and surface morphology of micro-aggregates on admixture requirement and mechanical performance of micro-concrete," *Cement Concr. Compos.*, vol. 29, no. 6, pp. 481–489, Jul 2007, http://dx.doi.org/10.1016/j.cemconcomp.2006.12.008.

[23] S. Fennis, T. Nijland, and J. Walraven, "Measuring the packing density to lower the cement content in concrete," in *Tailor Made Concrete Structures*, Boca Raton, FL, USA: CRC Press, 2008, pp. 108–108. http://dx.doi.org/10.1201/9781439828410.ch71.

[24] British Standards Institution, *Testing of Aggregates Part 2: Method of Determination of Density*, BS 812, 1995.

[25] ASTM International, *Standard Test Method for Relative Density (Specific Gravity) and Absorption of Coarse Aggregate*, C127, 2015.

[26] ASTM International, *Standard Test Method for Relative Density (Specific Gravity) and Absorption of Fine Aggregate*, C128, 2015.

[27] T. Sedran and F. de Larrard, "Manuel d'utilisation de René-LCPC, Logiciel d'optimisation granulaire", in *Bulletin de Liaison des Laboratoires des Ponts et Chaussees*. Paris (France): LCPC, 1994, pp. 87-93.

[28] K. T. Miller, R. M. Melant, and C. F. Zukoski, "Comparison of the compressive yield response of aggregated suspensions: pressure filtration, centrifugation, and osmotic consolidation," *J. Am. Ceram. Soc.*, vol. 79, no. 10, pp. 2545–2556, Aug 2005, http://dx.doi.org/10.1111/j.1151-2916.1996.tb09014.x.

[29] N. S. Klein, S. Cavalaro, A. Aguado, I. Segura, and B. Toralles, "The wetting water in cement-based materials: Modeling and experimental validation," *Constr. Build. Mater.*, vol. 121, pp. 34–43, Sep 2016, http://dx.doi.org/10.1016/j.conbuildmat.2016.05.164.

[30] A. Hermann, E. A. Langaro, S. H. L. Silva, and N. S. Klein, "Particle packing of cement and silica fume in pastes using an analytical model," *Rev. IBRACON Estrut. Mater.*, vol. 9, no. 1, pp. 48–65, Feb 2016, http://dx.doi.org/10.1590/S1983-41952016000100004.

[31] H. F. Campos, N. S. Klein, and J. Marques Filho, "Proposed mix design method for sustainable high-strength concrete using particle packing optimization," *J. Clean. Prod.*, vol. 265, pp. 121907, Aug 2020, http://dx.doi.org/10.1016/j.jclepro.2020.121907.

[32] H. F. Campos, N. S. Klein, J. Marques Filho, and M. Bianchini, "Low-cement high-strength concrete with partial replacement of Portland cement with stone powder and silica fume designed by particle packing optimization," *J. Clean. Prod.*, vol. 261, pp. 121228, Jul 2020, http://dx.doi.org/10.1016/j.jclepro.2020.121228.

[33] H. F. Campos, N. S. Klein, and J. Marques Filho, "Comparison of the silica fume content for high-strength concrete production: chemical analysis of the pozzolanic reaction and physical behavior by particle packing," *Mater. Res.*, vol. 23, no. 5, 2020, http://dx.doi.org/10.1590/1980-5373-mr-2020-0285.

[34] ASTM International, *Standard Test Method for Density of Hydraulic Cement*, C188, 2017.

[35] Associação Brasileira de Normas Técnicas, *Cimento Portland – Requisitos*, NBR 16697, 2018.

[36] ASTM International, *Standard Specification for Portland Cement*, C150, 2018.

[37] W. F. de Almeida, C. Matinc, A. B. Mendes, and O. Konrad, "Efeitos do uso de frequência de ultrassom na dispersão de sedimentos agregados," *Rev. Ibero-Americana Cienc. Ambientais*, vol. 8, no. 3, pp. 97–111, Aug 2017, http://dx.doi.org/10.6008/SPC2179-6858.2017.003.0010.

[38] ASTM International, *Standard Specification for Chemical Admixtures for Use in Producing Flowing Concrete*, C1017, 2003.

[39] P. A. Wedding and D. L. Kantro, "Influence of water-reducing admixtures on properties of cement paste—a miniature slump test," *Cem. Concr. Aggreg.*, vol. 2, no. 2, pp. 95, 1980, http://dx.doi.org/10.1520/CCA10190J.

[40] J. Cheung, A. Jeknavorian, L. Roberts, and D. Silva, "Impact of admixtures on the hydration kinetics of Portland cement," *Cement Concr. Res.*, vol. 41, no. 12, pp. 1289–1309, Dec 2011., http://dx.doi.org/10.1016/j.cemconres.2011.03.005.

[41] S. M. Iveson, J. D. Litster, K. Hapgood, and B. J. Ennis, "Nucleation, growth and breakage phenomena in agitated wet granulation processes: a review," *Powder Technol.*, vol. 117, no. 1–2, pp. 3–39, Jun 2001, http://dx.doi.org/10.1016/S0032-5910(01)00313-8.

[42] S. A. A. M. Fennis, *Design of Ecological Concrete by Particle Packing Optimization*. Netherlands: Gildeprint, 2011.

[43] L. Marquardt, "Determination of the composition of self-compacting concretes on the basis of the water requirements of the constituent materials – presentation of a new mix concept," *Bentonwerk + Fertigteiltechnik – BFT*, vol. 11, pp. 22–30, 2002.

[44] K. H. Hoang, P. Hadl, and N. V. Tue, "A New Mix Design Method for UHPC based on Stepwise Optimization of Particle Packing Density," in *First International Interactive Symposium on UHPC*, 2016, pp. 1–8.

[45] E. Yedra Álvarez, D. Ferrández Vega, P. Saiz Martínez, and C. Morón Fernández, "Low cost system for measuring the evolution of mechanical properties in cement mortars as a function of mixing water," *Constr. Build. Mater.*, vol. 244, pp. 118127, May 2020, http://dx.doi.org/10.1016/j.conbuildmat.2020.118127.

[46] N. Barroca, L. M. Borges, F. J. Velez, F. Monteiro, M. Górski, and J. Castro-Gomes, "Wireless sensor networks for temperature and humidity monitoring within concrete structures," *Constr. Build. Mater.*, vol. 40, pp. 1156–1166, Mar 2013., http://dx.doi.org/10.1016/j.conbuildmat.2012.11.087.

[47] E. Fraile-Garcia, J. Ferreiro-Cabello, E. Martinez de Pison Ascacibar, J. Fernandez Ceniceros, and A. V. Pernía Espinoza, "Implementing a technically and economically viable system for recording data inside concrete," *Constr. Build. Mater.*, vol. 157, pp. 860–872, Dec 2017, http://dx.doi.org/10.1016/j.conbuildmat.2017.09.139.

[48] S. K. Goudar, B. B. Das, S. B. Arya, and K. N. Shivaprasad, "Influence of sample preparation techniques on microstructure and nano-mechanical properties of steel-concrete interface," *Constr. Build. Mater.*, vol. 256, pp. 119242, Sep 2020, http://dx.doi.org/10.1016/j.conbuildmat.2020.119242.

[49] G. H. Nalon et al., "Effects of different kinds of carbon black nanoparticles on the piezoresistive and mechanical properties of cement-based composites," *J. Build. Eng.*, no. 32, pp. 101724, 2020, http://dx.doi.org/10.1016/j.jobe.2020.101724.

[50] C. Morón, D. Ferrández, P. Saiz, and E. Yedra, "Measuring system of capillary rising damp in cement mortars," *Measurement*, vol. 135, pp. 252–259, Mar 2019, http://dx.doi.org/10.1016/j.measurement.2018.11.071.

[51] D. F. Vega, E. Y. Alvarez, C. M. Fernandez, and A. M. Barrios, "Ensayos alternativos para la determinación del tiempo de fraguado. Métodos capacitivo y resistivo," *Dyna Ing. Industria*, vol. 95, no. 1, pp. 294–298, 2020, http://dx.doi.org/10.6036/9741.

[52] H. F. Campos, T. M. S. Rocha, G. C. Reus, N. S. Klein, and J. Marques Filho, "Determination of the optimal replacement content of Portland cement by stone powder using particle packing methods and analysis of the influence of the excess water on the consistency of pastes," *Rev. IBRACON Estrut. Mater.*, vol. 12, no. 2, pp. 210–232, Apr 2019, http://dx.doi.org/10.1590/s1983-41952019000200002.

IBRACON Structures and Materials Journal
Revista IBRACON de Estruturas e Materiais

ORIGINAL ARTICLE

Effect of carbon nanotubes on Portland cement matrices

Efeito de nanotubos de carbono em matrizes de cimento Portland

Thiago Melanda Mendes[a] (iD)
Marcelo Henrique Farias de Medeiros[b] (iD)

[a]Universidade Tecnológica Federal do Paraná – UTFPR, Departamento de Engenharia Ambiental, Londrina, PR, Brasil
[b]Universidade Federal do Paraná – UFPR, Departamento de Engenharia Civil, Programa de Pós-graduação em Engenharia Civil – PPGECC, Curitiba, PR, Brasil

Abstract: This study evaluates the effects of three carbon nanotubes with different geometric characteristics on the rheological behaviour and mechanical performance, as well as on the microstructure of mortars and cement pastes. For nanotube content ranging from 0.025 to 0.2 wt%, the yield stress and viscosity were determined by rotational rheometry, and mechanical performance was evaluated by flexural strength and dynamic modulus of elasticity. The microstructural analysis was performed by X-ray diffraction, thermogravimetric analysis and scanning electron microscopy (SEM). The obtained results showed that the yield stress presents a considerable increase as the carbon nanotube content increases. The viscosity was also influenced by the presence of carbon nanotubes. The flexural strength of mortars increases for different amounts of carbon nanotubes, and depending on the geometric characteristics of the carbon nanotubes, the material behaves like a composite. The microstructural analysis showed the nucleation of hydration products on the surface of the carbon nanotubes, and that the better mechanical performance of matrices containing carbon nanotubes is not related to the increase in hydration products.

Keywords: rheological properties, mechanical properties, x-ray diffraction, thermo-gravimetry, scanning electron microscopy.

Resumo: este estudo avaliou os efeitos de três nanotubos de carbono com diferentes características geométricas no comportamento reológico e desempenho mecânico, assim como na microestrutura de argamassas e pastas de cimento. Para teores de nanotubos de carbono variando de 0.025 a 0.2%, a tensão de escoamento e a viscosidade foram determinadas por meio de reometria rotacional, e o desempenho mecânico foi avaliado através da resistência a flexão e módulo de elasticidade dinâmico. A análise microestrutural foi conduzida através da difração de raios-X, análise termogravimétrica, e microscopia eletrônica de varredura. Os resultados obtidos mostram que a tensão de escoamento apresenta um aumento considerável com o aumento no teor de nanotubos. E a viscosidade também é influenciada pela presença dos nanotubos de carbono. A resistência à flexão das argamassas aumenta para os diferentes teores de nanotubos de carbono. E dependendo das características geométricas dos nanotubos, o material se comporta como um compósito. A análise microestrutural mostrou a nucleação de produtos de hidratação sobre a superfície dos nanotubos de carbono, e que o melhor desempenho mecânico das matrizes contendo nanotubos de carbono não está relacionada com o aumento dos produtos de hidratação.

Palavras-chave: comportamento reológico, desempenho mecânico, difração de raios-X, análise termogravimétrica, microscopia eletrônica de varredura.

1 INTRODUCTION

The use of carbon nanotubes is a recent practice. The first studies were developed in the 20th century and published by Li et al. [1] and Yakolev et al. [2]. Since this research, interest in this topic has increased considerably. The

rheological behaviour of cement-based materials is directly affected by the incorporation of carbon nanotubes. An increase in viscosity of cement pastes due to the incorporation of the same type of carbon nanotubes was demonstrated by Konsta-Gdoutos et al. [3]. A linear increase in yield stress was published by Andrade et al. [4], Reales et al. [5], [6], and Batiston et al. [7] for cement based-material pastes formulated with a carbon nanotube content of less than 0.2 wt%. For larger amounts of carbon nanotubes, Medeiros et al. [8] and Jiang et al. [9] observed an exponential increase in yield stress for mixtures containing up to 0.5 wt% of carbon nanotubes.

Many studies have evaluated the effect of the same type of carbon nanotubes with and without functionalization on mechanical performance of cement-based materials. However, only some of the available references evaluated the geometric characteristics of carbon nanotubes: the diameter was kept constant and the length varied by Konsta-Gdoutos et al. [10], Musso et al. [11], Al-Rub et al. [12] and Chen et al. [13]. While the length was kept constant and the diameter of carbon nanotubes was changed in the studies developed by Collins et al. [14] and Gao et al. [15]. The diameter and length were both varied in studies published by Sobolkina et al. [16], Souza et al. [17], Hawreen [18], [19] and Manzur et al. [20].

Considering that the effect of carbon nanotubes on mechanical performance of cement-based materials is a microstructure response, the mechanisms of these fibers in cementitious matrices were discussed by Fehervari et al. [21], Chen et al. [22] and Ramezani et al. [23]. Chen et al. [22] showed that part the carbon nanotubes can adsorb on the surface of cement particles, and part of them can perform as a reinforcing material. The improvement in the strength of mortars formulated with a low content of carbon nanofibers (< 1 wt%) was not related to the increase in hydration products or the reduction of porosity as published by Fehervari et al. [21]. Thus, this paper aims to study the effect of carbon nanotubes with different geometric characteristics on rheological behaviour, mechanical performance and cementitious matrix microstructure.

2 MATERIALS AND EXPERIMENTAL PROGRAM

Three different aqueous suspensions of multi-walled carbon nanotubes (MWCNT) were obtained from Nano Amorphous Materials. They were called CNT_1, CNT_2 and CNT_3, and their characteristics are listed in Table 1. According to the supplier procedures, the carbon nanotubes were dispersed using a combination of 90 wt% of aromatic modified polyethylene glycol ether (PEG) and 10 wt% of water. The amount of dispersing agent present in each product can be calculated (Nanoamor, 2022). According to information provided by the supplier, the diameter and length of different samples of carbon nanotubes was obtained from High Resolution Transmission Electron Microscopy and Raman spectroscopy.

Table 1 – Physical characteristics of MWCNT suspensions [2]

Description	CNT_1	CNT_2	CNT_3
Diameter (nm)	> 50	20-30	30-50
Length (μm)	10-20	10-30	10-20
Specific surface area (m^2/g)	43.00	39.38	55.94
Density (g/cm^3)	2.10	2.10	2.10
Solids concentration (wt%)	7-8	3	1
*CNT/water dispersant	1.7%	1.3%	1.1%
Water dispersant concentration (mmol/l)	1.78	0.559	0.154

The specific surface area was measured by gas adsorption (B.E.T). Samples were dried in an oven at 105°C and kept under a vacuum of 68.9 pascal at 60°C for 24 hours. The density of carbon nanotubes was obtained from the supplier. Table 2 presents the physical-chemical characteristics of Portland cement type CPV-ARI, equivalent to type III cement [24]. Chemical composition was determined by X-ray fluorescence in an unpressed sample, using the EDX 750 Shimadzu equipment. Lignosulfonate-based superplasticizer was used as a dispersing additive. The particle size distributions of carbon nanotubes and Portland cement CPV-ARI were determined with a Malvern 2200 laser granulometer, which was also used to evaluate the granulometry of carbon nanotubes by Yakovlev et al. [25], and Krause et al. [26] for carbon nanotubes in dry powder condition. Transmission Electron Microscopy (TEM) of carbon nanotube suspensions was carried out with Fei Tecnai G2 equipment, operating at 80 and 120 kV. The samples of nanotube suspensions were diluted to 1 mg/ml. Five milliliters (5μl) of these diluted suspensions were placed on a copper-carbon grid (300 mesh) and covered with Formvar.

Figure 1 shows the Portland cement diffractogram and the main phases were identified: Alite (C_3S) – $3CaO.SiO_2$, Belite (C_2S) – $2CaO.SiO_2$, Gypsum - $Ca.SO_4.1/2H_2O$ and Calcium hydroxide - $Ca(OH)_2$ [27], as well as the aluminum oxide (Al_2O_3) peaks at $2\theta = 25.5, 35.15, 43.35°$. The presence of Arkanite – $K_2.SO_4$, and Langbeinite – $K_2Mg_2(SO_4)_3$ phosphates phases was identified considering their peaks at $2\theta = 30.78°$ and $31.02°$, respectively. The chemical analysis

of cement (Table 2) did not reveal the presence of aluminum oxide, which does not allow the formation of Tricalcium aluminate (C_3A) and was not identified in X-ray diffraction considering its main peaks at $2\theta = 20.95°$ and $33.25°$.

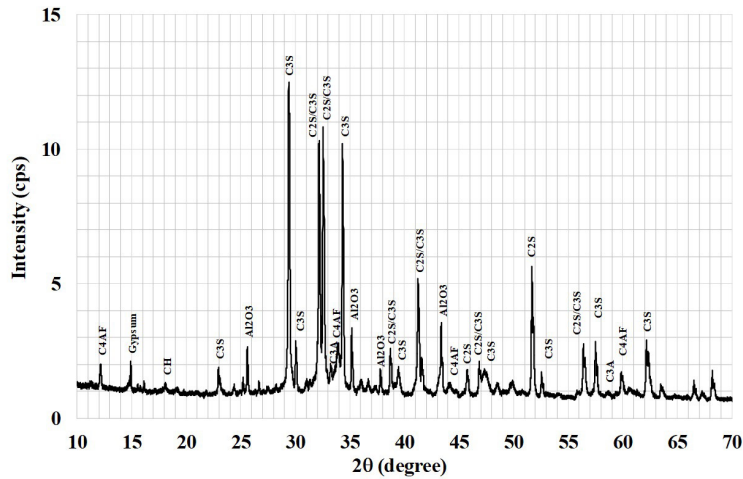**Figure 1.** Diffractogram of Portland cement CPV-ARI

The presence of tetra-calcium ferro-aluminate (C_4AF) – $4CaO.Al_2O_3.Fe_2O_3$ can be replaced by tetra calcium ferrite, $4CaO.Fe_2O_3$, as iron ions can take the place of aluminum ions in a crystalline structure of C_4F [27]. Chemical analysis also revealed a considerable percentage of potassium oxide, 5.87% of K_2O. This is even considering that the amount of this element was combined in sulfate phase, for example, the Arkanite $K_2.SO_4$. There is only 0.693% of SO_3 according to the chemical analysis, which can represent an amount around 1.5% of $K_2.SO_4$. Thus, subtracting the percentage of 0.816% of K_2O chemically bounded in the sulfate phase, there is 5.05% of K_2O which must be chemically bounded with the clinker phases. Taylor [27] reported that Woermann et al. found that up to 1.4% of Na_2O or K_2O can be incorporated into C_3S, where the sodium and potassium ions can replace calcium ions. Or even a type of belite phase compound (Glascrite) $KC_{23}S_{12}$ can be used, which contains 3.5% of potassium

Table 2 – Physical-chemical characteristics of Portland cement

Description	CaO	SiO$_2$	K$_2$O	Fe$_2$O$_3$	SO$_3$
Chemical composition (%)	65.01	22.62	5.86	5.05	0.69
Lost in ignition (%)				6.61	
Specific surface Area (m²/g)				1.419	
Density (g/cm³)				2.99	

A reference mixture without carbon nanotubes, and mixtures formulated with 0.025, 0.05, 0.1 and 0.2 wt% of CNT_1, CNT_2 and CNT_3 were evaluated. The lignosulfonate-based dispersant content was fixed at 1 wt.% of solids, and the water/solids ratio of 0.375 was kept constant. For all mixtures, the water content of the dispersant and carbon nanotube suspensions was subtracted from the total amount. For mortars, the cement:sand ratio was fixed at 1:1. In order to consider the possible influence of the amount of polyethylene glycol on the evaluated properties, the concentration of this dispersing agent in each formulation was calculated, whose values are listed in Table 3.

The suspensions of carbon nanotubes and the dispersant were previously diluted in deionized water. The mixing was carried out in a laboratory planetary mixer, applying the following process: (i) the dry powder was mixed at 60 rpm for 60s; (ii) 2/3 of suspension (water + dispersant) was added and mixed at 60 rpm for 120s; (iii) 1/3 of suspension was added (water + carbon nanotubes) and mixed at 60 rpm for 120s. Contents ranging from 600 to 650g were mixed for each batch. A temperature-controlled rheometer with Vane geometry with a diameter of 15 mm and a height of 30 mm was used to measure the rheological properties of pastes. Flow curves were obtained using a shear rate control, ranging from 10 to 100 s^{-1}, in 10 s^{-1} intervals. The shear rate (γ) was increased from 10 to 100 s^{-1} (upper curve) and reduced from 100 to 10 s^{-1} (downs curve). The pastes were held for 30 seconds at each shear rate and the values were recorded

in the last 3 seconds. The yield stress (τ_0) and the plastic viscosity (η) were calculated using the Bingham Equation ($\tau = \tau_0 + \eta*\gamma$), considering the upper-steps curve. All rotational rheometry tests were performed at 23°C after 5 minutes of adding water to the powder.

Table 3 - Mixtures

Properties	Cement (g)	Suspension of CNT (g)	PEG (mmol)	Water (L)	Concentration (mmol/L)
Reference	300	0	0	0.1125	0
0.025% CNT_1	300	1.07	1.907	0.1125	16.95
0.05% CNT_1	14.35	2.14	3.814	0.1125	33.90
0.1% CNT_1	18.02	4.28	7.628	0.1125	67.80
0.2% CNT_1	22.27	8.57	15.257	0.1125	135.6
0.025% CNT_2	19.42	2.5	1.398	0.1125	12.42
0.05% CNT_2	45.46	5	2.796	0.1125	24.85
0.1% CNT_2	32.44	10	5.593	0.1125	49.71
0.2% CNT_2	32.52	20	11.186	0.1125	99.42
0.025% CNT_3	21.71	7.5	1.159	0.1125	10.30
0.05% CNT_3	18.76	15	2.318	0.1125	20.60
0.1% CNT_3	19.16	30	4.637	0.1125	41.21
0.2% CNT_3	47.96	60	9.274	0.1125	82.43

Six prismatic samples (1.6x4x16cm) of mortars were molded; compaction was applied to avoid molding defects. The samples were kept at 23°C for 24 hours and immersed in a saturated calcium hydroxide solution at 23°C for 7 days. The flexural strength of mixtures was measured on six prismatic samples, which had the upper face milled to remove surface irregularities. The flexural strength was measured using a universal testing machine applying a strain rate of 0.1 mm/s. The dynamic modulus of elasticity was measured according to standard procedure [28].

For the microstructural analysis, the inner part of the paste sample was extracted, which was maintained under the same curing conditions described above. For X-ray diffraction and thermogravimetric analysis, the samples were ground and sieved through 200 mesh (0.075 mm). The diffractogram of samples was obtained in a Buckler X-ray diffractometer operating at 30 kV and 10 mA, with a copper tube, from 10 to 70° at 0.01°/s. Thermogravimetric analysis was performed from 100 to 950°C with a heating rate of 10°C/min in an alumina crucible, with a nitrogen flow of 20 ml/min. The microstructure of the samples was analyzed by scanning electron microscope (SEM) coupled to an energy dispersive spectrometer (EDS) using Quanta 600 FEI-Philips equipment, operating at 25 kV. The gold coating was applied to the surface of the sample for this analysis.

4 RESULTS AND DISCUSSIONS

Figure 2 presents the transmission electron micrographies of carbon nanotubes CNT_1, which shows in Figure 2a the presence of large agglomerates of nanotubes, with dimensions of 14 and 23 μm. Near this large particle, it is possible to observe a smaller particle of nanotube agglomerates with a diameter around 2 μm. A tangle of carbon nanotubes with a length around 6.5 μm can also be seen, as well as some individual fibers of carbon nanotubes with a size of 3.4 μm. Figure 2b and c show carbon nanotubes with lengths of 250 and 263 nm and diameters of 14 and 16 nm, respectively. Figure 3 presents the TEM micrographies of carbon nanotubes CNT_2, which shows a similar agglomeration of carbon nanotubes. Here the carbon nanotubes have a length of around 3.26 and 1,06 μm and diameters varying from 47 to 69 nm. Figure 4 presents the TEM micrographies of carbon nanotubes CNT_3, which in Figure 4a shows micrometric agglomerates of carbon nanotubes, as well as entangled fibers and individual particles of carbon nanotubes. The diameter of the carbon nanotubes varies from 37 to 39 nm. Considering the values of diameter and length declared by the supplier, there is a clear difference from the values observed in the TEM micrographies for CNT_1 and CNT_2 carbon nanotubes. For carbon nanotubes CNT_3, the diameter values observed in the TEM images are in interval range declared by the supplier. According to the supplier, for values described in the Table 1, the length was obtained from high resolution transmission electron microscopy and the diameter was found from Raman spectroscopy. The particle sizes of three carbon nanotubes, namely diameter and length, were also observed in a previous publication [29]. As seen in the TEM images, the sonication process used for preparation of samples of carbon nanotubes for microscopy, or even possibly used by the supplier for dispersing them, resulted in breaking carbon nanotubes into small parts.
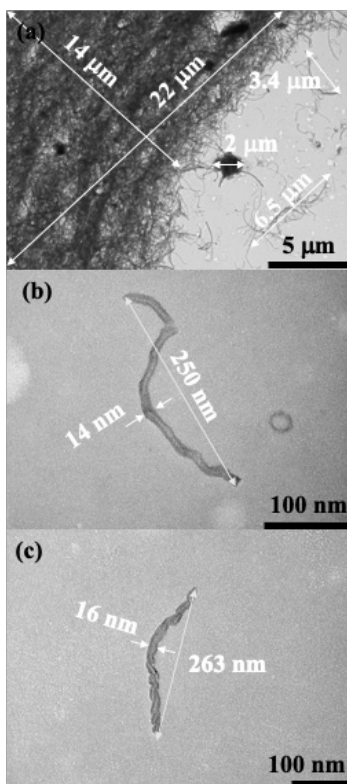
Figure 2. Transmission electron micrographies of carbon nanotubes CNT_1
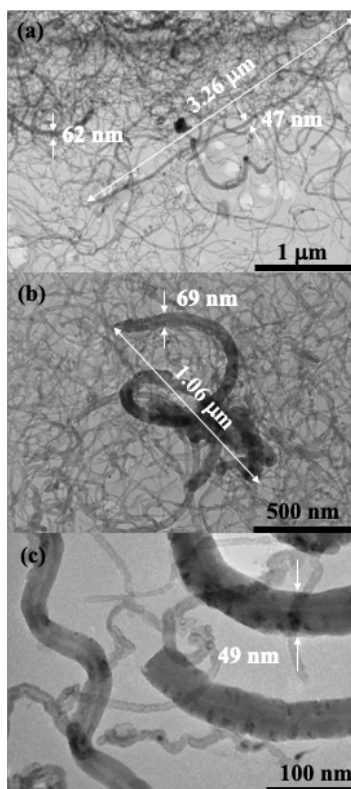
Figure 3. Transmission electron micrographies of carbon nanotubes CNT_2

Rev. IBRACON Estrut. Mater., vol. 16, no. 5, e16508, 2023

5/16
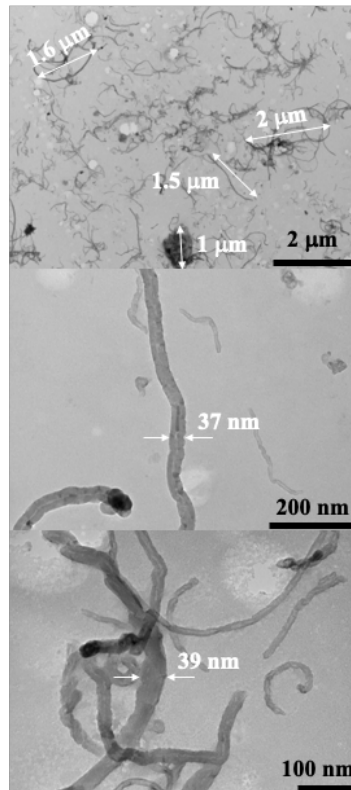
Figure 4. Transmission electron micrographies of carbon nanotubes CNT_3

Figures 5 presents the particle size distribution of carbon nanotubes and Portland cement obtained by laser granulometry. Carbon nanotubes have micrometric particles ranging from 1 to 100 μm and another population of particles smaller than 1 μm. CNT_1 is coarser than CNT_2 and CNT_3. Thus, considering the specific surface area of carbon nanotubes, it is verified in Table 1 that CNT_3 presented the highest SSA, while CNT_1 and CNT_2 presented similar values. The granulometry of carbon nanotubes before and after the ultrasonic dispersion was evaluated by Yakovlev et al. [25]. When in an agglomerated condition, nanotubes present the main volume of micrometric particles (> 1 μm), while the use of ultrasonic dispersion leads to the predominance of nanoparticles. The ultrasonic dispersion leads not only to a disentanglement of agglomerates of carbon nanotubes, but also to their rupture or breakage as reported by Hawreen et al. [18], [19] and Yakovlev et al. [25]. These two populations of particles, micrometric agglomerates or tangles of carbon nanotubes, are also observable in the TEM micrographies between 1 and 100 μm, as well as particles smaller than 1 μm, which are probably individual fibers of carbon nanotubes or pieces of them, resulting from the sonication process.
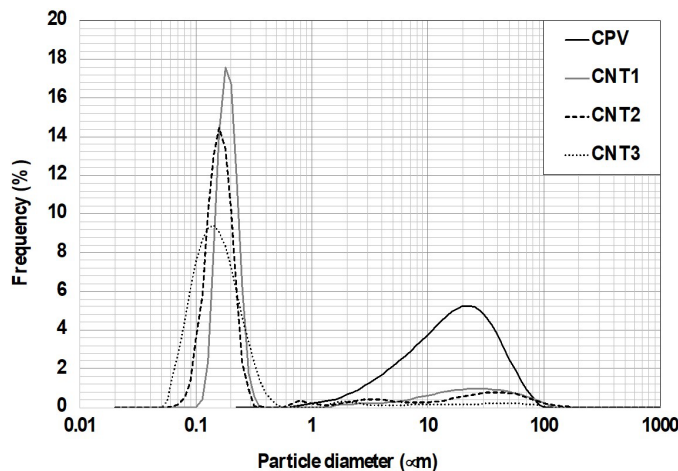
Figure 5. Particle size distribution Portland cement and carbon nanotubes

The laser granulometry test cannot assess the morphology of fibrous particles, such as diameter and length, even with equipment that combines laser granulometry and image analysis techniques. This technique provides information of the sizes of agglomerates or clamped particles, as well as dispersed carbon nanotubes and their small pieces, without a classification of their dispersion conditions [25], [26]. When combined with other techniques such as transmission electron microscopy and specific surface area, the laser granulometry test can help to understand how these particles affect the rheological behaviour of cementitious matrices [29]. Other techniques are available, such as UV-VIS spectroscopy [24], electro-acoustic attenuation spectroscopy [29], and LUMiSizer centrifugal methods [26].

Figure 6a shows the rheograms of reference paste and mixtures formulated with 0.1 and 0.2 wt% of CNT_1 carbon nanotubes. The Bingham Model was considered to fit a linear equation. The rheological behaviour was considerably altered due to the incorporation of carbon nanotubes in cementitious matrix. Table 4 lists the calculated volumetric concentration (V_S), volumetric surface area (VSA), porosity (P_0) and interparticle separation (IPS) calculations of the studied mixtures according to Funk and Dinger [30], and the yield stress and viscosity of cement pastes obtained from the Bingham model. Figure 6b shows the correlation between the interparticle separation (IPS) and yield stress of mixtures, in which a good correlation can be obtained. The most probable effect of carbon nanotubes is to reduce the interparticle separation of these suspensions, resulting in an exponential increase in yield stress, which is inversely proportional to interparticle separation IPS ($1/IPS^2$) [31]. Regarding the yield stress, the volumetric surface area (VSA) can be pointed as the main variable responsible for this rheological property. While the viscosity of suspensions is mainly affected by the increase of the solid concentration (V_S), which changed from 47.14% to 47.16%, viscosity does not present a good correlation with the Interparticle Separation (IPS).
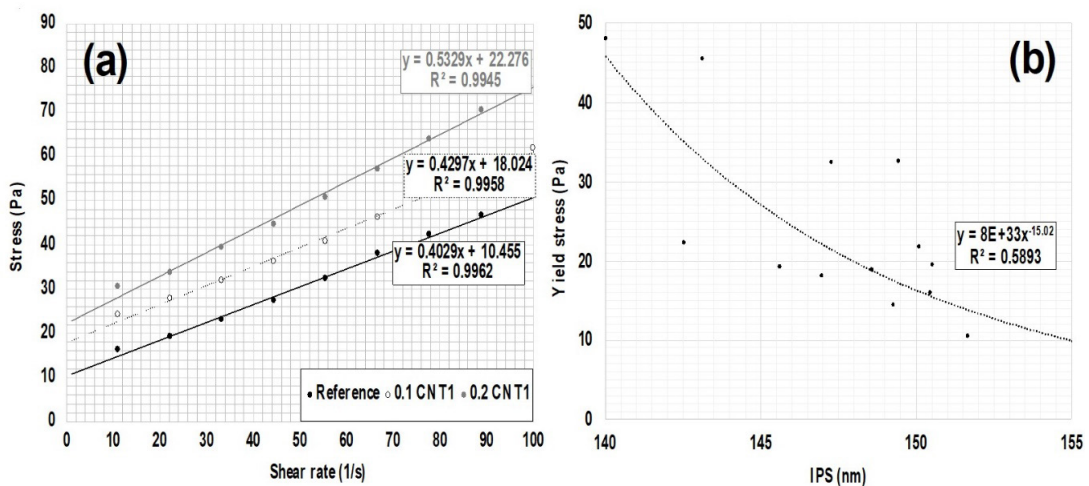
Figure 6. (a) Rheograms of mixtures (b) Effect of Interparticle separation (IPS) on the yield stress

Table 4 - Rheological properties of mixtures

Properties	V_S (%)	VSA (m²/cm³)	P_0 (%)	IPS (nm)	τ_0 (Pa)	η (Pa.s)
Reference	47.14	4.24	32.33	151.66	10.45	0.36
0.025% CNT_1	47.14	4.27	32.35	150.46	15.85	0.44
0.05% CNT_1	47.15	4.30	32.36	149.28	14.35	0.35
0.1% CNT_1	47.15	4.37	32.40	146.97	18.02	0.43
0.2% CNT_1	47.16	4.49	32.46	142.55	22.27	0.53
0.025% CNT_2	47.14	4.27	32.35	150.54	19.42	0.41
0.05% CNT_2	47.15	4.30	32.37	149.44	45.46	0.49
0.1% CNT_2	47.15	4.35	32.41	147.29	32.44	0.45
0.2% CNT_2	47.16	4.47	32.48	143.14	32.52	0.63
0.025% CNT_3	47.14	4.27	32.34	150.72	21.71	0.50
0.05% CNT_3	47.15	4.32	32.37	148.59	18.76	0. 43
0.1% CNT_3	47.15	4.40	32.41	145.63	19.16	0.44
0.2% CNT_3	47.16	4.56	32.48	140.03	47.96	0.36

V_S – solids content – VSA – Volumetric surface area – P_0 – calculated porosity – IPS – Interparticle separation - average flexural strength τ_0 - yield stress – η − viscosity

The type and content of surfactant was also cited as a variable responsible to the rheological change in cement formulated with carbon nanotubes [5], [6]. However, a similar increase of the rheological properties was observed by Batiston et al. [7] and Medeiros et al. [8] for mixtures containing carbon nanotubes, which used samples of carbon nanotubes in a powdered form without a surfactant agent for dispersing the carbon nanotubes. A polycarboxylate acid was used as a dispersing agent in both cases. Thus, considering the high amount of dispersing lignosulphonate employed here (1 wt%), which also acts as an entrapped air agent, and the lower dosage of surfactant in a mmol fraction, these same rheological properties, yield stress and viscosity, do not present a good correlation with the content of surfactant (Table 2).

The mechanical properties of mixtures formulated with carbon nanotubes CNT_1, CNT_2 and CNT_3 were also listed in Table 5. All mixtures have flexural strength values higher than reference. For mixtures containing carbon nanotubes CNT_1 and CNT_3, the maximum value was reached at 0.025 wt%. For CNT_2 carbon nanotubes, the optimal content, or the smallest quantity of nanotubes that led to the highest mechanical performance, was 0.05 wt%. Unlike the others, the flexural strength of CNT_2 carbon nanotubes increases after reaching the optimal content. Recently, a statistical study was published by Ramezani et al. [23], evaluating the large number of published studies on the use of carbon nanotubes in cement-based materials. Considering the flexural or tensile strength, the authors suggested an optimal content of 0.15 wt% of carbon nanotubes. For an experimental approach in the same study, they reached an optimal content of 0.1 wt% of carbon nanotubes, considering the flexural strength.

Figure 7a presents the stress (f_{tm}) x deflection (δ) curves of all evaluated samples. For the reference mixture, the typical behaviour of brittleness was identified. A maximum deflection (δ_{max}) of 0.2287 mm was achieved for this cementitious matrix. When 0.025 wt% of CNT_1 was added to this cementitious matrix, one of the six samples presented a higher deformation capacity. A maximum deflection (δ_{max}) of 0.4612 mm was observed, and the inclination of initial part of stress x deflection curve showed a reduction compared to the other samples. These two differences suggest a typical composite behaviour for this sample. The tenacity of this sample reached 1.88 J, considerably higher than the average value of 0.79 for mixtures containing 0.025 wt% of CNT_1 and listed in Table 5. A similar change in deformability of the same samples was observed for other mixtures formulated with CNT_1, as seen in Figure 7c, d and e. Figure 7f presents the typical behaviour of the reference mixtures and all samples containing CNT_1, which present the behaviour of a composite. A type of "plasticity" was verified in some stress x deflection curves, which can be attributed to the sample cracking and the performance of carbon nanotubes as a reinforcing material.

The same approach was considered for the mixtures formulated with carbon nanotubes CNT_2 and CNT_3, which are showed in Figures 8 and 9. There are many samples for different contents of carbon nanotubes, which present a typical composite behaviour. The behaviour of a composite type was mainly observed in Figure 8f, Figure 9f and Figure 7f. Thus, there is a higher probability of obtaining a composite type behaviour for CNT_2 (12/24), followed by a smaller probability for CNT_3 (7/24) and the least probability for CNT1 (5/24). According to Callister [32], a minimum critical length was required when fibers are added into a matrix (Equation A).

Table 5 - Mechanical properties of mixtures

Properties	f_{tm} (MPa)	Tenacity (J)	E_d (GPa)	δ_{MAX} (mm)
Reference	5.89 +/- 0.68	0.50 +/- 0.20	29.22 +/- 0.58	0.2287
0.025% CNT_1	7.53 +/- 1.50	0.79 +/- 0.57	29.78 +/- 0.30	0.4612
0.05% CNT_1	6.86 +/- 1.61	0.84 +/- 0.23	29.95 +/- 1.42	0.4262
0.1% CNT_1	6.35 +/- 1.14	0.75 +/- 0.38	28.31 +/- 0.78	0.3937
0.2% CNT_1	6.68 +/- 0.81	0.76 +/- 0.60	28.52 +/- 1.25	0.4512
0.025% CNT_2	6.02 +/- 0.55	0.62 +/- 0.32	30.38 +/- 1.07	0.3012
0.05% CNT_2	7.28 +/- 0.85	1.01 +/- 0.23	30.03 +/- 1.95	0.3762
0.1% CNT_2	6.92 +/- 1.17	0.71 +/- 0.27	29.80 +/- 2.61	0.3413
0.2% CNT_2	7.81 +/- 2.13	1.14 +/- 0.51	30.92 +/- 0.71	0.4325
0.025% CNT_3	7.80 +/- 1.58	0.88 +/- 0.41	29.98 +/- 2.55	0.3063
0.05% CNT_3	6.33 +/- 0.83	0.62 +/- 0.27	30.03 +/- 2.31	0.3312
0.1% CNT_3	5.98 +/- 2.14	0.46 +/- 0.17	28.28 +/- 2.05	0.2062
0.2% CNT_3	6.92 +/- 0.99	0.68 +/- 0.20	28.71 +/- 0.93	0.3012

Rev. IBRACON Estrut. Mater., vol. 16, no. 5, e16508, 2023

8/16
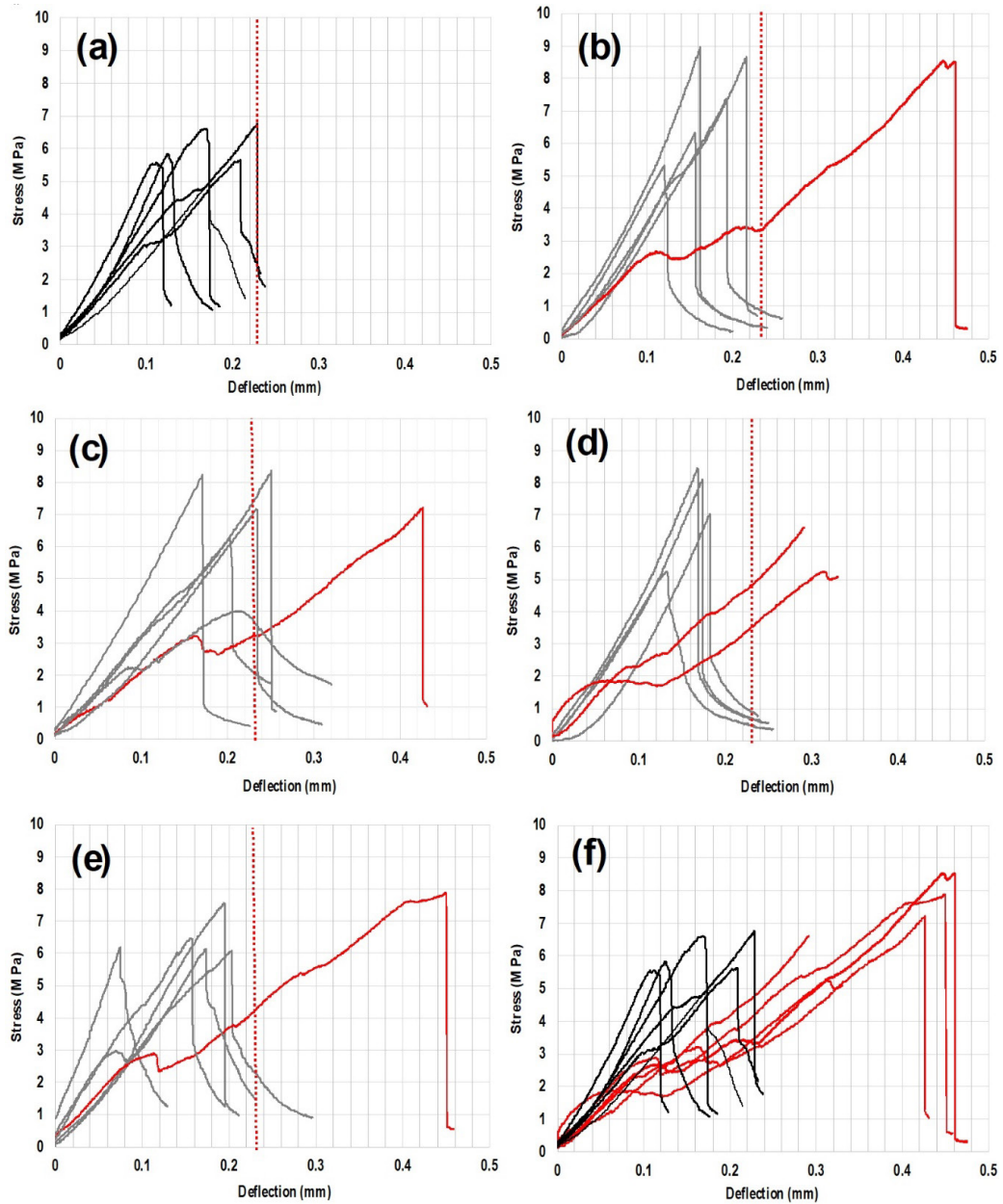
Figure 7. Stress x deflection of flexural tests (a) Reference (b) 0.025 wt.% CNT_1 (c) 0.05 wt.% CNT_1 (d) 0.1 wt.% CNT_1 (e) 0.2 wt.% CNT_1 (f) Reference and composite's samples containing CNT_1

Rev. IBRACON Estrut. Mater., vol. 16, no. 5, e16508, 2023

9/16
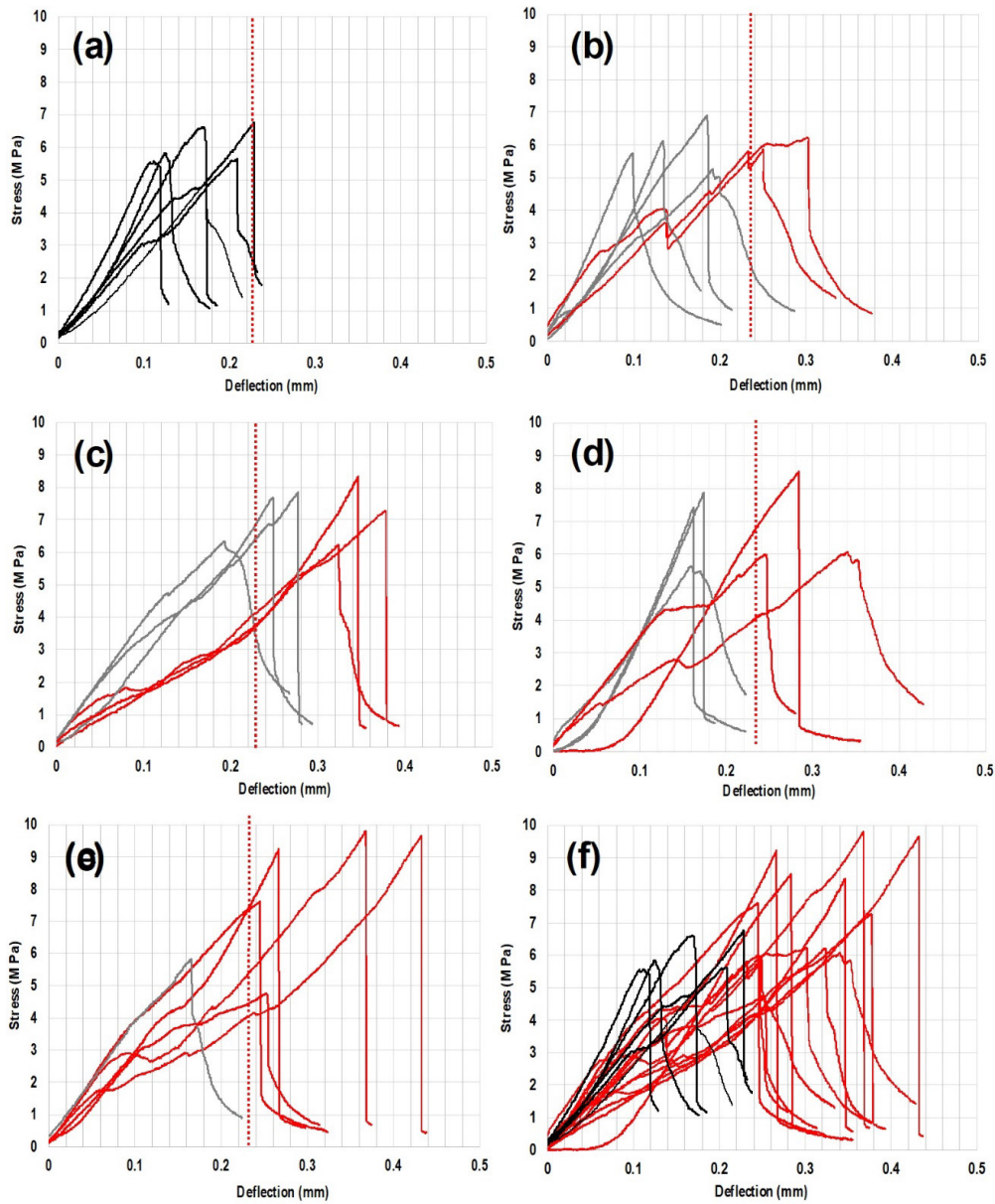
Figure 8. Stress x deflection of flexural tests (a) Reference (b) 0.025 wt.% CNT_2 (c) 0.05 wt.% CNT_2 (d) 0.1 wt.% CNT_2 (e) 0.2 wt.% CNT_2 (f) Reference and composite's samples containing CNT_2

Figure 9. Stress x deflection of flexural tests (a) Reference (b) 0.025 wt.% CNT_3 (c) 0.05 wt.% CNT_3 (d) 0.1 wt.% CNT_3 (e) 0.2 wt.% CNT_3 (f) Reference and composite's samples containing CNT_3

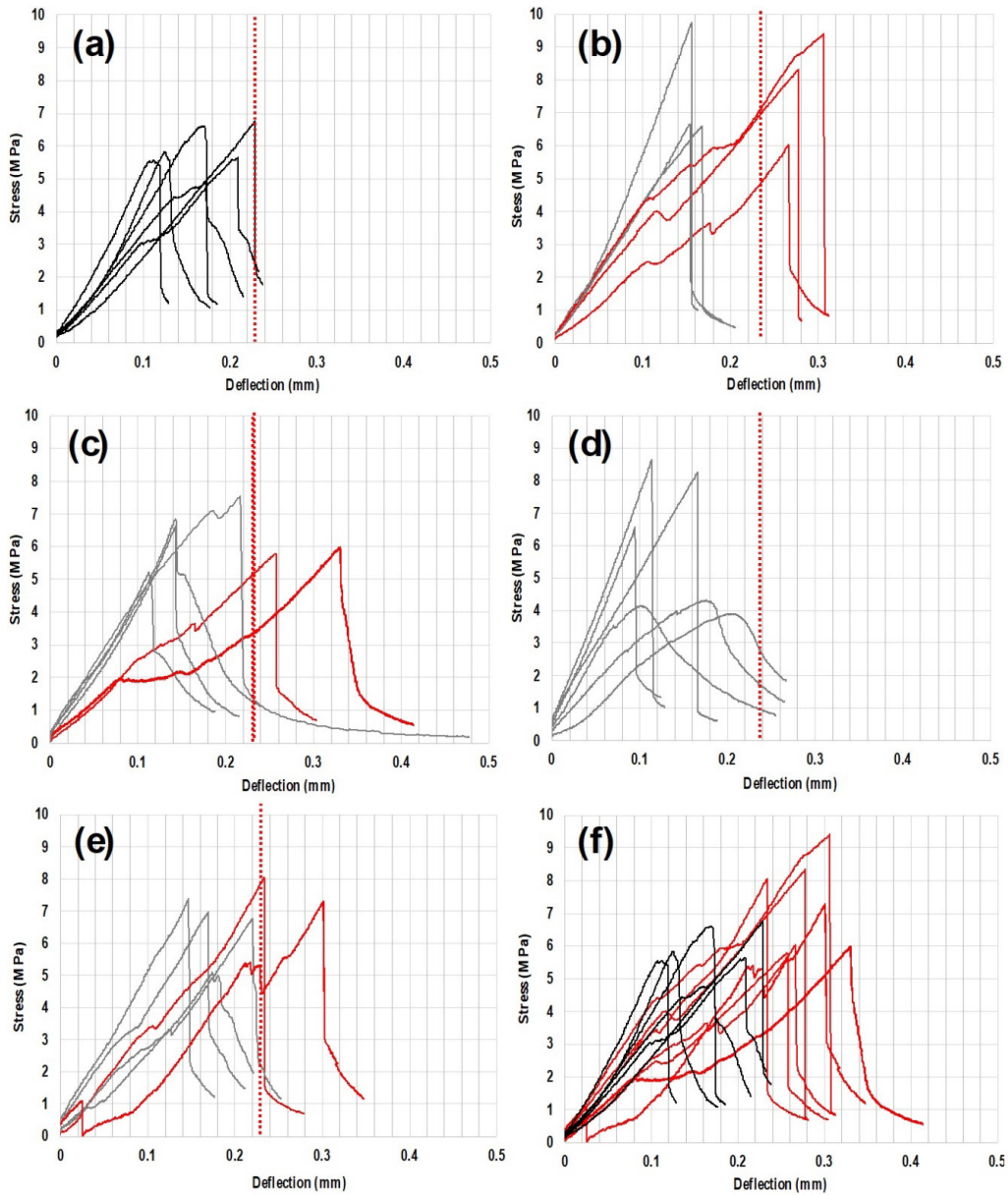Considering that the length (l_c), the diameter (d) and the tensile strength of carbon nanotubes (σ_f) are chosen, this last one can be considered equal to 850 MPa [33] or kept constant. The matrix strength (σ_m) or the adherence strength between carbon nanotubes and cementitious matrix is the only variable considered, which is proportional to its tensile strength. Peyvandi et al. [34] evaluated the effect of cementitious paste density, and consequently strength, on the performance efficiency of carbon nanofibers. The authors demonstrated that the efficiency of carbon nanofiber reinforcement was improved when the mechanical strength of cementitious matrix was increased. To assess how the adherence strength influenced the reinforcement efficiency of carbon nanotubes in cement-based materials, an efficiency factor called reinforced efficiency (R_E) can be estimated by Equation B. This is given by the ratio between the adherence strength (σ_m) required from Equation A, and the tensile strength of refence mixture without carbon nanotubes (σ_{REF} = 5.89 MPa). Table 6 presents the calculated values for CNT_1, CNT_2 and CNT_3, considering their geometric characteristics.

Rev. IBRACON Estrut. Mater., vol. 16, no. 5, e16508, 2023

11/16

$$l_c = [(\sigma_f.d)/(2.\sigma_m)]$$

<div align="right">Equation A</div>

$$R_E = (\sigma_{REF}/\sigma m)$$

<div align="right">Equation B</div>

Table 6 - Geometric and adherence strength properties of carbon nanotubes

Properties	CNT_1	CNT_2	CNT_3
l_c (micra)	15	20	15
d (nm)	50	25	40
l/d	300	800	375
σ_f (MPa)	850	850	850
σ_m (MPa)	1.416	0.531	1.133
R_E	5.89/1.416= 4.15	5.89/0.531= 11.08	5.89/1.133= 5.19

Figure 10a presents the probability of occurrence of similar composite behaviour for different Reinforced efficiency (R_E) values, which are indirectly related to the aspect ratio of carbon nanotubes. As the adherence mechanism is improved due to the geometric characteristics of carbon nanotubes, the probability of occurrence of behaviour similar to composite increases. In the mixtures formulated with CNT_2, which presented the best adherence mechanism between fiber and cementitious matrix, the probability of occurrence of behaviour similar to composite also increases according to CNT_2 content, as shown in Figure 10b. For the other carbon nanotubes, this relationship between fiber volume and composite like behaviour was not identified.
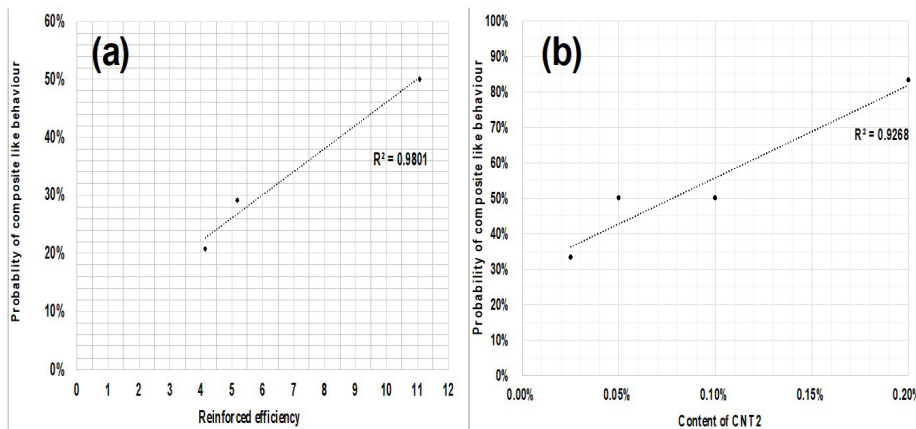
Figure 10. Probability of composite like behaviour as function of (a) Reinforced efficiency (b) volume of carbon nanotubes CNT2

Figure 11 shows the effects of carbon nanotubes on the hydration of Portland cement pastes containing 0.2 wt% of carbon nanotubes CNT_1, CNT_2 and CNT_3, named C01, C02 and C03. The thermogravimetric analysis of these mixtures showed that the composition C01 presents the highest mass loss, followed by compositions C03 and C02. Considering the mass loss between 100 and 400ºC, which represents the calcium silicate and aluminate hydrates (C-S-H/C-A-H) [27], the mixtures C01, C03 and C02 showed values of 8.4, 7.8 and 5.2%, respectively. As for calcium hydroxide content, for temperatures ranging from 400 to 600ºC [27], these formulations showed a mass loss of 4.7, 3 and 2.3%, respectively. For temperatures above 600ºC [27], the decarbonation of calcium carbonate showed similar values ranging from 11.1 to 12.1%.

Figure 12 shows the diffractogram of composites C01, C02 and C03, containing 0.2 wt% of carbon nanotubes CNT_1, CNT_2 and CNT_3. Considering the C_3S peaks at $2\theta = 29.5º$, the highest consumption of this phase was observed for the composite C01, followed by C02 and C03, respectively. Consequently, an inverse trend was observed for the main calcium hydroxide peaks at $2\theta = 34.1º$. These results revealed that the increase in flexural strength observed for these formulations was not related to hydration products, since the C02 mixture, which presented the highest flexural strength, had the lowest mass loss for the hydration products. Likewise, the C02 mixture, which presents the highest flexural strength, did not present the maximum consumption of C_2S/C_3S phases, or the lowest peak for these phases. Recently,

Rev. IBRACON Estrut. Mater., vol. 16, no. 5, e16508, 2023

12/16

Fehervari et al. [21] revealed that mechanisms for improved strength of mortars formulated with carbon nanofibers were not related to the hydration products. For higher dosages of carbon nanofibers (1 wt%), as compared with the values considered here, authors reported no difference on the porosity of mixtures formulated with or without these nanoparticles. The obtained results indicate that the geometric characteristic of carbon nanotubes can be pointed as an important issue. This approach of considering the aspect ratio and mechanical performance was also used by Hawreen et al. [19] and Batiston et al. [7]. For mixtures containing 0.1 wt% of carbon nanotubes with different aspect ratios, they showed that flexural strength was improved as the aspect ratio of carbon nanotubes increases.
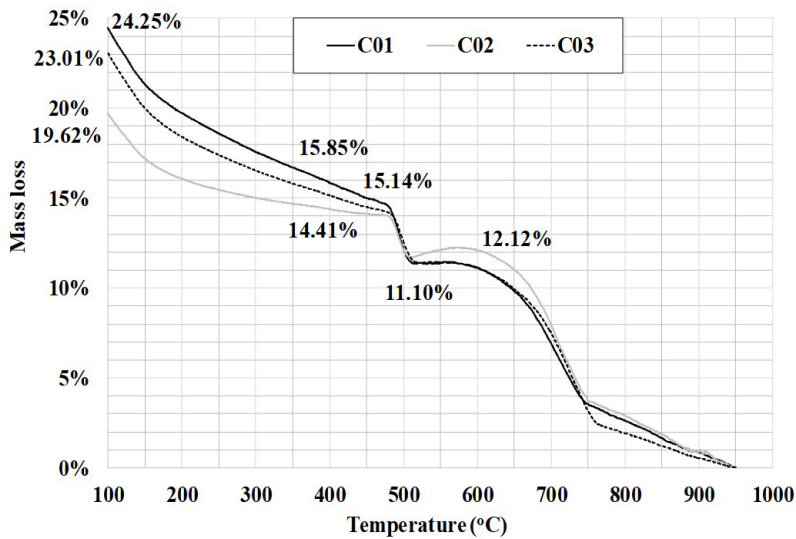
Figure 11. Thermo-gravimetric analysis of composites C01, C02 and C03
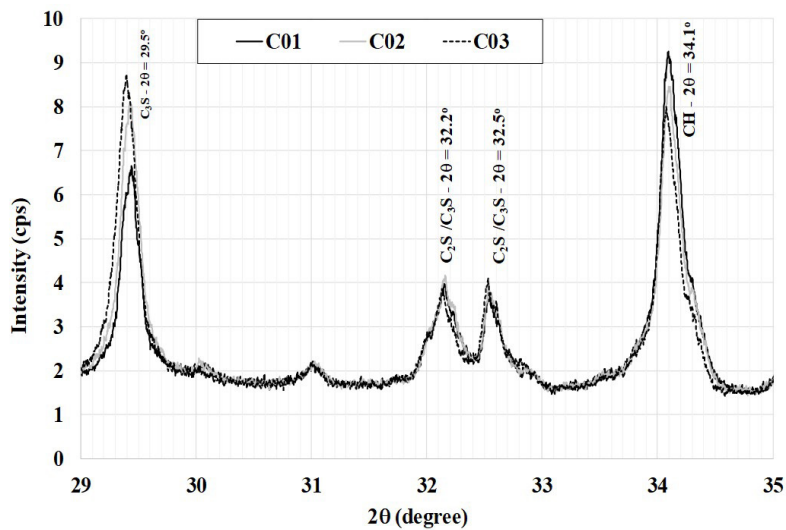
Figure 12. Diffractograms of composites C01, C02 and C03

Figure 13a shows a clear increase of diameter of the carbon nanotubes due to the growth of hydration products on the surface of nanoparticles. Figure 13b shows that the carbon nanotubes are entrapped into the hydration products. Figure 13c shows one carbon nanotube adhered on the surface of a cement particle, with the longest length covered by hydration products. Figure 13d shows many carbon nanotubes in a pore of the cementitious matrix, and the indication of the growth of a hydration product due to the nucleation effect of carbon nanotubes.
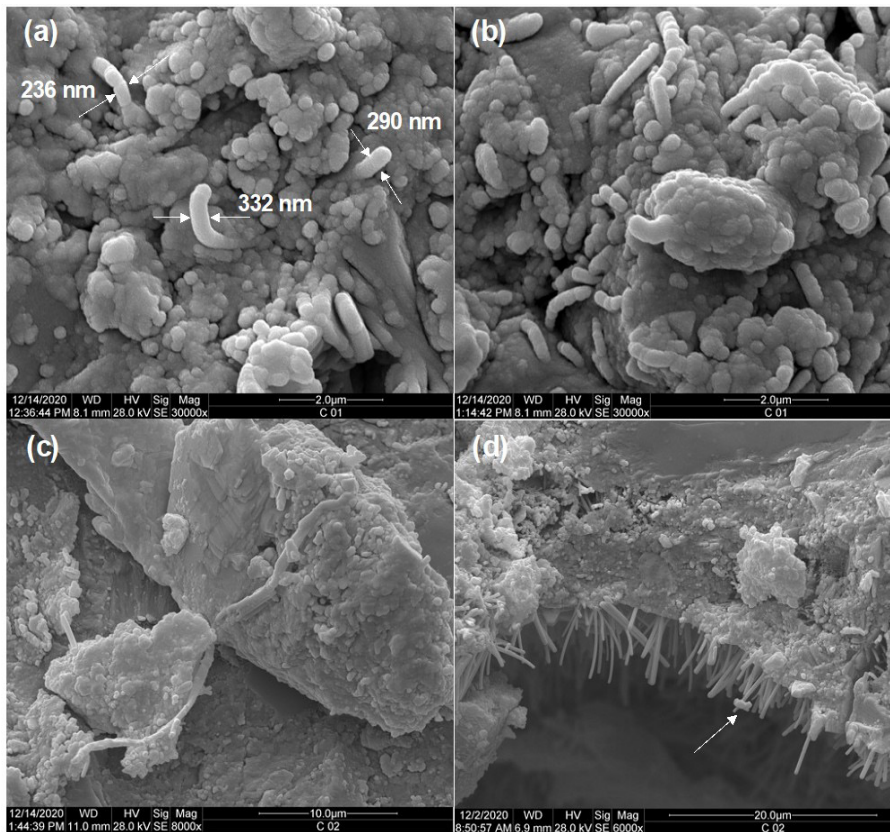
Figure 13. Scanning electron micrographies of carbon nanotubes in Portland cement matrix

4 CONCLUSIONS

Carbon nanotubes affect the rheological properties of the Portland cement matrix. The high specific surface area of nanoparticles led to a reduction of the interparticle separation, and, consequently, to increasing the yield stress and viscosity of suspensions.

The mechanical performance is improved due to the incorporation of carbon nanotubes into the Portland cement matrix. A composite like behaviour was observed, which is directly related to the geometric characteristics of these nanoparticles.

The microstructural analysis showed that the geometric characteristics of carbon nanotubes do not change the hydration of these composite materials. The nucleation of hydration products takes place on the surface of carbon nanotubes.

ACKNOWLEDGEMENTS

REFERENCES

[1] G. Y. Li, P. M. Wang, and X. Zhao, "Mechanical behavior and microstructure of cement composites incorporating surface treated multi-walled carbon nanotubes," *Carbon*, vol. 43, no. 6, pp. 1239–1245, 2005, http://dx.doi.org/10.1016/j.carbon.2004.12.017.

[2] G. Yakolev, J. Keriene, A. Gailius, and I. Girniere, "Cement based foam concrete reinforced by carbon nanotubes," *Medziagotyra*, vol. 12, no. 2, pp. 147–151, 2006.

[3] M. S. Konsta-Gdoutos, Z. S. Metaxa, and S. P. Shah, "Highly dispersed carbon nanotube reinforced cement-based materials," *Cement Concr. Res.*, vol. 40, no. 7, pp. 1052–1059, 2010, http://dx.doi.org/10.1016/j.cemconres.2010.02.015.

[4] J. S. Andrade No., T. Santos, S. A. Pinto, C. M. R. Dias, and D. V. Ribeiro, "Effect of the combined use of carbon nanotubes (CNT) and metakaolin on the properties of cementitious matrices," *Constr. Build. Mater.*, vol. 271, pp. 121903, 2021, http://dx.doi.org/10.1016/j.conbuildmat.2020.121903.

Rev. IBRACON Estrut. Mater., vol. 16, no. 5, e16508, 2023

14/16

[5] O. A. M. Reales, Y. P. A. Jaramillo, J. C. O. Botero, C. A. Delgado, J. H. Quintero, and R. D. Toledo Fo., "Influence of MWCNT/surfactant dispersions on the rheology of Portland cement pastes," *Cement Concr. Res.*, vol. 107, pp. 101–109, 2018, http://dx.doi.org/10.1016/j.cemconres.2018.02.020.

[6] O. A. M. Reales, P. Duda, and R. Dias Toledo Filho, "Effect of a carbon nanotube/surfactant aqueous dispersion on the rheological and mechanical properties of portland cement pastes," *J. Mater. Civ. Eng.*, vol. 30, no. 10, pp. 04018259, 2018, http://dx.doi.org/10.1061/(ASCE)MT.1943-5533.0002452.

[7] E. Batiston, P. J. P. Gleize, P. Mezzomo, F. Pelisser, and P. R. Matos, "Effect of Carbon Nanotubes (CNTs) aspect ratio on the rheology, thermal conductivity and mechanical performance of Portland cement paste," *Rev. IBRACON Estrut. Mater.*, vol. 14, no. 5, e14510, 2021, http://dx.doi.org/10.1590/s1983-41952021000500010.

[8] M. H. F. Medeiros, F. Dranka, A. J. Mattana, and M. R. M. M. Costa, "Portland cement composites with carbon nanotubes (CNT) addition: properties in freshly state and compressive strength," *Rev. Materia*, vol. 20, no. 1, pp. 127–144, 2015, http://dx.doi.org/10.1590/S1517-707620150001.0014.

[9] S. Jiang et al., "Rheological properties of cementitious composites with nano/fiber fillers," *Constr. Build. Mater.*, vol. 158, pp. 786–800, 2018., http://dx.doi.org/10.1016/j.conbuildmat.2017.10.072.

[10] M. S. Konsta-Gdoutos, Z. S. Metaxa, and S. P. Shah, "Multi-scale mechanical and fracture characteristics and early-age strain capacity of high-performance carbon nanotube/cement nanocomposites," *Cement Concr. Compos.*, vol. 32, no. 2, pp. 110–115, 2010., http://dx.doi.org/10.1016/j.cemconcomp.2009.10.007.

[11] S. Musso, J. M. Tulliani, G. Ferro, and A. Tagliaferro, "Influence of carbon nanotubes structure on the mechanical behavior of cement composites," *Compos. Sci. Technol.*, vol. 69, no. 11-12, pp. 1985–1990, 2009., http://dx.doi.org/10.1016/j.compscitech.2009.05.002.

[12] R. K. A. Al-Rub, A. I. Ashour, and B. M. Tyson, "On the aspect ratio effect of multi-walled carbon nanotubes reinforcements on the mechanical properties of cementitious nanocomposites," *Constr. Build. Mater.*, vol. 35, pp. 647–655, 2012., http://dx.doi.org/10.1016/j.conbuildmat.2012.04.086.

[13] Z. Chen, J. L. G. Lim, and E. Yang, "Ultra-high-performance cement-based composites incorporating low dosage of plasma synthesized carbon nanotubes," *Mater. Des.*, vol. 108, pp. 479–487, 2016, http://dx.doi.org/10.1016/j.matdes.2016.07.016.

[14] F. Collins, J. Lambert, and W. H. Duan, "The influences of admixtures on the dispersion, workability and strength of carbon nanotube-OPC paste mixtures," *Cement Concr. Compos.*, vol. 34, no. 2, pp. 201–207, 2012, http://dx.doi.org/10.1016/j.cemconcomp.2011.09.013.

[15] F. Gao, W. Tian, Z. Wang, and F. Wang, "Effect of diameter of multi-walled carbon nanotubes on mechanical properties and microstructure of the cement-based materials," *Constr. Build. Mater.*, vol. 260, pp. 120452, 2020, http://dx.doi.org/10.1016/j.conbuildmat.2020.120452.

[16] A. Sobolkina et al., "Dispersion of carbon nanotubes and its influence on the mechanical properties of the cement matrix," *Cement Concr. Compos.*, vol. 34, no. 10, pp. 1104–1113, 2012, http://dx.doi.org/10.1016/j.cemconcomp.2012.07.008.

[17] D. J. Souza, L. Y. Yamashita, F. Dranka, M. H. F. Medeiros, and R. A. Medeiros-Junior, "Repair mortars incorporating multiwalled carbon nanotubes: shrinkage and sodium sulfate attack," *J. Mater. Civ. Eng.*, vol. 29, no. 12, 2017, http://dx.doi.org/10.1061/(ASCE)MT.1943-5533.0002105.

[18] A. Hawreen, J. A. Bogas, and A. P. S. Dias, "On the mechanical and shrinkage of cement mortars reinforced with carbon nanotubes," *Constr. Build. Mater.*, vol. 168, pp. 459–470, 2018, http://dx.doi.org/10.1016/j.conbuildmat.2018.02.146.

[19] A. Hawreen, J. A. Bogas, M. Guedes, and M. F. C. Pereira, "Dispersion and reinforcement efficiency of carbon nanotubes in cementitious composites," *Mag. Concr. Res.*, vol. 71, no. 8, pp. 408–423, 2019, http://dx.doi.org/10.1680/jmacr.17.00562.

[20] T. Manzur, N. Yazdani, and M. B. Emon, "Effect of carbon nanotube size on the compressive strengths of nanotube reinforced cementitious composites," *J. Mater.*, vol. 2014, pp. 960984, 2014, http://dx.doi.org/10.1155/2014/960984.

[21] A. Fehervari et al., "On the mechanisms for improved strengths of carbon nanofiber-enriched mortars," *Cement Concr. Res.*, vol. 136, pp. 106178, 2020, http://dx.doi.org/10.1016/j.cemconres.2020.106178.

[22] S. J. Chen, W. Wang, K. Sagoe-Crentsil, F. C. X. L. Zhao, M. Majumderc, and W. H. Duan, "Distribution of carbon nanotubes in fresh ordinary Portland cement pastes: understanding from a two-phase perspective," *RSC Advances*, vol. 6, no. 7, pp. 5745–5753, 2016, http://dx.doi.org/10.1039/C5RA13511G.

[23] M. Ramezani, Y. H. Kim, and Z. Sun, "Z. Sun Z. Mechanical properties of carbon-nanotube-reinforced cementitious materials: database and statistical analysis," *Mag. Concr. Res.*, vol. 72, no. 20, pp. 1047–1071, 2020, http://dx.doi.org/10.1680/jmacr.19.00093.

[24] L. Silvestro et al., "Influence of ultrasonication of functionalized carbon nanotubes on the rheology, hydration, and compressive strength of Portland cement pastes," *Materials*, vol. 14, no. 18, pp. 5248, 2021, http://dx.doi.org/10.3390/ma14185248.

[25] G. I. Yakovlev et al., "Modification of cement matrix using carbon nanotubes dispersion and nano-silica," *Procedia Eng.*, vol. 172, pp. 1261–1269, 2017, http://dx.doi.org/10.1016/j.proeng.2017.02.148.

[26] B. Krause, M. Mende, P. Pötschke, and G. Petzold, "Dispersability and particle size distribution of CNTs in an aqueous surfactant dispersion as a function of ultrasonic treatment time," *Carbon*, vol. 48, no. 10, pp. 2746–2754, 2010, http://dx.doi.org/10.1016/j.carbon.2010.04.002.

[27] H. F. W. Taylor, *Cement Chemistry*. London: Academic Press, 1990, 451 p.

[28] American Society for Testing and Materials, *Standard Test Method for Dynamic Young´s Modulus, Shear Modulus, and Poisson´s Ratio by Impulse Excitation of Vibration*, E1876, 2009.

[29] T. M. Mendes and W. L. Repette, "Carbon nanotubes added to Portland cement matrices containing nanosilica," *Acta Scientiarum*, vol. 2, pp. 1, 2022.

[30] J. E. Funk and D. Dinger, *Predictive Process Control of Crowed Particulate Suspension*. Massachusetts: Springer, 1994, 786 p.

[31] R. J. Flatt and P. Bowen, "Yodel: a yield stress model for suspensions," *J. Am. Ceram. Soc.*, vol. 89, no. 4, pp. 1244–1256, 2006, http://dx.doi.org/10.1111/j.1551-2916.2005.00888.x.

[32] W. D. J. Callister, *Fundaments of Materials Science and Engineering*. Rio de Janeiro: LCT, 2006.

[33] H. Kim et al., "Tensile properties of millimeter-long multi-walled carbon nanotubes," *Sci. Rep.*, vol. 7, no. 1, pp. 9512, 2017, http://dx.doi.org/10.1038/s41598-017-10279-0.

[34] A. Peyvandi, L. A. Sbia, P. Soroushian, and K. Sobolev, "Effect of the cementitious paste density on the performance efficiency of carbon nanofiber in concrete nanocomposite," *Constr. Build. Mater.*, vol. 48, pp. 265–269, 2013, http://dx.doi.org/10.1016/j.conbuildmat.2013.06.094.

IBRACON Structures and Materials Journal
Revista IBRACON de Estruturas e Materiais

ORIGINAL ARTICLE

Proposal for estimating the punching shear load-carrying capacity of steel fibers reinforced concrete flat slabs

Proposta para estimativa de capacidade de carga na punção de lajes lisas de concreto armado reforçado com fibras de aço

Lucas Guedes Dantas[a]

Leonardo Henrique Borges de Oliveira[b]

Antônio Carlos dos Santos[a]

Leandro Mouta Trautwein[c]

[a]Universidade Federal de Uberlândia – UFU, Faculdade de Engenharia Civil, Uberlândia, MG, Brasil

[b]Universidade Federal Rural do Semi-Árido – UFERSA, Departamento de Engenharia e Tecnologia, Pau dos Ferros, RN, Brasil

[c]Universidade Estadual de Campinas – UNICAMP, Faculdade de Engenharia Civil, Arquitetura e Urbanismo, Campinas, SP, Brasil

Abstract: This paper proposes an adjusted function for estimating the punching shear load-carrying capacity of concrete flat slabs without shear reinforcement according to the Brazilian standard code. The Adjusted function considers the influence of the steel fiber content. Data from 68 steel fiber reinforced concrete slabs (SFRC slabs) were used, simulating the connection of flat slabs with square section columns. These slabs were obtained from a study conducted by 14 different researchers. The parameters used for the adjusted function were the fiber content and the compressive strength of the concrete. The adjusted function was obtained by curve-fitting. The result from the adjusted function shows a relation in the order of 1.3 between the experimental rupture load and the calculated load, a value close to that already obtained by the normative text when the calculation is for conventional concrete. This shows that the proposal presented here keeps the same level of security with a confidence index of 96% in comparison with other authors' models presented in this study.

Keywords: load-carrying capacity, steel fiber reinforced concrete, SFRC, punching shear, flat slabs.

Resumo: Este trabalho propõe uma função para estimar a capacidade de carga com ruptura na punção de lajes lisas de concreto sem armadura de cisalhamento de acordo com a norma brasileira. A função considera a influência do teor de fibra de aço na adição do concreto. Foram utilizados dados de 68 lajes de concreto armado com fibras de aço, simulando a ligação de lajes lisas com pilares de seção quadrada. Essas lajes foram obtidas a partir de um estudo realizado por 14 pesquisadores diferentes. Os parâmetros utilizados para a função foram o teor de fibras e a resistência à compressão do concreto. A função foi obtida por ajuste de curva. O resultado da função ajustada mostra uma relação da ordem de 1,3 entre a carga de ruptura experimental e a carga calculada, valor próximo ao já obtido pelo texto normativo quando o cálculo é para concreto convencional. Isso mostra que a proposta aqui apresentada mantém o mesmo nível de segurança com um índice de confiança de 96% em comparação com os modelos de outros autores apresentados neste estudo.

Palavras-chave: capacidade de carga, concreto armado reforçado com fibras de aço, CRF, punção, lajes lisas.

L. G. Dantas, L. H. B. Oliveira, A. C. Santos, and L. M. Trautwein

1 INTRODUCTION

The traditional structural system of reinforced concrete structures is characterized by slabs, beams and columns. In this system, loads are applied directly to the slabs, which transfers it to the beams. The beams transfer the efforts to the columns, which are supported by the foundation of the building. However, a new system emerged at the beginning of the 20th century, as an innovative structural model, to which beams are not used and the forces from the slabs are directly transferred to the columns. Because the slabs have uniformity due to the absence of the beams, they were called flat slabs Gasparini [1]. However, in this structural system there is the possibility of collapsing the flat slabs by punching shear mechanism.

Punching Shear can occur as the result of a concentrated load applied to a structural element. In flat slabs, for example, the collapse occurs in the connection with structural elements. The magnitude of shear efforts generated by the concentrated forces are high, which can cause the rupture of the slab.

One of the punching shear load carrying-capacity design methods adopted by several standards codes is called the critical perimeter surface. It consists of verifying whether a uniform shear stress that is applied to a determined critical surface, perpendicular to the slab's median plane, located at a distance from the face of the column is compatible with the concrete's shear strength in this same region. If the shear strength is not sufficient to withstand the shear stress, the use of punching shear reinforcement is indicated. ABNT NBR 6118 (2014) [2] indicates studs-type connectors preferably as a punching shear reinforcement.

According to ABNT NBR 6118 (2014) [2], the shear stress is given by :

$$\tau_{Sd} = \frac{F_{Sd}}{ud} \tag{1}$$

Where:
F_{Sd} = Load-carrying capacity (Force);
u = shear critical perimeter (Length);
d = average slab effective depth in both directions (Length).

For slabs without punching shear reinforcement, the stress of the compressive concrete diagonal is checked, considering the critical perimeter as the perimeter of the column or loaded area. In addition, a control perimeter with a slab distant up to twice the average of the slab's effective depth (d) is checked. Figure 1 shows the control perimeter for central columns sections of rectangular and circular sections .
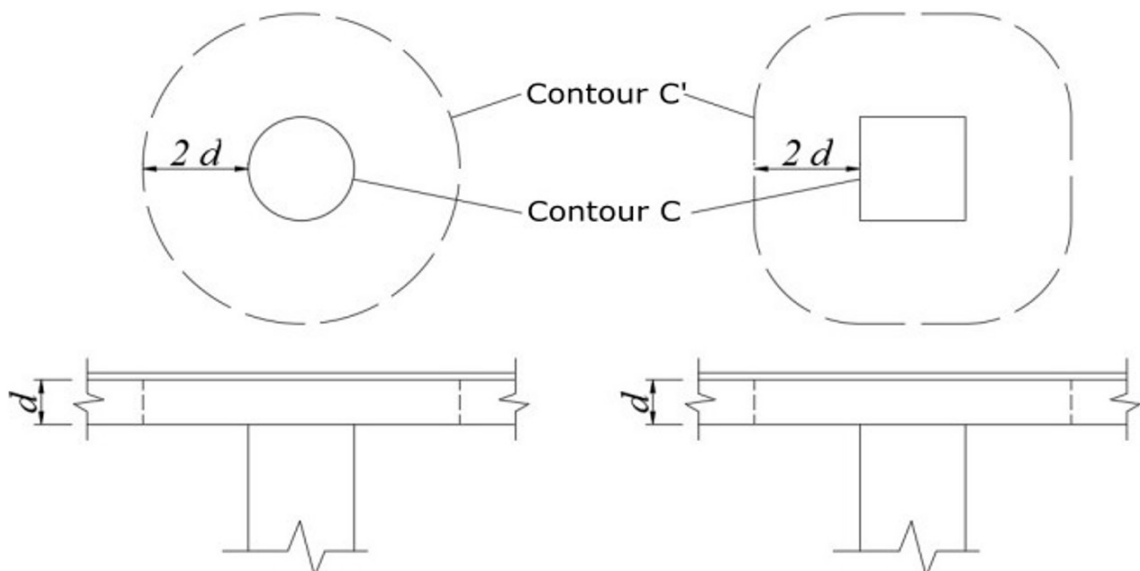
Figure 1. Critical Shear Perimeter C and C '(Adapted from ABNT NBR 6118 (2014) [2]).

Equations 2 and 3 show the shear strengths of the control surfaces related to the contours C and C ', respectively.

$$\tau_{rd1} = 0.27(1 - \frac{f_{ck}}{250})f_{cd} \tag{2}$$

$$\tau_{rd2} = 0.13 \left(1 + \sqrt{\frac{20}{d}}\right)(100\rho f_{ck})^{1/3} \tag{3}$$

Where:

τ_{rd1}, τ_{rd2} = shear strength of slabs without punching reinforcement (MPa);

f_{ck} = concrete's compressive strength;

$f_{cd} = (f_{ck}/\gamma_c)$ – concrete design strength;

d = Average slab effective depth in both directions;

$\rho = (\rho_x\rho_y)^{0.5}$ – Flexural Reinforcement Ratio in both directions of the slab, at up to $3d$ from the edge of the column or loaded area (dimensionless).

The estimated load-carrying capacity of slabs can be found by replacing τ_{rd1} or τ_{rd2} in Equation 1 and isolating the calculation force, as shown in Equation 4:

$$F_{rd} \leq \begin{cases} \tau_{rd1}ud \\ \tau_{rd2}ud \end{cases} \tag{4}$$

The accuracy of the standard code equations in comparison to experimental results presents a significant discrepancy. According to Dantas [3], who compares a series of experimental results of slabs without shear reinforcement, on average the relationship between the experimental load-carrying capacity and one obtained according to ABNT NBR 6118 (2014) [2] is 1.3. It is important to note that this relationship is obtained without the use of normative safety factors of increase / reduction.

In general, the addition of steel fibers to the referred mechanism contributes to the ductility of the system, cracking control and load redistribution [4]–[10]]. Also, experimental tests showed that monitored reinforcement bars presented a reduction in the strains observed in comparison to concrete slabs without steel fibers [8]. Other authors presented that the critical shear perimeter presented an increase by the addition of steel fiber content ([4] and [11]]). This differences in performance contribute to increasing the load-carrying capacity of flat slabs.

Recently, it was published a Brazilian Standard Code for designing fiber reinforced concrete elements, the ABNT NBR 16935 (2021) [12]]. The Brazilian code recommendations for punching shear depends on post-cracking parameters $f_{Ftu,k}$, demanding a $P \times CMOD$ from a three-point bending test. This study presents an alternative study for estimating the load-carrying capacity for steel fibers reinforced concrete flat slab collapsing by punching based on the results from 68 experimental tests and without the need for post-cracking parameters.

Regarding design, recent research has shown that the use of steel fibers can increase the punching shear strength of flat slabs, as well as transform the dynamics of the rupture of the slab-column connection, from fragile to ductile [4]–[6], [13]–[23]. The models studied in this paper presented this increase compared to other to slabs molded by conventional concrete.

This work aims to propose an adjusted function in the formulation existing in the NBR 6118 standard code ABNT NBR 6118 (2014) [2] that estimates the load-carrying of flat reinforced concrete slabs, considering the steel fibers contents. To determine this adjustment function, results from 68 tests of fiber reinforced concrete slabs supported on their edges and tested under concentrated load applied in a square section, using the slab-column connection (without the use of shear reinforcement).

2 ANALYTICAL METHOD

The proposed adjustment Function G is based on two parameters. The first parameter is given by the steel fiber content. The second is the dimensionless parameter k, which is adjusted according to the experimental results and defined according to the concrete compressive strength (f_c). The adjustment function applied to the NBR 6118 standard equation ABNT NBR 6118 (2014) [2] is given by (5) and (6):

$$\tau_{rd1} = 0.27 \left(1 - \frac{f_{ck}}{250}\right) f_{cd} G(V_f, k) \tag{5}$$

$$\tau_{rd2} = 0.13 \left(1 + \sqrt{\frac{20}{d}}\right) (100\rho f_{ck})^{1/3} G(V_f, k) \tag{6}$$

Since τ_{rd2} is lower than τ_{rd1} in most cases, adjustment of the dimensionless parameter k is performed only in Equation 6. Still, according to Dantas [3], several types of adjusted function are proposed for the Function G, of which, the one with the best adaptability in relation to the experimental results is given by Equation 7.

$$G(V_f, k) = (1 + ln(1 + kV_f)) \tag{7}$$

Where:
k = Parameter that correlates the compressive strength of concrete (dimensionless);
V_f = Steel fiber content (% by volume of concrete).

2.1 Definition of the Parameter k

The function G was adjusted by a logarithmic fitting-curve of the experimental tests conducted by authors presented in a database. Table 1 shows the list of researchers and the number of tests used to adjust the proposed function. All experimental tests from this study database simulate the slab-column connection, with square section columns molded in reinforced concrete and SFRC slabs without shear reinforcement.

The parameter k is adjusted according to the compressive strength of the concrete (Table 2). The method used to adjust the parameter is based on two hypotheses: the average of the experimental / theoretical rupture load ratio is the closest to one (1); in none of the individual results, the experimental / theoretical rupture load ratio is less than one (1). Table 2 shows each compressive strength used. Figure 2 shows the iterative process to obtain the parameter k.

Table 1. Experimental papers

Author	Tests	Author	Tests
Narayanan and Darwish [4]	12	Musse [19]	2
Theodorakopoulos and Swamy [13]	20	De Hanai and and Holanda [20]	8
Shaaban and Gesund [14]	12	Cheng and Parra-Montesinos [21]	10
Harajli et al. [15]	10	Nguyen-Minh et al. [22]	12
Vargas [16]	6	Gouveia et al. [23]	6
Azevedo [17]	6	Barros et al. [5]	8
McHarg et al. [18]	4	Alves [6]	3

The process of adjusting the Parameter k consists of an iterative method where the Equation 4 to 7 are applied from each result of the experimental test of the data base varying k. The steel fibers behavior is sensitive to the concrete compressive strength, which indirectly influences the bond mechanism of the fiber in the concrete matrix. Thus, the Parameter k from the Function G is adjusted for each compressive strength values of the database experimental tests (see Figure 2). Parameter k is defined by minimizing an Error Parameter of subsequent iterations(R_i and R_{i-1}, where i is the iteration number, see Figure 2).

Table 2. Analysis intervals of parameter k.

Concrete strength (MPa)	Parameter
20~30	k_{20}
30~40	k_{30}
40~50	k_{40}
50~60	k_{50}
60~70	k_{60}
70~80	k_{70}
80~90	k_{80}

Rev. IBRACON Estrut. Mater., vol. 16, no. 5, e16509, 2023

4/12
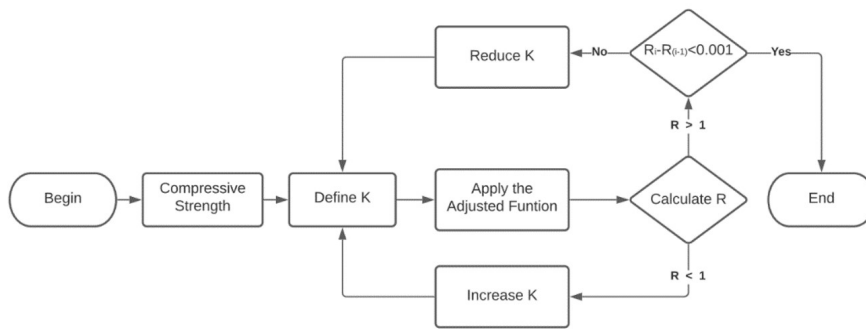
Figure 2. Flowchart of the iterative process .

The parameters used in the proposed adjustment function are the concrete compressive strength (f_c), flexural reinforcement ratio (ρ), slab effective depth (correlated with slab thickness, h), equivalent square column width (b_p), steel fiber content in percentage of the concrete volume (V_f).

From the pre-selected data, the experimental results of some researchers are discarded for the determination of parameter k. This assumption is because the relation of the experimental load capacity (P_{exp}) and the load-carrying capacity estimated by ABNT NBR 6118 (2014) [2] (P_{NBR}) of the slabs reference values are outside the "appropriate safety" range according to Collins [24], Dantas [3]. Still, in the whole process of the analytical model, despite being based on the equations of ABNT NBR 6118 (2014) [2], the load increase and / or resistance reduction coefficients of that standard are not used. In total, there are 90 slabs, 22 of which are reference slabs.

3 RESULTS AND DISCUSSIONS

Figure 3 show the dispersion of h, f_c, ρ, b_p, and V_f, of the 68 slabs to adjust the parameter k.

From the results of the adjusting process showed in Figure 2, Table 3 shows the average results of the relationship ($R_{e,tm}$) experimental load-carrying capacity (P_{exp}) and theoretical load-carrying capacity of the model (P_{mod}). In addition, Table 4 presents the results of the Parameter k for each compressive strength range.
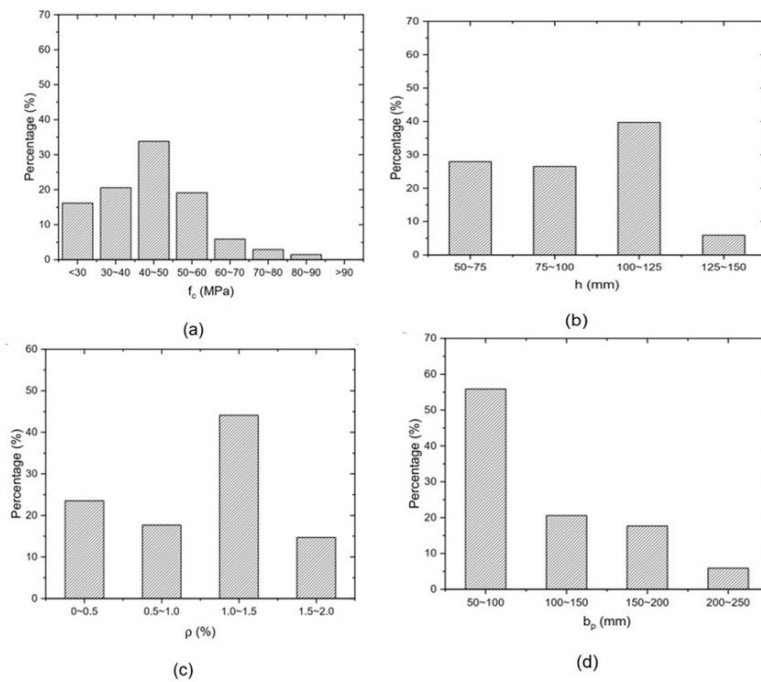
Figure 3. Dispersion of parameters.

Rev. IBRACON Estrut. Mater., vol. 16, no. 5, e16509, 2023

5/12

The adjusted ABNT NBR 6118 (2014) [2] equations are presented in Equations 8 to 10:

$$F_{rd} = Minimum(\tau_{rd1}, \tau_{rd2})ud \tag{8}$$

$$\tau_{rd1} = 0.27(1 - \frac{f_c}{250})f_c[1 + ln(1 + kV_f)] \tag{9}$$

$$\tau_{rd2} = 0.13\left(1 + \sqrt{\frac{20}{d}}\right)(100\rho f_c)^{\frac{1}{3}}[1 + ln(1 + kV_f)] \tag{10}$$

Where:
k = Dimensionless parameter, defined by the strength class of the concrete (Table 4);
V_f = Steel fiber content in % of m^3 volume of concrete.

Table 3. Experimental / theoretical rupture load ratio by strength class.

f_c (MPa)	Number of slabs	k	$R_{e,m}$		
			X	S	CV
20~30	10	0.248	1.118	0.171	15.32
30~40	15	0.132	1.262	0.167	13.21
40~50	23	0.208	1.305	0.201	15.39
50~60	13	0.319	1.11	0.082	7.37
60~70	4	0.548	1.031	0.027	2.61
70~80	2	0.615	1.019	0.026	2.6
80~90	1	0.218	1	-	-
Total	68	-	1.199	0.187	15.59

$R_{e,m}$ – Relationship between the experimental and proposed load-carrying capacity load; X – Sample mean; S – Sample standard deviation; CV – Coefficient of variation in %.

The experimental results include only connections of center and square section slabs and columns. Therefore, this adjusted function is recommended to be applied in similar situations. There is a relatively small number of tests that fit to compressive strength above 60 MPa, which prevent the definition of a Parameter k for this range that is statistically satisfactory.

Although the analysis of the fibers is done according to the fiber content (in percentage), factors such as fiber strength and fiber geometry also affect the behavior of the SFRC, but not as significantly, compared to the fiber content Narayanan and Darwish [4] De Hanai and Holanda [20]. Figure 4 presents the results of the relation between the experimental load-carrying capacity and proposed adjusted function (R_{em}) according to the concrete compressive strength applied on each experimental tests from database.

Table 4. Parameter k.

Compressive Strength (f_c)	Parameter	Value
20~30	k_{20}	0.248
30~40	k_{30}	0.132
40~50	k_{40}	0.208
50~60	k_{50}	0.319
60~70	k_{60}	0.548
70~80	k_{70}	0.615
80~90	k_{80}	0.218

The results of $R_{e,m}$ showed that the proposed adjusted function presented a conservative estimative of the load-carrying capacity of experimental tests for all compressive strength from the studied experimental test of the database. In other words, all values of $R_{e,m}$ are higher than 1.0 which means that the load-carrying capacity estimated by the

L. G. Dantas, L. H. B. Oliveira, A. C. Santos, and L. M. Trautwein

proposed adjusted function is lower than the experimental tests from the authors of the data base. Compressive strength in a range of 30-40MPa present the most conservative estimative while compressive strength in a range of 60-70MPa present $R_{e,m}$ less conservative in comparison with other results from Figure 4.

A comparative study of the load-carrying capacity of the experimental tests from data base and other analytical and theoretical model proposed by Narayanan and Darwish [4], Harajli et al. [15], De Hanai and Holanda [20] and Higashiyama et al. [11] is showed in Figure 5. A comparative estimative from the proposed model presented in this paper is also presented in Figure 5a. For each graph in Figure 5, the x-axis presents the load-carrying capacity measured on the experimental tests, the y-axis presents the load-carrying capacity estimated by the respective theoretical model and each point of the graph is an experimental test from the database. For an estimated load-carrying capacity equal to the measured on the experimental test the point should be projected in a 1:1 line. Points projected above the 1:1 line presents experimental results lower than the estimated results by the theoretical model. Points projected below the 1:1 line presents experimental results higher than estimated by the theoretical model (conservative results).
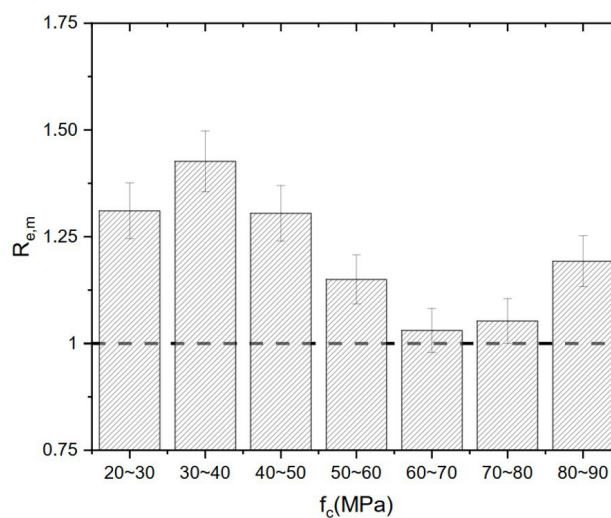
Figure 4. Average results of the application of the adjustment function in relation to f_c.

From Figure 5, the proposed model (Figure 5a) presents a lesser dispersion of the relationship between experimental and theoretical load-carrying capacity, especially for results up to 200 kN. The proposed model also presents a tendency to estimate the load carrying capacity of slabs that reach higher values (for example, 500kN). The dispersion of the projected point that represents the experimental tests from the data base is higher for the other authors estimative models, which means that the results were not accurate. In addition, some results are projected above the 1:1 line, which means that the load-carrying capacity measured on the experimental tests are lower that the estimated results, which presents a risky estimative. This could be observed in Figure 5b to 6e (Narayanan and Darwish [4], Harajli et al. [15], De Hanai and Holanda [20] and Higashiyama et al. [11], respectively).

Table 5. Confidence index.

Model	$R_{e,m}$ (Mean)	$R_{e,m}$ (Standard Deviation)	$R_{e,m}$ (Variation Coefficient)	Confidence Indicator
Proposed Model	1.29	0.23	18%	96%
Narayanan and Darwish [4]	1.59	0.76	48%	74%
Harajli et al. [15]	1.50	0.65	44%	74%
De Hanai and Holanda [20]	1.50	0.60	40%	77%
Higashiyama et al. [11]	1.49	0.56	37%	72%

Figure 5. Comparison of rupture load prediction models.

Defining as a confidence index the percentage of slabs for which the experimental load is greater than the theoretical load, the proposed model presents a confidence indicator of 96%. The confidence indicator was calculated considering all slabs from database. However, the other models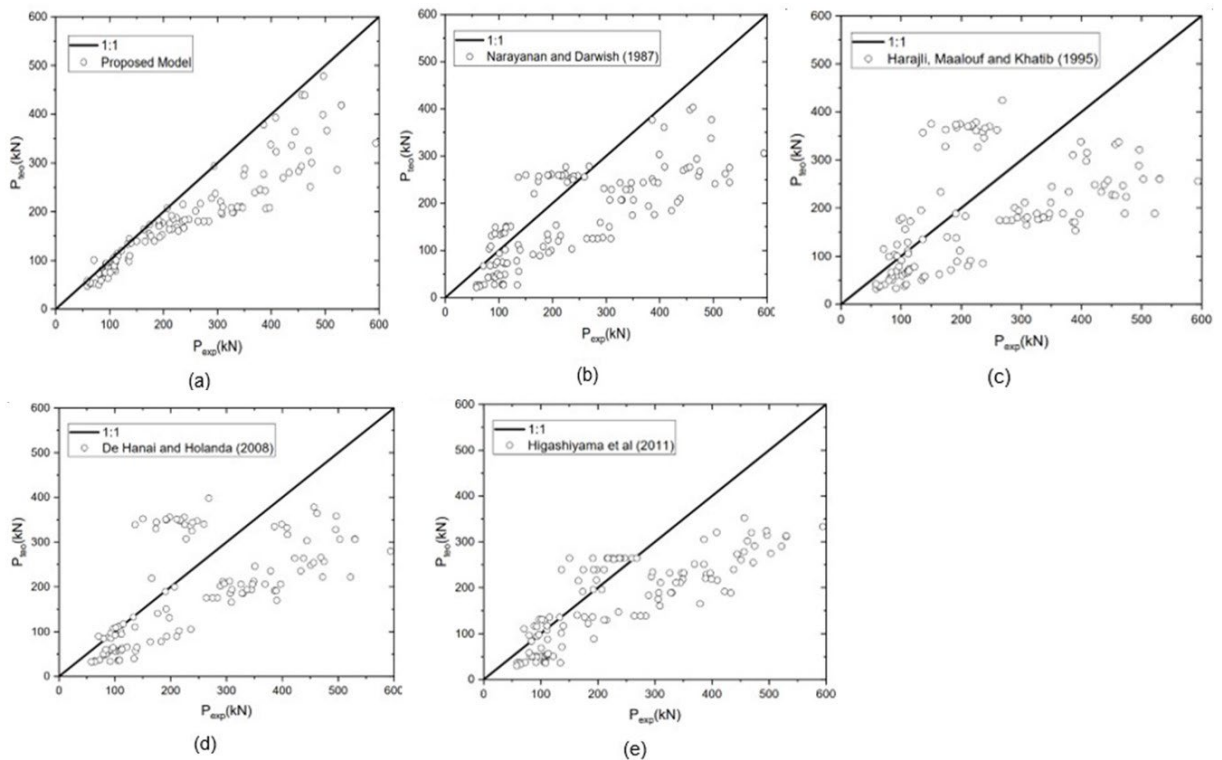 analyzed presented lower confidence indicators. In addition, the proposed model presents an average relationship between experimental and estimated results of 1.29 while Models proposed by other authors presents $R_{e,m}$ from 1.49 (Higashiyama et al. [11]) to 1.59 (Narayanan and Darwish [4]), this could be observed by the dispersion of the results on Figure 5. Table 5 shows the relationship of the confidence index.

Phenomena observed in steel fiber reinforced concrete are considered in Narayanan and Darwish [4], Harajli et al. [15] and Higashiyama et al. [11] models, for example, the change in the punching shear rupture surface due to the addition of steel fibers in the concrete mixture. However, the parameters in these models to considered are empirical values and could lead in to not accurate estimative.

4 COMPARISON WITH THE BRAZILIAN CODE ABNT NBR 16935 (2021) [12]

To compare the recommendations of ABNT NBR 16935 (2021) [12] and the proposed model in this paper, a case study of estimating the punching shear load-carrying capacity was conducted. Four flat slabs experimental tests conducted by Alves et al. [25] were estimated.

ABNT NBR 16935 (2021) [12] demands the post-cracking parameters, such as P x CMOD curve of steel fiber concrete. The study and production of the fiber and concrete materials proportion for these flat slabs experimental tests were conducted by Silva [26], which studied the P x CMOD curve of the same concrete used to mold the experimental tests of Alves et al. [25].

The experimental test was conducted in 1800mm x 1800mm x 130mm flat slabs, molded in steel fiber reinforced concrete with the addition of 50kg/m³ ($v_f = 0.64\%$) of a hooked-end type DRAMIX RC 50/60. The fibers had a nominal diameter of 0.90 mm, a length of 60 mm and a size factor of 65. The experimental P x CMOD test was conducted in a 150mm x 150mm x 500mm concrete specimen with 125mm notch in its midspan. Table 6 presents the properties of the experimental tests conducted by Alves et al. [25]. Table 7 presents the properties of the steel fiber reinforced concrete properties of the experimental tests conducted by Silva [26]. For further details of the experimental tests the authors recommend reading study of Alves et al. [25] and Silva [26].

Table 6. Experimental tests properties from Alves et al. [25].

Slab	L (mm)	h (mm)	d (mm)	a (mm)	ρ	v_f (%)	f_c (MPa)	P_{exp} (kN)
L1-50-1	1800	130	99	250	0.016	0.64	42.01	469
L1-50-2	1800	130	99	250	0.016	0.64	42.01	469
L2-50	1800	130	98	250	0.016	0.64	42.01	513
L3-50	1800	130	99	250	0.016	0.64	42.01	455

L – Slab length; h – Slab thickness; d – Average effective depth measured after the experimental tests; a – Column length; ρ – Flexural reinforcement ratio; v_f – Steel fiber content; f_c – Average concrete compressive strength; P_{exp} – Punching shear load-carrying capacity measured in the test;

Table 7. Steel fibers reinforced concrete P x CMOD properties from Silva [26]

Identification	CMOD	Opening (mm)	$F_{R,i}$ (kN)	$f_{R,i}$ (MPa)
C40/50-1	$CMOD_1$	0.5	13.24	4.24
	$CMOD_2$	1.5	12.89	4.12
	$CMOD_3$	2.5	12.67	4.06
	$CMOD_4$	3.5	11.05	3.54
C40/50-2	$CMOD_1$	0.5	12.83	4.10
	$CMOD_2$	1.5	13.21	4.23
	$CMOD_3$	2.5	11.79	3.77
	$CMOD_4$	3.5	11.90	3.81

$CMOD_i$ – Crack mouth opening displacement for the i opening displacemnet; $F_{R,i}$ – Residual force measured at $CMOD_i$; $f_{R,i}$ – Residual tensile strength measured at $CMOD_i$;

From Table 6 and Tabel 7, L1-50-1 and L2-50 were molded with C40/50-1 and L1-50-2, L3-50 were molded with C40/50-2, the average compressive strength for both specimens was 42MPa. The load-carrying capacity estimate model by the recommendation of ABNT NBR 16935 (2021) [12] is presented in Equation 11 to 14.

$$V_{Rd} = V_{Rd,F} + V_{Rd,s} \tag{11}$$

$$V_{rd,F} = V_{Rd,f} + V_c \tag{12}$$

$$V_{Rd,f} = \frac{f_{Ftu,k}}{\gamma_F} \mu d \tag{13}$$

$$f_{Ftu,k} = \frac{f_{R3}}{3} \tag{14}$$

Where V_{Rd} is the load-carrying capacity, $V_{Rd,F}$ is the contribution of the steel fiber reinforced concrete, $V_{Rd,s}$ is the contribution of the shear reinforcement ratio, $V_{Rd,f}$ is the fiber contribution in the load carrying capacity of the steel fiber reinforced concrete, V_c is the contribution of the concrete in the load carrying capacity of the steel fiber reinforced concrete, $f_{Ftu,k}$ is the tensile residual strength of the steel fiber reinforced concrete, μ is the critical punching shear perimeter, d is the effective depth and f_{R3} is the residual tensile strength measured at $CMOD_3$.

Table 8 presents the results from the comparison of the estimative of the load-carrying capacity conducted by ABNT NBR 16935 (2021) [12]. Table 9 presents the results from the Proposed Model. Table 10 presents the comparison of the ABNT NBR 16935 (2021) [12] and the Proposed Model.

Rev. IBRACON Estrut. Mater., vol. 16, no. 5, e16509, 2023

9/12

Table 8. Estimative of the load-carrying capacity – ABNT NBR 16935 (2021) [12]

Slab	d (mm)	ρ	f_c (MPa)	f_{R3} (MPa)	$f_{Ftu,k}$ (MPa)	τ_{Rd1} (MPa)	μ (mm)	V_c (kN)	$V_{Rd,f}$ (kN)	$V_{Rd,ABNT}$ (kN)
L1-50-1	99	0.016	42	4.06	1.35	1.77	2244.07	393.66	300.32	693.98
L1-50-2	99	0.016	42	3.77	1.26	1.77	2244.07	393.66	279.32	672.98
L2-50	98	0.016	42	4.06	1.35	1.77	2231.50	393.66	295.62	684.28
L3-50	99	0.016	42	3.77	1.26	1.77	2231.50	393.66	274.95	663.61

Table 9. Estimative of the load-carrying capacity – Proposed model

Slab	D (mm)	ρ	f_c (MPa)	v_f (%)	V_c (kN)	k	$V_{Rd,Prop}$ (kN)
L1-50-1	99	0.016	42	0.64	393.66	0.208	442.86
L1-50-2	99	0.016	42	0.64	393.66	0.208	442.86
L2-50	98	0.016	42	0.64	393.66	0.208	437.23
L3-50	99	0.016	42	0.64	393.66	0.208	437.23

Table 10. Comparison Experimental, ABNT NBR 16935 (2021) [12] and Proposed Model

Slab	$V_{Rd,ABNT}$ (kN)	$V_{Rd,Prop}$ (kN)	V_{exp} (kN)	$V_{Rd,ABNT}/V_{Rd,Prop}$	$V_{exp}/V_{Rd,ABNT}$	$V_{exp}/V_{Rd,Prop}$
L1-50-1	693.98	442.86	469	1.57	0.68	1.06
L1-50-2	672.98	442.86	469	1.52	0.70	1.06
L2-50	684.28	437.23	513	1.57	0.75	1.17
L3-50	663.61	437.23	455	1.52	0.69	1.04

Since there were no shear reinforcement in Alves et al. [25] experimental tests, $V_{rd,s}$ was assumed as zero. As a simplification, ABNT NBR 16935 (2021) [12] recommend calculate the V_c with the same recommendation for conventional concrete presented in ABNT NBR 6118 (2014) [2]. f_{R3} was obtained by the P x CMOD curves conducted by Silva [26] and presented in Table 7. In addition, the safety factors were assumed as 1, including γ_F presented in Equation 13. This decision was assumed to compare the results of the proposed method and the ABNT 16935 (2021) [12] without any interference of safety factors. The Equation 4, Equation 9 and Equation 10 were used to estimate the load-carrying capacity for the proposed model.

From the comparison presented in Table 10, the results from ABNT NBR 16935 (2021) [12] and Proposed Models differs for estimating the load-carrying capacity of the slabs tested by Alves et al. [25]. The ABNT NBR 16335 (2021) presented estimative over 1.5 times higher in comparison with the Proposed model.

This could be justified by the simplification of model proposed by ABNT NBR 16935 (2021) [12], where the tensile strength of the steel fiber reinforced concrete in the punching shear critical perimeter was $f_{R3}/3$. Silva [26] presented that the residual tensile strength of the steel fiber does not present a constant behavior in relation with the crack opening. This is also observed by other authors ([3], [4], [7], [8], [13]–[15], [22], and [23]). In additions, the use of safety factor for the steel fibers ($\gamma_F = 1,5$) still gives estimative higher than experimental tests.

The Proposed model recommend the use of a statistical parameter (k), which is based on experimental tests with similar conditions of the compressive behavior. The more experimental results used to calibrate the parameter k the better results for estimate the load-carrying capacity. From Table 3, for estimate the results of load-carrying capacity of Alves et al. [25] tests, the parameter k was calibrated with 23 experimental tests with similar compressive conditions (compressive strength in a range of 40-50 MPa, similar properties of steel fibers and similar content of steel fibers).

Although the results presented in Table 10 were in a good agreement with experimental test, the parameter k should be better calibrated for slabs reaching compressive strength of 60-90 MPa. A larger number of slabs is needed to improve the values of k in that range. However, Figure 5a presented that the estimative for the proposed model of all the 68 slabs data base were conservative results. In other words, in Figure 5a all the points representing the experimental tests were projected below the 1:1 line, where experimental load-carrying capacity is higher than the estimative from the proposed model.

5 CONCLUSIONS

This study presented a proposed model for estimate the punching shear load-carrying capacity for steel fiber reinforced concrete flat slabs. The proposed model was based on the Brazilian standard code by a logarithmic adjusted curve G for the contribution of steel fibers on punching. The adjusted function G was based on the results of 68 slabs experimental tests database.

For testing the accuracy of the load-carrying capacity estimate by the proposed model, the results were compared by the estimative of other authors steel fibers reinforced concrete punching shear models. The proposed model presents a better response in the analyzed slabs (mainly for load-carrying capacity up to 200kN) compared to the other analyzed models with an average of R_{em} of 1.3 and the highest confidence index of 96%, despite considering only the content of steel fiber as a parameter of fibers.

In relation to the R_{em}, average, the proposed equation has same level of safety as the Brazilian standard equation, the Brazilian standard equation for slabs without fibers already has an experimental / theoretical load-carrying capacity ratio of 1.3, similar value found for the proposed model (both without safety factors).

In addition, a comparison with the ABNT 16935 (2021) [12] presented an estimative higher than the experimental results conducted by Alves et al. [25] where the proposed model presented a good agreement. This could be justified by the simplification on considering the residual tensile strength proposed by the ABNT NBR 16935 (2021) [12] while the proposed model is based on statistical parameter that could be improved incorporating more results from experimental tests.

The result of this paper is constantly in update with testing of parameters k and adjusted function G. The authors intend to incorporate other experimental tests in the database and analyze its sensibility to geometric and physical database parameters such as h, f_c, ρ, b_p, and V_f.

ACKNOWLEDGEMENTS

REFERENCES FORMATS

[1] D. A. Gasparini, "Contributions of C. A. P. Turner to Development of Reinforced Concrete Flat Slabs 1905–1909," *J. Struct. Eng.*, vol. 128, no. 10, pp. 1243–1252, 2002, http://dx.doi.org/10.1061/(ASCE)0733-9445(2002)128:10(1243).

[2] Associação Brasileira de Normas Técnicas, *Projetos de Estruturas de Concreto – Procedimento*, NBR 6118, 2014.

[3] L. G. Dantas, "Proposta para o cálculo de carga de ruptura por punção em lajes de concreto reforçado com fibras de aço," M.S. thesis, Univ. Fed. Uberlândia, Uberlândia, MG, Brasil, 2020. https://doi.org/10.14393/ufu.di.2020.374.

[4] R. Narayanan and I. Y. S. Darwish, "Punching shear tests on steel-fibre-reinforced micro-concrete slabs," *Mag. Concr. Res.*, vol. 39, no. 138, pp. 42–50, 1987, http://dx.doi.org/10.1680/macr.1987.39.138.42.

[5] J. A. O. Barros, B. N. Moraes Neto, G. S. S. A. Melo, and C. M. V. Frazão, "Assessment of the effectiveness of steel fibre reinforcement for the punching resistance of flat slabs by experimental research and design approach," *Compos., Part B Eng.*, vol. 8, no. 1, pp. 8–25, 2015, http://dx.doi.org/10.1016/j.compositesb.2015.03.050.

[6] V. S. S. Alves, "Avaliação do efeito de punção em lajes lisas de concreto com fibras com a variação do índice de retangularidade," M.S. thesis, Fac. Eng. Civ., Univ. Fed. Uberlândia, Uberlândia, MG, Brasil, 2017.

[7] A. Stanislav, N. Tošić and A. De La Fuente, "A limit state design approach for hybrid reinforced concrete column-supported flat slabs," *Struct. Concr.*, vol. 23, no. 6, pp. 3444–3464, 2022, http://dx.doi.org/10.1002/suco.202100785.

[8] L. H. B. Oliveira, "Resistência à punção em lajes lisas de concreto armado com adição de fibras de aço e aberturas adjacentes ao pilar," Ph.D. dissertation, Univ. Estad. Campinas, Fac. Eng. Civ., Arquit. Urb., Campinas, SP, Brasil, 2020.

[9] L. Facconi, F. Minelli, and G. Plizzari, "Steel fiber reinforced selfcompacting concrete thin slabs: experimental study and verification against model Code 2010 provisions," *Eng. Struct.*, vol. 122, pp. 226–237, 2016., http://dx.doi.org/10.1016/j.engstruct.2016.04.030.

[10] D. Fall, J. Shu, R. Rempling, K. Lundgren, and K. Zandi, "Two-way slabs: experimental investigation of load redistributions in steel fibre reinforced concrete," *Eng. Struct.*, vol. 80, pp. 61–74, 2014., http://dx.doi.org/10.1016/j.engstruct.2014.08.033.

[11] H. Higashiyama, A. Ota, and M. Mizukoshi, "Design equation for punching shear capacity of SFRC slabs," *Int. J. Concr. Struct. Mater.*, vol. 5, no. 1, pp. 35–42, Jun 2011.

[12] Associação Brasileira de Normas Técnicas, *Projetos de Estruturas de Concreto – Procedimento*, NBR 16935, 2021.

[13] D. D. Theodorakopoulos and N. Swamy, "Contribution of steel fibers to the strength characteristics of lightweight concrete slab-column connections falling in punching shear," *ACI Struct. J.*, vol. 90, no. 4, pp. 342–355, 1993, http://dx.doi.org/10.14359/3957.

[14] A. M. Shaaban and H. Gesund, "Punching shear strength of steel fiber reinforced concrete flat plates," *ACI Struct. J.*, vol. 91, no. 3, pp. 406–414, 1994, http://dx.doi.org/10.14359/4145.

[15] M. H. Harajli, D. Maalouf, and H. Khatib, "Effect of fibers on the punching shear strength of slab-column connections," *Cement Concr. Compos.*, vol. 17, no. 2, pp. 161–170, 1995, http://dx.doi.org/10.1016/0958-9465(94)00031-S.

[16] E. N. Z. Vargas, "Punção em lajes-cogumelo de concreto de alta resistência reforçado com fibras de aço. Dissertação, Esc. Eng. São Carlos, Univ. São Paulo, São Carlos, SP, Brasil, 1997.

[17] A. P. Azevedo, "Resistência e ductilidade das ligações laje-pilar em lajes-cogumelo de concreto de alta resistência armado com fibras de aço e armadura transversal de pinos," M.S. thesis, Eng. Estrut., Esc. Eng. São Carlos, Univ. São Paulo, São Carlos, SP, Brasil, 1999.

[18] P. J. McHarg, W. D. Cook, D. Mitchell, and Y. S. Yoon, "Benefits of concentrated slab reinforcement and steel fibers on performance of slab-column connections," *ACI Struct. J.*, vol. 97, no. 2, pp. 225–234, 2000, http://dx.doi.org/10.14359/851.

[19] T. H. Musse, "Punção em lajes cogumelos – fibras de aço e armadura de cisalhamento", M.S. thesis, Univ. Fed. Goiás, Goiânia, GO, Brasil, 2004.

[20] J. B. De Hanai and K. M. A. Holanda, "Similarities between punching and shear strength of steel fiber reinforced concrete (SFRC) slabs and beams," *Rev. IBRACON Estrut. Mater.*, vol. 1, no. 1, pp. 1–16, 2008.

[21] M. Y. Cheng and G. J. Parra-Montesinos, "Evaluation of steel fiber reinforcement for punching shear resistance in slab-column connections—Part I: monotonically increased load," *ACI Struct. J.*, vol. 107, no. 1, pp. 101–109, 2010, https://doi.org/10.14359/51663394

[22] L. Nguyen-Minh, M. Rovnak, and T. Tran-Quoc, "Punching shear capacity of interior SFRC Slab-Column connections," *J. Struct. Eng.*, vol. 138, no. 5, pp. 613–624, 2012, http://dx.doi.org/10.1061/(ASCE)ST.1943-541X.0000497.

[23] N. D. Gouveia, N. A. G. Fernandes, D. M. V. Faria, A. M. P. Ramos, and V. J. G. Lucio, "SFRC flat slabs punching behaviour – Experimental research," *Compos., Part B Eng.*, vol. 63, no. 1, pp. 161–171, 2014, http://dx.doi.org/10.1016/j.compositesb.2014.04.005.

[24] M. P. Collins, *Evaluation of shear design procedures for concrete structures. A Report prepared for the CSA technical committee on reinforced concrete design*, CSA, Canadian, 2001.

[25] V. Alves, L. Oliveira, A. Santos and L. Trautwein, Experimental evaluation of the load carrying capacity of SFRC flat slabs varying the rectangularity index of columns," *KSCE J. Civ. Eng.*, vol. 25, pp. 574–585, 2021.

[26] J. R. Silva, *Correlação de valores de tenacidade do concreto reforçado com fibras de aço obtidos pela ASTM C1609: 2012 E EN 14651: 2007*, M.S. thesis, Univ. Fed. Uberlândia, Uberlândia, MG, Brasil, 2018.

Editors: Ricardo Carrazedo, Guilherme Aris Parsekian.

Rev. IBRACON Estrut. Mater., vol. 16, no. 5, e16509, 2023

12/12

ERRATUM

Erratum: Proposal for estimating the punching shear load-carrying capacity of steel fibers reinforced concrete flat slabs

In the article **"Proposal for estimating the punching shear load-carrying capacity of steel fibers reinforced concrete flat slabs"**, DOI number https://doi.org/10.1590/S1983-41952023000500009, published in IBRACON Structures and Materials Journal ISSN 1983-4195, v.16, n.5, e16509, 2023, on page 11:

ACKNOWLEDGEMENTS

Where it reads:

The authors would like to express their gratitude for the graduate program in civil engineering of the *Universidade Federal de Uberlandia* and the funding agency CAPES.

It should be read:

The authors would like to express their gratitude for the graduate program in civil engineering of the *Universidade Federal de Uberlândia* and the funding agency *Fundação de Amparo à Pesquisa do Estado de Minas Gerais* (FAPEMIG) and *Coordenação de Aperfeiçoamento de Pessoal de Nível Superior* (CAPES).

IBRACON Structures and Materials Journal
Revista IBRACON de Estruturas e Materiais

ORIGINAL ARTICLE

A new method for determining mortar shrinkage in the first 24 hours of hydration

Um novo método para a determinação da retração de argamassas nas primeiras 24 horas de hidratação

Matheus Suss[a]
Marienne do Rocio de Mello Maron da Costa[a]
Ronaldo Alves de Medeiros Junior[a]

[a]Universidade Federal do Paraná – UFPR, Programa de Pós-graduação em Engenharia Civil, Curitiba, PR, Brasil

Abstract: The shrinkage of cementitious materials is a complex phenomenon of volume reduction that can result in cracking, affecting the durability of these materials. The Brazilian standard ABNT NBR 15261 addresses long-term shrinkage without emphasis on the initial phase (< 24h) of hydration, which contains the plastic state of the cementitious material. Therefore, a method was proposed to measure the shrinkage in the first 24h of mortar hydration, on a laboratory scale, from prismatic samples, using molds from the Brazilian standard ABNT NBR 15261 (285x25x25mm) and rigid elements that transmit horizontal displacements of the sample to dial gauges. Cement mortar specimens were studied with the water/dry materials ratio fixed at 0.168 and varying the binder/aggregates ratio linearly: 33% (1:3); 25% (1:4); and 17% (1:6). Different exposures to the environment (sealed, open and wind) were applied. The analysis indicated that the proposed method was sensitive enough to indicate statistically significant relationships between the maximum initial shrinkages and the variation in the concentration of the binders, as well as indicating variations in the behavior of the initial shrinkage. The increase in cement concentration caused an increase in the average initial shrinkage of 76% in the samples exposed to air, 54% in those exposed to 5 m/s wind, and 22% in the sealed samples.

Keywords: early age shrinkage, mortar, measurement method, durability.

Resumo: A retração de materiais cimentícios é um fenômeno complexo de redução de volume que pode resultar em fissuras que afetam a durabilidade desses materiais. A norma brasileira ABNT NBR 15261 aborda a retração a longo prazo sem ênfase na fase inicial (< 24h) da hidratação, que contém o estado plástico do material cimentício. Portanto, foi proposto um método de mensuração da retração nas primeiras 24h de hidratação de argamassas, em escala laboratorial, a partir de amostras prismáticas, utilizando: o molde da norma brasileira ABNT NBR 15261 (285x25x25mm) e elementos rígidos que transmitem deslocamentos horizontais da amostra para relógios comparadores. Foram estudados traços de argamassa de cimento com a relação água/materiais secos fixa em 0,168 e variando a relação aglomerante/agregados linearmente: 33% (1:3); 25% (1:4); e 17% (1:6). Foram aplicadas diferentes exposições ao ambiente (selado, aberto e vento). As análises indicaram que o ensaio proposto foi sensível o suficiente para indicar relações estatisticamente significativas entre as retrações iniciais máximas e a variação da concentração dos aglomerantes, assim como indicar variações de comportamento da retração inicial. O aumento da concentração de cimento causou um aumento da retração inicial média de 76% nas amostras expostas ao ar, 54% nas expostas ao vento de 5 m/s e 22% nas seladas.

Palavras-chave: retração inicial, argamassa, método de medição, durabilidade.

1 INTRODUCTION

After their first contact with water, cementitious materials undergo volumetric shrinkage changes. This is due to the smaller volume of hydration products compared to their anhydrous components, due to the loss of water to the environment, substrate, and hydration [1]. This volume contraction is called in the literature as shrinkage, Mehta and Monteiro [2] state that this volumetric reduction that cementitious materials undergo during hydration, whether plastic, drying, or autogenous, can be one of the causes of cracking of cementitious materials, thus compromising their service life and resistance, in addition to increasing the interference of aggressive agents. According to Maltese et al. [3, pp. 1], "shrinkage is one of the main reasons for failures in mortars, such curling, cracking and detachment", Kayondo et al. [4] found that the main mechanisms that promote plastic cracking are settlement of solid particles; exudation; evaporation; capillary movement; and surface finish. These mechanisms combined lead to a three-dimensional volume contraction of the cementitious material, which in its early hours has not yet developed the mechanical strength to support it. Therefore, if this movement is contained, cracks in the plastic state will occur as a result.

The shrinkage phenomenon can be divided into two stages: early and late (or "long-term") [5]. The initial stage is usually attributed to the first day of cement hydration, which is when the beginning and end of the setting of this material occurs, in addition to the initial hardening. The later age refers to those from 24 hours onwards. In the literature, in general, long-term shrinkage receives much more attention than the one that occurs in the initial stage [6]. Both stages should not be mistaken by the six main types of shrinkage recognized in the literature: plastic, chemical, autogenous, drying, thermal, and carbonation [7]. Except for plastic shrinkage – which refers to the volume reduction that occurs in the plastic state of the material [8] and occurs until the initial setting time [9] –, the types of shrinkage are categorized by their cause and not by the stage that they develop. Therefore, in each stage, early and long-term, multiple types of shrinkage contribute to the total volume reduction, also called total shrinkage.

There are several ways to interpret the dimensional variation caused by early shrinkage. One of them is to measure the autogenous shrinkage with a sealed flexible corrugated mold system (ASTM C1698-19 [10]) that prevents water loss, but it doesn't measure total early shrinkage since it ignores drying shrinkage.

Another standardized way is by the quantification of cracks on fresh restrained concrete surfaces (ASTM C1579-21 [11], specifically for restrained fiber reinforced concrete, and GBT 29417-2012 [12]), but it fails to measure the actual volume or length changes caused by total early shrinkage.

Other ways of interpretation, such as horizontal [13]-[23] or vertical linear displacements [16], [21], [24], were not developed in standardized methods yet. However, large research centers, excluding Brazilian research, have already explored these methods extensively (Silva [20]). In Brazil, the only standard that proposes to measure shrinkage in mortars is ABNT NBR 15261 [25], but it provides for measuring shrinkage only in the hardened state ignoring the early age.

In Brazil, there are few proposals for methods of measuring shrinkage at an early age. Bastos et al. [18], Silva [20] and Girotto et al. [26] are some examples.

Détriché's method [27], amplified by the conditions applied by Bastos et al. [18], is based on free shrinkage by horizontal displacements using LVDT (Linear Variable Differential Transformer) as measuring equipment. The same equipment was used by Silva [20] in his unilateral free-shrinkage adaptation for coating mortars, based on the study of fibers in concrete developed by Wongtanakitcharoen and Naaman [28]. Girotto et al. [26] proposed the adaptation of the method by Soroushian and Ravanbakhsh [29], who analyzed cracking in concrete for mortars. It is based on the same principle of differential mold depth to induce cracking as stated in ASTM C1579-21 [11].

Measuring the volumetric variation allows a better understanding of the mechanisms that govern the behavior of these materials under the influence of early shrinkage, in addition to predicting future durability complications. Greater knowledge about this phenomenon contributes to the study of how to avoid it. Hence the need for easily reproducible and accessible methods, thus with the potential to become standardized. Within this context, the objective of this article was to propose a new test method for determining total shrinkage in mortars in the first twenty-four hours of hydration, through the approach of horizontal linear displacements without making distinctions between different types of shrinkage, inspired by the study by Bastos et al. [18], expanding the study to simple cement mortars, adopting different exposures to air, opting for affordable instrumentation and facilitating ABNT NBR 15261's [25] long-term measurements.

2 MATERIALS AND EXPERIMENTAL PROGRAM

2.1 Materials

Natural river sand was used as fine aggregate. Table 1 shows its characteristics and the respective standard used in determining it. Particle size distribution was determined according to ABNT NBR NM 248 [30] (Figure 1).

Table 1. Fine aggregate characterization

Property	Result	Standard
Unit mass	1.45×10^{-3} kg/m^3	ABNT NBR 16972:2021 [31]
Specific gravity	2.49×10^{-3} kg/m^3	ABNT NBR 16972:2021 [31]
Pulverulent material content	4.09%	ABNT NBR 16973:2021 [32]
Water absorption	1.00%	ABNT NBR 16916:2021 [33]
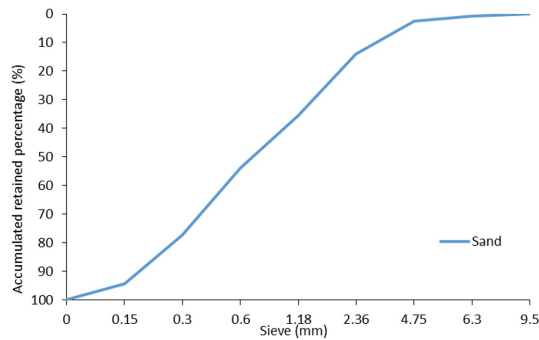
Figure 1. Sand's granulometric curve

A cement type CP-II-F, corresponding to American cement: IL Portland-limestone cement – ASTM C595/C595M - 21 [34], was used in the mortar (Tables 2-3). This cement was chosen because filler (limestone) is chemically inert, thus not conferring a chemical influence on the shrinkage behaviour.

Table 2. Chemical characterization of cement CP-II-F

Determination	Mass (%)
Loss on ignition	6.74
SiO_2	18.32
Al_2O_3	4.06
Fe_2O_3	2.77
CaO	61.58
MgO	2.47
SO_3	2.65
Na_2O	0.73
Insoluble Residue	1.20

Table 3. Physical characterization of cement CP-II-F

Property	Value
Hot expansibility (mm)	0
Setting time – beginning (min)	185
Setting time – end (min)	255
Blaine fineness (cm^2/g)	3,360
#200 sieve fineness (%)	2.30
#325 sieve fineness (%)	11.40
Unit mass (g/cm^3)	1.45
Specific gravity (g/cm^3)	3.11
Standard consistency (%)	29.50
Compressive strength – 1 day (MPa)	15
Compressive strength – 3 days (MPa)	27
Compressive strength – 7 days (MPa)	33
Compressive strength – 28 days (MPa)	40

2.2 Mortar formulation

According to Neville [35], the plastic shrinkage is greater as the cement content of the mixture increase. According to Silva [20], one of the main factors responsible for the restrictions to deformations in the fresh state of mortars is the aggregates.

Therefore, mortar mixture proportions with different aggregate/binder ratios were adopted to evaluate likely similar behaviors, but with different magnitudes of initial shrinkage (< 24 hours). Mortar mixture proportions were studied in a volume of cement mortar.

A constant water/dry materials ratio of 0.17 was adopted varying the binder/aggregates ratio by 8.33% by volume and 8.03% by mass. Table 4 shows the mortar mixtures proportions and their consistency index determined by ABNT NBR 13276 [36].

Table 4. Cement mortar mixtures characteristics

| Composition/ Relation/ Index	Constituent/ Relation	Cement mortar mixtures		
		1:3	1:4	1:6
Composition by volume	Cement	1.00	1.00	1,00
	Sand	3.00	4.00	6.00
	Water	0.70	0.88	1.23
Composition by mass	Cement	1.00	1.00	1.00
	Sand	3.11	4.15	6.23
	Water	0.70	0.88	1.23
Water/Binder		0.70	0.88	1.23
Binders / Aggregates		0.32	0.24	0.16
Water/Dry Materials		0.17	0.17	0.17
Consistency Index (ABNT NBR 13276 [36])		259 mm	243 mm	223 mm

2.3 Mold and instrumentation

The proposed method used the same metallic prismatic mold of ABNT NBR 15261 [25], with dimensions of (285 x 25 x 25) mm. A rigid element was inserted in the fresh mortar during casting. This element was used to transfer material displacements, caused by shrinkage, to dial gauges. The rigid element consists of a metal plate (STEEL SAE 1006) with holes for better anchoring in the mortar (Figure 2).
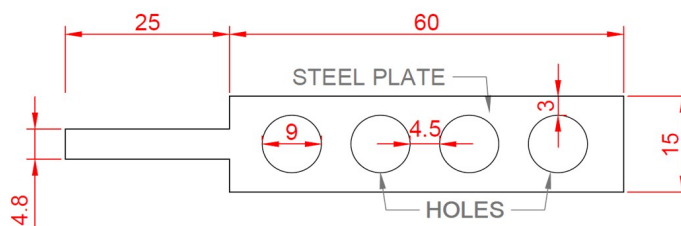

Figure 2. Rigid element vertical view (measurements in mm)

A rivet with a 2.5 mm thread was welded to the end of the rigid element (Figure 3) that allowed the connection between the metal plate with a connector.
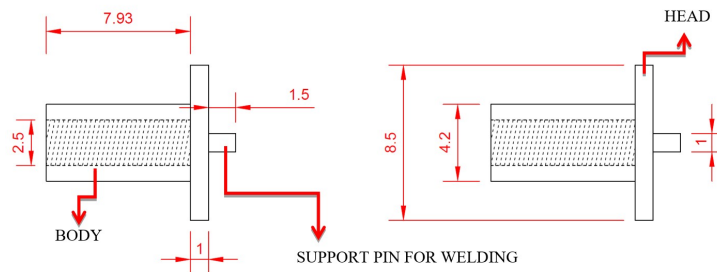
Figure 3. Rivet measurements in mm

The rivet dimensions were chosen according to the need to fit with the mold's block (Figure 4). The length was delimited by the thickness of the mold's block so that there would be no blocking during demolding. The rivet diameter was designed to be close to the diameter of the hole in the mold's block to avoid the eventual escape of water or material but still, allow its free movement. Moreover, the diameter of the rivet head is larger than the hole of the mold block to prevent water and material from coming out.
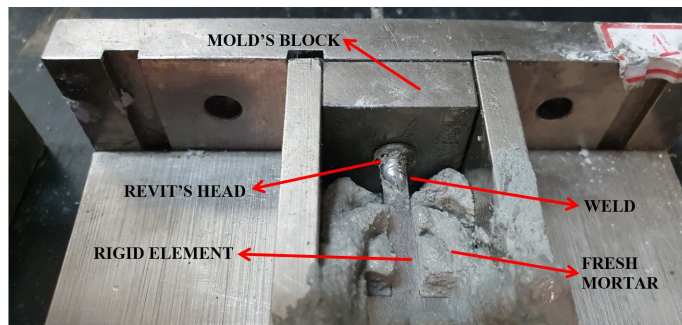

Figure 4. Rivet's head bigger than the mold's block hole

As the rivet and dial indicator have 2.5 mm threaded ends, a connector was developed from 2.5 mm headless screws and joined by a headless rivet through threading and instant glue, as exemplified in Figure 5. Figure 6 shows the projection of the rigid element on a mortar specimen, demonstrating how it is positioned internally.
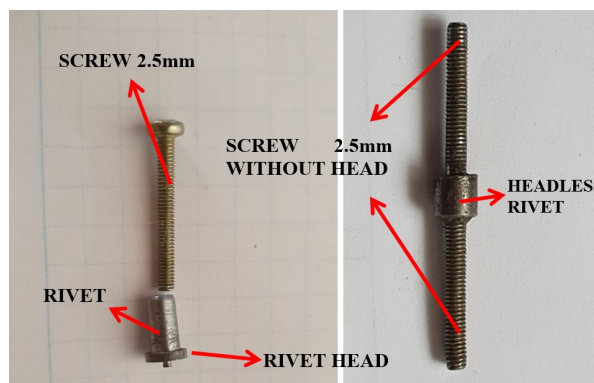

Figure 5. Connector assembly details. NOTE: on the left, screw and rivet before they are cut and connected; on the right, connector ready: two screws threaded and glued to a headless rivet.
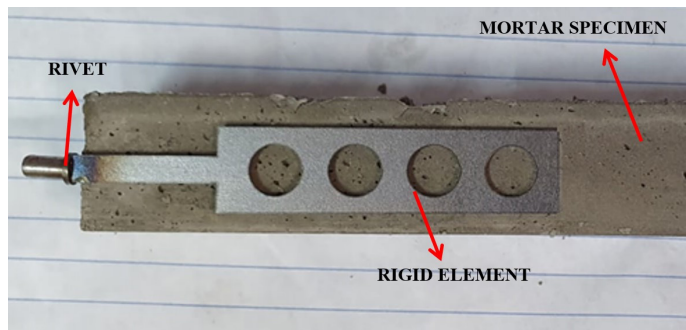
Figure 6. Overlay of the rigid element on the sample to demonstrate its position internally.

A digital indicator gauge was chosen as the measuring equipment. The equipment had 0.001 mm (10^{-6}m) accuracy – enough to capture the displacements of shrinkage and close to the reading accuracy provided by an LVDT. Two cameras were used to obtain the readings of the four dial gauges. These cameras filmed the specimens for 24 hours (Figure 7) in order to perform the readings without the need for operator to monitor the test during the 24 hours of the experiment. The final connection between the elements can be seen in Figure 8.
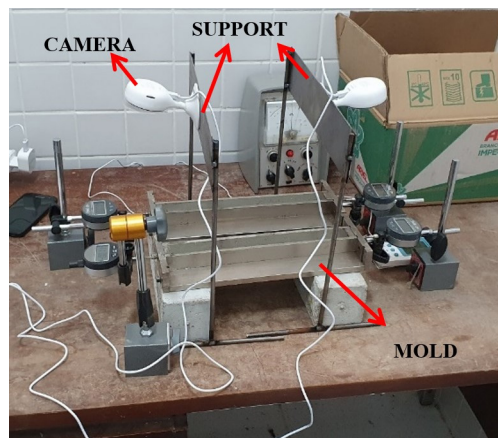
Figure 7. Cameras and their supports.
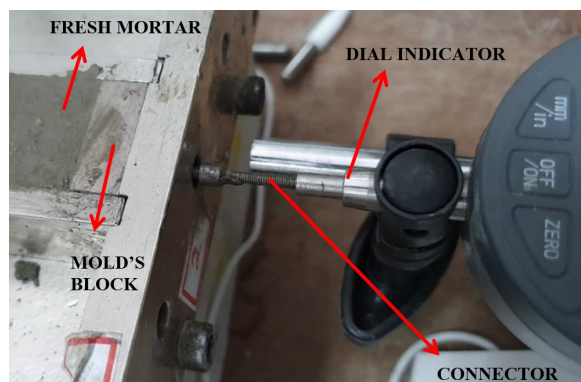
Figure 8. Final connection between the created elements and the dial indicator gauge.

2.4 Adopted air exposure conditions

ABNT NBR 15261 [25] requires that the samples remain during the first (48 ± 6) h in laboratory conditions, covered by PVC film and, after demolding, in a dry chamber (23 ± 2 ºC and $50 \pm 5\%$). According to this standard, the shrinkage

Rev. IBRACON Estrut. Mater., vol. 16, no. 5, e16510, 2023

6/14

readings must be performed at 0, 1, 7, and 28 days after demolding the sample (therefore only in the hardened state). This article used three conditions of exposure to air in laboratory ambient conditions:

1. Sealed: covered by PVC film (according to ABNT NBR 15261 [25] guidelines);
2. Exposed to air: no PVC film or wind incidence on the surface, simply exposed to air;
3. Exposed to 5 m/s wind produced by a fixed fan, during the first 24h of hydration.

The relationship between water loss and shrinkage is quite direct. Therefore, those exposure conditions that induce different influences on water loss from the mixture were chosen to evaluate the proposed method and its sensitivity.

2.5 Step by step to run the proposed test

The new test proposed by this article was performed in the following sequence:

1. Two metallic molds (indicated in ABNT NBR 15261 [25]) are greased with mineral oil;
2. The hole of the mold's blocks and the outer surface of the rivet body receive a layer of vaseline paste to prevent the possible escape of water and material and to reduce possible friction between them;
3. With the materials already weighed and separated, the mortar mixture follows the procedure proposed by ABNT NBR 16541 [37] and the mixing start time is registered;
4. Two samples are then casted, one in each mold (each test is repeated twice, resulting in 4 samples per test). As guided by ABNT NBR 15261 [25], they are casted in two layers with 25 blows each and final flattening with a spatula;
5. After the blows of the first layer of the samples, the rigid elements are inserted in each of the mold's ends and threaded in their connectors. Then the second layer is executed;
6. The mass of each of the sets, mold, and fresh mortar specimens is recorded.
7. Then, the molds are taken to the dry chamber and positioned below the cameras. The connectors are threaded to the dial gauges that are already in a level position to receive them. Thus, the measurements begin.
8. Along with the displacements, the variation in temperature and humidity are recorded by the two cameras, one on each pair of dial gauges for 24 hours;
9. After 24 hours, in addition to the molds being weighed, the samples are demoulded, their first measurements on the ABNT NBR 15261 [25] are performed and then the samples are stored in the dry chamber, where the long-term shrinkage was registered in the following ages: 7, 14, 21 and 28 days.

The decision to demold the specimens after 24 hours, instead of 48 hours as prescribed by ABNT NBR 15261 [25], came from a need to keep the proposed schedule feasible. Therefore, the long-term shrinkage results obtained in this study cannot be directly compared with the results external to the research that follow the 48-hour demolding standard of ABNT NBR 15261 [25].

The readings of displacement, temperature, and humidity of the environment were performed by watching the recordings and noting the variations recorded every 5 minutes for 24 hours. To obtain the total linear displacement (mm) of a specimen, the readings obtained from the two clocks connected to it were added. Finally, to obtain the total shrinkage that occurred in each reading (mm/m), the sum of the readings was divided by the distance from the center of the rigid elements.

A recurring fact in the measuring of early shrinkage was the absence of displacement in one or more of the dial gauges. The event was observed at all points of all molds, and at least once in each dial. When one or both ends of a mold did not register any displacement, the reading was discarded, and the test was repeated until there were at least four specimens for the test. In 86.46% of the tests, the movement was registered, and they were not discarded. It is suspected that thread wear between the connector and the dial gauge could have been one of the causes. Also, despite the efforts, there may have been percolation of cementitious material into the hole of the mold's block, with consequent blocking of the rivet's movement.

3 RESULTS AND DISCUSSIONS

A one-way ANOVA analysis of variance with a 5% level of significance was adopted. This evaluation seeks to statistically discover the validity of two hypotheses: H0 (null hypothesis), in which there are no significant differences between groups (groups being the results of a sample influenced by a factor); H1 (alternative hypothesis), there is a significant difference between the groups caused by the controllable factor investigated [38]. H0 can be ruled out, that is, there are significant differences between the groups caused by the controllable factor under study, when the calculated F-value is greater than F-critical (tabulated value), concomitantly, the P-value is less than 0.05, according to a significance level of 5% [38].

3.1 Early shrinkage

3.1.1 Exposed to air

Figure 9 demonstrates early shrinkage curves recorded for the samples exposed to air. The binder/aggregate variation resulted in different shrinkage magnitudes. The dotted lines represent individual tests for each mixture and the thicker continuous ones represent the mixture's average curve.

To statistically understand whether there was a significant influence on the shrinkage achieved between the adopted mixtures, an analysis of variance (ANOVA) was performed (F-value: 40.870; F-critical: 4.270; P-value: 0). According to the ANOVA results, the variation of the binder/aggregates ratio had a significant impact on early shrinkage's magnitude.
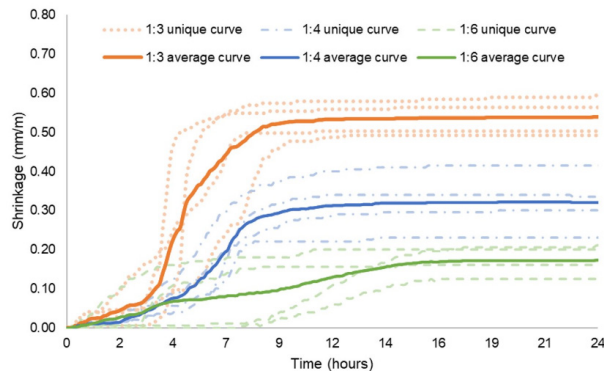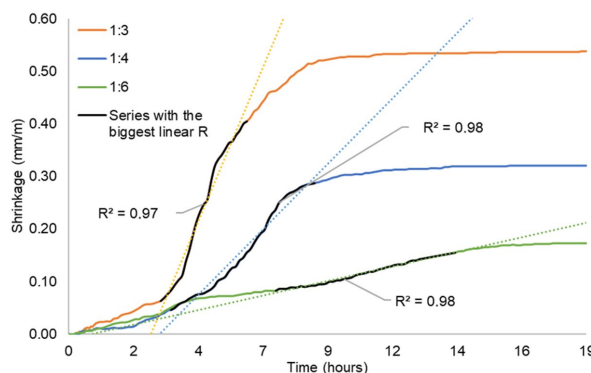

Figure 9. Early shrinkage curves of exposed to air samples. NOTE: dotted lines indicate individual tests, and continuous ones are their respective average curves.

In order to better characterize the difference in behaviour between the average shrinkage curves, the series of each data curve was selected, within the intermediate stage (when retraction progresses faster), which obtained the highest linear correlation (R). This series selection was made from all data within the intermediate stage and excluding the extremes simultaneously, thus increasing the linear correlation of the series until it decreased.

For each mixture, a linear function ($f(x) = ax + b$) was found, using a time x_0 and x that resulted, respectively, in a shrinkage y_0 and y. From it, the rate of change of the average shrinkage concerning the analysed time was calculated, which can be interpreted as a shrinkage speed. Considering the proposed period, the speed found would be the highest shrinkage speed for each average analysed.

The average shrinkage speed of the 1:3 mixture was 2.89E-5 mm/m/s, 75% higher than the 1:4 mixture (1.65E-5 mm/m/s), and 835% higher than the 1:6 mixture (3.09E-6 mm/m/s). Figure 10 shows the series selected for each mixture used to find the maximum speed.

Figure 10. Average early shrinkage curves of exposed to air samples and their selected series for shrinkage speed calculation. NOTE: time scale of the graph used in 19 hours to improve the visualization of the selected series for calculating the intermediate stage's slope. The dotted lines represent the linear trend line taken from the series with the highest linear R within the intermediate stage.

The lowest mass loss (14.47%) after 24 hours was observed in the mixture with the highest cement/aggregate ratio (mixture 1:3), while the mass loss of mixture 1:6 had the highest value (19.23%). The 1:4 mixture showed an intermediate value (16.19%).

Analysis of variance (F-value: 16.366; F-critical: 4.256; P-value: 0.001) confirmed an inversely proportional influence between cement content and mass loss. This suggests that a greater amount of cement consumes more available water from the mixture, indicating greater hydration, and consequently greater chemical shrinkage. At the same time, water exits from thinner channels when the binder content is higher, which also causes greater shrinkage. Thus, the new test proposed in this article showed sufficient sensitivity to identify the effect of different cement contents in shrinkage mortars.

3.1.2 Sealed with PVC film

The sealed samples showed low-magnitude early shrinkage (maximum of 0.085 mm/m) and low dispersion curve behavior between mixtures (Figure 11).
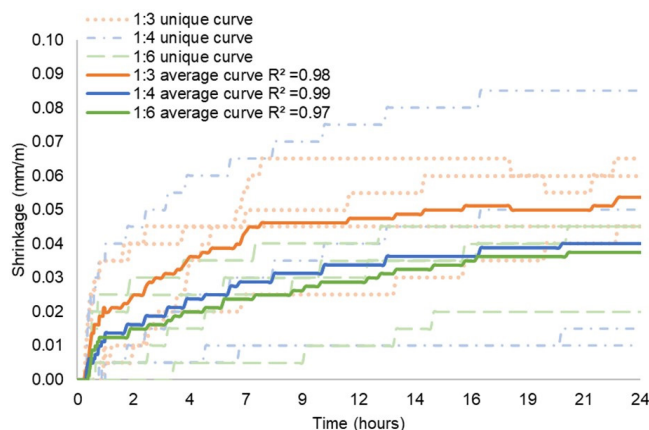
Figure 11. Early shrinkage curves of cement mortars sealed with PVC film. NOTE: dotted lines indicate individual tests, continuous ones are their respective average curves and their legend contains their linear R used to find shrinkage speed.

Visual analysis of Figure 11 does not provide a clear differentiation between mixture behaviour and this observation is confirmed by analysis of variance, which resulted in non-significant for the sealed specimens (F-value: 0.701; F- critical: 4.267; P-value: 0.521). Despite the statistical insignificance, a small difference can be visually observed between the average curves.

The high dispersion of data can be attributed to the fact that 64% of the sealed samples did not show any displacement in one of the dial gauges, and 14% did not show any displacement. This may indicate a failure in the ability of the proposed method to detect low-magnitude shrinkage. The behaviour of the average shrinkage curves for the sealed condition showed a pattern that differs from that found in the other exposure conditions. Therefore, the shrinkage speed study did not use the same linear correlation method, but a logarithmic correlation with the entire data series of the average shrinkage curve of each mixture (Figure 11 shows de R found for each average). An average maximum shrinkage speed of 8,98E-06 mm/m/s was observed for the 1:3 mixture, 47% higher than the 1:4 mixture (6.12E-06 mm/m/s), and 94% higher than the 1:6 mixture (4.63E-06 mm /m/s).

The analysis of variance in the relationship between mixture and mass loss (F-value: 13.229; F-critical: 4.256; P-value: 0.002) remained consistent with what was found in samples exposed to air. The mass loss after 24 hours decreased as the cement content increased. The 1:3, 1:4, and 1:6 mortar mixture had mass loss equal to 3.05%, 3.89%, and 5.09%, respectively. This would correspond to a 76.16% lower mass loss, on average, compared to measurements performed in the mixture exposed to air, which indicates that the PVC film drastically reduces evaporation during the first 24 hours of hydration.

3.1.3 Exposed to wind (5 m/s)

The shrinkage curves of the cement mortar mixtures exposed to 5 m/s wind were marked by an initial abrupt growth followed by an abrupt stagnation (Figure 12). As well as the mortars exposed to the air, the mortars exposed to the wind

also showed a significant response in the maximum shrinkage caused by the variation of the mortar mixture (F-value: 10.790; F-critical: 4.103; P-value: 0.003), that is, by the cement content. The average shrinkage speed within the intermediate stage, for the mixtures exposed to 5 m/s wind, resulted in 1.08E-4 mm/m/s for the 1:3 mixture, 46% higher than the 1:4 mixture (7.41E-5 mm/m/s), and 113% greater than the 1:6 mixture (5.09E-5 mm/m/s). Besides showing all test results from the exposed to wind samples, Figure 12 shows the R linear for each mixture average curve used to find the shrinkage speed.
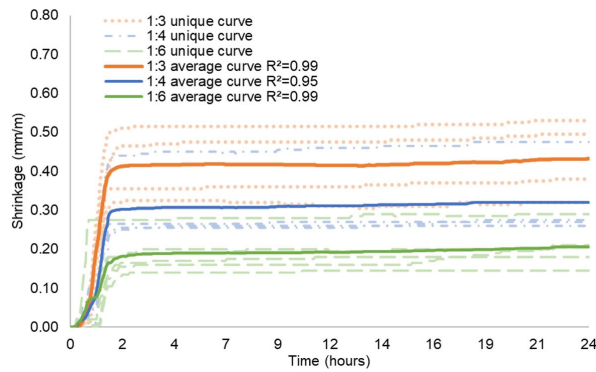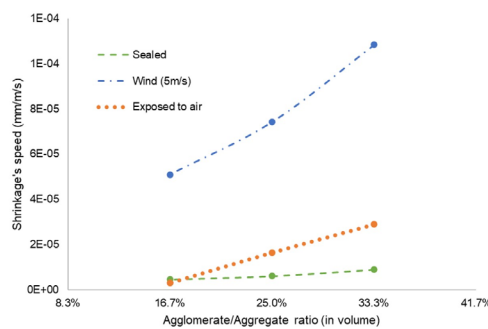

Figure 12. Early shrinkage curves of cement mortars exposed to 5 m/s wind. NOTE: dotted lines indicate individual tests, continuous ones are their respective average curves and their legend contains their linear R used to find shrinkage speed.

The mass loss recorded after the first 24 hours for the samples exposed to wind also resulted in significant variation as a function of the binder concentration (F-value: 72.070; F-critical: 4.102; P-value: 0). Again, the highest mass loss found was in the 1:6 mixture (24.68% on average), the intermediate value in the 1:4 mixture (19.71%), and the lowest value in the mixture with the highest cement concentration, 1:3 (16.7%). Therefore, the proposed new method had sufficient sensitivity for this curing condition.

### 3.1.4 Comparison between exposures for each mixture

Figure 13 shows the comparison between the average shrinkage speeds of cement mortars in the intermediate period, separated by the different exposures used in the tests and the different binder/aggregate ratios.

Figure 13. Average early shrinkage speeds of cement mortars under different air exposure conditions

A trend can be observed concerning the increase in the shrinkage speed to a more intense condition of exposure to air. It is also noted that the difference in speed magnitude between the mixtures with different binder/aggregate ratios is intensified by the greater intensity of exposure to air since the curves become steeper as a function of this exposure.

The analysis of variance for the effect of different exposures on the maximum shrinkage recorded in cement mortars was significant for all mortar mixtures. Figure 14 shows the shrinkage results for the 1:3 mixture under different exposure conditions. Mixtures 1:4 and 1:6 had similar behaviours to 1:3.
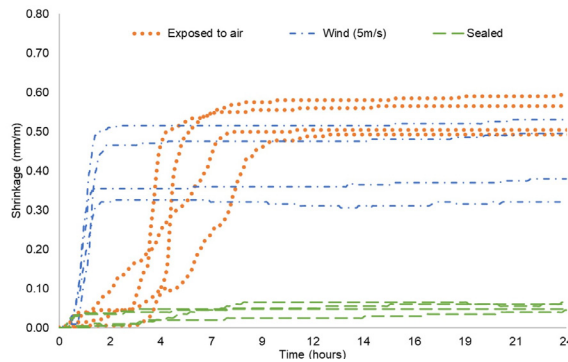
Figure 14. Early shrinkage curves of the individual specimens from the 1:3 mixture and the variation of different exposures to air.

According to Figure 14, the magnitude of the maximum shrinkage is smaller for the tests sealed with PVC film when compared to those exposed to air. This indicates that the lower loss of water by evaporation drastically reduces early shrinkage – which shows the large contribution of drying shrinkage (by evaporation) to early shrinkage. However, the shrinkage recorded in the sealed condition was not null, possibly accusing the test's ability to record the contribution of other types of shrinkage in addition to drying, like chemical shrinkage. Also, there is an expressive difference between the behaviour of shrinkage curves of exposed to wind samples when compared with the behaviour of exposed to air samples. It is visually evident that the wind causes the increase in shrinkage to start earlier and faster, hence the "steepest" appearance of the curve in the early stage.

The maximum shrinkage of the mortar exposed to the wind was smaller or only marginally larger than that exposed to the air. This is justified by the early water loss. As the wind accelerates the loss of water by evaporation, it is likely that later, within the first 24 hours, the mortars exposed to wind will have less water for hydration than those exposed to air, which could minimize the impact of the hydration contribution for total shrinkages, such as chemical shrinkage. Other lower wind speeds would possibly slope the shrinkage curves less and produce different magnitudes of early shrinkage.

3.2 Long term shrinkage

The results for the long-term shrinkage were obtained by the method proposed by ABNT NBR 15261 [25] with the variation of two aspects: demolding of the specimens after 24 hours instead of 48 hours due to schedule and adoption of alternative initial cure conditions.

Although in all exposures the average maximum long-term shrinkage was greater for the 1:3 mixture (0.722 mm/m), intermediate for the 1:4 mixture (0.661 mm/m), and smaller for the 1:6 mixture (0.550 mm/m), the variation of the concentration of binder/aggregates in the cement mortar mixtures was significantly influential on the maximum long-term shrinkage only in the case of specimens exposed to air.

According to Table 5, the maximum long-term average shrinkage was higher for sealed specimens (0.770 mm/m), intermediate for those exposed to air (0.648 mm/m), and lower for those exposed to wind (0.516 mm/m).

Table 5. Comparison of the magnitude of average long-term maximum shrinkage for the different exposures adopted (mm/m)

Exposition	Mixture		
	1:3	1:4	1:6
Sealed	0.848	0.800	0.661
Exposed to air	0.768	0.656	0.520
Wind (5m/s)	0.550	0.528	0.469

The statistically significant influence of exposure on the long-term mean maximum shrinkage was not found only for the 1:6 mixture. It is believed that this occurs due to the 1:6 mixture's smaller magnitude shrinkage, which reduces the dispersion (smaller shrinkage results are closer to each other) and makes it difficult to verify the accuracy with the sample size. Figure 15 illustrates the observed long-term shrinkage behavior for the 1:3 mixture. The other mortar mixtures had similar behavior.
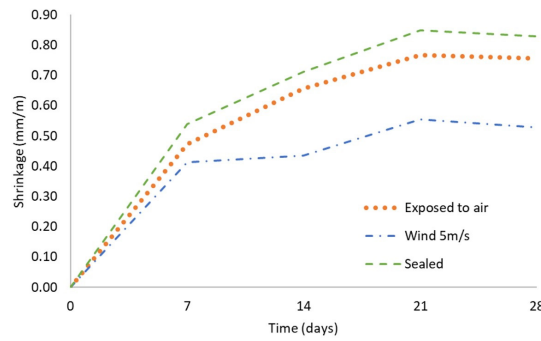
Figure 15. 1:3 mixture's long-term average shrinkage at different air exposures.

As discussed in the 24-hour shrinkage results, the PVC film minimized evaporation on the first day of hydration. Therefore, the sealed specimens would have more water available at long-term ages than those exposed to air and wind, making them more susceptible to drying shrinkage, resulting in greater long-term shrinkage.

The long-term shrinkage behaviour found was reaffirmed by the long-term average maximum mass loss results, with the sealed specimens showing the highest percentage (7.76% on average for all mixtures). The air and wind conditions showed mass loss of 3.37% and 1.18%, respectively. Therefore, within the comparative analysis between the exposures, the specimens that showed the greatest long-term shrinkage were also those that lost more mass in the long term, possibly highlighting the role of drying shrinkage.

3.3 Comparison between early age and long-term shrinkage

Assuming that the total shrinkage consists of the sum of the initial and the long-term values, Table 6 shows the contribution of the initial and long-term shrinkages to the total (represented by the blue bars).

Table 6. Comparison between initial and long-term shrinkage and their contributions to total shrinkage

Exposure	Mixture	Total shrinkage (mm/m)	Percentage of contribution to total shrinkage	
			Early age	**Long term**
Exposed to air	1:3	1.31	41.20%	58.80%
	1:4	0.98	32.90%	67.10%
	1:6	0.69	25.00%	74.90%
Sealed	1:3	0.90	6.00%	94.00%
	1:4	0.84	4.80%	95.20%
	1:6	0.70	5.30%	94.70%
Wind 5 m/s	1:3	0.99	44.00%	56.00%
	1:4	0.85	37.80%	62.20%
	1:6	0.65	28.30%	71.70%

According to Table 6, specimens tend to shrink and lose more water in the long term when sealed in the first 24 hours of hydration than specimens under other conditions. However, the sealed ones shrink in total on average 15% less than those exposed to air and 1% less than those exposed to wind.

Excluding sealed specimens, the cement mortar specimens' long-term shrinkage was 98% greater than their early shrinkage. However, considering that early shrinkage refers to one day of hydration and long-term shrinkage refers to the first 28 days, the initial stage's importance to total shrinkage becomes significant.

The method proposed by the ABNT NBR 15261 [25] standard is similar to the PVC film-sealed condition adopted in the present study and in this condition the total shrinkage occurs mostly in the long-term period (Table 6), which points to the fact that the standard is not losing so much of the total shrinkage reading in this condition by disregarding the initial shrinkage.

However, the condition of exposure of mortars within the practice of civil engineering is much closer to the conditions exposed to air and wind and, as demonstrated, the behavior of total shrinkage observed in these conditions is quite different. Therefore, if the purpose is to study coating mortars and their day-to-day behavior, the standard is

lacking in precision because it ignores the early shrinkage, and the newly proposed method of this paper is the beginning of an attempt to fill this gap.

4 CONCLUSIONS

A method of measuring the early shrinkage in mortars was proposed using the horizontal displacement approach. The test is interesting in terms of low cost, considering that dial gauges were used, and this instrument is cheaper than the LVDT, which is generally adopted in tests that use the same approach. Also, the reading did not depend on data collectors (digital, instruments used to connect watches to computers) since cameras were used in this study. Thus, this article demonstrates the experimental technical feasibility of the proposed method to measure the early shrinkage in mortars.

The test proved to be sensitive to evaluate the effect of cement content on shrinkage, despite the test showing difficulties for low shrinkage values (sealed condition). It was shown that it can detect not only different magnitudes of early shrinkage, but different speeds influenced by cement content and early curing conditions. Also, the test developed by this paper enables the study of early age conditions on long-term shrinkage and the correlation between these ages.

REFERENCES

[1]   C. Hua, P. Acker, and A. Ehrlacher, "Analyses and models of the autogenous shrinkage of hardening cement paste: I. Modelling at macroscopic scale," *Cement Concr. Res.*, vol. 25, no. 7, pp. 1457–1468, Oct. 1995, http://dx.doi.org/10.1016/0008-8846(95)00140-8.

[2]   P. K. Mehta and P. J. M. Monteiro, *Concrete—Microstructure, Properties, and Materials*. New York, NY, USA: McGraw-Hill, 2008.

[3]   C. Maltese, C. Pistolesi, A. Lolli, A. Bravo, T. Cerulli, and D. Salvioni, "Combined effect of expansive and shrinkage reducing admixtures to obtain stable and durable mortars," *Cement Concr. Res.*, vol. 35, no. 12, pp. 2244–2251, Dec. 2005, http://dx.doi.org/10.1016/j.cemconres.2004.11.021.

[4]   M. Kayondo, R. Combrinck, and W. P. Boshoff, "State-of-the-art review on plastic cracking of concrete," *Constr. Build. Mater.*, vol. 225, pp. 886–899, Nov. 2019, http://dx.doi.org/10.1016/j.conbuildmat.2019.07.197.

[5]   E. E. Holt, *Early Age Autogenous Shrinkage of Concrete*. Espoo: VTT Tech. Res. Centre of Finland, 2001.

[6]   E. Holt, "Contribution of mixture design to chemical and autogenous shrinkage of concrete at early ages," *Cement Concr. Res.*, vol. 35, no. 3, pp. 464–472, Mar. 2005, http://dx.doi.org/10.1016/j.cemconres.2004.05.009.

[7]   R. S. Khairallah, "Analysis of autogenous and drying shrinkage of concrete," M.S. thesis, Civil Eng. Dept., McMaster Univ., Hamilton, Canada, 2009.

[8]   R. D. Tolêdo Fo, K. Ghavami, M. A. Sanjuán, and G. L. England, "Free, restrained and drying shrinkage of cement mortar composites reinforced with vegetable fibres," *Cement Concr. Res.*, vol. 27, pp. 537–546, May 2005.

[9]   T. A. Hammer, "Deformations, strain capacity and cracking of concrete in plastic and early hardening phases," Ph.D. dissertation, Norwegian Univ. Sci. Technol., Trondheim, Norway, 2007.

[10] ASTM International, *Standard Test Method for Autogenous Strain of Cement Paste and Mortar, ASTM C1698-19*, 2019.

[11] ASTM International, *Standard Test Method for Evaluating Plastic Shrinkage Cracking of Restrained Fiber Reinforced Concrete (Using a Steel Form Insert), ASTM C1579*, 2021.

[12] China Building Industry Press, *Standard Test Methods for Drying Shrinkage Stress and Cracking Possibility of Cement Mortar and Concrete, GB/T 29417-2012*, 2012.

[13] D. Ravina, "Early longitudinal dimensional changes of fresh fly ash mortar exposed to drying conditions," *Cement Concr. Res.*, vol. 16, pp. 902–910, Nov. 1986.

[14] L. Brüll, K. Komlos, and B. Majzlan, "Early shrinkage of cement pastes, mortars, and concretes," *Matér. Constr*, vol. 13, pp. 41–45, Jan. 1980.

[15] M. A. Sanjuán and A. Moragues, "A testing method for measuring plastic shrinkage in polypropylene fibre reinforced mortars," *Mater. Lett.*, vol. 21, pp. 239–246, Nov. 1994.

[16] A. Kronlöf, M. Leivo, and P. Sipari, "Experimental study on the basic phenomena of shrinkage and cracking of fresh mortar," *Cement Concr. Res.*, vol. 25, pp. 1747–1754, Dec. 1995.

[17] R. D. Tolêdo Fo and M. A. Sanjuán, Effect of low modulus sisal and polypropylene fibre on the free and restrained shrinkage of mortars at early age," *Cement Concr. Res.*, vol. 29, pp. 1597–1604, Oct. 1999.

[18] P. K. X. Bastos, C. Détriché, J. Balayssac, and M. Concotto, "Retração e desenvolvimento de propriedades mecânicas em argamassas de revestimento," *Amb. Constr.*, vol. 2, pp. 57–70, Apr./Jun. 2002. In Portuguese.

[19] A. Messan, P. Ienny, and D. Nectoux, "Free and restrained early-age shrinkage of mortar: Influenceof glass fiber, cellulose ether and EVA (ethylene-vinyl acetate)," *Cement Concr. Res.*, vol. 33, pp. 402–410, Mar. 2011.

[20] N. G. D. Silva, "Avaliação da retração e da fissuração em revestimento de argamassa na fase plástica," Ph.D. dissertation, Univ. Federal Santa Catarina, Florianópolis, Brazil, 2011. In Portuguese.

[21] T. Le-Bihan, J. F. Georgin, M. Michel, J. Ambroise, and F. Morestin, "Measurements and modeling of cement base materials deformation at early age: The case of sulfo-aluminous cement," *Cement Concr. Res.*, vol. 42, pp. 1055–1065, Aug. 2012.

[22] H. Pei, Z. Li, B. Zhang, and M. Hongyan, "Multipoint measurement of early age shrinkage in low w/c ratio mortars by using fiber Bragg gratings," *Mater. Lett.*, vol. 131, pp. 370–372, Sep. 2014, http://dx.doi.org/10.1016/j.matlet.2014.05.202.

[23] Y. Bao, W. Meng, Y. Chen, G. Chen, and K. Khayat, "Measuring mortar shrinkage and cracking by pulse pre-pump Brillouin optical time domain analysis with a single optical fiber," *Mater. Lett.*, vol. 145, pp. 344–346, Apr. 2015.

[24] H. Kwak, S. Ha, and W. J. Weiss, "Experimental and numerical quantification of plastic settlement in fresh cementitious systems," *J. Mater. Civil Eng.*, vol. 22, pp. 951–966, Oct. 2010.

[25] Associação Brasileira de Normas Técnicas, *Mortar for Laying and Covering Walls and Ceilings – Determination of Dimensional Variation (Linear Shrinkage or Expansion), ABNT NBR 15261*, 2005. In Portuguese.

[26] L. S. Girotto, M. O. Vita, M. P. Barbosa, and W. L. Repette, "Cracking and plastic shrinkage test of self-compacting concrete in fresh state: test procedure," in *An. 53º Congr. Brasileiro Concreto*, Instituto Brasileiro do Concreto, Org. Nov. 2011, pp. 1-12. In Portuguese.

[27] C. H. Détriché, "Contribution à l'étude des déformations des couches minces de mortiers de liants hydrauliques," Ph.D. dissertation, Univ. Paul Sebatier Toulouse, Toulouse, France, 1977.

[28] T. Wongtanakitcharoen and A. F. Naaman, "Unrestrained early age shrinkage of concrete with polypropylene, PVA, and carbon fibers," *Mater. Struct.*, vol. 40, no. 3, pp. 289–300, Apr. 2007.

[29] P. Soroushian and S. Ravanbakhsh, "Control of plastic shrinkage cracking with specialty cellulose fibers," *Mater. J.*, vol. 95, no. 4, pp. 429–435, Jan. 1998.

[30] Associação Brasileira de Normas Técnicas, *Aggregates - Determination of Granulometric Composition, ABNT NBR NM 248*, 2003. In Portuguese.

[31] Associação Brasileira de Normas Técnicas, *Aggregates - Determination of Unit Mass and Void Ratio, ABNT NBR 16972*, 2021. In Portuguese.

[32] Associação Brasileira de Normas Técnicas, *Aggregates - Determination of the Fine Material Passing Through the 75 µm Sieve per Wash, ABNT NBR 16973*, 2021. In Portuguese.

[33] Associação Brasileira de Normas Técnicas, *Fine Aggregate — Determination of Density and Water Absorption, ABNT NBR 16916*, 2021. In Portuguese.

[34] American Society for Testing and Materials, *Standard Specification for Blended Hydraulic Cements, ASTM C595/C595M - 21*, 2021.

[35] A. M. Neville, *Properties of Concrete. Elasticity, Shrinkage and Creep*. London: Pitman Publishing Limited, 2002.

[36] Associação Brasileira de Normas Técnicas, *Mortar for Laying and Covering Walls and Ceilings - Determination of Consistency Index, ABNT NBR 13276*, 2016. In Portuguese.

[37] Associação Brasileira de Normas Técnicas, *Mortar for Laying and Covering Walls and Ceilings - Preparation of the Mixture for Testing, ABNT NBR 16541*, 2016. In Portuguese.

[38] J. L. D. Ribeiro and C. T. Caten, *Experiment Design*. Porto Alegre: UFRGS, 2003. In Portuguese.

ERRATUM

Erratum: Proposal for estimating the punching shear load-carrying capacity of steel fibers reinforced concrete flat slabs

In the article **"Proposal for estimating the punching shear load-carrying capacity of steel fibers reinforced concrete flat slabs"**, DOI number https://doi.org/10.1590/S1983-41952023000500009, published in IBRACON Structures and Materials Journal ISSN 1983-4195, v.16, n.5, e16509, 2023, on page 11:

ACKNOWLEDGEMENTS

Where it reads:

The authors would like to express their gratitude for the graduate program in civil engineering of the *Universidade Federal de Uberlandia* and the funding agency CAPES.

It should be read:

The authors would like to express their gratitude for the graduate program in civil engineering of the *Universidade Federal de Uberlândia* and the funding agency *Fundação de Amparo à Pesquisa do Estado de Minas Gerais* (FAPEMIG) and *Coordenação de Aperfeiçoamento de Pessoal de Nível Superior* (CAPES).